FUNCTIONAL ARCHITECTURE OF MEDIAL TEMPORAL LOBE

PATHWAYS AND MNEMONIC DISCRIMINATION

IN YOUNG AND ELDERLY ADULTS

Dissertation

zur Erlangung des akademischen Grades

doctor rerum naturalium
(Dr. rer. nat.)

genehmigt durch die Fakultät für Naturwissenschaften
der Otto-von-Guericke-Universität Magdeburg

von: **Dipl.-Psych. David Berron**
geboren am 15. März 1986 in Riedlingen

Gutachter: Prof. Dr. Emrah Düzel

Prof. Dr. Dr. h.c. Herta Flor

eingereicht am: 21. Februar 2017

verteidigt am: 5. September 2017

ACKNOWLEDGMENTS

ABSTRACT

Subregions in the medial temporal lobe (MTL) are critically involved in human episodic memory. While the perirhinal cortex (PrC) plays a key role in memory for objects, the parahippocampal cortex (PhC) is preferentially involved in memory for context. Furthermore, a fundamental property of an episodic memory system is the ability to minimize interference between similar episodes. The dentate gyrus (DG) subfield of the hippocampus is widely viewed to realize this function through a computation referred to as pattern separation, which creates distinct non-overlapping neural codes for individual events. In this thesis, high-resolution magnetic resonance imaging (MRI) techniques were used to investigate the functional organization of the MTL as well as age-related effects on memory pathways. In the first experiment, high-resolution MRI at 7 Tesla (T) was used to develop a segmentation protocol that enables researchers to manually delineate hippocampal subfields as well as extrahippocampal subregions. Critically, the protocol incorporates novel neuroanatomical findings which led to more detailed boundaries between subregions. Most notably, it includes more anatomically accurate boundary definitions for subregions that are differentially involved in hippocampal computations (e.g. DG and CA3) and are affected in early Alzheimer's Disease (AD) (e.g. area 35). In the second experiment, ultra-high-resolution fMRI at 7T and multivariate pattern analysis (MVPA) was used to provide compelling evidence that the DG subregion specifically sustains representations of similar scenes that are less overlapping than in other hippocampal (e.g. CA3) and MTL regions (e.g. entorhinal cortex) – a key prediction of memory models on pattern separation. Studies in rodents and nonhuman primates suggest that the entorhinal cortex (ErC) can be further divided into subregions that connect differentially with PrC vs. PhC and with hippocampal subfields along the proximo-distal axis. However, the functional organization of the human ErC to date remains largely unknown. Consequently, ultra-high-resolution fMRI at 7T was used in combination with functional connectivity analyses in the third experiment to parallel the animal studies and identify functional subdivisions of the human ErC based on their preferential intrinsic functional connectivity with PrC and PhC as well as proximal and distal subiculum. The results suggest an anterior-lateral (alErC) and a posterior-medial (pmErC) functional subregion in the human ErC. In the fourth experiment, the domain-specific organization of MTL pathways was investigated using a novel mnemonic discrimination task with objects and scenes. It was shown that domain-specific pathways in the MTL extend towards the subregions of the ErC where the alErC was preferentially involved in object memory while the pmErC was more involved in memory for scenes. Also, both pathways were differentially involved in mnemonic discrimination of objects but also showed some overlap in the discrimination of scenes. In addition, the results suggest that the two pathways are differentially affected by ageing where the object (PrC-alErC) but not the scene processing pathway (PhC-pmErC) shows reduced activity. The present results advance our knowledge of the functional and computational organization of the entorhinal-hippocampal circuitry and have implications for theories and models of memory, and mnemonic discrimination in particular. Given that the finding of reduced activity in the object processing pathway – PrC and alErC – in ageing overlaps with the locus of early AD pathology, the results are critical for future studies investigating functional impairment in ageing and early AD. Furthermore, the results demonstrate the potential of ultra-high-resolution MRI for fine-grained analysis of functional activity as well as structural morphometry of subregions in the human MTL.

TABLE OF CONTENTS

CHAPTER

1

GENERAL INTRODUCTION

1.1 ORGANIZATION OF MEDIAL TEMPORAL LOBE NETWORKS

The parahippocampal gyrus (PhG) and the adjacent hippocampal formation are key anatomical structures in the human medial temporal lobe (MTL) (Eichenbaum et al., 2007; Squire et al., 2004), and are heavily involved in several cognitive functions including human memory (Eichenbaum et al., 2007; Squire et al., 2004), spatial navigation (Ekstrom et al., 2003; Epstein, 2008; Wolbers and Büchel, 2005), perception (Aly et al., 2013) and imagination (Maguire and Hassabis, 2011; Schacter et al., 2012). Thus, the following paragraphs will introduce the anatomical and functional organization as well as the main connections between subregions in the MTL that are most relevant for the current thesis.

1.1.1 ANATOMY OF THE HUMAN PARAHIPPOCAMPAL-HIPPOCAMPAL NETWORK

The human PhG consists of subregions that can be distinguished along its longitudinal axis. While the anterior PhG is occupied by the entorhinal (ErC) and perirhinal cortex (PrC), the posterior portion of the PhG is referred to as the parahippocampal cortex (PhC) (Ding and Van Hoesen, 2010; Insausti and Amaral, 2012; Pruessner et al., 2002) (see Figure 1A). The hippocampal formation refers to the subiculum, the cornu ammonis 1-3 (CA1, CA2 and CA3) and the dentate gyrus (DG) (Insausti and Amaral, 2012, van Strien et al., 2009) (see Figure 1B for subfield proportions in a section from the hippocampal body). Throughout this thesis, the term "hippocampus" will be used to refer to all subfields of the hippocampal formation although some authors use it to specifically refer to the CA regions (e.g. Insausti and Amaral 2012).
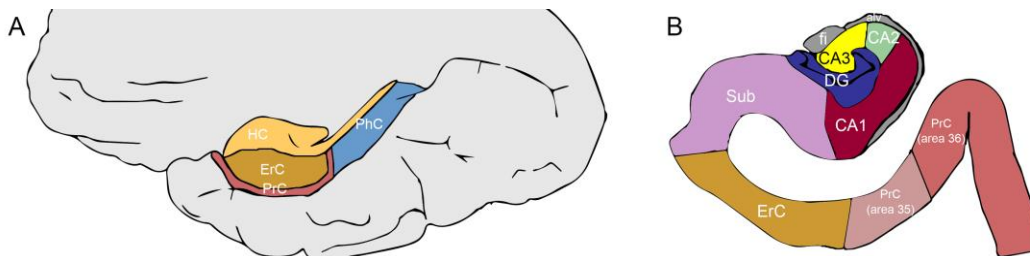
Figure 1. Anatomical organization of subregions in the MTL. (A) shows a sagittal view of MTL subregions. **(B)** shows a coronal slice through the hippocampal body and adjacent gyri (adapted from Ding et al., 2016). *HC, hippocampus; ErC, entorhinal cortex; PrC, perirhinal cortex; PhC, parahippocampal cortex; Sub, subiculum; CA, cornu ammonis; DG, dentate gyrus; fi, fimbria; alv, alveus.*

1.1.2 CONNECTIVITY IN THE PARAHIPPOCAMPAL-HIPPOCAMPAL SYSTEM

The regions in the PhG and the hippocampus are densely connected and most information of their connectivity comes from rodent tract tracing studies (see van Strien et al., 2009 for review). First, I will discuss connections within the PhG. The PrC and the postrhinal cortex (POR), which is the homologue of the human PhC, project to the medial and lateral ErC (mErC and lErC) (Burwell and Amaral, 1998a, 1998b). However, while PrC has stronger connections to the lateral portion of the ErC, the POR has stronger connections to the medial portion of the ErC. Likewise, mErC and lErC both project to PrC and POR. In addition, there are extensive direct connections between PrC and POR (Burwell and Amaral, 1998a, 1998b; Furtak et al., 2007). Thus, the main pattern of connectivity suggests two parallel

pathways in the parahippocampal gyrus which is of functional relevance as described later. One that includes the perirhinal cortex and lateral entorhinal cortex and the other including parahippocampal cortex and the medial entorhinal cortex.

With respect to connections between the PhG and the hippocampus, the perforant pathway constitutes the major input pathway and projects from the ErC to all hippocampal subregions. While mainly the entorhinal layer II projects to the DG and CA3 (Steward and Scoville, 1976; Swanson and Köhler, 1986), mainly layer III projects to CA1 and the subiculum (Kerr et al., 2007; Tamamaki and Nojyo, 1995; Witter and Amaral, 1991). This is true for both the mErC and the lErC (van Strien et al., 2009). However, there is a difference in ErC projections to CA1 and the subiculum. While lErC projects to the distal portion of CA1 and the proximal portion of the subiculum, mErC projects mostly to proximal CA1 and distal subiculum (Naber et al., 2001a; Tamamaki and Nojyo, 1995). This indicates that the parallel pathways in the parahippocampal gyrus (PrC-lErC and PhC-mErC) extend toward subregions of the hippocampus.

Hippocampal subfields are themselves inter-connected via the polysynaptic pathway (van Strien et al., 2009). Cells in the DG project to CA3 via the mossy fibers, and neurons in CA3 are in turn connected to CA1 via the Schaffer collaterals (Ishizuka et al., 1990; Kajiwara et al., 2008; Witter, 2007). Finally, cells in CA1 project to the subiculum. An important feature of the hippocampal connectivity system are the recurrent collaterals within CA3 (Ishizuka et al., 1990; Li et al., 1994), which form an auto-associative network. This is a network of neurons with collaterals that terminate on dendrites of the parent cell (van Strien et al., 2009), and which is of special interest for computational models described in chapter 1.2. Finally, the hippocampal outputs to the PhG originate in the subiculum and CA1 and project primarily to the deep layers of the ErC (Swanson and Cowan, 1977). For a simplified schematic showing the main connections described above see Figure 2.

As it is not possible to perform tract tracing studies in humans, all the data on connections within the MTL are derived from rodent studies and in general most of our knowledge to date comes from work on the brain of rodents and monkeys (Lavenex and Amaral, 2000). However, despite the differences in anatomical locations as well as the size of MTL regions, high consistency across species with respect to anatomy as well as connectivity is assumed. Nevertheless, one should bear in mind that very little is known about the connectivity of the ErC and hippocampal subfields as well as neocortical regions in the human. This results from the lack of signal-to-noise ratio (SNR) and spatial resolution in current functional magnetic resonance imaging (fMRI) studies at 3 Tesla (T) MRI.
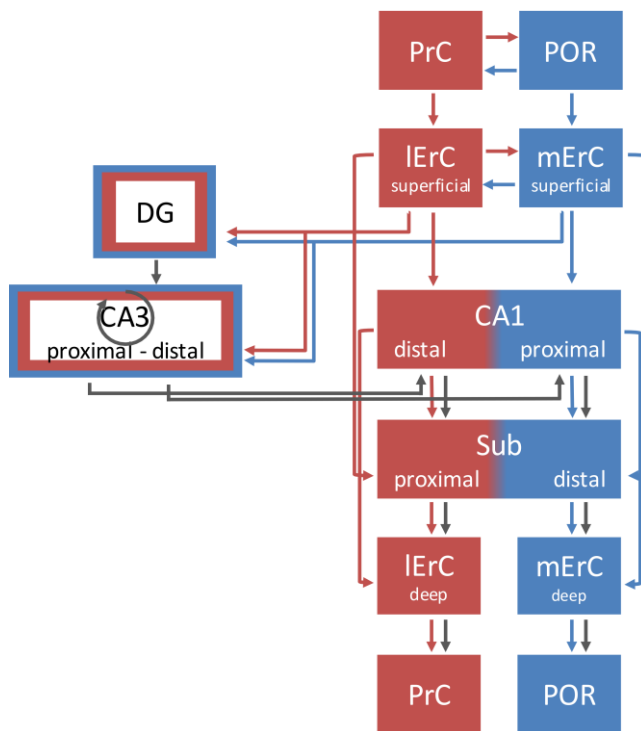
Figure 2. Parallel processing streams into the hippocampus (adapted from Knierim et al., 2014). Neocortical regions project to the PrC and POR, which in turn provide the main source of input to the hippocampus. The PrC projects to the lateral entorhinal cortex (lErC), and the POR projects to the medial entorhinal cortex (mErC). The ErC projects to all subfields of the hippocampus via the perforant pathway. The lErC and mErC thereby connect to distinct regions of CA1 and subiculum, segregated along the transverse axis of the hippocampus. CA1 and subiculum send return projections to the deep layers of the ErC. There is crosstalk along these pathways, both prior to their entry into the hippocampus and especially in the convergent projections to the DG and CA3. It is suggested that the mErC and lErC streams are merged onto the same CA3 pyramidal cells and DG granule cells. The DG projects to CA3 via the mossy fibres. The recurrent collaterals in CA3 are represented by the grey circle. CA3 Schaffer collaterals project to CA1 and the combined representations are then merged in CA1 with the separate input streams from the direct ErC–CA1 projections. See van Strien et al., 2009 and Knierim et al., 2014 for details. Distal and proximal means distal and proximal with respect to DG.

1.1.3   DOMAIN-SPECIFIC FUNCTIONAL PROCESSING STREAMS IN THE MTL

Based on the anatomical organization of the MTL described above, there are two emerging parallel processing pathways which will be described in the following paragraphs. While the PrC gets most of its neocortical inputs from brain regions that process information about objects (what-information), the PhC receives its inputs mostly from areas in the brain that are involved in the processing of spatial information (where-information) (Eichenbaum et al., 2012, 2007). These inputs originate from the visual ventral and dorsal stream respectively (Kravitz et al., 2011; Mishkin et al., 1983). It has been shown that these pathways are functionally involved in different forms of memory-guided behavior (for review see Ranganath and Ritchey, 2012). The precuneus, the posterior cingulate, the retrosplenial cortex (RsC), and the PhC as well as the ventromedial prefrontal cortex and the mammillary bodies are particularly involved in spatial processing and memory. In contrast, the PrC as well as regions in the anterior temporopolar cortex, the orbitofrontal cortex and the amygdala are preferentially involved in the processing and memory of objects (Ranganath and Ritchey, 2012; Ritchey et al., 2015). The two networks are referred to as the posterior-medial (PM system) and the anterior temporal system (AT system) respectively (see Figure 3).

It is known from animal studies that these functional systems extend towards the ErC, that is, the mErC is more involved in spatial processing whereas the lErC is more involved in the processing of non-spatial information (Deshmukh and Knierim, 2011). More precisely, while the mErC seems to be involved in computations based on a global reference frame using information about scenes and boundaries in

the environment, lErC is suggested to process information about individual objects and locations based on a local reference frame (Knierim et al., 2014). Therefore, mErC is suggested to provide the hippocampus with information about the spatial context, while lErC provides information about the content of an experience. Although there are connections between the PrC and PhC as well as between lErC and mErC (van Strien et al., 2009) spatial and object information remain mostly segregated (Eichenbaum et al., 2007) (see Figure 2). Anatomical studies in rodents add to the complexity and suggest that spatial/context and non-spatial/object information might even remain separate in hippocampal subregions CA1, CA3 and subiculum (Nakamura et al., 2013; Sauvage et al., 2013) before they are assumed to converge in the DG (Knierim et al., 2014).
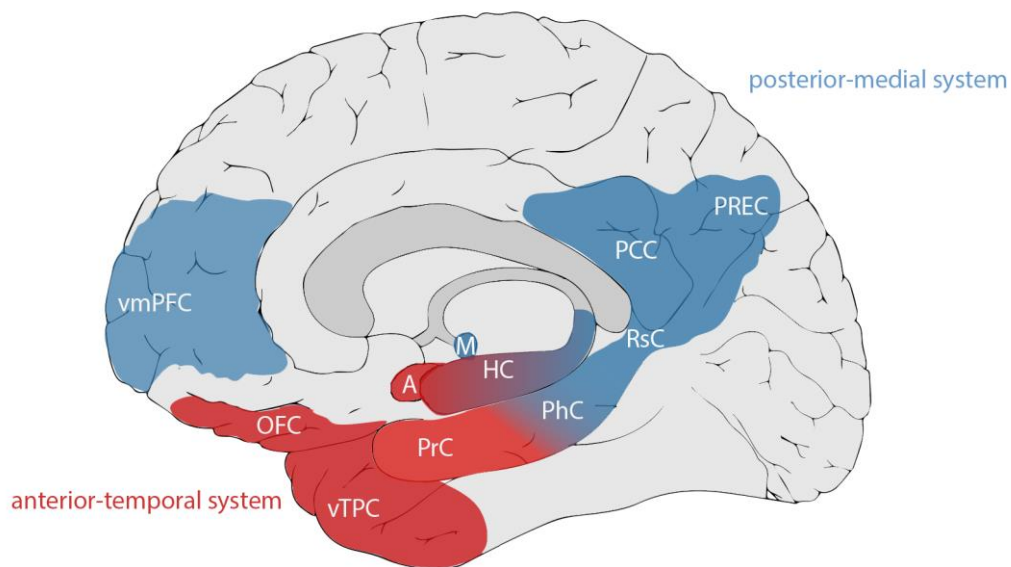
Figure 3. Anterior-temporal and posterior-medial cortical systems. While regions in red indicate the anterior-temporal system, regions in blue belong to the posterior-medial system (Figure adapted from Ranganath and Ritchey, 2012). *vmPFC, ventromedial prefrontal cortex; OFC, orbitofrontal cortex; vTPC, ventral temporopolar cortex; PrC, perirhinal cortex; A, amygdala; M, mammillary bodies; HC, hippocampus; PhC parahippocampal cortex; RsC retrosplenial cortex; PCC, posterior cingulate cortex; PREC, precuneus.*

1.2 COMPUTATIONAL MECHANISMS OF HIPPOCAMPAL FUNCTION

1.2.1   *HIPPOCAMPAL COMPUTATIONS: PATTERN SEPARATION AND PATTERN COMPLETION*

Many computational models of hippocampal function were influenced by the work of David Marr. In his theory of the archicortex, a structure that is now better known as the hippocampus, he presented a model that already integrated the available knowledge of hippocampal anatomy at that time (Marr, 1971). In the model, simple representations of memories, that do not contain the full and detailed information about an event, are stored in the hippocampus. These simple representations contain information that is needed to trigger the associated full representation, which is stored in neocortical regions that were involved during this event. The hippocampus was thought to temporarily memorize patterns of activity that represent events during the day and then transfer them to the neocortex for permanent storage during the night. Two features of the model are particularly important for the understanding of hippocampal computations and will be further discussed below.

First, Marr suggested that sparse encoding of simple representations using only a small portion of cells would make any two similar patterns more distinct from one another and therefore would be most effective for high storage capacity. This relates to the question how interference between similar memories can be reduced. In an everyday situation where one locks his bike regularly in front of a train station, which is crowded by bicycles, it will be difficult to find it later when coming back. That is because there are so many competing similar memories where the bike was locked at different locations in front of the same train station. How does the brain resolve such interference between similar memories? One potential solution is pattern separation in the hippocampus. Pattern separation is a mechanism whereby similar patterns are decorrelated (or orthogonalized) to create distinct and independent representations that reduce the interference between these similar memories. The unique anatomical and physiological organization of the entorhinal-hippocampal circuitry inspired computational theories which suggested the DG to be ideally suited to perform pattern separation (McClelland et al., 1995; Treves and Rolls, 1994). According to those models, orthogonalization is most efficient if the brain region that is involved in pattern separation contains many more cells than the region where the input is coming from. In the rat, there are about 200 000 ErC layer II cells that project to about 1 million granule cells in the DG (Amaral et al., 1990). Thus, the information coming from the ErC diverges onto a much larger number of dentate granule cells, which increases the sparseness of the representation. Studies in rodents showed that the activity in the DG indeed appears to be very sparse (Diamantaki et al., 2016; Jung and McNaughton, 1993; Leutgeb et al., 2007) and there are sparse connections between DG granule cells and CA3 pyramidal cells via the mossy fibers which further induce a sparse firing rate in CA3 (Amaral et al., 1990; Kesner and Rolls, 2015). DG inputs converge to only 330 000 cells in CA3 where each CA3 cell receives only approximately 50 mossy fiber inputs. Thus, there is a low probability that different input patterns in the ErC activate the same subset of cells in CA3. This highlights the important role of the DG in pattern separation - that is the decorrelation of similar input patterns from the ErC to prevent interference with existing memories.

Second, retrieval was implemented in Marr's model so that a partial cue could gradually recreate the correct simple representation, which in turn would reactivate the full neocortical representation of an event. This directly relates to pattern completion - a hippocampal computation that allows us to retrieve memories from partial cues. As reviewed above, most inputs to CA3 cells come from other CA3 cells throughout the hippocampus via recurrent collaterals (Amaral et al., 1990; Amaral and Witter, 1989; Ishizuka et al., 1990). It is suggested that CA3 thus acts as an auto-associative network, which allows retrieval of the whole memory representation even if it is only triggered by partial information via pattern completion (McNaughton and Morris, 1987; Treves and Rolls, 1994).

1.2.2   EVIDENCE FROM RODENT STUDIES

The hippocampus was suggested to function as a spatial map as it contains neurons that are active when the animal moves through a particular location and thus create a representation of the environment – so called place cells (O'Keefe, 1976; O'Keefe and Dostrovsky, 1971). The spatial pattern of place cell activity remains constant if there are no changes in the environment. However, if the environment changes exceed a certain threshold, remapping of place cells can be observed (Colgin et al., 2008). Empirical studies in rodents lend strong support for the important role of the DG in pattern separation. Leutgeb and colleagues recorded place cell activity from hippocampal subfields CA3 and DG in experiments where the animal freely moved around (Leutgeb et al., 2007). Critically, to investigate whether cells in the DG and CA3 indeed represent small changes in the environment – a key prediction from computational models – the environment was gradually changing from square- to circular-shaped. They found that even minimal changes to the environment had substantial effects on the firing patterns in the DG (rate remapping) while larger changes led to recruitment of new cell populations in CA3 (global remapping). However, pattern separation is defined as a transformation of correlated input patterns in the ErC to less correlated patterns in the DG. Neunuebel and Knierim therefore recorded in two different studies from cells in the ErC as well as DG and CA3 during a task where global and local cues were put in conflict in order to induce parametric changes in the environment (Neunuebel et al., 2013; Neunuebel and Knierim, 2014). While cells in the DG showed correlations between the patterns from sessions without changes in the environment (i.e. indicating a similar representation of the same environment), they showed decorrelated patterns as soon as changes were introduced (i.e. indicating a different representation for slightly different environments) (Neunuebel and Knierim, 2014). Critically, these patterns were more decorrelated compared to the ErC and CA3 (Neunuebel et al., 2013), thus demonstrating that the DG hosts more distinct representations for similar environments than CA3 and ErC. As the DG receives its inputs from the ErC, this was direct evidence that the DG is involved in the decorrelation of similar input patterns from the ErC.

1.2.3   EVIDENCE FROM HUMAN STUDIES

It is difficult to investigate pattern separation mechanisms in humans as noninvasive techniques cannot assess direct neuronal computations. Therefore, researchers have developed tasks that are supposed to pose high demands on pattern separation functions by varying sensory input to induce interference between similar events (see Liu et al., 2016 for a summary of behavioral paradigms). The most commonly used task is a continuous object recognition paradigm which is known as the Mnemonic Similarity Task (MST) (Bakker et al., 2008; Kirwan and Stark, 2007). In the MST, participants are presented with a continuous stream of objects which can be either first presentations (new), repetitions (old) or similar to an earlier stimulus (similar). In the explicit memory version of the task,

subjects had to respond to each stimulus with old, new or similar judgements whereas they were asked for indoor/outdoor judgements in the implicit task version. The analysis of the fMRI data followed a repetition suppression (or fMRI adaptation) approach (Grill-Spector et al., 2006). Repetition suppression fMRI is widely-used to assess neural representations and it builds on the fact that blood-oxygen-level dependent (BOLD) fMRI activity levels decrease with repeated stimuli possibly due to neuronal adaptation (Grill-Spector et al., 2006; Krekelberg et al., 2006). For pattern separation, this leads to the following assumptions: If a brain region is not involved in pattern separation, it should show repetition suppression for similar lures that is comparable to repetitions. This might be due to a similar neuronal population involved in the underlying neural representation of both stimulus versions (see Figure 4A). Critically, a region that is involved in pattern separation should not show repetition suppression for lures due to the orthogonalized neural representation of the similar lure stimulus (see Figure 4B). Thus, the critical measure is the novelty signal (i.e. no repetition suppression) in similar lures compared to the lack of a novelty signal in repetitions (i.e. repetition suppression) (Yassa and Stark, 2011). Throughout the experiments presented in this thesis I will refer to the enhanced activity for lure stimuli compared to repeated ones (lures > repetitions) as lure-related novelty. The fMRI results from the MST pointed towards lure-related novelty responses (higher activity for lures than repeats) in bilateral DG/CA3 but not in other hippocampal subfields (e.g. CA1) or extrahippocampal regions (ErC, PrC and PhC) (Bakker et al., 2008; Lacy and Stark, 2012). Although these results fit nicely to the findings in the rodent literature and the predictions from computational models, one has to bear in mind that repetition suppression is an indirect measure of neuronal computations and its underlying mechanisms are not yet entirely understood in human fMRI (Grill-Spector et al., 2006).
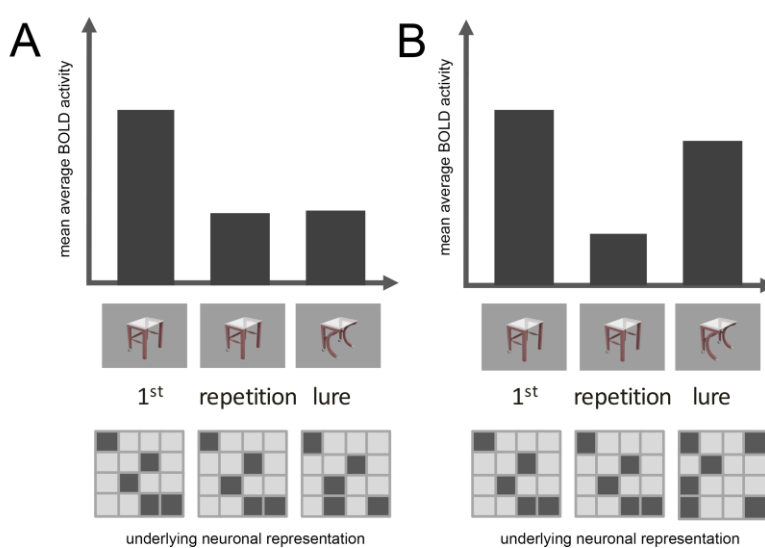
Figure 4. Repetition suppression fMRI to investigate representations. A brain region shows a decrease in activity with repeated stimulus presentations (e.g. the repeated presentation of the same table). This decrease is referred to as repetition suppression. **(A)** If a brain region is not involved in pattern separation, there should be repetition suppression for similar lures that is comparable to repetitions due to the similar neuronal population involved in the underlying neural representation of both stimulus versions. **(B)** A brain region that is involved in pattern separation should not show repetition suppression for lures due to the orthogonalized underlying neural representation of the lure stimulus. See Grill-Spector et al., 2006 and Yassa and Stark, 2011 for more details.

1.3 VULNERABILITY TO AGEING AND ALZHEIMER'S DISEASE

Ageing as well as neurodegenerative diseases affect the structural integrity of the human brain and particularly the MTL. Those changes are accompanied by specific alterations in critical medial temporal circuits and computations resulting in behavioral impairments. Therefore, I will review the known effects of ageing and Alzheimer's disease (AD) on the MTL in the following paragraphs.

1.3.1 AGEING

Aged individuals often show difficulties in episodic memory, which is the encoding and conscious remembering of events (Grady and Craik, 2000). Executive functions including working memory, attention, processing speed and task switching are also subject to age-related decline (see Grady, 2012 and Hedden and Gabrieli, 2004 for reviews). Furthermore, ageing has widespread effects on the neocortex – especially on prefrontal and temporal cortices (Fjell and Walhovd, 2010; Raz and Rodrigue, 2006; Salat et al., 2004).

Structural integrity of the hippocampal system

Hippocampal volume decreases with increasing age (Fraser et al., 2015; Raz et al., 2005) and correlates with memory performance in ageing (Gorbach et al., 2016; Hedden et al., 2016; O'Shea et al., 2016). A more detailed analysis of the volumetric changes of hippocampal subfields seems to be promising and there is evidence that ageing especially affects the DG and CA3 (Mueller and Weiner, 2009; Pereira et al., 2014; Shing et al., 2011; Small et al., 2004, 2002; West, 1993). However, it should be noted that there are also contrasting results that suggest that more research and harmonized segmentation criteria are needed to understand the effects of ageing on volume of hippocampal subfields (de Flores et al., 2015a; Yushkevich et al., 2015a).

Ageing may affect the hippocampus in various ways (see Leal and Yassa 2015 for review). First, entorhinal inputs to DG and CA3 are reduced by synapse loss in the rodent perforant pathway (Smith et al., 2000). Simultaneously, the number of synapses onto CA3 cells coming from their recurrent collaterals is not reduced during ageing. Diffusion-tensor imaging studies in humans could also show atrophy of the perforant pathway in healthy (Yassa et al., 2010a) and memory-impaired older adults (Kalus et al., 2006) compared to young healthy individuals. This degradation of the perforant pathway was furthermore correlated with memory deficits (Yassa et al., 2011b). Other factors include the reduced modulation by cholinergic and dopaminergic systems in ageing, the reduced activity of inhibitory interneurons and weakened synaptic plasticity (see Wilson et al., 2006 for review).

Functional impairments of the hippocampal system

It was suggested that these changes might lead to an imbalance of hippocampal computations where the DG as a result fails to orthogonalize similar input patterns while CA3 shows increased pattern completion activity (Wilson et al., 2006). This might lead to problems to encode new information

sufficiently differently from already-stored memories resulting in increased interference. Indeed, studies in humans using the MST, where elderly subjects had to discriminate similar from repeated images, lends support to these hypotheses (Yassa et al., 2011b). In this study, similar images were more often identified as old by the older age group, which suggests that elderly individuals required more dissimilarity between images to generate lure-related novelty signals in the hippocampus. In addition, lure-related novelty responses in BOLD fMRI were associated to measures of memory performance and perforant pathway integrity suggesting that indeed changes in hippocampal integrity are linked to alterations in hippocampal computations and memory impairment.

Structural and functional integrity of the parahippocampal gyrus

Age-related effects on volume of extrahippocampal regions are less pronounced (Salat et al., 2004). While there are correlations of age with hippocampal volume, there is no or only weak evidence for reduced volume of ErC, PhC and PrC in ageing (Dickerson et al., 2009; Raz et al., 2005). There are, however, studies suggesting functional impairment of the aged PrC. Burke and colleagues showed that during the exploration of environments including objects, aged rats had reduced PrC Arc protein levels (Burke et al., 2012) and their PrC's firing rates were reduced (Burke et al., 2014), which might both explain an observed behavioral object discrimination deficit (Burke et al., 2011). A similar finding has been shown by Ryan and colleagues in humans. In their fMRI study, participants had to complete an object matching task using objects with high and low overlap of features in order to modulate task difficulty. They showed that the PrC of young individuals was engaged during the matching of highly similar object pairs. Intriguingly, elderly participants not only performed worse but also showed reduced activity in bilateral anterior PrC (Ryan et al., 2012). Taken together these findings point to early alterations and functional impairment in the aged PrC.

Differentiation of ageing and neurodegeneration

Studies focused on healthy ageing try to exclude elder participants with early cognitive signs of dementia. However, it is challenging to successfully distinguish between brain ageing and neurodegeneration (see Jagust 2013 for review). Post-mortem studies show that even cognitively normal elderly adults presented substantial AD pathology (Bennett et al., 2006). This fits well with studies using positron emission tomography (PET) or cerebrospinal fluid (CSF) measures that show evidence of AD pathology (amyloid-beta; see following paragraph) already in normal elderly subjects (Jagust et al., 2009; Morris et al., 2010). Therefore, it is possible that a significant number of ageing studies have included subjects with preclinical AD and that some of the alterations seen in ageing may be related to pre-symptomatic AD (Jagust, 2013). However, it is now possible to stratify elderly subjects for amyloid positive and negative markers using amyloid PET imaging. Following this approach Oh and colleagues showed that even elderly subjects without evidence of fibrillar brain amyloid-beta show declines in memory and executive function in comparison to young subjects (Oh et al., 2012).

1.3.2 ALZHEIMER'S DISEASE

Neuropathological characterization of AD

The hallmarks of AD pathology are amyloid plaques and neurofibrillary tangles (Hyman et al., 2012). While amyloid plaques are extracellular amyloid-beta (Abeta) depositions, neurofibrillary tangles (NFT) constitute intracellular aggregates of hyperphosphorylated tau protein (Jack and Holtzman, 2013). NFTs follow a specific topographic pattern of progression. They first appear in the brain stem (locus coeruleus) and the transentorhinal region before they spread to the ErC, and the hippocampus (Braak and Braak, 1991). In later stages, NFTs spread to limbic areas of the medial and inferior temporal lobe, posterior cingulate cortex, cortical association areas and finally to primary sensory-motor areas as well as visual areas (Braak et al., 2006; Braak and Braak, 1991; Braak and Tredici, 2011).

Structural MRI

Regions in the MTL are among the earliest sites affected by neurodegeneration in AD. MRI in humans showed that cortical thinning in the ErC becomes evident already in cognitively normal individuals that later progress towards AD (Stoub et al., 2005) as well as in patients with mild AD (Dickerson et al., 2009). Other studies highlighted early atrophy in preclinical AD and amnestic mild cognitive impairment (MCI) compared to normal controls in the PrC and mainly the lateral portion of the ErC, which was more pronounced in the left hemisphere (Miller et al., 2015; Yushkevich et al., 2015b). Although hippocampal volume seems to be a good predictor for the conversion from the MCI stage towards AD (Jack et al., 1999), more fine-grained measures at the level of hippocampal subfields might provide more sensitive markers of degeneration (Maruszak and Thuret, 2014). Indeed, most studies report focal atrophy of the CA1 subfield in the early stages of AD and some studies suggest that the analysis of focal atrophy patterns compared to whole hippocampal volumetry might improve the diagnosis at the MCI stage (see de Flores et al., 2015 for review).

Functional imaging studies

Recently, a functional imaging study examined cognitively normal elderly subjects that later progressed towards AD using high-resolution cerebral blood volume (CBV) fMRI to assess metabolism in brain regions that are early affected during the disease (Khan et al., 2014). Their results suggest that the ErC and PrC showed decreased metabolism in elderly subjects that progressed towards mild AD compared to subjects that did not. Detailed analyses suggested that the lErC might be more affected than the mErC and that the impairment in metabolism correlated with brain regions in the PhG and the precuneus which further suggests that AD effects spread along connected brain regions (see also Liu et al., 2012). In a different line of research, several human imaging studies showed evidence for hyperactivity in the MTL in early disease stages using fMRI (Bakker et al., 2015, 2012; Dickerson et al., 2005; O'Brien et al., 2010; Yassa et al., 2011a). Dickerson and colleagues showed that MCI patients presented hyperactivity in the hippocampus compared to normal controls and AD patients (Dickerson

et al., 2005). In a later study, they reported that elderly subjects that already had memory impairments showed higher BOLD activity and a steeper decline of BOLD activity 2 years later (O'Brien et al., 2010). This suggests that early pre-symptomatic stages of AD are characterized by hyperactivity whereas later stages of profound AD show a decrease in activity (see Dickerson and Sperling, 2008 for a review). Studies using mnemonic discrimination tasks that pose high demands on pattern separation also showed evidence for hyperactivity in hippocampal subregions DG and CA3 as well as decreased discrimination performance of visually similar lure stimuli in patients with amnestic MCI and even normal controls (Yassa et al., 2011a, 2010b). Bakker and colleagues showed that a pharmacological intervention was successful in decreasing activity in DG and CA3 which was in turn associated with an increase in discrimination performance (Bakker et al., 2015, 2012). The experiments from *Bakker et al.* point towards a pathological role of MTL hyperactivity which is further corroborated by other studies (Huijbers et al., 2015; Leal et al., 2017). Overall, these findings are in line with the predictions reviewed earlier that ageing and disease processes have effects on the balance of hippocampal computations and thus lead to an encoding impairment of novel events (see Wilson et al., 2006 for review).

Alterations in preclinical AD

AD pathology is assumed to be present in the human brain several years before clinical symptoms occur. Thus, it is important to foster research that aims for the early detection of AD related impairments which is hoped to lead to earlier diagnosis and is why the concept of preclinical AD was introduced to neurodegenerative research (Sperling et al., 2014, Dubois et al., 2016). Given our knowledge on specific and targeted impairments in MTL structures in these early stages, subtle but specific impairments might be expected in preclinical AD that precede hippocampal impairment. As these early impairments overlap substantially with object processing pathways described earlier (PrC-alErC), it will be important to understand how these networks are functionally affected by ageing and disease. It might well be that specific functional networks are affected earlier than others which might have effects on specific cognitive measures (Didic et al., 2011).

1.4 HIGH-RESOLUTION STRUCTURAL AND FUNCTIONAL MRI OF THE MTL

In all experiments presented in this thesis MRI was used. Thus, the technique will be shortly introduced in the following paragraphs and differences between MRI at low and high magnetic fields will be described. Finally, challenges in the analysis of ultra-high-resolution MRI data will be summarized.

1.4.1 HIGH-RESOLUTION MRI AT LOWER FIELD STRENGTHS

In order to understand the functional role of the various small subregions, their functional networks, and their specific susceptibility to ageing and disease described above, it is important to image the whole parahippocampal-entorhinal circuitry. Tract-tracing methods as well as single cell recordings in animals can only provide information on subregions of the system of interest. In contrast, MRI allows

non-invasive investigation of the whole brain by providing structural and functional measures. FMRI has become a very powerful and important technique to investigate human brain function. It is based on the BOLD contrast, which is an indirect measure of neuronal activity depending on the different magnetic properties of oxygenated and deoxygenated blood hemoglobin (Ogawa et al., 1990). Standard fMRI sequences can image the whole brain with approximately 3mm isotropic resolution. This resolution, however, does not allow the investigation of small subregions such as hippocampal subfields – neither structurally nor functionally. Recent approaches using high-resolution fMRI that is optimized to image the human MTL make this technique particularly useful to identify the functional role of small subregions. Current approaches can image partial volumes that cover the MTL with a resolution of about 1.5mm isotropic voxels (Bakker et al., 2008; Carr et al., 2010). High-resolution imaging consequently comes at the cost of a partial imaging volume, which means that due to the increase in resolution and thereby increased number of scanning slices only a specific portion of the brain can be imaged within the same time. Therefore, high-resolution MRI should only be applied if there is a strong hypothesis about specific and small brain regions or networks.

1.4.2 ULTRA HIGH-FIELD MRI AT 7T

Although high-resolution MRI at lower field strengths enables researchers to investigate subregions in the MTL, the resolution as well as the SNR is not enough to resolve important boundaries. MRI at higher field strengths is favorable due to the increase in spatial resolution and SNR. As SNR increases almost linearly with field strength, 7T provides significantly higher SNR compared to 3T and this increase is highest at high resolution (Pohmann et al., 2016; Triantafyllou et al., 2005). Early studies at 7T showed that it is possible to image the human hippocampus in detail at 7T using structural (Kerchner et al., 2010; Theysohn et al., 2009; Thomas et al., 2008) as well as fMRI (Theysohn et al., 2013). Theysohn and colleagues could show reliable memory related activity in the hippocampus which was significantly stronger compared to 3T, suggesting higher BOLD sensitivity at 7T.

The experiments described in chapter 2-4 focused on the detection of fine grained representations in small MTL subregions as well as their functional connectivity and morphometry. Thus, these experiments are all based on 7T MRI sequences. The structural sequences used here include T1, T2 and T2* weighted contrasts and range from 0.33 to 0.6mm in-plane resolution and 0.6 to 2mm slice thickness (see Figure 5). The functional echo-planar imaging (EPI) sequence that is used in those experiments has an isotropic resolution of 0.8mm. Due to the high resolution, functional as well as structural sequences only cover partial brain volumes (see Figure 5).
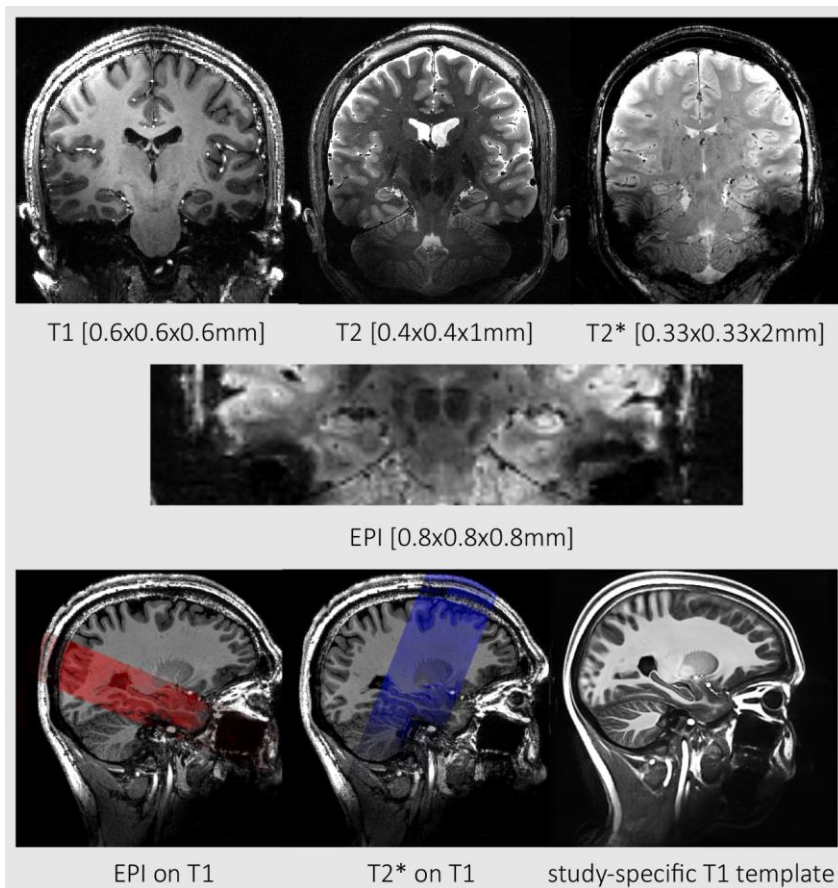
Figure 5. Examples of main sequences that were used in this thesis. For structural brain scans, high-resolution T1 weighted (0.6mm isotropic), T2 weighted (0.4x0.4x0.4mm) and T2* weighted (0.33*0.33*3mm) sequences were used (upper row). In order to investigate functional activity, an echo-planar imaging (EPI) sequence (0.8 isotropic) was used (middle row). Due to the high in-plane resolution and small slice thickness, EPI as well as T2 and T2* weighted sequences did only cover parts of the brain. The resulting overlap of partial volumes with the whole brain T1 weighted sequence is displayed in the bottom row. In order to do group analyses in a common space, study specific group templates were generated using ANTs (see right image in bottom row).

High-resolution approaches that aim for the investigation of small subregions are challenging and require specific analysis techniques. Most analysis tools that are provided in neuroimaging packages are not optimized for the higher-resolution available at 7T. Therefore, tools from different neuroimaging packages were combined in the following analyses. This includes the Statistic Parametric Mapping package (SPM, Wellcome Trust Centre for Neuroimaging, London), the FMRIB Software Library (FSL, Oxford Centre for Functional MRI of the Brain) and Advanced Normalization Tools (http://stnava.github.io/ANTs/). Three challenges will be introduced that played an important role in the experiments described in chapter 3, 4 and 5. MRI studies at standard resolution using 3T MRI scanners usually face the problem that due to motion in the scanner or separate scanning sessions, structural (e.g. T1 or T2 weighted sequences) and functional (e.g. EPI sequences) images are not perfectly aligned to each other. To assign functional results to specific brain regions both whole brain images have to be coregistered. This can be achieved using coregistration algorithms implemented in the common neuroimaging packages (e.g. SPM, FSL). The situation in high-resolution imaging studies at 7T is different as the images that must be coregistered only cover a specific portion of the image. Thus, they share less overlapping information that can be used to realign the images (see Figure 5, bottom row). Coregistration issues become even more critical as the experiments in this thesis focused on subregion-specific activity in the MTL where only small inaccuracies in coregistration can have severe implications for the analysis. Therefore, a combination of carefully tuned coregistration

algorithms from FSL and ANTs packages was used to align structural and functional images in this thesis.

To analyze group activity patterns, as will be shown in chapters 3, 4 and 5, it is critical to project the data of each individual participant to a common space that represents all the participants. Group templates based on T1-weighted standard resolution (1mm isotropic voxels) images representing the general population are provided with all neuroimaging packages. However, these group templates do not provide the resolution and contrast available at 7T. In addition, they do likely not accurately represent aged individuals, which will be necessary in chapter 5. Therefore, a sample specific group template was generated in chapters 3, 4 and 5 using Advanced Normalization Tools (ANTs) (see Figure 5; buildtemplateparallel.sh, Avants et al, 2010).

In high-resolution studies focused on small brain regions rather than whole brain analyses one additional problem is the definition of regions of interest (ROI). In MRI studies at 3T a common approach is to define an ROI based on an atlas in standard space (e.g. Talairach space or Montreal Neurological Institute (MNI) space). However, this approach is prone to individual inaccuracies in coregistration and spatial normalization. In addition, this approach does not take into account the individual variability in anatomical patterns. Therefore, all subregions in chapter 3, 4 and 5 were manually delineated based on anatomical boundaries following manual segmentation protocols (e.g. Wisse et al., 2012). Recent findings in neuroanatomy, however, have altered previously assumed subregion boundaries. Consequently, for the reasons described above, a new segmentation protocol was established in chapter 2.

As activity patterns in subregions of the MTL were of specific importance in these experiments, it was necessary to make sure that functional maps of all individuals shared as much overlap as possible in these subregions. Therefore, a landmark-guided normalization technique was used that matched target regions delineated on the individual images as well as the common group template space using Region of Interest-Advanced Normalization Tools (ROI-ANTS (Avants et al., 2011; Yassa and Stark, 2009). First, the hippocampal head (HH; on the first slice on which it appears), ErC (on the first 4 consecutive slices, starting on the HH slice), the hippocampal body (HB) and the PhC (same slices as HB) were labeled on the group-specific template as landmarks for the subsequent landmark-guided alignment. Similarly, subject-specific ROIs were drawn on the individual T1-weighted images to match the template priors. Finally, the expectation-based point set registration (SyN[0.5]) was used to register the individual T1 weighted images on the T1-template based on the labeled landmarks.

1.5 AIM AND OUTLINE

In this thesis, high-resolution imaging techniques were used to investigate the anatomy and connectivity between subregions in the MTL. The main purpose was to further understand the detailed organization of MTL pathways and derive more fine-grained subdivisions based on the animal

literature. In addition, the aim was to elucidate the functional and computational role of subregions in domain-specific processing as well as mnemonic discrimination that poses high demands on pattern separation. Further understanding of both the structural and functional organization of MTL pathways, is important as brain regions in the human MTL as well as specific episodic memory functions show enhanced vulnerability to ageing and early stages of disease (Dickerson et al., 2009; Stark et al., 2015, 2013). Consequently, a specific focus of this thesis is the question which memory pathway shows earlier impairments in ageing and might thus be important for the early detection of AD related alterations.

In this General Introduction, I introduced concepts that relate closely to the experiments that are presented in this thesis including a summary of MTL anatomy and connectivity, an overview of functional MTL networks and computations as well as an introduction to the vulnerability of the MTL to ageing and Alzheimer's Disease (Chapter 1). In the following, I will present the empirical work of this thesis in four chapters (Chapters 2-5). In chapter 2, a novel manual segmentation protocol is presented, which is based on recent anatomical and histological findings with the aim to enable researchers to investigate the role of MTL subregions with respect to function but also ageing and early neurodegeneration in AD. In chapter 3, the central prediction of computational models that subregions in the MTL and hippocampal subfields are differentially involved in pattern separation is tested using ultra-high-resolution functional imaging at 7 Tesla. In chapter 4, the functional anatomy of networks in the MTL is investigated and intrinsic functional connectivity analyses were used to test whether the ErC in humans is similarly organized compared to rodents and primates. In chapter 5, a task was designed to investigate the functional organization and integrity of these functional networks that are vulnerable to alterations in ageing and early stages of AD. Finally, all experiments are summarized and discussed in chapter 6.

CHAPTER

2

PROTOCOL FOR MANUAL SEGMENTATION OF SUBREGIONS IN THE MEDIAL TEMPORAL LOBE AT 7T

2.1 INTRODUCTION

The human hippocampus and the adjacent medial temporal lobe (MTL) regions have been implicated in a number of cognitive functions including episodic memory, spatial navigation and perception. At the same time, MTL regions are affected by a number of pathological conditions such as depression (Huang et al., 2013), posttraumatic stress disorder (Wang et al., 2010), epilepsy (Bernasconi et al., 2003), and neurodegenerative diseases like Alzheimer's Disease (Dickerson et al., 2004; Du et al., 2007; Rusinek et al., 2004). In vivo MRI research on the functional anatomy of the human hippocampus and the MTL has made considerable progress over the past years and novel neuroanatomical findings have increased our knowledge on subdivisions of the MTL (for a recent atlas, see Ding et al., 2016). More specifically, novel data became available on the boundaries of the subdivisions in the perirhinal cortex (PrC) - area 35 and area 36 - depending on sulcal patterns that differ between hemispheres in continuity and depth (Ding and Van Hoesen, 2010). Likewise, the boundaries of subiculum (Sub) and CA1 in the hippocampal head (HH), have been shown to feature anatomical variations between individuals that depend on the number of hippocampal digitations (Ding and Van Hoesen, 2015).

Until recently, a major barrier to further advances in research on the MTL was the sparse anatomical reference from histological studies to guide in vivo segmentation of these regions. Often only a few slices from a small number of cases are presented in histological reference materials. As a result, there is limited information available about the location of subregion boundaries for in vivo segmentation protocols, especially with regard to anatomical subvariants. Additionally, most of the extant histological reference material is based on samples sectioned at orientations different from in vivo T2-weighted MR images, used for MTL subfield segmentation, that are typically obtained perpendicular to the long axis of the hippocampus (Yushkevich et al., 2015a). It is unclear how much this difference in orientation affects the relative location of the boundaries within the MTL and how well it translates to in vivo MR images, especially in the more complex head region of the hippocampus (these issues were also mentioned in Wisse et al., 2016a). The aforementioned new histological study by Ding and Van Hoesen addresses this point as they presented data from 15 samples sectioned perpendicular to the long axis of the hippocampus, thereby matching commonly used MR images, and providing more than a single case to account for anatomical variations between brains (Ding and Van Hoesen, 2015).

However, the delineation of these small MTL structures on in vivo MRI is also limited by the information available in commonly used MR images. T2-weighted 3T images with high in-plane resolution are generally used to delineate hippocampal subfields because of the visualization of the stratum radiatum lacunosum moleculare (SRLM), which appears as a thin dark band on these scans and can be used to define borders between some of the subfields. Such high in-plane resolution can often only be obtained at the cost of either lower signal-to-noise ratio or larger slice thickness, given the limited scan time available especially in clinical populations. This limits the precision of the measurements in-plane and along the long axis of the hippocampus. Recent developments at 3T, and the increased availability

of ultra-high resolution MRI at 7T now allow for increased signal-to-noise ratio and resolution and thereby a more consistent visualization of internal features from slice to slice while maintaining a smaller slice thickness (of up to 1mm) in a reasonable scan time.

Indeed, several segmentation protocols have been published for 7T (Boutet et al., 2014; Goubran et al., 2014; Maass et al., 2015, 2014; Parekh et al., 2015; Suthana et al., 2015; Wisse et al., 2012) leveraging the improved visualization for the distinction of small subfields such as the dentate gyrus (DG) and CA3 in the hippocampus (Parekh et al., 2015) , the SRLM (Kerchner et al., 2012), and allowing for specific analyses of subregions of the ErC (Maass et al., 2015) and even entorhinal layers (Maass et al., 2014). However, most 7T protocols limit the segmentation to the hippocampal body, with the exception of Wisse et al. (2012) and Suthana et al. (2015). Additionally, most published 7T protocols have not reported inter- or intra-rater reliability. Aside from that, there is also a considerable number of hippocampal subfield segmentation protocols available at lower field strengths (Daugherty et al., 2015; Joie et al., 2013; Malykhin et al., 2010; Mueller et al., 2007; Winterburn et al., 2013; Zeineh et al., 2001). However, none of these protocols – neither at 3 nor at 7T – have incorporated the anatomical variations dependent on hippocampal indentations (Ding and Van Hoesen, 2015).

Manual segmentation protocols that include extrahippocampal regions PrC and PhC mainly exist for T1 weighted images with standard resolution at 3T MRI (Feczko et al., 2009, Insausti et al., 1998, Kivisaari et al., 2013, Pruessner et al., 2002; but see Suthana et al., 2015 and Yushkevich et al., 2015b for T2 weighted high-resolution MRI). The manual segmentation of the ErC and PrC is complex, as the anatomical boundaries change based on the depth of the collateral sulcus, which is further complicated by the variability of sulcal patterns across hemispheres. Only few protocols at 3T provide depth-specific rules (Insausti et al., 1998; Kivisaari et al., 2013) and even less consider different subvariants of sulcal patterns (Feczko et al., 2009). Crucially, no protocol has yet incorporated the more comprehensive and novel information on MTL anatomy (Ding et al., 2009; Ding and Van Hoesen, 2010) while leveraging the high resolution at 7T to provide subvariant-specific and depth-dependent rules that account for the variability across and within subjects.

There is a large multi-investigator effort currently underway to develop a harmonized protocol for hippocampal subfields and extrahippocampal subregions (Wisse et al., 2016a), following the harmonized protocol for the total hippocampus (Apostolova et al., 2015; Frisoni et al., 2015). This harmonization effort was launched to overcome significant differences reported between extant segmentation protocols (Yushkevich et al., 2015a). However, the harmonization effort is currently aimed at 3T MRI (first limited to the hippocampal body, to be followed by expansion to the head and tail), and the protocol for 7T and extrahippocampal regions is not anticipated for several more years.

The aim of this study was therefore to establish a segmentation protocol to manually delineate subregions in the parahippocampal gyrus as well as hippocampal subfields while leveraging the information available at 7T MRI images. We incorporated newly available information from histological

studies and conferred with a neuroanatomist (S.-L.D.) to provide anatomically valid and reliable rules. Intra- and inter-rater reliability results are included for 22 hemispheres of younger adults. Additionally, this manuscript provides a comprehensive description of the segmentation of extrahippocampal regions, including detailed information on anatomical variation between subjects.

Please note, although this protocol is presented as the first study within this thesis, it was only finished after the other studies were already done. Therefore, the protocol presented in this chapter was not used for the manual delineation of subregions in the following studies throughout this thesis but relied on earlier published protocols instead.

2.2 MATERIALS AND METHODS

2.2.1 PARTICIPANTS

Participants were included using baseline data from a study investigating the effects of physical exercise on the brain. Exclusion criteria were reports of regular sports activities that improve cardiovascular fitness as well as high physical activity levels. In addition, participants were screened for known metabolic disorders and neurological or psychiatric history, and excluded from further examination in case of incidents reported during history taking. Participants were recruited from the Otto-von-Guericke University campus in Magdeburg. Fifteen young and healthy individuals (16 hemispheres) were included from the baseline scan before any intervention. Seven additional subjects (8 hemispheres) were included after refining the rules for sulcus depth measurements (age range 19-32; mean age = 26, 12 female; see 2.2.9 and 2.3.1). In total, we used 24 hemispheres of these subjects. All subjects gave informed and written consent for their participation in accordance with ethic and data security guidelines of the Otto-von-Guericke University Magdeburg. The study was approved by the local ethics committee.

2.2.2 WORKSHOP

In order to test the usability of the manual segmentation protocol, we hosted a segmentation workshop for 35 participants who were mostly novices (29 out of 35). The protocol was sent out four weeks prior to the workshop in combination with example MR images to give participants the opportunity to familiarize themselves with the segmentation approach. On site, we presented the protocol followed by an intensive hands-on session. From that, we used the given feedback and most commonly occurring problems to refine the protocol and improve comprehensibility for novice raters. This includes figures that provide a quick overview of the rules Figure 14), more detailed annotations of the slice-by-slice plots (Figure 8, Figure 9, Figure 11, Figure 12) as well as supplemental material (see Supplementary Figures) of cases with rare anatomic variants.

2.2.3 IMAGE ACQUISITION

Imaging data were collected at the Leibniz Institute for Neurobiology in Magdeburg on a 7T MR scanner (Siemens, Erlangen, Germany) with a 32-channel head coil (Nova Medical, Wilmington, MA). We acquired 22 partial turbo spin echo (TSE) T2-weighted images oriented orthogonal to the long axis of the hippocampus (in-plane resolution = 0.44 × 0.44mm, 55 slices, slice thickness = 1mm, distance factor = 10%, TE = 76 ms, TR = 8000ms, flip angle = 60°, FOV = 224mm, bandwidth = 155 Hz/Px, echo spacing = 15.1ms, TSE factor = 9, echo trains per slice = 57). The slice thickness of 1mm together with the 10% distance factor results in a distance of 1.1mm between slices. Scan-time was 7:46 minutes.

2.2.4 SEGMENTATION SOFTWARE

Structures were manually traced by two experienced raters (A.H. and A.L.) on oblique coronal slices using ITK-SNAP (Version 3.4; www.itksnap.org; Yushkevich et al., 2006). The images were adjusted for equivalent contrast range prior to segmentation (by capping the contrast curve at a maximum of 500). ITK-SNAP provides very useful features for implementing this protocol, i.e. an annotation tool for drawing lines and measuring distances.

2.2.5 MANUAL SEGMENTATION PROTOCOL

The protocol describes rules for manual segmentation of structures in the MTL in coronal MR images. The segmentation guidelines for the parahippocampal cortex (PhC), perirhinal cortex (PrC; area 35 and 36), entorhinal cortex (ErC) as well as the outer contours of the hippocampus are described in the first part (2.2.7), and further subdivision of the hippocampus into subfields are described in the second part (2.2.8; for a segmentation hierarchy see Figure 6). Boundary rules are based on recent data from neuroanatomical atlases (Ding and Van Hoesen, 2015, 2010; Ding et al., 2016; Mai et al., 2015). In this protocol, we separately report neuroanatomical evidence and resulting rules which can be applied to MR images. Boundary rules are provided in millimeters to make the protocol applicable to scans of different resolution and facilitate comparisons with the neuroanatomical literature. The protocol is particularly focused on T2-weighted images acquired at 7T with 0.44×0.44mm² in-plane resolution and 1mm slice-thickness with 0.1mm spacing. Some inner boundaries described in the section about hippocampal subfields, especially the boundaries of CA3 and DG that rely on the visualization of the endfolial pathway (Lim et al., 1997), are likely only applicable to 7T high-resolution T2 images. However, the described protocol could potentially also be applicable to other images that are acquired orthogonally to the long axis of the hippocampus with similar in-plane resolution and larger slice-thickness (e.g. 2mm slice thickness).
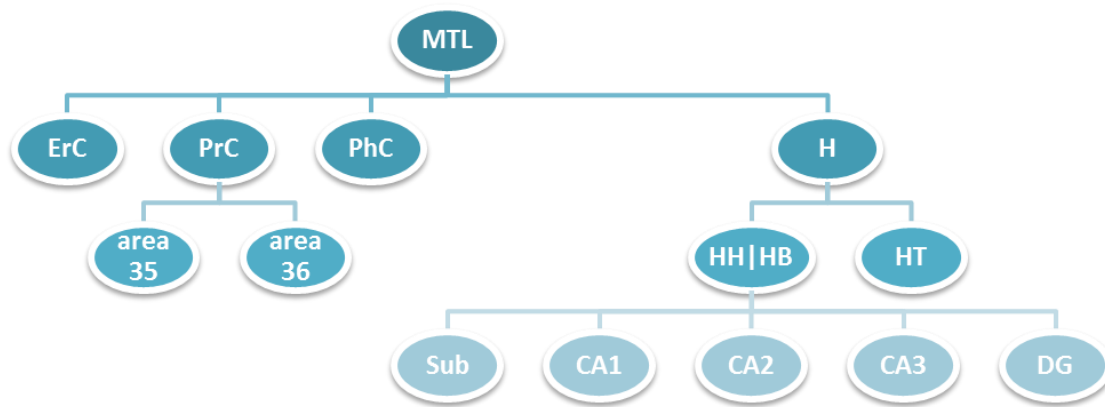
Figure 6. Segmentation hierarchy. Segmentation of entorhinal cortex (ErC), area 35 and 36 of the perirhinal cortex (PrC), parahippocampal cortex (PhC) and the whole hippocampus separated into head (HH), body (HB) and tail (HT) are described in 2.2.7 (dark blue) and segmentation of hippocampal subfields is described in 2.2.8 (light blue).

2.2.6 ANATOMICAL LABELS USED IN THE PROTOCOL

In this protocol, we segment ErC, PrC and PhC. We differentiate between area 35 and 36, which are frequently considered together as constituting the PrC in manual segmentation protocols (Duncan et al., 2014; Ekstrom et al., 2009; Olsen et al., 2013; Preston et al., 2010; Zeineh et al., 2001), except for (Kivisaari et al., 2013; Yushkevich et al., 2015b). However, these regions constitute different neuroanatomical parts of PrC (Ding and Van Hoesen, 2010). Therefore, following the terminology of Ding and Van Hoesen, we refer to these regions as area 35 and 36. Note that these regions are slightly different from Brodmann areas 35 and 36 as the latter extend more posterior than area 35 and 36 in our study (for discussion see Ding and van Hoesen, 2010). We note that area 35 roughly corresponds to the transentorhinal region (Braak and Braak, 1991) and also to the medial PrC (Kivisaari et al., 2013). Detailed guidelines for hippocampal subfields involve the boundaries between the subiculum (Sub), CA fields 1-3 and the dentate gyrus (DG). Note that our segmentation of Sub includes subiculum proper, prosubiculum, presubiculum and parasubiculum (Ding, 2013). Also, the DG here includes the hippocampal hilus or region CA4, as these cannot be separated at this field strength. The SRLM is equally divided between its surrounding structures and not segmented separately. Hippocampal subfield segmentation encompasses the whole hippocampal head (HH) and body (HB) and is not performed in the tail (HT) because of the limited information with regard to the subfield boundaries in this region.

2.2.7 HIPPOCAMPUS AND SUBREGIONS IN THE PARAHIPPOCAMPAL GYRUS

2.2.7.1 Exclusions: alveus, fimbria, cerebrospinal fluid and blood vessels

Fimbria and alveus as well as blood vessels, all appearing hypointense, (see Figure 7) are excluded from anatomical masks as they do not belong to any particular subfield (Duvernoy et al., 2013). In general, the hippocampus is enclosed by white matter, visible as a hypointense line surrounding it. This line is spared from segmentation in this protocol. Additionally, there are several blood vessels within and

close to the hippocampus. Both blood vessels and potential concomitant signal dropout should be excluded from the segmentation. Cerebrospinal fluid (CSF) and cysts appear hyperintense on T2-weighted MRI. Cysts, often located in the hippocampal sulcus (hippocampal fissure) at the ventrolateral flexion point of CA1 (van Veluw et al., 2013) are given a separate label. CSF - either surrounding the hippocampus or along a whole sulcus (e.g. hippocampal, uncal, collateral, occipito-temporal sulci) - is entirely excluded from the anatomical masks. CSF in sulci can be given a separate label as CSF (see explanation below).
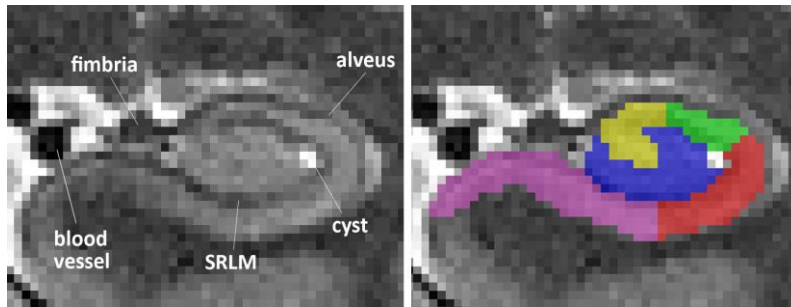
Figure 7. Excluded structures in a coronal view. Anterior hippocampal body slice from a T2 MRI scan including alveus, fimbria, SRLM, a blood vessel and a cyst in the ventrolateral flexion point of CA1 in the vestigial hippocampal sulcus. *SRLM, stratum radiatum lacunosum moleculare.*

2.2.7.2 Hippocampal formation

In the following we provide segmentation rules separately for the hippocampal head, body and tail. This is done to structure the following section rather than to construct independent masks of head, body and tail portions.

Hippocampal head

The anterior tip of the hippocampal head (HH) can be easily identified without additional landmarks (see Figure 8, HH0). Once the uncal sulcus can be followed from its fundus to the medial surface, the ErC becomes the inferior boundary of the HH, which is segmented by connecting the most medial point of the white matter to the most medial point of the grey matter (see Figure 8, HH4; Wisse et al. 2012). At the posterior end of the HH, the uncus separates from the hippocampus (see Figure 8, HH14). While it is still connected to the rest of the HH (via grey matter), the hippocampus is segmented as one structure (see Figure 8, HH13). Once the uncus is separated (e.g. only connected via the fimbria), the HH and uncus are segmented as separate structures in the coronal plane (see Figure 8, HH15).

Hippocampal body

The hippocampal body (HB) begins when the uncus has disappeared (1 slice posterior to the uncal apex; see Figure 8, HB 0). White matter and CSF surround the HB superiorly, medially and laterally. The medial-inferior boundary of the HB is the connection of the most medial point of the white matter to the most medial part of the grey matter, where it successively borders ErC, area 35 and PhC (see Figure 8 HB 0 - HB 3, e.g. Ding and van Hoesen 2010). Sometimes, in more posterior slices, a small sulcus (the anterior tip of calcarine sulcus; CaS) appears medially between HB and PhG. In this case, the lateral and medial banks of the CaS are spared from segmentation (see Figure 9). However, often the CaS only

appears in HT. The HB is segmented as long as the inferior and superior colliculi are visible (medial butterfly-shaped structures) (Wisse et al., 2016b). Segmentation does not stop before the colliculi have disappeared entirely. This rule has to be applied for each hemisphere separately (see Supplementary Figure 1).

Hippocampal tail

The hippocampal tail (HT) is a structure that is surrounded by white matter laterally, superiorly and ventrally. Most of these white matter structures are represented by alveus, fimbria and fornix, and are therefore excluded from segmentation. The medial-inferior boundary is constructed in the same way as that for the HB (see Figure 9, e.g. HT0-6). In more posterior slices, the HT (supero)laterally neighbors CSF in the trigone of the lateral ventricle (see Figure 9, e.g. HT3). The last slice of the hippocampus is the last slice where the HT is clearly visible (see Figure 9, HT11) which can also be checked on sagittal slices. It should be noted that at the very end of HT the hippocampus might medially blend with a gyrus, sometimes referred to as subsplenial gyrus (Ding et al., 2016). This gyrus is included in the hippocampal mask until it is no longer connected to the rest of the hippocampal grey matter. Note that different definitions of the body/tail border exist. Here, we chose the colliculi as they are easily identifiable, and are intended to provide a reliable posterior border for subfield segmentation.

2.2.7.3 Entorhinal cortex

Segmentation of the ErC (as well as area 35 and area 36) begins 4.4mm (= 4 slices here) anterior to the first slice of HH. That is, 4 slices have to be counted anterior to the hippocampus to define the starting slice. Although the ErC extends through most of the anterior temporal lobe (Ding and Van Hoesen, 2010; Kivisaari et al., 2013) we chose this border because it is easily identifiable, and high-resolution structural imaging protocols often do not cover the entire anterior MTL. The superior border in anterior slices is the semiannular sulcus (Ding et al., 2016; Mai et al., 2015). Sometimes, this sulcus is not visible from the most anterior end of ErC, in which case it should be extrapolated from more posterior slices where it can be clearly identified (see Figure 8, HH2). The ErC covers the ambient gyrus (AG; see Figure 8, HH0-3). Note that the ambient gyrus is made up of different subfields in an anterior-to-posterior direction. While the ambient gyrus is occupied by the ErC in more anterior slices (Insausti and Amaral, 2012), it consists of Sub and CA1 in more posterior sections (Ding and Van Hoesen, 2015). Moving posteriorly, at the point where the uncal sulcus can be followed from its fundus to the medial surface, Sub becomes the new superior border (see Figure 8, HH4). It is constructed by drawing a line from the most medial part of the white matter to the most medial part of the grey matter (Mueller et al., 2007; Wisse et al., 2012; Yushkevich et al., 2015b). This rule applies until the posterior end of ErC. The lateral border of ErC mainly consists of white matter. With respect to the inferomedial border, in some subjects CSF can be discerned between the ErC and the laterally located meninges (Xie et al., 2017, 2016). Therefore, bright voxels medial to the ErC have to be spared from the segmentation (see Figure

8, HH1-7). It should be noted that the intensity can depend on how much space there is between the meninges and the cortex. Sometimes these voxels appear slightly darker than CSF at other locations because of partial voluming with surrounding voxels. Inferolaterally, the ErC is bordered by area 35. This boundary is constructed at ¼ of the longest expansion of the collateral sulcus (CS) (from edge to top of the grey matter) as the shortest connection between CS and white matter (see Figure 10). The only exception from this rule occurs when CS is less than 4 mm deep (very shallow CS); in that case, the boundary between ErC and area 35 moves more lateral to the extension of the fundus of the CS. ErC disappears approximately 2 mm after the HH (Insausti and Amaral, 2012). Segmentation of the ErC stops therefore after 2.2 mm (= 2 slices here) into the HB, i.e. after 2.2 mm posterior to the uncal apex (see Figure 8, HB0). The last slice of ErC serves as an intermediate step between ErC and the increasing size of area 35. Therefore, the lateral border of the ErC shifts by dividing ErC in half (Ding and Van Hoesen, 2010; Insausti et al., 1998; Mai et al., 2015).

2.2.7.4 Perirhinal cortex

Segmentation of area 35 and area 36 of the PrC is dependent on the sulcal pattern within the MTL – especially the collateral sulcal patterns are highly variable between brains but can also differ between hemispheres of the same brain. There are two main types of MTL anatomy – one deep CS (Type 1; 45 %), and a discontinuous CS, which can be divided into an anterior (CSa) and a posterior section (CSp) (Type II; 52%) (Ding and Van Hoesen, 2010). CSp is usually longer and deeper than CSa. Studies have found a negative correlation of the depth of the CS and the depth of the occipito-temporal sulcus (OTS). In subjects with a shallow CS, the OTS is often deep and vice versa (Ding and Van Hoesen, 2010). In some cases, the CS is bifurcated, i.e. it appears to have two conjoined sulci; the more medial sulcus is used here in this case (i.e. for evaluating the depth of CS). When it is difficult to identify the sulcal pattern in one slice, it is recommended to check in adjoining slices and interpolate to the difficult slices. Given the differences in anatomy, different segmentation guidelines have to be applied for the different sulcal patterns as well as the depths of the CS. It is highly recommended to define the sulcal pattern for each hemisphere before starting the manual tracing. The following descriptions are visualized in Figure 10.
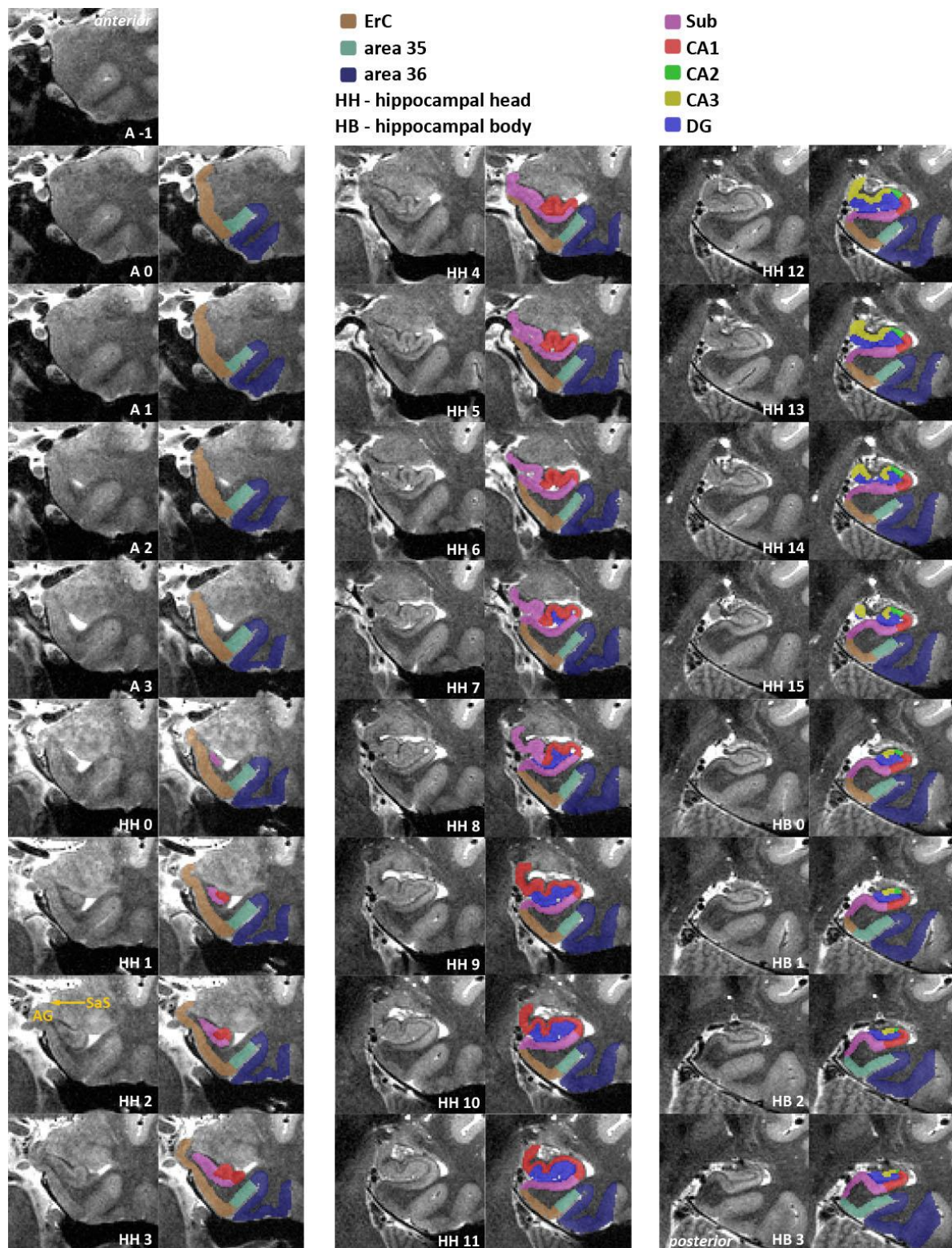
Figure 8. Slice-by-slice segmentation for a type 1 collateral sulcus (CS) – anterior part. Slices are 1.1mm apart. Included are entorhinal cortex (ErC; brown), perirhinal cortex (area 35 in mint green, area 36 in dark blue), subiculum (pink), CA1 (red), CA2 (green), CA3 (yellow) and dentate gyrus (blue). Shown in HH2, ErC covers the ambient gyrus (AG) and superiorly ends at the semiannular sulcus (SaS). SaS constitutes the superior border of ErC and should be extrapolated to anterior slices when it cannot be identified there.
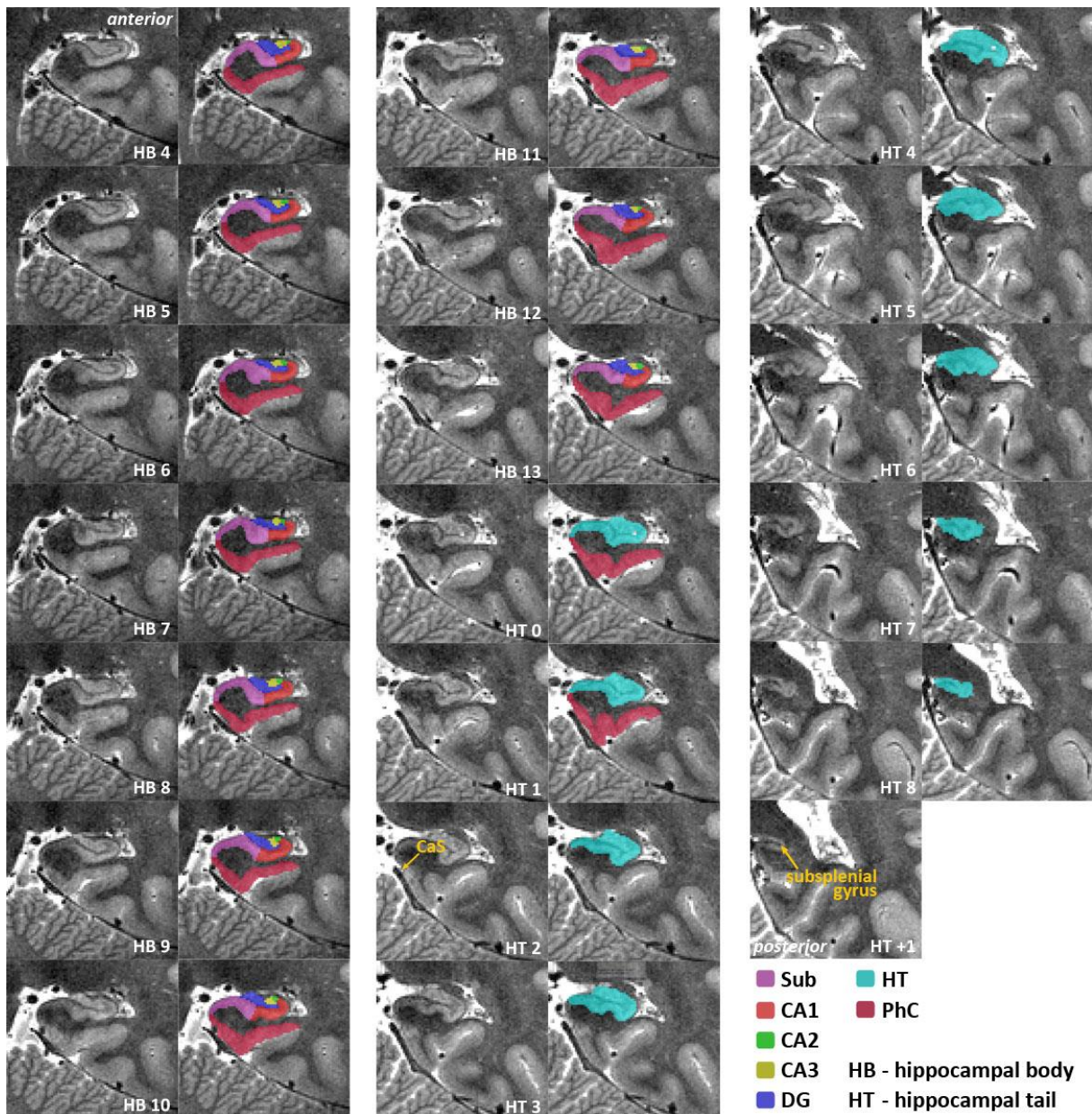
Figure 9. Continuation of Figure 8 - Slice-by-slice segmentation for a type 1 collateral sulcus (CS) – posterior part. Slices are 1.1 mm apart. Included are parahippocampal cortex (PhC; dark pink), subiculum (pink), CA1 (red), CA2 (green), CA3 (yellow), dentate gyrus (blue), and the hippocampal tail which, is not divided into subfields. In HT7, the subsplenial gyrus starts medially blending into the hippocampus. As soon as it is detached from the hippocampus, it is excluded from segmentation (HT+1). Delineation of PhC stops at the calcarine sulcus (CaS) in HT2.

Area 35

Segmentation of area 35 starts at the same artificially chosen slice as ErC, i.e. 4.4mm (= 4 slices) anterior to the first HH slice. Neuroanatomical atlases indicate that the posterior border of area 35 falls within 5mm of the anterior portion of the HB. Segmentations therefore end 4.4mm (= 4 slices) into HB, which is also 2.2mm posterior to ErC (Ding and Van Hoesen, 2010; Insausti et al., 1998). In the most posterior 2.2mm, area 35 borders the Sub medially (see Figure 8, HB1-HB3); in all anterior slices it borders ErC. The superolateral and inferomedial borders are in accordance with those of ErC (e.g. white matter and CSF or meninges). The lateral border of area 35 depends on the depths of the sulci, and is measured from edge to fundus of the respective sulcus on each individual slice. For that purpose, the edges adjacent to the sulcus are connected via a tangent line. The depth of the sulcus is now

measured from the middle of this line to the fundus of the sulcus (see Figure 10 and Supplementary Figure 3A). If the sulcus bends, the depth is measured in separate legs along the middle of the sulcus (see Supplementary Figure 3B).

Very deep CS (>10 mm)
Area 35 occupies the two middle fourths of the medial bank of the CS. Its lateral boundary with area 36 is constructed at ¾ of the medial bank of the CS (see Figure 10).

Deep CS (7-10 mm)
From the border to ErC, area 35 occupies the remaining ¾ of the medial bank of the CS (see Figure 10); i.e. from ¼ of the medial bank up to the top of grey matter.

Shallow CS (4-7 mm)
From the border to ErC, area 35 extends up to half of the lateral bank of the CS (see Figure 10).

Very shallow CS (<4 mm)
From the border to ErC, area 35 extends up to half of the crown of the fusiform gyrus (FG; see Figure 10).

When both CSa and CSp are visible on the same slice, the lateral boundary of area 35 is constructed at half of the crown between the two CS (see Figure 11, HH4). As soon as the CSa has disappeared, the same depth rules apply to CSp as shown in Figure 10. A decision tree can be used to facilitate the necessary decisions (see Supplementary Figure 4). The relationship of area 35 to area 36 length in histological studies roughly resembles a 1:3 ratio. Our rules are designed in order to approximate this ratio.

Area 36
Segmentation of area 36 is done in the same slices as area 35, that is, starting 4.4mm anterior to the first HH slice, and ending 2.2mm posterior to ErC. Area 36 directly borders area 35, thus its medial boundary depends on the different sulcal patterns described for area 35. Its lateral border is defined by the next lateral sulcus – the OTS. This border extends previous protocols (Feczko et al., 2009; Insausti et al., 1998; Kivisaari et al., 2013; Pruessner et al., 2002) and is specifically based on Ding and van Hoesen (2010). It is constructed by following the longest expansion of OTS, from medial edge to top of the grey matter, thereby including the whole medial bank of OTS (see Figure 10). It should be noted here that OTS is very variable, i.e. it can be bifurcated, or there could be two OTS. In these cases, the more medial OTS should be used as the border. Generally, OTS is rather deep and shows a reciprocal relationship with CS (see section on area 35 for more detail), and thus can be differentiated from other small sulci that sometimes appear in-between CS and OTS, e.g. the mid-fusiform sulcus in posterior slices (for reference, see Ding et al., 2016).

Sometimes, another small sulcus, the rhinal sulcus, is visible in very anterior slices. Generally, it is medial to CS and more shallow; it often 'travels' up the CS (see Supplementary Figure 7). In very rare

cases, the rhinal sulcus can be separate from CS so far posterior that it affects segmentation. That is, when the rhinal sulcus is separate and visible on the medial cortical surface, the rules change in a way as if one were to substitute the CS with the rhinal sulcus and the OTS with the CS. The boundaries follow the same depth rules as above but are applied to the rhinal sulcus. The very lateral border of area 36 is now the CS and not the OTS. When the rhinal sulcus disappears, area 35 and area 36 change to the usual patterns.
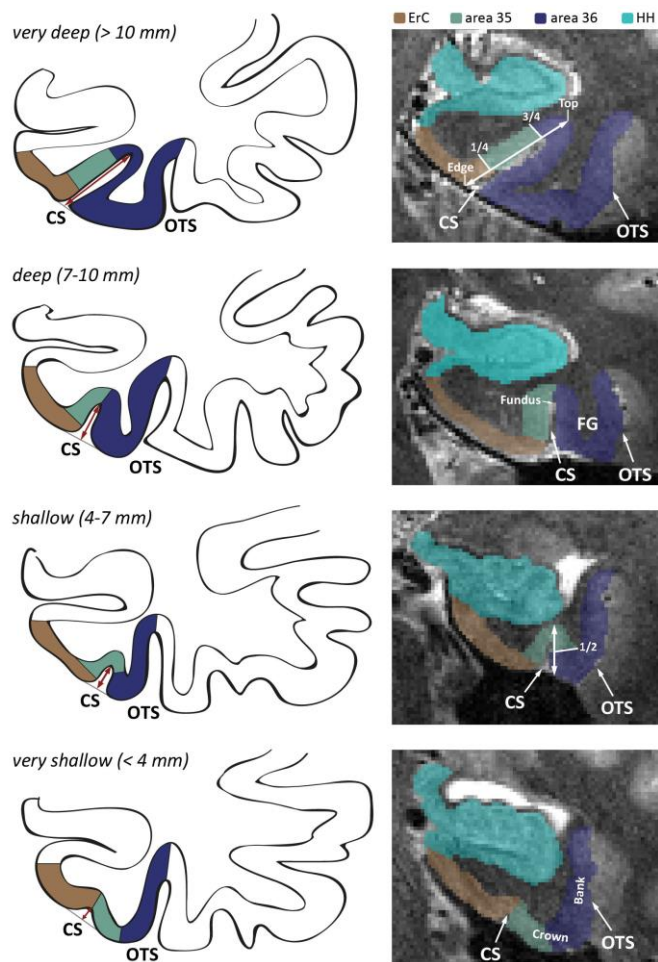
Figure 10. Different depths of the collateral sulcus (CS) with respective segmentation rules applied. Sulcus depth is measured from edge to fundus of CS as indicated by the red arrows. Edge, fundus, crown and bank are indicated for easy anatomical descriptions of the gyral and sulcal patterns. Quartiles for segmentation rules are defined by measuring the full extent of grey matter from edge to top along the respective bank as indicated by the white two-sided arrows in the images on the right. Entorhinal cortex (brown) ends laterally at ¼ of the grey matter bank medial to CS, when CS is deeper than 4 mm. For very shallow CS (< 4mm), entorhinal cortex covers the whole medial bank of CS and ends at the extension of the fundus of CS. Segmentation rules for area 35 (green) change depending on the depth of CS: *very deep* – area 35 covers the middle part from ¼ to ¾ of the grey matter bank medial to CS; *deep* – area 35 covers the whole superior ¾ of the grey matter bank medial to CS; *shallow* - area 35 extends up to half of the lateral bank of CS; *very shallow* - area 35 extends up to half of the crown of the fusiform gyrus (FG). Area 36 (blue) directly neighbors area 35 laterally, and extends towards the entire bank medial to occipitotemporal sulcus (OTS). The hippocampal head (HH) is depicted in turquoise.

2.2.7.5 Parahippocampal cortex

Anteriorly, the segmentation of the PhC directly adjoins the posterior end of area 35. Thus, it begins 5.5mm (= 5 slices) posterior to the uncal apex (see Figure 8, HB4; Ding and van Hoesen, 2010, Insausti et al. 1998). As with area 35, the PhC has a medial-superior boundary with Sub (see Figure 8, starting HB3). The superolateral and inferomedial borders are in accordance with those of ErC (e.g. white matter and CSF). The lateral boundary is the fundus of the CS extended to the top of grey matter. Posterior regions of the parahippocampal and fusiform gyrus include areas TH, TL and TF (Ding and Van Hoesen, 2010). While TH and TL cover regions in the parahippocampal gyrus, TF occupies parts of the fusiform gyrus. The PhC in this study only covers temporal areas TH and TL, but not TF (confer Ding and van Hoesen 2010, Ding et al. 2016). Segmentation stops when the anterior tip of the CaS appears

medially - a small sulcus that mostly folds in a superior-to-inferior direction (see Figure 9, HT2). Since little anatomical literature is available on the PhC, we based this decision on Song-Lin Ding's expertise annotating this region in histology samples, and because the CaS can be reliably identified in every subject. There is another small sulcus lateral to CaS, the newly discovered parahippocampal-ligual sulcus (PhligS; Ding et al. 2016; see Supplementary Figure 8), which would be a better indicator of PhC's borders. However, it was not possible to reliably distinguish this sulcus in every subject's MRI and we therefore chose to use the CaS as a landmark.

2.2.7.6 Transitions and labeling of the sulci

In order to maintain smooth transitions between slices that resemble the anatomy more closely we introduce transitions. Whenever there are sudden changes from one rule to the other, or sudden appearances of anatomical structures, one intermediate slice serves as a transition. Thus, the last slice where the anatomy fulfills the criteria of one rule serves as a transition slice to the next rule by applying an intermediate step in the middle between both rules (e.g. see Figure 8, HB1; Figure 11, HH0 and HB1). This procedure should be used in the following cases: (1) when ErC ends posteriorly, (2) when only CSa changes to only CSp without both being visible on the same slice and (3) when the OTS "jumps" (appears/disappears) from one slice to the next. An optional additional label for the CS and OTS can be added to facilitate thickness measurements using automated tools (e.g. ASHS (Yushkevich et al., 2015b). In case the CSF within the sulci is visible, these voxels can be labelled as sulcus. If the sulcus is not completely visible, there are usually some hints to it, such as an indentation on the inferior portion or a patch of CSF in the middle. If the sulcus cannot be identified, it can be estimated based on the thickness of the medial and lateral grey matter banks on surrounding slices. Inferring the sulcus in this way ensures that all voxels labelled as sulcus have adjacent edges (that is: not 1 voxel thick diagonal). In addition, if the gyri around CS and OTS touch, i.e. if no white matter in-between their grey matter banks is visible, the line of voxels in the middle between the two sulci should be artificially excluded from segmentation to allow meaningful thickness measurements. Alternatively, if the separation of the two banks can be inferred from the surrounding slices, a voxel line approximating that separation should be used instead.

2.2.8 HIPPOCAMPAL SUBFIELDS

These guidelines are mostly based on ex-vivo parcellations by Ding & van Hoesen (2015), and on comparative, additional information derived from other publications, such as the Mai atlas (Mai et al., 2015) and the protocol from Wisse et al. (2012).
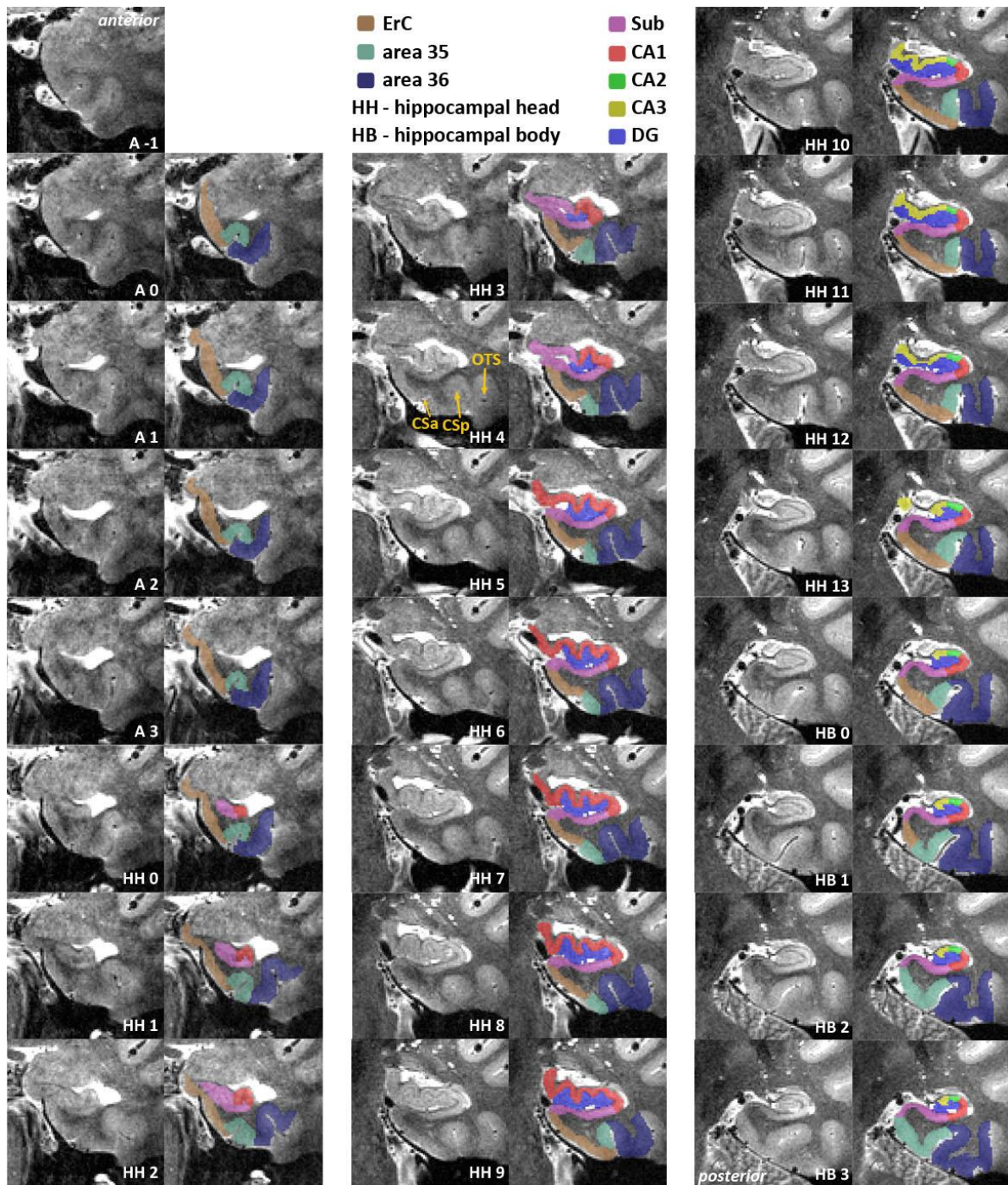
Figure 11. Slice-by-slice segmentation for a type II collateral sulcus (CS) – anterior part. Slices are 1.1 mm apart. Included are entorhinal cortex (ErC; brown), perirhinal cortex (area 35 in mint green, area 36 in dark blue), subiculum (pink), CA1 (red), CA2 (green), CA3 (yellow) and dentate gyrus (blue). HH4 is an example of a transition slice between anterior (CSa) and posterior CS (CSp) and the corresponding segmentation of area 35. The occipitotemporal sulcus (OTS) establishes the lateral border of area 36.

2.2.8.1 Subiculum and CA1 segmentation starts

Mostly, the first anterior slice of the HH appears as one structure. Sub is then assigned to all of it (see Figure 12A). Approximately 1-2 mm posterior to that, a hypointense line appears (i.e. uncal sulcus/SRLM; Ding and van Hoesen 2015) dividing the hippocampus into a superior and an inferior part and shaping the hippocampus similar to a lip (see Figure 12B). From here, the SRLM is equally divided between the regions it separates unless it is only 1 voxel wide, in which case it is segmented such that it always belongs to the superiorly located structure. Also at this point, the segmentation of CA1 starts.

The guidelines can be more readily understood by looking at Figure 12B and B'. The inferior boundary (i.e. on the "lower lip") between Sub and CA1 is an orthogonal line to the longitudinal Sub. It is positioned by finding the most lateral voxel of the SRLM, moving to the next medial one, and is constructed there from inner to outer side of the structure. The superior boundary between Sub and CA1 is extrapolated from a posterior slice where the digitation of the HH can be clearly identified, i.e. when the "upper lip" has at least two dents (Figure 12B'). At the second indentation counted from lateral to medial, a straight line is constructed orthogonal to the structure, and copied to anterior slices. Posteriorly, the border is positioned at this same indentation on each individual slice. This border closely approximates what is observed in the hippocampal subvariants with two and three indentations, as described by Ding et al. (see Figure 6 and 7 in Ding and Van Hoesen, 2015). Once the uncal sulcus opens, the separation of CA1 and Sub continues along the uncal sulcus (MR image in Figure 12B'). This may coincide with the appearance of DG, although it may also occur slightly more posterior.

2.2.8.2 DG segmentation starts

When DG appears, and does not yet stretch to the most lateral extension of the uncal sulcus (confer Figure 11, HH4), the inferior boundary between Sub and CA1 is constructed exactly like before. If, however, DG extends towards the most lateral point of the uncal sulcus (confer Figure 11, HH5), the reference point changes from one voxel medial from the most lateral SRLM to the most lateral DG voxel (Figure 12C). It is crucial to not confuse DG with cysts (which are brighter). However, if there is a cyst within DG that establishes the most lateral border, the cyst is used instead of DG to identify the CA1/Sub border (Figure 12D). Based on Ding and Van Hoesen (2015), the superior part of the subiculum disappears 1.2-1.8 mm after the appearance of the DG. We therefore chose to end segmentation of the superior part of the subiculum 2.2 mm (= 2 slices) after the first appearance of DG and this portion is then occupied by CA1 (Figure 12D). These borders are identified in the same way again on all following slices, although they often just stay the same as on the previous slices. From here, the SRLM is equally divided if thicker than 1 voxel, and otherwise segmented so it always belongs to the outer structure (i.e. CA1/Sub/etc., but not DG). It should be noted that contrary to the white matter surrounding the hippocampus, the hypointense line on the superior side of Sub is always included in the segmentation as it consists of the molecular layer of the Sub. Additionally, the inferior side of Sub is prone to signal drop-out due to the crossing perforant path; therefore voxels of intermediate intensity on the inferior side of Sub should be included because a very conservative visual segmentation of only the brightest voxels might result in an underestimation of Sub (Bronen and Cheung, 1991; Wisse et al., 2016b).
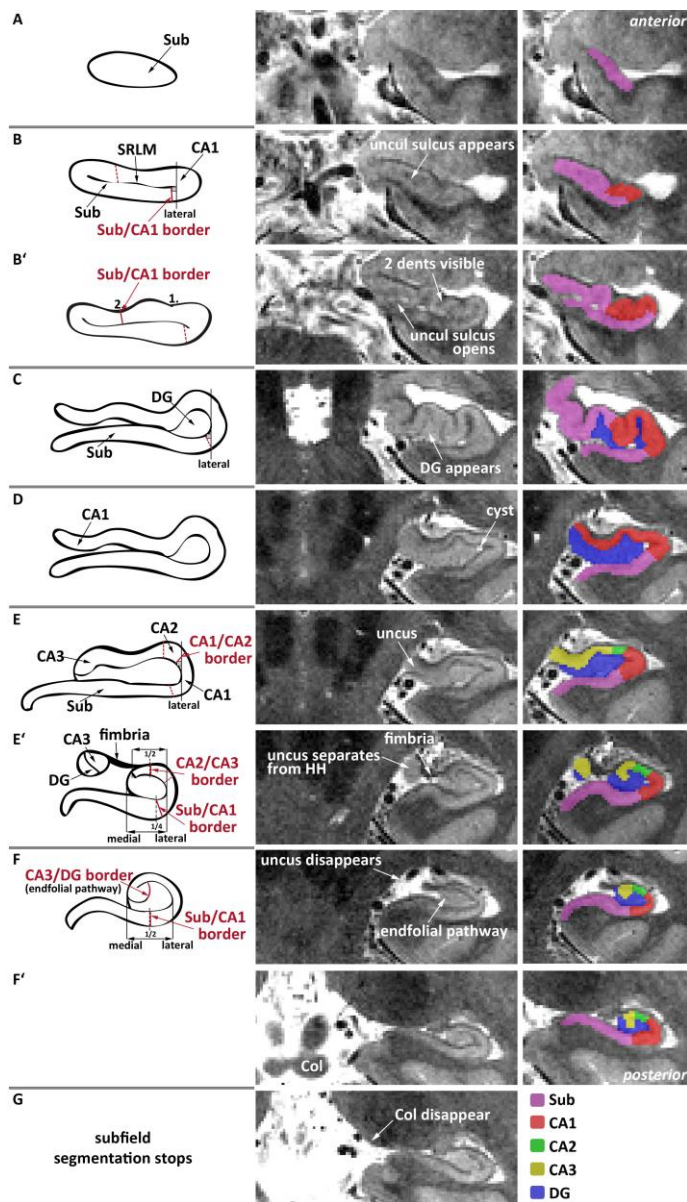
Figure 12. Rules for hippocampal subfield segmentation shown on the relevant slices from anterior to posterior. Schematic descriptions of all rules are depicted in the first column. Specific rule changes or new borders are indicated in red. Dashed lines are used, when the rule in question is inferred from another slice; e.g. the inferior Sub/CA1 border is defined in B, but the superior Sub/CA1 border is defined in B' and extrapolated anteriorly. The relevant anatomical changes are indicated by white labels and arrows in the middle column, e.g. when the uncus separates from the hippocampal body (HB), or the colliculi (Col) disappear. The resulting segmentation is shown in the last column; subiculum (Sub) in pink, CA1 in red, CA2 in green, CA3 in yellow and dentate gyrus (DG) in blue.

2.2.8.3 CA2 and CA3 segmentation starts

Neuroanatomical data indicate that the anterior border of CA3 in the head falls within 3-5.4 mm relative to the start of the head (Ding and Van Hoesen, 2015). The segmentation of CA2 and CA3 therefore begins in the last 4.4 mm (= 4 slices) of the HH. Although CA2 generally appears before CA3 (Ding and Van Hoesen, 2015), there is limited information on the exact distance between the two and on potential differences between subjects. Therefore, we chose to start segmenting CA2 at the same slice as CA3. Additionally, CA2 and CA3 show an alternating pattern in the most anterior slices; we chose to simplify this and count all medial grey matter towards CA3. Although we realize that we may count some portions of CA2 towards CA1 or CA3, we chose for these simplifications to achieve high reliability. Again, it might help to consider Figure 12E and E' alongside this description. The border between CA1 and CA2 is constructed orthogonal to the CA structures at one voxel medial of the lateral

boundary of DG; this is identical to the determination of the previous CA1/Sub border rule only on the superior instead of the inferior side. As in the previous section, if there is a cyst within DG that establishes the most lateral border, the cyst is used instead of DG to identify the CA1/CA2 border. The next step is to identify the point where the uncus separates from hippocampus. In some cases, only the fimbria is attached to both (Figure 12E'). The border between CA2 and CA3 is extrapolated from that slice to more anterior slices (to include the last 4.4 mm of HH). It is constructed halfway between the most medial point of the CA fields and the most lateral point of DG (it can therefore only be determined after the medial border of CA3 is determined). For all posterior slices, this border is determined slice by slice as a line orthogonal to the structure. The detached uncus is defined as CA3 unless there is a hypointense line, which can be used to differentiate between CA3 superiorly and DG inferiorly (Duvernoy et al., 2013) (Figure 12E'). The Sub/CA1 border also changes within the last 4.4 mm of HH (Ding and Van Hoesen, 2015). As soon as the uncus separates from hippocampus, the new border is marked at 1/4 from most lateral DG to most medial hippocampus proper. This line is extrapolated anteriorly to include the last 4 mm of HH (Figure 12E'). In the HB, i.e. when the uncus has disappeared, this border shifts to 1/2 from most lateral DG to most medial hippocampus proper (Figure 12F). This boundary is identified in the same way on all posterior slices.

2.2.8.4 CA3 and DG differentiation

Unique to our protocol is the delineation of CA3 and DG. Depending on image quality and resolution, we propose two different rules. Both rules apply to the whole HB and the most posterior HH slices where the uncus is only connected via the fimbria. Many protocols have defined everything on the inner side of the SRLM as DG. Based on ex-vivo segmentations (Ding and Van Hoesen, 2015; Mai et al., 2015) and the better contrast of T2 images and higher resolution of 7T imaging, the visualization of the endfolial pathway is possible, which can be used to more clearly differentiate between CA3 and DG (see the full HB segmentations in Figure 8; also in Parekh et al. 2105, Wisse et al. 2016b). The endfolial pathway is followed from the medial edge of CA3 towards the point where it intersects the SRLM. All voxels that lie supero-medially to this line belong to CA3 (see Figure 12F). However, if the endfolial pathway is not identifiable, or the aim of the research project is a comparison of groups where the endfolial pathway cannot be reliably distinguished in one group, an approximation can be achieved pursuing the following rules alongside Figure 13. First, construct a line from the middle and most superior part of the hippocampus to the medial edge of DG touching Sub (Figure 13-1). From the latter point, draw a line laterally along the dark band until Sub starts curving (Figure 13-2). Then, compose a line parallel to this which centrally intersects the first line (Figure 13-3) between the outermost extent of hippocampus until it intersects the SRLM. On the halfway point construct an orthogonal line towards the superior SRLM and close CA3 infero-laterally (Figure 13-4). All voxels lying superiorly to those lines belong to CA3 (Figure 13-5).
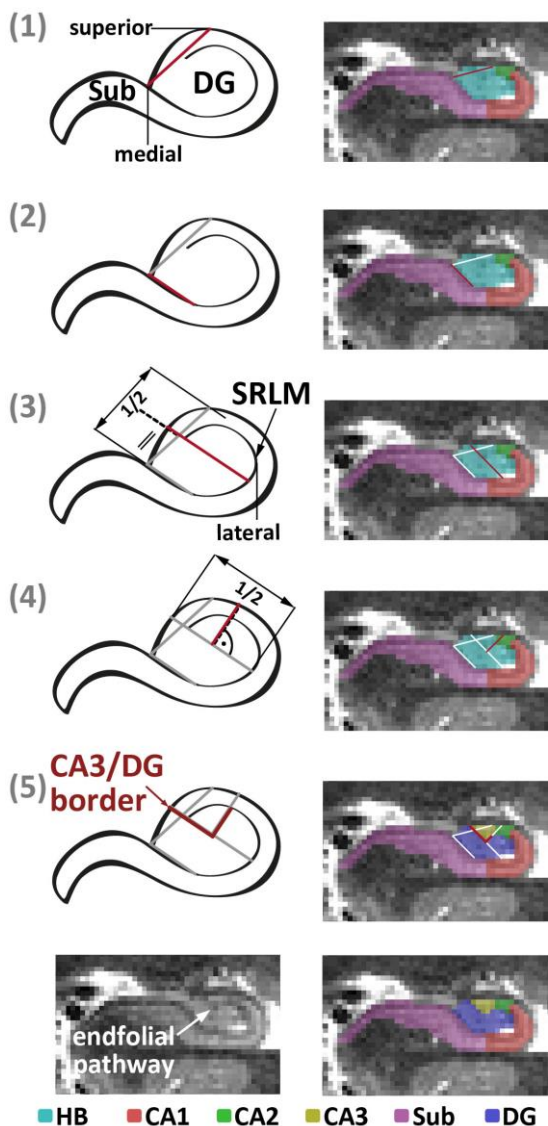
Figure 13. Heuristic rules for separation of DG and CA3 if the endfolial pathway is not visible. (1) construct a line from middle most superior part of the hippocampus to medial DG touching Sub; (2) from that point, draw a line laterally along the dark band until Sub starts curving, (3) parallel to this intersect line 1 centrally between SRLM and outermost extent of the hippocampus proper; (4) centrally intersect line 3 orthogonally; (5) CA3 assigned to voxels superior to lines 3 and 4. Applied rules are shown in the lower panel; unspecific hippocampal body (HB) in turquoise, subiculum (Sub) in pink, CA1 in red, CA2 in green, CA3 in yellow and dentate gyrus (DG) in blue. Compare the right panels for visual segmentation based on the endfolial pathway on the same slice

Figure 14. Exemplary segmentation profile. This anterior-to-posterior axis (i.e. along the longitudinal axis of the hippocampus) illustrates the key decision points of this protocol (numbers indicate mm distance from the first anterior slice in the protocol). Extrahippocampal regions and hippocampal head (HH), body (HB) and tail (HT) divisions are on the left; hippocampal subfields are depicted on the right. The start and end of each structure are depicted in the same color; often they depend on certain landmarks, e.g. the start and end of HH are used as a reference for the occurrence of the entorhinal cortex (ErC), area 35 and area 36, and the parahippocampal cortex (PhC). Most of these points are variable between brains but usually fall into a similar range as shown here. We recommend identifying these points prior to segmentation.

2.2.8.5 Subfield segmentation ends

As described for the end of HB above, subfield segmentation stops when the colliculi (see Figure 12F') have disappeared entirely. This rule applies hemisphere-specific (Figure 12G; also Supplementary Figure 2). Afterwards, manual subfield segmentation is no longer reliable.

2.2.8.6 General advice for manual segmentation

Segmentation of all regions is accomplished by tracing along white-to-grey matter boundaries, and several hypointense lines. These lines are not always continuous; we therefore recommend attempting smooth curvature even if the hypointense lines are discontinuous. Additionally, switching back and forth between coronal slices should ensure smooth transitions between slices, and avoid sudden jumps between regions. This is most important along the SRLM between Sub and CA1 in HH, at the endfolial pathway between CA3 and DG in HB, and for better identification of the sulcal pattern in PrC. Furthermore, special care is needed when measuring the depth of CS, because only slight variations can lead to different rule sets being required, i.e. at 7mm rules for a shallow sulcus apply and at 7.1mm rules for deep sulci apply (see Supplementary Figure 3 for impact of incorrect measurements see also results 2.3.1). As shown above, there are many cross-references between areas, therefore we recommend defining certain key decision points prior to segmentation (see Figure 14). For example, the beginning and end of HH are needed as a reference for the start and end of ErC and areas 35 and 36. Additionally, we advise to check the full segmentation at the end (for a checklist, see Supplementary Figure 10).

2.2.9 STATISTICAL ANALYSES

Two experienced raters (A.H. and A.L.) traced all subregions in the same 16 hemispheres independently (8 left and 8 right, 8 type I and 8 type II CS patterns). Both raters have each segmented around 40 subjects with the current rules prior to reliability testing. During that time, they met twice a week to discuss difficult cases, rule exceptions and to implement rule changes (e.g. the very shallow CS category was only introduced after specific feedback from S.-L.D.). From 14 subjects only one hemisphere was included, but from one subject two hemispheres were included to reach an equal number of type I and II CS patterns. In addition, all subregions were segmented for a second time by one rater (A.H.) after 4 weeks.

The intra-rater reliability was assessed in 16 hemispheres in terms of relative overlap between the two time-points using the Dice similarity index (DSI) (Dice, 1945). The DSI was calculated for each MTL subregion. The consistency of volume measurements within one rater was assessed using intraclass correlation coefficients (ICC) using SPSS 22 (IBM SPSS Statistics for Macintosh, Version 22.0. Armonk, NY: IBM Corp.). The ICC variant that measured absolute agreement under a 2-way mixed ANOVA model was used (ICC(3), Shrout and Fleiss 1979).

The agreement of both raters was assessed in terms of relative overlap using the DSI and was calculated as before. The consistency of volume measurements between both raters was assessed using the ICC. This time, the ICC variant that measured absolute agreement under a 2-way random ANOVA model was used (ICC(2), Shrout and Fleiss, 1979). Due to the low ICC values for area 35 in type II CS patterns in the first inter-rater reliability analysis, 8 additional hemispheres with type II CS were

segmented by both raters, after sulcus depth measurements had been made more concrete in the protocol following careful evaluation of the mismatches encountered during the first round. Average subregion volumes (mean and standard deviation) were calculated for the final 16 hemispheres for both raters (i.e. the 8 type I hemispheres and the 8 type II hemispheres from the second iteration after refinement of depth measurement).

2.3 RESULTS

2.3.1 RELIABILITY

2.3.1.1 Intra-rater reliability

Table 1 shows the intra-rater reliability of a single rater (A.H.) for 16 hemispheres (all from the first iteration). Almost all DSI values were above 0.9. Regions that were smaller and more complicated, such as CA2, CA3 and area 35, showed slightly lower values but were still over 0.85. ICCs were all over 0.95 with the exception of CA3, which was at 0.78 which may be explained by the more difficult but anatomically valid separation from DG along the endfolial pathway.

Table 1. Intra-rater reliability for all subregions		
	DSI (mean ± SD)	ICC
ErC	0.91 ± 0.01	0.98
area 35	0.88 ± 0.02	0.97
area 36	0.91 ± 0.02	0.96
PhC	0.93 ± 0.03	0.99
CA1	0.91 ± 0.02	0.98
CA2	0.87 ± 0.05	0.97
CA3	0.85 ± 0.03	0.78
DG	0.90 ± 0.02	0.98
Sub	0.92 ± 0.02	0.95
HC	0.96 ± 0.01	0.97

ErC, entorhinal cortex; PhC, parahippocampal cortex; CA, cornu ammonis; DG, dentate gyrus; Sub, subiculum; HC, hippocampus.

2.3.1.1 Inter-rater reliability

In a first analysis, almost all DSI values were above 0.84. The DSI for smaller, more complicated regions CA2, CA3 and area 35 was slightly lower, though still over 0.77. Similarly, ICCs were above 0.87 for almost all subregions. The ICCs for DG and subiculum were slightly lower though still over 0.76. However, the ICC for area 35 was 0.68, and 0.47 for CA3. Since this number was discrepant from the remaining values, all segmentations were checked to find out whether the rules for CA3 were unclear and could therefore not be reliably implemented. An error was found in one subject by one rater. In this subject, the number of head slices in which CA3 was segmented was miscounted. As the last head

slice was correctly identified and implemented for other labels depending on the most posterior head slice, we therefore concluded that this was a counting error rather than misinterpretation of the image or unclarity in the segmentation protocol with regard to CA3. This error was corrected and the ICC increased to 0.78.

In addition, we tested the inter-rater reliability of the heuristic rule for CA3 (see Figure 13). ICC was 0.78, and DSI was 0.79 indicating that the heuristic rule could be applied as reliably as using the endfolial pathway. On top of that, we compared the overlap between the two rules, therefore calculating an inter-rule DSI for all 32 hemispheres segmented by the two raters which was 0.63 ± 0.09. It should be noted here, that the upper limit for these DSI values are the DSI values of the inter-rater reliability for the two different sets of rules, i.e. with 100% rule overlap the DSI would be 0.79. Volume comparisons revealed that using the heuristic rule slightly underestimates CA3 (0.24mL compared to 0.31mL) and overestimates DG (1.0mL compared to 0.93mL) as compared to a separation at the endfolial pathway. This confirms that the heuristic rule is a good alternative to the anatomical landmark. However, if divergent from the endfolial pathway, in the majority of the slices CA3 will be underestimated, similar to all current segmentation protocols for CA3.

As an additional exploratory experiment, we performed reliability analyses of area 35 and 36 *separately* for the type I and type II sulcal variants. For area 36 the DSI was similar for the two types, 0.87 ± 0.02 for type I and 0.86 ± 0.04 for type II (Table 2). The ICC for area 36 for type II was 0.99, higher than 0.84 for type I. For area 35, the DSI for type I was slightly higher than type II; 0.84 ± 0.06 vs. 0.78 ± 0.07, but the difference was more notable for ICC of 0.87 for type I and -0.12 for type II. Although the ICC for area 35 is higher for type I as compared to type II, the absolute difference, or 'measurement error', between the two raters is similar for both sulcal pattern types (mean absolute difference: type I: 0.06mL, type II: 0.07mL) while the range of volumes for type II is only a third of the range of type I (range type I: 0.49-0.81mL, type II: 0.59-0.72mL). Thus, the absolute difference between the raters relative to the normal variation in the population (the range) for type II is larger than for type I. This is further illustrated in Bland-Altman plots in Supplementary Figure 11. Additionally, these plots show that neither rater had a bias as the differences lie around 0.

Further inspection of the segmentation of area 35 type II cases revealed that a difference in segmentation between the two raters mainly resulted from measuring the sulcal depth. A small difference in sulcal depth, as can be seen in Figure 10, can lead to a different segmentation rule. We therefore refined the segmentation protocol with regard to the sulcal depth measurements (see Supplementary Figure 3). Following this refinement of the protocol, 8 new type II hemispheres were segmented by both raters. The results of the reliability analyses for area 35 and 36 for these new type II hemispheres are presented in Table 2. ICC and DSI for ErC were 0.86 and 0.87, for area 35 they were 0.83 and 0.9, and for area 36 0.88 for both.

Table 2. Inter-rater reliability for ErC, area 35 and 36 in type 1 and type 2 CS patterns separately						
	DSI (mean ± SD)			ICC		
	Type I	Type II	Type II*	Type I	Type II	Type II*
ErC	0.88 ± 0.02	0.87 ± 0.03	0.86 ± 0.02	0.94	0.80	0.87
area 35	0.84 ± 0.06	0.78 ± 0.07	0.83 ± 0.04	0.87	-0.12	0.90
area 36	0.87 ± 0.02	0.86 ± 0.05	0.88 ± 0.03	0.84	0.99	0.88

ErC, entorhinal cortex

Dice similarity coefficient (DSI) and intraclass-correlation coefficient (ICC) for 8 hemispheres in each category

*Results from a second inter-rater reliability analysis following refinement of segmentation rules

As a result, the ICC and DSI for the combined type I and II cases improved to over 0.84 for all three regions. Table 3 shows the final results of all subregions for the comparison of both raters (i.e. average of the 8 type I hemispheres and the 8 type II hemispheres from the second iteration).

Table 3. Inter-rater reliability between two raters				
	DSI (mean ± SD)		ICC	
ErC	0.87 ± 0.02		0.94	
area 35	0.84 ± 0.05		0.87	
area 36	0.87 ± 0.02		0.88	
PhC	0.86 ± 0.12		0.94	
CA1	0.84 ± 0.04		0.89	
CA2	0.81 ± 0.06		0.92	
CA3	0.78 ± 0.05	*0.79 ± 0.05	0.76	*0.78
DG	0.86 ± 0.03		0.76	
Sub	0.85 ± 0.04		0.78	
Hippocampus total	0.94 ± 0.01		0.98	

ErC, entorhinal cortex; PhC, parahippocampal cortex; CA, cornu ammonis; DG, dentate gyrus; Sub, subiculum; DSI, Dice Similarity Index; ICC, Intraclass correlation coefficient.

*these values correspond to the alternative heuristic rule (see Figure 13)

2.3.2 VOLUMES IN COMPARISON TO ANATOMY

Mean volumes across both raters are shown in Table 4. Due to very different segmentation schemes for PrC as well as PhC, we did not compare volumes of those regions to earlier studies (Insausti et al., 1998; Pruessner et al., 2002). Volumes of hippocampal subfields are compared to studies that used manual segmentation procedures at 7T (Wisse et al., 2016c), automated approaches at 3T (Iglesias et al., 2015; Yushkevich et al., 2015b) and histological techniques (Simić et al., 1997). The comparison of the mean volumes found in the current study with the other manually derived volumes from Wisse et al. (2016c) highlights the changes in the recent protocol and reflects the novel anatomical findings from *Ding et al.* While CA1 has less volume compared to earlier estimations, subiculum shows an increase in volume. This probably relates to the new rule of subiculum segmentation in the hippocampal head as well as the new boundary between CA1 and subiculum in the hippocampal body.

On the other hand, CA3 has increased while DG has reduced volume compared to Wisse et al. (2016c). Again, this most probably highlights our new rule which follows the endfolial pathway to separate DG and CA3 more accurately. Using this approach the portion of CA3 that folds into the DG is also segmented as CA3, which should result in an increase in CA3 volume. Additionally, hippocampal subfield volumes obtained with the current protocol approximate those obtained from post mortem studies (Iglesias et al., 2015; Simić et al., 1997), especially for the subfields in the hippocampus proper.

Table 4. Volumes of ErC, area 35, area 36, PhC and hippocampal subfields in mL.					
	Current study	Simic et al. (1997)[1]	Iglesias et al. (2015)[2]	Yushkevich et al. (2015)[3]	Wisse et al. (2016)[4]
ErC	**0.99 ± 0.2**	-	-	-	0.53
area 35	**0.64 ± 0.11**	-	-	-	-
area 36	**2.22 ± 0.39**	-	-	-	-
PhC	**0.58 ± 0.24**	-	-	-	-
Sub	**1.07 ± 0.16**	-[◊]	0.64*	0.34	0.63
CA1	**0.82 ± 0.15**	0.64	0.52	1.25	1.48
CA2	**0.07 ± 0.02**	-	-	0.018	0.07
CA3	**0.17 ± 0.02**	-	-	0.067	0.12
CA2&3	**0.24**	0.14	0.18	0.085	0.19
DG(&CA4)	**0.50 ± 0.09**	0.31	0.46	0.76	0.80
Hippocampus	**3.16 ± 0.40**	1.54	2.26	2.44	3.1

ErC, entorhinal cortex; PhC, parahippocampal cortex; CA, cornu ammonis; DG, dentate gyrus; Sub, subiculum.
We provide standard deviations for the data from the current study.
[1]Data derived from table 2, 'Normal'; [2]Data derived from table 3, 'Ex vivo atlas'; [3]Data derived from table 6, 'ASHS', mean of right and left side; [4]Data derived from table 1, 'Manual segmentation', mean of right and left side.
[◊]not shown because only entails subiculum and prosubiculum
*values for parasubiculum, presubiculum and subiculum were summed up from table 3

2.4 DISCUSSION

We have developed and tested a new protocol for manual segmentation of the entorhinal cortex, perirhinal cortex (distinguishing area 35 and 36), parahippocampal cortex, and hippocampus as well as its subfields including subiculum, CA1, CA2, CA3, and dentate gyrus, in-vivo at 0.44x0.44 mm in-plane resolution using 7T MRI. We showed that our protocol had an intra-rater reliability ICC higher than 0.95, except CA3 (0.78) and DSI higher than 0.85 and an inter-rater reliability ICC higher than 0.76 and DSI higher than 0.81, except CA3 (>0.78) for all regions in young adults. The strengths of the protocol are outlined as follows.

First, we leveraged recent developments in neuroanatomy. This has enabled us to incorporate more distinct rules as previously known. Chiefly, subdivisions in HH and HB (Ding and Van Hoesen, 2015), PrC (Ding and Van Hoesen, 2010) and PhC (Ding et al., 2016) have substantially extended earlier work as they provide more details on the order of appearance and location of the subregions and

additionally provide information on between-subject variability in some of the regions, which were incorporated in the current segmentation protocol, e.g. location of subregions in relation to different numbers of digitations in the hippocampal head and pattern of the collateral sulcus. Also note, that sectioning in one article was done perpendicular to the long axis of the hippocampus making it more comparable to the commonly used T2-weighted images (Ding and Van Hoesen, 2015). The other two atlases were based on histology data sectioned in a coronal plane (Ding et al., 2016; Ding and Van Hoesen, 2010). However, no histological data on extrahippocampal regions is currently available with slices perpendicular to the long axis of the hippocampus. Additionally, earlier protocols mostly collapsed across subregions of the PrC instead of differentiating between medial and lateral parts (Insausti et al., 1998; Pruessner et al., 2002) but see (Kivisaari et al., 2013; Yushkevich et al., 2015b). We have extended that framework by differentiating more specifically between area 35 and 36 using available data from neuroanatomy (Ding and Van Hoesen, 2010). Another example is the PhC, where studies have mostly included the posterior PhG up to CS across the whole length of the hippocampal tail because of lack of a well-established boundary (Pruessner et al., 2002; Yushkevich et al., 2015a). However, a recent histological atlas disentangles the subdivisions of the posterior PhC (Ding et al., 2016). That is, the posterior PhC not only consists of areas TH and TL of the PhG, but also area TF of the fusiform gyrus. In addition, areas TL and TF extend further posteriorly than area TH, which in most cases disappears (replaced with ventral visual area V2) after the shallow parahippocampal-ligual sulcus (PhligS) appears. Although the newly identified PhligS would be anatomically the most valid landmark, it could not be identified reliably in all subjects. We observed that the anterior part of the CaS can serve as a landmark in close proximity to the PhligS, which can be distinguished reliably. The CaS is a rather conservative border and leads to an exclusion of a portion of posterior PhC. However, as this posterior portion also consists of visual area V2, its exclusion may benefit the study of parahippocampal function. This fine-tuning of the segmentation protocol with more detailed information on the borders and anatomical variability may further facilitate research on memory such as different memory pathways in the MTL (Das et al., 2015; Ranganath and Ritchey, 2012; Reagh and Yassa, 2014). Additionally, if the protocol is validated in older populations, it may facilitate research on ageing and neurodegenerative diseases. For example, early stages of tau pathology in Alzheimer's Disease constitute especially in the transentorhinal region and the entorhinal cortex (Braak and Braak, 1991; Ding et al., 2009). The transentorhinal region as described by Braak and Braak corresponds roughly to area 35 in the recent protocol. Therefore, a detailed volumetry of these regions that closely follows the anatomy becomes critical to detect early disease effects in volume and regional thickness measures (Wolk et al., 2017; Xie et al., 2017).

A second strength of this protocol is that we used ultra-high resolution 7T MRI, which enabled us to get more fine-grained images, and allowed for a more detailed delineation of smaller structures. In particular, the delineation of hippocampal subfields in the head as well as the visual distinction

between CA3 and DG in the body benefit from the higher resolution. As can be seen from Figure 8 and Figure 11, the appearance of hippocampal head and presence of subfields can change drastically from slice to slice. The thinner slices obtained at 7T allow us to establish more precise segmentation rules for the hippocampal head – that is, determining the distance between the appearance of subfields in the order of 1mm rather than the more frequently reported thickness of 2mm. In addition, it likely also allows for a more reliable segmentation. This may add value when investigating diseases or cognitive functions for which the anterior portion of the hippocampus is proposed to be specifically important (Poppenk et al., 2013; Sahay and Hen, 2007). Additionally, we propose the use of the endfolial pathway, a white matter band aligned with the actual border of CA3, to separate CA3 from the DG in the hippocampal body in populations where it is visible. This accurate distinction of DG and CA3 may enable functional MRI studies to dissociate the contributions of DG and CA3, because they are assumed to be involved differently in memory functions such as pattern separation and pattern completion (Neunuebel and Knierim, 2014). Although some of our rules are still geometrical in nature, the rules follow neuroanatomy more closely and take between-subject variability into account where possible. Additionally, most rules are independent of the in-plane orientation of the MTL; that is, most boundaries are drawn perpendicular to the structure rather than that they are based on the image orientation.

Thirdly, we aimed to develop a protocol that is easy to apply. Therefore, we included comprehensive slice-by-slice plots of high-resolution images that show the application of the rules along the full longitudinal axis for the most prevalent sulcal patterns – a continuous type 1 as well as a discontinuous type II CS (Ding and Van Hoesen, 2010). In addition, we provide practical segmentation tips, a checklist for segmentation and schematic descriptions of the rules throughout the protocol as well as a decision tree for the segmentation of area 35 and examples of some difficult cases in the supplemental material. To further facilitate the understanding of our rules, we incorporated specific feedback from a workshop on our protocol in Magdeburg. One of our main aims was to understand the difficulties that novice raters encounter while learning to apply the protocol rules. During the workshop, we identified the most common difficulties and adjusted the protocol accordingly. For example, it became clear that the frequent cross-referencing to certain anatomical structures (e.g. uncal apex) was difficult to follow. Therefore, we included recommendations in what order to approach segmentation (Figure 14).

The intra-rater reliability showed that the protocol could be reliably applied across different time-points with DSI values higher than 0.85 and ICC values higher than 0.95 with the exception of 0.78 for CA3. The latter is probably due to the fact that we are using a more complex separation along the endfolial pathway, or using the heuristic rule. Analyses of the reliability between two raters showed that we were able to apply this protocol in a consistent manner, with almost all DSI values above 0.84 and almost all ICC values over 0.89. Even for smaller regions and for regions, such as area 35, for which

the segmentation protocol is more difficult to accommodate anatomical variants, the ICC and DSI were reasonable (ICC over 0.68 for area 35 and over 0.76 for the other regions and DSI over 0.77), showing that these smaller and more complicated regions can be segmented with reasonable reliability. It should be noted that the ICC for the DG and CA3 was also slightly lower which can be explained by the more complex separation as already discussed for the intra-rater reliability. The high DSI values in general are encouraging for the application of this protocol to functional MRI studies as spatial overlap is most important in this context.

In relation to other studies, the ICC values and DSI values reported here are well within the range of previously reported reliability values (Bonnici et al., 2012a; de Flores et al., 2015b; Goubran et al., 2014; Lee et al., 2014; Mueller et al., 2007; Palombo et al., 2013; Prasad et al., 2004; Winterburn et al., 2013; Yushkevich et al., 2010). Although some other studies reported slightly higher values for CA1 (Lee et al., 2014; Shing et al., 2011; Yushkevich et al., 2010) or subiculum (de Flores et al., 2015b; Travis et al., 2014), our protocol includes more specific rules and may be more complicated. Additionally, the reliability for small regions such as CA2 and CA3 are among the highest reported in the literature. The ICCs for ErC, area 36 and PhC are also well in the range of previously reported reliability values (Feczko et al., 2009; Pruessner et al., 2002). The ICC value for area 35 was below the reliability estimates of earlier protocols (combining area 35 and 36). When splitting up the group in the two types of sulcal patterns, it became clear that this lower ICC value for area 35 was mainly driven by the type II variant. Importantly, our aim to incorporate the findings from histological studies (Ding and Van Hoesen, 2010) and match anatomy as closely as possible resulted in a slightly more detailed protocol with segmentation rules dependent on sulcal depth measurements. Small differences in sulcal depth measurement could result in different segmentation rules especially in the type II variant. After initial evaluation of the results, we therefore refined the guidelines for sulcal depth measurements (see Supplementary Figure 3). A second reliability test in eight new type II hemispheres revealed an improved DSI of 0.83 and ICC of 0.90 which is similar compared to type I hemispheres. Although a learning effect could have affected the reliability measures, it seems unlikely that this played a large role as both raters had already segmented 40 subjects before the initial reliability test and this second reliability test was performed in 8 new hemispheres. These results indicate that with the refined segmentation protocol also a challenging region such as area 35 in the type II variant can be segmented reliably.

There are also limitations to the current study. First, by focusing specifically on anatomical validity and accounting for anatomical variability as much as possible, the resulting protocol is more elaborate and time-consuming compared to earlier approaches. However, we made considerable efforts to explain the protocol and make it understandable to novice raters. Additionally, we are planning to bring the rules of this protocol into the automatic segmentation framework of ASHS (Yushkevich et al., 2015b). A second limitation is that although we tried to match anatomy as closely as possible, for some of the

borders we still use heuristic rules to improve reliability of the protocol. This means that portions of subregions may be included in the labels of adjacent subregions. Third, our protocol was mainly based on work from *Ding et al.* and might not be in agreement with work from other neuroanatomists. However, our protocol is roughly consistent with other neuroanatomical references (Duvernoy et al., 2013; Insausti et al., 1998; Mai et al., 2015), and the volumes as obtained by the current protocol approximate the volumes from post mortem studies, as shown in Table 4 (Iglesias et al., 2015; Simić et al., 1997). The volume of the subiculum is slightly larger as compared to *Iglesias et al.*, which may be due to the difference in age between the current study and the post mortem studies as subiculum volume is suggested to be affected by age (La Joie et al., 2010). It should be noted though that differences exist between these and other references in terms of nomenclature, for example the existence of the 'prosubiculum' and perhaps also in the placement of certain boundaries. Fourth, although we embrace the possibilities provided by higher resolution, we are fully aware that not all researchers have access to 7T, which may limit the applicability of the current protocol. In order to facilitate application to 3T protocols, we provided all segmentation rules in millimeters and have included heuristic rules to guide segmentation of CA3 and DG when the anatomical landmark, the endfolial pathway, is not visible. Indeed we are currently trying out this segmentation protocol in a set of older adults and patients with MCI for whom a high resolution $0.4\times0.4\times1.2mm^3$ T2-weighted MRI was obtained. Of note, although most studies on MTL subregions are using 3T imaging protocols, 7T might play a more prominent role in the future with an increasing number of sites with access to a 7T scanner. For example, recently the European Ultrahigh-Field Imaging Network for Neurodegenerative Diseases (EUFIND) was founded with the aim to summarize and investigate the potential of ultrahigh-field imaging in neurodegenerative research (www.neurodegenerationresearch.eu/initiatives/annual-calls-for-proposals/closed-calls/brain-imaging-working-groups-2016/brain-imaging-working-groups/). Finally, the distance between appearance of the different subfields is given in millimeters, although lengths of the MTL and hippocampus differ between individuals and might be affected by disease. It is unclear how this affects subfield measurements in the current protocol; a limitation true for all current segmentation protocols. Although a potential solution could be to provide relative distances rather than absolute distances between subregions, based on the total length of the MTL; this would further complicate the protocol. Additionally, the relative distance between subfields is not necessarily similar between subjects nor are they similarly affected by disease. Using this measure would therefore inherently also induce a measurement error.

The current protocol is not meant to replace the protocol of the harmonization effort for hippocampal subfields (www.hippocampalsubfields.com) or hamper the progress of this collaborative effort of many groups in various disciplines aiming to harmonize all the different protocols for hippocampal and parahippocampal subregions (Wisse et al., 2016a). Due to the iterative and thorough nature of the harmonization effort, the timeline for development of protocols for parahippocampal subregions and

7T images are further down the road and the current protocol is therefore meant to facilitate the segmentation of MTL regions, and especially parahippocampal subregions, for centers with a 7T scanner in the meantime.

In summary, we present a protocol to delineate medial temporal lobe structures as well as hippocampal subfields and provide evidence that it can be reliably applied. The inclusion of the most recent anatomical literature guiding the detailed subdivision of MTL regions and hippocampal subfields will make this an especially useful protocol for the investigation of the functional role of subregions in the MTL using fMRI, as well as research on the effect of exercise on MTL subregions and their differential relation with depression, autism, ageing and neurodegenerative diseases.

2.5 CONTRIBUTIONS

The protocol was developed in collaboration with the Ageing and Cognition working group at the German Center for Neurodegenerative Diseases (DZNE) in Magdeburg, the Penn Image Computing and Science Laboratory at the University of Pennsylvania, Philadelphia, and the Allen Institute for Brain Science, Seattle; i.e. Paula Vieweg, Anne Hochkeppler, Laura Wisse, John Pluta, Song-Lin Ding, Anne Maass, Anica Luther, Long Xie, David Wolk, Sandhitsu Das, Paul Yushkevich, and Emrah Düzel. Most notably, P.V., L.W., A.H., J.P. and I developed the initial set of rules. Together with S.-L.D. I validated the rules based on his earlier neuroanatomical findings. In addition, S.-L.D. reviewed the segmentations. A.H. and A.L. segmented all datasets for reliability testing. L.W. and I did the reliability analysis. P.V. created the figures except for the Bland-Altman plots (by L.W.). P.V.., L.W. and I refined the rules and wrote the manuscript. All authors edited the manuscript.

CHAPTER

3

Strong Evidence for Pattern Separation in the Human Dentate Gyrus

3.1 INTRODUCTION

As already stated in the General Introduction, the hippocampus is assumed to assign distinct neuronal codes to related episodes in order to avoid confusing memories for similar experiences. This process, often referred to as pattern separation, is generally viewed to be a critical computation performed by an episodic memory system – specifically the dentate gyrus (DG) subregion of the hippocampus (Marr, 1971; Norman and O'Reilly, 2003; O'Reilly and McClelland, 1994; Rolls and Treves, 1994). Whilst empirical evidence demonstrates that the hippocampal DG region in rodents supports pattern separated representations (Colgin et al., 2008; Lee et al., 2015; Leutgeb et al., 2007; McHugh et al., 2007; Neunuebel and Knierim, 2014), previous studies in humans have provided only indirect evidence for a role for the DG in this process (Azab et al., 2014; Bakker et al., 2008; Kyle et al., 2015; Lacy et al., 2011; Reagh and Yassa, 2014) and lacked the anatomical resolution to distinguish between DG and CA3. Specifically, a previous study used an fMRI repetition suppression paradigm in combination with the Mnemonic Similarity Task (MST) to show that items that were similar to those previously experienced ("lures") elicited elevated levels of activity in DG/CA3 (i.e. comparable to that elicited by the initial presentation), as compared to exact repetitions of the item (Bakker et al., 2008) (also see follow-up studies Bakker et al., 2012; Lacy et al., 2011, Yassa et al., 2011a, 2010b). Whilst this lure-associated novelty signal was used to infer the existence of pattern-separated representations for the original and lure item in the DG/CA3 region, there is an alternative possibility that cannot be discounted: these novelty signals may reflect the output of a match-mismatch process – where the lure item triggers pattern completion of the original stored item, and a resultant mismatch signal (Kumaran and Maguire, 2009). As such these previous studies do not necessarily imply a role for the human DG/CA3 in pattern separation.

The study presented in this chapter, therefore, was configured to provide a more definitive test of the hypothesis that the human DG performs pattern separation. Firstly, we were able to distinguish between the DG and CA3 subregions by obtaining high-field functional magnetic resonance imaging (fMRI) data at 7 Tesla with a functional resolution of 0.8 x 0.8 x 0.8mm (corresponding to a volume of 0.51mm^3) covering the whole medial temporal lobe (MTL) memory system including the hippocampus, entorhinal (ErC) as well as perirhinal (PrC) and parahippocampal cortex (PhC). In contrast, previous fMRI studies of the MTL that investigated pattern separation relied on 3 Tesla fMRI and isotropic voxel sizes up to 1.5mm (corresponding to a volume of 3.375mm^3) (Bakker et al., 2008; Carr et al., 2010). Secondly we utilized multivariate fMRI methods to investigate whether the DG performs pattern separation – an analytic technique that is particularly appropriate given that this computation is defined at the level of the underlying representations (Davis and Poldrack, 2013; Haynes, 2015; Haynes and Rees, 2006; Knierim and Neunuebel, 2016; McClelland et al., 1995; Norman and O'Reilly, 2003;

Treves and Rolls, 1994). Strong evidence for pattern separation would require the demonstration that multivoxel activity patterns for similar stimuli in the DG were more distinct than in regions upstream the hippocampus like the ErC, PhC and PrC as it has been shown in the animal literature (Neunuebel et al., 2013; Neunuebel and Knierim, 2014). To optimize our paradigm for multivariate analysis, we used a modified repetition suppression paradigm that included only two stimuli (A,B) (cf Bakker et al., 2008 that used trial-unique stimuli). The stimuli constituted very similar versions of the same spatial environment – inspired by A-B-B-A type-paradigms used in non-human primate studies, where repetition suppression responses are observed even with highly familiar stimuli (Hölscher and Rolls, 2002; Miller and Desimone, 1994). In addition, this allowed us to ask whether the DG generates stimulus specific novelty responses that can be related to the underlying representations detected by multi voxel pattern analysis (MVPA).

3.2 MATERIALS AND METHODS

3.2.1 SUBJECTS

Twenty young subjects (11 male, recruited at the campus of the Otto-von-Guericke University Magdeburg, mean age 27,6 ± 4 yrs, range = 21-35) participated in the experiment. Subjects were screened for known metabolic disorders and neurologic or psychiatric history and excluded from further examination in case of incidents reported during history taking. All subjects had normal or corrected to normal vision and were right handed. One subject was discarded from further analyses due to too many incorrect responses (19 % incorrect). The study was conducted and designed in accordance with the Declaration of Helsinki (Williams, 2008) and all subjects gave informed and written consent for their participation in accordance with ethic and data security guidelines of the Otto-von-Guericke University Magdeburg. The study was approved by the local ethics committee.

3.2.2 TASK AND DESIGN

Prior to scanning subjects had to complete a four-minute training and stimulus familiarization phase outside the scanner (ten stimulus sequences). During the following fMRI session, the same two stimuli (A and B) (Figure 15) were presented in short sequences consisting of 3-5 stimulus presentations. Sequences were presented in an event-related design. Each stimulus was presented for 2s and stimuli were separated by a presentation of a scrambled noise picture for 3.5s (+/- 1s) to prevent an afterimage or pop out effects. Sequences were separated by a presentation of a fixation star for 4.5s. Subjects had to indicate the third occurrence of the first item seen in a sequence via button press with their right index finger. This provided a behavioral measure of mnemonic discrimination performance. For the fMRI analysis, we focused only on the first and second stimulus presentation within each sequence to counterbalance stimuli and to exclude the motor response. All sequences were counterbalanced in terms of stimulus A and B. Also, the length and order of the sequences was

counterbalanced between stimulus A and B repetitions and lures (see Figure 15 for example sequences). We presented 32 sequences in each of the four runs. This resulted in a total of 128 sequences. While in half of the sequences the first stimulus was repeated (repetitions), in the other half there was a change of the stimulus within the first two stimulus presentations (lures). Therefore, we could include 128 first presentations, 64 repetitions and 64 lures in the subsequent fMRI analyses. Right after the scanning procedure there was a post-scan debriefing, where we asked subjects to draw both stimuli as detailed as possible. This was done in order to make sure that all subjects were not only aware of the difference between both stimuli but that they also had a detailed representation of the whole living room scene.
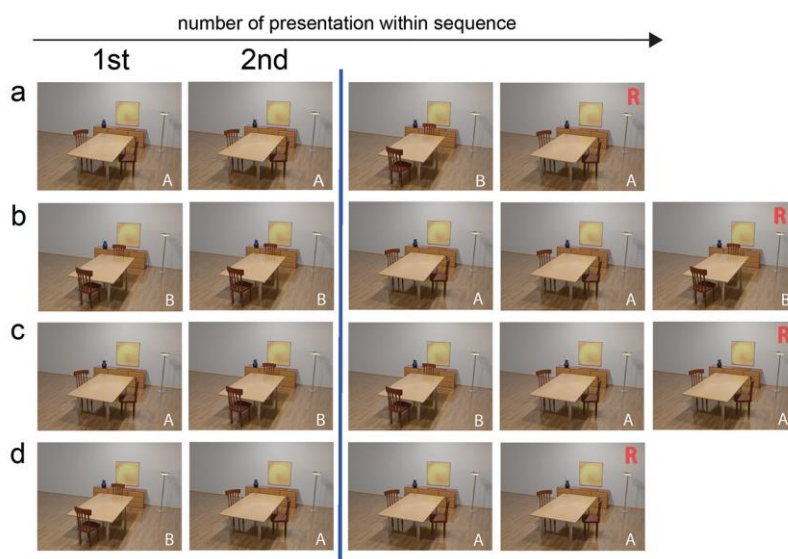
Figure 15. Experimental paradigm. Stimuli A and B were presented in short sequences (three to five stimuli; **a–d** show selected examples). Subjects were instructed to indicate the third occurrence of the first item seen in a sequence via button press. In half of the sequences, there was a repetition of identical stimuli in the beginning (repetition trials; **a, b**). In the other half, stimuli changed in the very beginning (lure trials; **c, d**). We included only the first and second stimulus in further analyses as indicated by the blue line. R indicates the appropriate response for each example sequence. We refer to the first stimulus in each sequence as "first presentation" although only the two scenes displayed in the figure were used in the entire experiment and therefore each scene was highly familiar. Note that the length and order of the sequences was counterbalanced between stimulus A and B repetitions and lures.

3.2.3 STIMULI

The stimuli consisted of two colored computer-generated (3ds Max, Autodesk Inc., San Rafael, USA) and isoluminant images. The images showed two similar versions of the same living room with a size of 800 x 600 pixels (Figure 15). A scrambled noise picture with identical dimensions was shown between the images. The fixation target was a black image with identical dimensions and a white fixation star in the center. Stimuli were projected onto the center of a screen and the participants watched them through a mirror mounted on the head coil, subtending a visual angle of about ±3° by ±2°.

3.2.4 MRI

MRI data were acquired using a 7T MR system (Siemens, Erlangen, Germany). A 32-channel head coil was used. We used the same scanning protocol as previously reported in a high-resolution fMRI study on the MTL (Maass et al., 2014). Furthermore, task residuals from the data of the recent study were used for functional connectivity analyses of MTL regions in chapter 4 (Maass, Berron et al., 2015). Prior to the functional MRI session, a whole head MP-RAGE volume (TE = 2.8ms, TR = 2500ms, TI = 1050ms,

flip angle = 5°, resolution 0.6mm isometric) was acquired. Subsequently, the four fMRI sessions were run (see FMRI data acquisition) followed by the acquisition of a high-resolution partial structural volume (T2*-weighted imaging, TE = 18.5ms, TR = 680ms, resolution 0.33mm x 0.33mm, 45 slices, slice thickness 1.5mm + 25% gap, FOV 212mm x 179mm, matrix 640 x 540), with a slice alignment orthogonal to the hippocampus main axis. Total MRI duration was around 100 minutes.

3.2.5   FMRI DATA ACQUISITION

Each subject's functional MRI scan consisted of 1600 volumes, each comprising 28 T2*-weighted echo planar slices with a resolution of 0.8 x 0.8mm (TE = 22ms, TR = 2000ms, slice thickness 0.8mm, FOV 205mm, matrix 256 x 256, parallel imaging with grappa factor 4) in four sessions of 13.5 minutes. The slices were acquired in an odd–even interleaved fashion oriented parallel to the hippocampus long axis. EPI volumes were distortion corrected using a point spread function (PSF) mapping method (Zaitsev et al., 2004) and motion corrected during the online reconstruction.

3.2.6   FMRI DATA ANALYSES

3.2.6.1 Univariate analysis

FMRI data preprocessing and statistical modeling was done using SPM8 (Wellcome Trust Centre for Neuroimaging, University College London, London, UK) as well as FSL (Centre for Functional Magnetic Resonance Imaging of the Brain, University of Oxford, Oxford, UK). Raw image data were converted to NIfTI images, while preserving the original image parameters. As the data was already corrected for distortions as well as for motion (see 3.2.5), the preprocessing included only slice timing correction, and smoothing with a 2mm full-width half-maximum Gaussian kernel (FWHM). We used a 2mm smoothing kernel since it provides a good compromise between high sensitivity and high specificity as we have previously reported (Maass et al., 2014). Coregistration of the functional and structural images was done using boundary based registration on a white matter segmentation of the structural MP-RAGE image using FSL (Greve and Fischl, 2009). In order to model the functional data, delta functions defined by the onset of a stimulus on a trial-by-trial basis were convolved with a hemodynamic response function (HRF) and its first temporal derivative. First and second level data were analyzed using a mixed-effect general linear model (GLM) approach (Worsley and Friston, 1995) and experimental conditions were entered into the GLM as separate regressors for 1st presentations, repetitions and lures for A and B stimuli, respectively. An additional regressor for all other trials as well as a regressor including motor responses was entered into the GLM. Furthermore, six motion correction parameters were added as regressors of no interest to minimize false positive activations due to task correlated motion (Johnstone et al., 2006). In total this resulted in 16 conditions for each of the four sessions. In order to assess differences in activity, two types of contrasts were calculated. First, we contrasted all 1st presentations to repetitions (1st > repetitions) in order to capture activation due to the immediate repetition of a stimulus (repetition suppression). On the other hand we

contrasted lures to repetitions (lures > repetitions) to identify voxels that show less repetition suppression to lures compared to repetitions. All models were calculated in native space.

Cross-participant alignment for univariate group analyses

In order to visualize and compare group activity levels in the hippocampus, we created a sample specific template for optimal cross-participant alignment of the functional data (Avants et al., 2011, 2010). Each participant's contrast image for lures > repetitions and 1st > repetitions was then aligned to the sample specific template space (see 1.4.2 for details). Finally, the aligned contrast images were submitted to a second-level group analysis in SPM (one-sample t-test).

Simulation of type-1 error rates

In order to determine the probability of false positive clusters (type 1 error) for a given smoothness, voxel-wise threshold (p < 0.005) and cluster size, we used 3dClustSim implemented in AFNI (http://afni.nimh.nih.gov/afni/; release from December 2015). These analyses were restricted to the bilateral hippocampus since our hypotheses were specifically focusing on neural processing within the subfields of the hippocampus. 3dClustSim computes the cluster size threshold at chosen values for the alpha significance level and voxel-wise threshold (alpha = Prob(Cluster ≥ given size)). 3dClustSim requires an estimate of the spatial correlation across voxels, which was determined in SPM with respect to the applied smoothing kernel of 2mm (FWHM = 2.5 x 2.8 x 2.1mm^3). For visualization, second-level result maps were thresholded at $p_{voxel\ level}$ < 0.005 and a cluster size of 35 voxels. The type-1 error rates of the resulting clusters are listed in Table 5.

3.2.6.2 Multivariate pattern analysis (MVPA)

While mass univariate analysis approaches consider the regional average activity across a brain region, multi voxel pattern analysis (MVPA) considers the multi voxel pattern of activity across and between different stimulus categories or task conditions (Haynes, 2015) (see Figure 16). In the following MVPA approach we extracted multi voxel patterns from MTL subregions to test for representational overlap across regions and conditions.
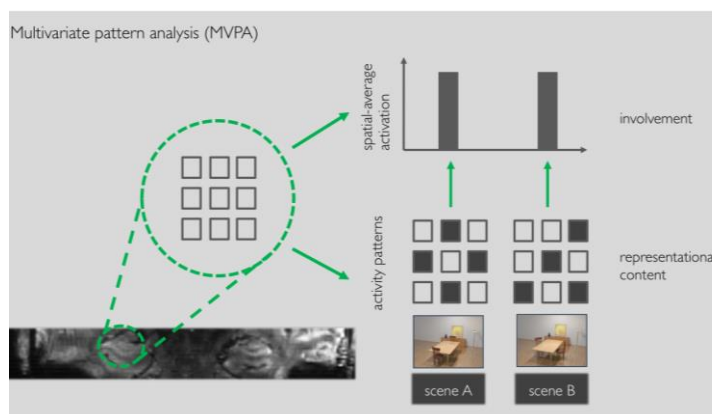
Figure 16: Concept of multi voxel pattern analysis (adapted from Mur et al., 2009). In contrast to mass univariate approaches, MVPA considers multi voxel activity patterns. Here we extracted multi voxel patterns for two different stimuli from high-resolution EPI images at 7T which were acquired during a novel memory task where subjects had to discriminate between two very similar images of the same indoor scene. A machine learning classifier based on a linear support vector machine was trained on the multi voxel patterns associated to the presentation of both stimuli across different conditions and subregions to test for representational overlap (i.e. the accuracy of the classifier in distinguishing between both stimuli solely based on its multi voxel activity patterns).

Raw image data were converted to NIfTI images, while preserving the original image parameters. The preprocessing included only slice timing correction (SPM8). We avoided spatial smoothing to keep the high resolution and fine-grained structure of activity. All models were calculated in native space.

We estimated trial-by-trial activation patterns using an effective approach for rapid event-related designs (Mumford et al., 2012). We obtained each trials' estimate through a general linear model including a regressor for that trial as well as another regressor for all other trials. The first derivative of the HRF was included in the model to take individual onset variations of the HRF into account. This process was repeated for each stimulus and resulted in 256 separate general linear models. Therefore, we could include 128 first presentations, 64 repetitions and 64 lures as samples in the multivariate classification procedure. There were no missing trials and the data was balanced in terms of samples for stimulus A and B for every run.

For our main analysis we did not remove the mean pattern ("cocktail blank removal", Op de Beeck, 2010) or the mean value of the ROI ("mean centering", Coutanche, 2013) from our multi voxel patterns prior to our multivariate analysis. This was done as recent papers highlight the negative effects of mean pattern removal (e.g. inducing negative correlations) (Garrido et al., 2013; Walther et al., 2015) but also argue against the removal of the mean value (Davis and Poldrack, 2013).

Trial estimates (64 per session, 256 in total) were analyzed for multivariate effects using PyMVPA 2.2.0 (Hanke et al., 2009). Each sample consisted of the beta estimate of a specific trial as well as its first derivative. Independent data chunks were defined by each of the four sessions. For the purpose of evaluation of classification validity a leave-one-run-out cross-validation was performed. In each of the four validation steps a linear support vector machine (Chang and Lin, 2011) was trained on the data of three runs and tested on the remaining run. We followed an anatomical feature selection approach (see 3.2.6.3). Therefore, the analysis was done for each condition (first presentations, repetitions and lures), hippocampal subregion (subiculum, CA1, CA2/3, DG) and subject. In a second analysis, this was also done for ErC, PrC, and PhC. As the regions in the anterior MTL are more affected by signal drop outs, this analysis was done separately and excluded 4 subjects with drop outs in the ErC or PrC. Accuracy of the validation step was calculated as the proportion of the samples that were classified correctly. Overall classification accuracy was defined as the mean accuracy of all four validation steps. There were more trial estimates for first presentations (128) compared to repetitions and lures (64). In order to parallel the analysis, we randomly chose 64 first presentations, which were balanced between stimulus A and B as well as run one to four. This procedure was repeated 100 times and decoding accuracies were averaged across all permutations.

Group analysis

First, results were tested for significance using one-sample t-tests. Furthermore, we applied permutation testing. We averaged the accuracy of all subjects to get the 'true' group accuracy value. In a second step, we relabeled the samples of the training set 1000 times and tested them on the

testing set using the same leave-one-run-out cross-validation scheme as before. This was to generate the individual null distributions that we used to calculate 1000 group means. Finally, we used the 1000 group means to generate the group null distribution. By comparing the 'true' group accuracy value we could identify the rank and thus the p-value (1000 permutations allow for p < 0.001) of the 'true' group accuracy value (Nichols and Holmes, 2002). We employed a 3 x 4 repeated measures ANOVA with the within-subject factors condition (first presentations, repetitions and lures) and subfield (subiculum, CA1, CA2-3 and DG) to test whether there are significant differences in classifier performance across task conditions and hippocampal subfields. Greenhouse-Geisser correction was used to correct for violations of sphericity.

3.2.6.3 Segmentation of subregions in the MTL

For each subject, regions of interest (ROIs) for the subfields of the hippocampus were manually traced on the high-resolution T2*-weighted images acquired orthogonal to the long axis of the hippocampus (see Figure 17A and B). The coregistered T1-weighted MPRAGE images provided additional information due to different contrast, lower slice thickness and less susceptibility artifacts. This was the case especially in the anterior MTL including the PrC and ErC. Therefore, PhC, PrC and ErC were manually labeled only on the high-resolution T1-weighted MPRAGE images. All ROIs were coregistered and resliced to the mean functional image. Finally, segmented masks were verified and adjusted (if necessary) on the mean functional images (see Figure 17C for the overlay of masks on a mean EPI). ROIs were identified in bilateral MTL and traced on consecutive coronal slices. Segmentation was performed for each hemisphere separately using a freehand spline drawing tool based on MeVisLab (MeVis Medical Solutions AG, Bremen, Germany). This tool provided a user-friendly interface for spline drawing and editing, with which the outer borders of the ROIs were traced closely. The outer border contours were converted to NIfTI images for further processing (Wisse et al., 2012; Kuijf, 2013). Subfields in the head and body of the hippocampus were traced according to the recently published protocol for hippocampal subfield segmentation at 7T (Wisse et al., 2012). Thereby the hippocampal head and body was divided into the subiculum, CA1, CA2, CA3 and DG. For further analyses CA2 was collapsed with CA3 to a combined CA2-3 region.

An important aim in our study was to separate functionally between the DG and CA3. The *Wisse et al.* protocol was at that time the only segmentation protocol which enables the division of these subfields on 7 Tesla MRI data. However, it must be noted that the suggested boundary between CA3 and DG slightly underestimates CA3, as it does not include the part of CA3 which is folded within DG. As this boundary was not visible on our T2* weighted images, we relied on the geometrical boundary suggested by the protocol as it can be reliably identified and replicated across subjects. In chapter 2 this shortcoming was revisited in a new segmentation protocol based on T2 weighted images. The hippocampal tail was not delineated. Tracing of the ErC started anteriorly at the level of the amygdala,

moving caudally along the parahippocampal gyrus (PHG). In the anterior part, the ErC borders the amygdala nuclei medially (Fischl et al., 2009). As soon as the ambient gyrus disappears and the hippocampal fissure opens, the ErC borders the parasubiculum medially. Laterally, the ErC borders the PrC. The opening of the collateral sulcus typically coincides with the lateral border of the ErC, and was therefore chosen as the lateral boundary. Contrary to other protocols for the ErC and PrC (Insausti et al., 1998), the part of the ErC within medial banks of the collateral sulcus that depends on the depth of the collateral sulcus was not segmented, since this border shows remarkable within and between subject variability and is also sometimes difficult to identify due to partially occurring susceptibility artefacts. Again, the between subject variability in sulcal patterns was the motivation behind the new segmentation protocol presented in chapter 2. The PrC was defined as the region between the medial and lateral edges of the collateral sulcus (covering medial and lateral banks). Segmentation of the PhC started one slice after the disappearance of the ErC, directly posterior to PrC and ErC. Labeling was continued posteriorly, ending on the last slice where the inferior and superior colliculi were jointly visible. The PhC was delineated as the region between subiculum (medial border) and the deepest point of the collateral sulcus (Zeineh et al., 2001) (see Figure 17C).
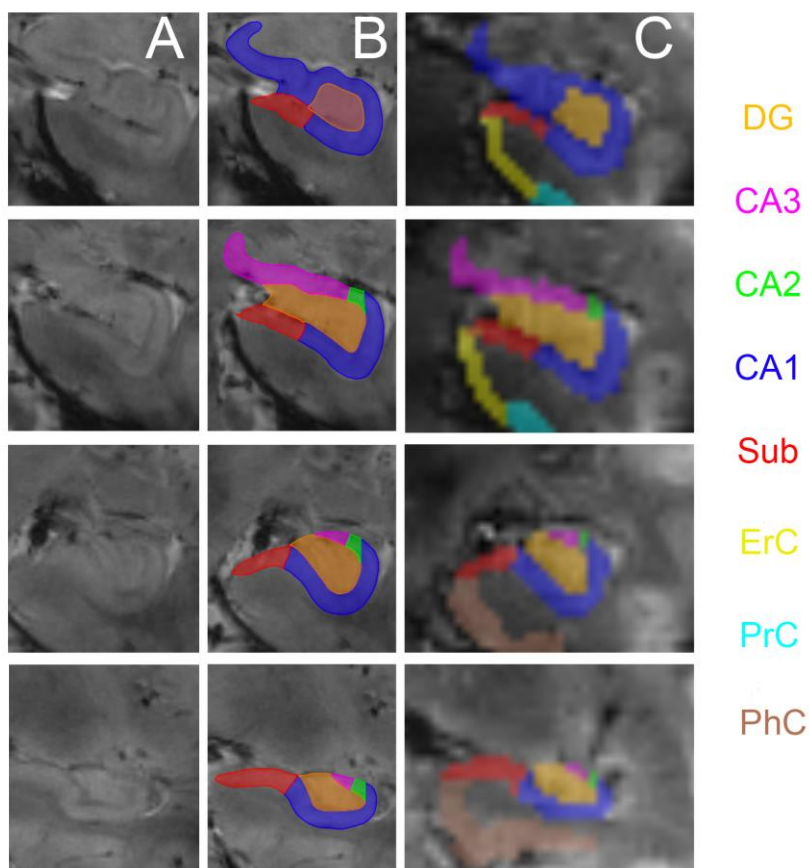

Figure 17. Segmentation of MTL subregions and hippocampal subfields. Hippocampal ROIs were traced on high-resolution T2* images **(A, B)**, whereas ErC, PrC, and PhC were traced on the high-resolution T1 images. All ROIs were later coregistered and resliced to the mean functional image **(C)**.

3.3 RESULTS

3.3.1 BEHAVIORAL PERFORMANCE

During the memory task, subjects saw sequences with several presentations of the same two stimuli (A and B, see Figure 15). Their task was to indicate the third occurrence of the first stimulus seen in a sequence via button press. Given this, the subjects were required to distinguish between the two similar stimuli in each of the sequences. To assess subjects' behavioral performance, button presses were evaluated. Missed or invalid button presses were counted as incorrect responses. The average incorrect rate was 2 percent (corresponding to 3 false sequences), indicating that subjects were highly accurate in discriminating between the similar scenes. Following the MRI session subjects were asked to draw both scenes as detailed as possible. These debriefings confirmed the results and showed that all remaining 19 subjects had a highly-detailed memory for the whole indoor scene.

3.3.2 DG SHOWS LESS REPETITION SUPPRESSION FOR LURES COMPARED TO REPETITIONS

The sequences that were used in the task consisted of presentations of the same two stimuli. Both stimuli (A and B) had the same probability to be the first stimulus (target) in a given sequence. The second stimulus within a sequence could be either a repetition of the first one or a presentation of the other stimulus. We refer to the presentation of the other stimulus as a lure trial and to the exact repetition of a stimulus as a repetition trial. Note that in contrast to earlier studies, being a lure or a repetition stimulus was independent of the identity of the stimulus. This depended only on the position within the sequence.

Two different contrasts were analyzed. First, we assessed which regions show repetition suppression by comparing all first presentations within each sequence (the first stimulus of each sequence) to repetitions (1st > repetitions). Second, we contrasted all lure trials against repetitions (lures > repetitions). In order to assess the regions that were significantly activated across subjects, we calculated second level group activation maps after cross-participant alignment using ROI-ANTS (see 1.4.2 for details). Activated clusters were identified within bilateral hippocampus (small-volume correction: $p_{\text{voxel-level}}$ < 0.005 and p_{cluster}< 0.05; see 3.2.6.1 for details). Higher activation in first presentations compared to repetitions was found in the right CA1 (Figure 18A and Table 5). However, there were no voxels that showed significant repetition enhancement (i.e. repetition > first). We did observe significantly higher activation for lure trials compared to repetitions in the DG of the right anterior hippocampus (Figure 18A and Table 5). Additional activation clusters in the subiculum, CA1 and CA1/DG, which did not survive multiple comparisons can be found in Table 5.

We extracted mean beta estimates for the significantly activated clusters on the group level in the right CA1 and DG. Mean activity within these clusters is shown for first presentations, repetitions and lures in Figure 18B.
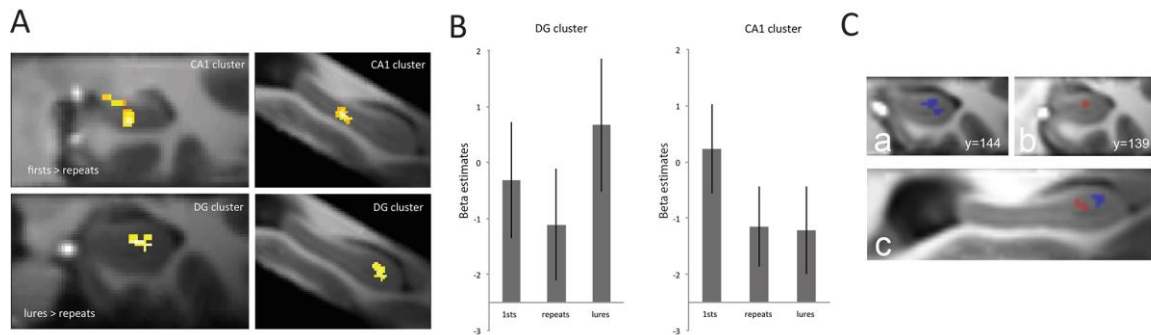
Figure 18. Univariate group results. **(A)** Cluster in CA1 (top row) shows significantly more activity in first presentations compared with repetitions. However, the cluster in the anterior DG (bottom row) shows significantly higher activation in lures compared with repetitions. Both clusters are in the right hippocampus. Results are small-volume corrected for the bilateral hippocampus ($p_{voxel-level}$=0.005 and $p_{cluster}$=0.05). Images on the right show a coronal view and those on the left show a sagittal view. **(B)** Beta estimates from clusters in DG (left) and CA1 (right). Error bars indicate SEM. **(C)** Stimulus-specific novelty contrasts. Clusters of activity resulting from lure-related novelty contrasts of individual stimuli. (a) lure A > repetition A; (b) lure B > repetition B. (c) sagittal view. Results are illustrated on the group T1 template ($p_{voxel-level}$=0.005, k > 10 voxels).

Table 5. Group activation after ROI-based alignment							
Contrast	Cluster size	Cluster p_{uncorr}	Alpha (sim)	Peak T	Peak location	Template x, y, z (mm)	hemisphere
Lures vs. repetitions							
	41	**0.005**	**< 0.05**	**4.14**	**DG (head)**	**22.4 28.1 -18.6**	**R**
	16	0.061	> 0.05	3.73	CA1/DG (body)	25.6 11.8 -10.1	R
Firsts vs. repetitions							
	55	*0.003*	*< 0.05*	*5.39*	*CA1 (body)*	*18.4 16.9 -9.3*	*R*
	25	0.031	> 0.05	5.69	CA1 (body)	-22.4 13.1 -12.7	L
	17	0.085	> 0.05	4.47	Sub (body)	23.2 18.6 -15.9	L
	15	0.069	> 0.05	4.19	CA1 (body)	-20.0 16.0 -12.5	R
	13	0.120	> 0.05	3.74	CA1 (head)	-16.8 13.2 -10.9	L
	12	0.107	> 0.05	3.36	Sub (body)	-24.8 26.6 -19.6	L

Hippocampal subregions showing group-level activation (thresholded at $p_{voxel level}$ < 0.005; k = 10 voxels; N = 19) for the repetition suppression (firsts > repetitions) and lure-related novelty contrast (lures > repetitions). Alpha levels (type 1 error rates) were simulated using 3dClustSim (AFNI). Note, regions in bold survive corrections for multiple comparisons. *DG, dentate gyrus; Sub, subiculum; R, right; L, left.*

An exploratory analysis was done to further investigate the nature of the novelty signal related to lures and to see whether there are distinct novelty signals for the two different stimuli. As mentioned previously, this was only possible due to the use of few stimuli in our paradigm (cf trial unique stimuli in Bakker et al., 2008). Therefore, we calculated the individual contrasts for stimulus A and B (lure A > repetition A and lure B > repetition B). The different contrasts yielded two spatially related but distinct clusters in the anterior DG. Whilst neither cluster (cluster A: pvoxel-level < 0.005 (unc), k= 10 voxels; cluster B: p voxel-level < 0.005 (unc), k = 30 voxels; see Figure 18C) survived multiple comparisons, interestingly however, the two resulting clusters were entirely non-overlapping (i.e. the two clusters did not share any voxels in common).

3.3.3   DG *BUT NOT OTHER SUBREGIONS CONTAINS REPRESENTATIONAL STIMULUS INFORMATION*

In order to assess the fine-grained activity patterns for A and B stimuli, a multivariate classifier (linear CSVMC) was trained on the A and B stimulus trials from 3 runs. Classifier performance was then tested on the unseen portion of trials corresponding to the left out run (see 4.2.6.2). This analysis was carried

out separately for first presentations, repetitions and lure trials. Each classifier yielded an accuracy value for each condition (first presentations, repetitions and lure trials) and hippocampal subfield (subiculum, CA1, CA2/CA3, DG) for each participant (Figure 19A). For every analysis, a comparison between the accuracies in the left and right hemisphere was conducted using 2 x 4 repeated-measures ANOVAs with the within-subject factors hemisphere and subfield. None of these tests demonstrated any significant hemispheric differences, and therefore all results reported are collapsed across hemispheres.

Mean group classifier accuracies were tested for significance using non-parametric permutation testing as well as one-sample t-tests (see 3.2.6.2). Mean group classification performance in the top 1% of the random permutations indicated above-chance accuracy (at p < 0.001). It was not possible to decode stimulus identity from first presentations or repetition trials with accuracies significantly above chance. Classifier accuracies derived from lure trials were significantly different from chance level (50 %) only in DG (M = 57.2 %, SEM = 1.6, permutation testing: p = 0.001, t-test: t_{18} = 4.6, p < 0.001) (corrected for multiple comparisons by using Holm-Bonferroni correction, with an initial critical α of p < 0.004).
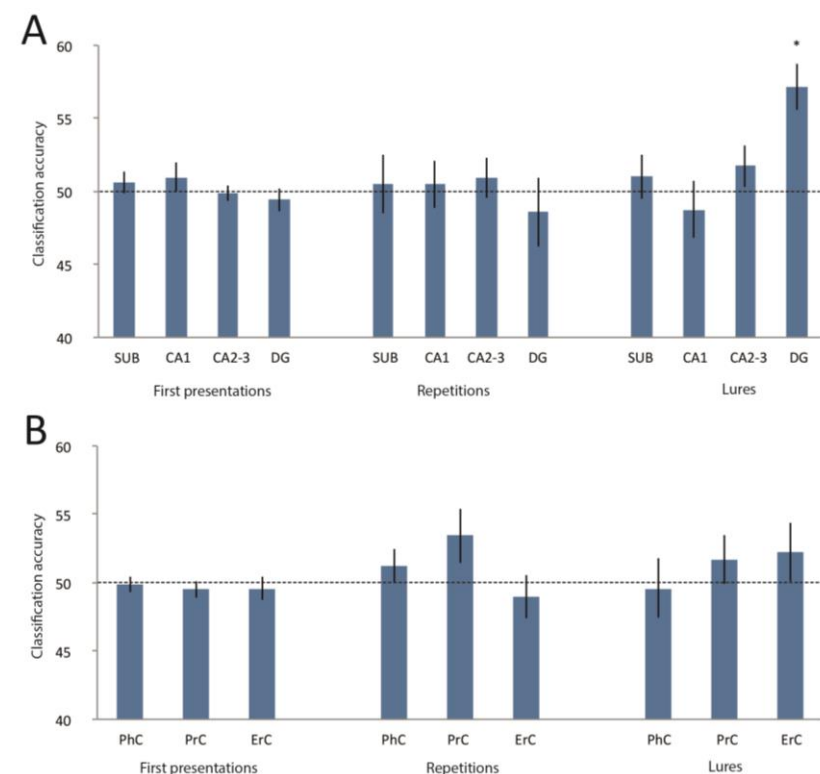
Figure 19. Classification accuracies for first presentations, repetitions, and lures across hippocampal subfields and extrahippocampal MTL structures. A linear classifier (linear support vector machine) was trained to distinguish between the presentation of stimulus A and B. **(A)** Although classification accuracies (in percentages) for hippocampal subfields are not significantly different from chance level (50%) in first presentations and repetitions, they exceed chance level significantly for lure-related activity in the DG (permutation testing: p<0.001, t-test: p<0.001). **(B)** Classification accuracies (in percentages) in extrahippocampal regions in the MTL are neither significantly different from chance level in first presentations, repetitions, and lures. The dashed line indicates chance level. Error bars indicate SEM. *sub, subiculum; DG, dentate gyrus; PhC, parahippocampal cortex; PrC, perirhinal cortex; ErC, entorhinal cortex.*

In order to test whether classifier performance is significantly different within the four hippocampal subregions across the three task conditions, we performed a 3 x 4 repeated measures ANOVA with the within-subject factors condition (first presentations, repetitions and lure trials) and subfield (subiculum, CA1, CA2-3, DG). This ANOVA revealed a significant main effect for the factor condition ($F_{1.2,21.6}$ = 4.2, p = 0.047 (Greenhouse-Geisser corrected)) and a significant condition x subfield interaction ($F_{3.29,59.15}$ = 4.4, p = 0.006 (Greenhouse-Geisser corrected)). This was due to significantly

higher classification accuracy during lure trials in DG (M = 57.2, SEM = 1.6) compared to the subiculum (M = 51, SEM = 1.5, t_{18} = -2.5, *p* = 0.02), CA1 (M = 48.8, SEM = 1.9, t_{18} = -3.7, *p* = 0.002) and CA2-3 (M = 51.7, SEM = 1.5, t_{18} = -2.4, *p* = 0.03). Furthermore, classification accuracy was higher in DG during lure trials (M = 57.2, SEM = 1.6) compared to first presentations (M = 49.4, SEM = 0.8, t_{18} = -5.3, *p* = 0.000) and repetition trials (M = 48.6, SEM = 2.4, t_{18} = -3, *p* = 0.008) (corrected by using Holm Bonferroni correction, with an initial critical α of *p* < 0.01) (see Figure 19A and Table 6). In other words, when A and B were presented as lures, they could be decoded from each other, whereas this was not possible when A and B were presented as first presentations or repetitions.

An interesting question concerns why we could successfully decode stimuli A and B in the DG region during lure trials, but not first presentations or repetitions. Since the ability to decode two stimuli (i.e. classifier accuracy) depends on the extent to which their representations (or multivoxel patterns) overlap, we considered how this might change as a function of trial type. To do this, we conducted a simulation: in this the underlying representations of stimulus A and B were overlapping, given their high level of perceptual similarity: for example, while stimulus A might activate units 1-5, stimulus B activates 3-7. As such, the nature of representations in our simulation is consistent with theoretical models suggesting that when there are small differences between input patterns (e.g. within the ErC), neural representations within DG will still overlap to a substantial degree (Knierim and Neunuebel, 2016; O'Reilly and McClelland, 1994). Based on previous work showing that neurons show repetition suppression in similar settings to our own (Hölscher and Rolls, 2002; Miller and Desimone, 1994) – where the stimulus set is small and extensively familiarized – we assumed that the first presentation would maximally activate units, whereas second presentations (repetitions, lure trials) would activate these units to a lesser degree (i.e. in our model, the r parameter specifies the degree to which neurons respond: e.g. 0.2 means 20% of their response on the first presentation). Consider, for example, a lure trial (e.g. stimulus A followed by stimulus B, Figure 20A): units 3-5 (i.e. that respond to both stimuli) would show reduced activity (i.e. 20%) compared to units 6-7 (i.e. that show selective response to stimulus B) which would show maximal activity (100%) – with units 1-2 (i.e. selective for stimulus A) being inactive when stimulus B is being presented, given that the delay between stimuli was ~ 3.5 seconds.

To evaluate the effect of the amount of repetition suppression, we varied the r parameter and calculated the Euclidean distance between the 2 activity patterns (i.e. pertaining to stimuli A and B) – a metric which naturally relates to the ability of a classifier to decode the stimuli. Our simulation shows that as the amount of repetition suppression increases (i.e. as r decreases), the euclidean distance between activity patterns increases during lure trials – whereas there is no effect of the r parameter during first or repetition trials (see Figure 20B). This implies, therefore, that if a region exhibits repetition suppression (e.g. Miller and Desimone 1994) to any degree, the ability of a classifier to decode two similar stimuli with representations that overlap will be greater during lure trials, as

compared to first and repetition trials. Therefore, our simulations provide one possible explanation for successful decoding in the DG region only during lure trials. It is worth noting, however, that we cannot entirely exclude other potential explanations for the profile of findings observed, including those related to the task being performed.

3.3.4 *NO EVIDENCE FOR REPRESENTATIONAL INFORMATION IN REGIONS UPSTREAM THE MTL*

To investigate whether the two similar stimuli are already separable in regions upstream the MTL, we trained another linear SVM in a separate analysis on the voxels of the PhC, PrC and ErC in first, repetition and lure trials. As four subjects had signal drop-outs in the anterior ErC, we performed a separate analysis including only 15 subjects to prevent any bias of the results. Again, the results did not differ significantly across hemispheres and therefore all results reported are collapsed across hemispheres. It was not possible to decode stimulus identity with above chance accuracy in extrahippocampal regions in repetition as well as in lure trials (see Figure 19B and Table 6).

Table 6. Mean classifier accuracies for firsts, repetition and lures in MTL structures and hippocampal subfields

	MTL structures			Hippocampal subfields			
firsts	PhC	PrC	ErC	SUB	CA1	CA2-3	DG
mean	49.8	49.5	49.6	50.6	51	49.9	49.4
sem	0.5	0.5	0.8	0.8	1	0.5	0.8
$p_{t\text{-}test}$	0.78	0.42	0.63	0.43	0.34	0.79	0.88
$p_{permutation}$	0.652	0.645	0.644	0.332	0.229	0.528	0.687
repetition	PhC	PrC	ErC	SUB	CA1	CA2-3	DG
mean	51.3	53.4	49	50.5	50.5	50.9	48.6
sem	1.2	2.0	1.6	2.0	1.6	1.4	2.4
$p_{t\text{-}test}$	0.32	0.11	0.53	0.81	0.76	0.52	0.56
$p_{permutation}$	0.224	0.015	0.741	0.093	0.716	0.245	0.092
lures	PhC	PrC	ErC	SUB	CA1	CA2-3	DG
mean	49.6	51.7	52.2	51	48.8	51.7	57.2
sem	2.1	1.8	2.1	1.5	1.9	1.5	1.6
$p_{t\text{-}test}$	0.85	0.36	0.32	0.52	0.53	0.25	0.00*
$p_{permutation}$	0.584	0.126	0.066	0.234	0.773	0.120	0.001*

Classification accuracies were tested for significance using one-sample t-tests ($p_{t\text{-}test}$) as well as permutation tests with 1000 iterations and a leave-one-run-out cross-validation approach ($p_{permutation}$).

* indicate corrected results using Holm's sequentially rejective Bonferroni correction with an initial critical α of p < 0.004.

PhC, parahippocampal cortex; PrC, perirhinal cortex; ErC, entorhinal cortex; sub, subiculum; dg, dentate gyrus; MTL, medial temporal lobe; sem, standard error of the mean.

Please note that the analysis regarding MTL structures corresponds to N=15 (due to drop out in the anterior temporal lobe), whereas the subfield analysis involved N= 19.

3.4 DISCUSSION

We used 7T ultra-high-resolution functional magnetic resonance imaging (fMRI) to measure activity in medial temporal brain regions and hippocampal subfields in a memory task that putatively imposed high demands on pattern separation. Convergent results from multivariate and univariate analyses indicate that the dentate gyrus (DG), but not other hippocampal subfields, the entorhinal (ErC), perirhinal (PhC) or parahippocampal cortex (PhC), harbours detectably distinct neural representations for similar events. These findings provide strong evidence that the human DG performs pattern separation.

In our paradigm, stimuli A and B were highly familiar because they were experienced prior to the fMRI scanning and repeatedly used in the experiment. Despite this high level of familiarity, we expected to observe novelty responses based on previous findings in the well established A-B-B-A type paradigm used in non-human primate studies where repetition suppression responses are typically observed even if the same stimuli are repeatedly used across sequences (Hölscher and Rolls, 2002; Miller and Desimone, 1994). Indeed, we did observe repetition suppression effects whereby items that were repeated within a sequence elicited reduced neural responses (cf first presentations) in CA1. However, increased responses related to lure stimuli (cf exact repetitions) were found exclusively in the DG. We refer to the activity increase for lures as "novelty" because in any given short sequence they appeared for the first time. Thus, unlike previous studies (Bakker et al., 2008; Lacy et al., 2011) this within-sequence "novelty" was not related to the use of trial unique stimuli but rather to the first appearance in a sequence.

As mentioned previously, the lure-related novelty responses we observed in the DG (and in DG/CA3 in Bakker et al., 2008), however, do not alone provide sufficient evidence to justify the inference of the operation of pattern separation computations in this region – because they are also consistent with the hypothesis that they reflect generic novelty signals produced by a match-mismatch process (Kumaran and Maguire, 2009). Importantly, we provide two lines of evidence to bolster the validity of an inference about pattern separation from such novelty responses. Firstly, our results suggest that novelty responses for different lures (A and B) were topographically distinct in right anterior DG – that is found in non-overlapping subsets of voxels, as would be predicted by idealized models of pattern separation (McClelland et al., 1995; Norman and O'Reilly, 2003) where even very similar stimuli are represented by orthogonal representations. Notably, we were able to achieve this through a paradigm optimized to detect this effect through the use of only two stimuli (cf trial-unique in Bakker et al. 2008) and ultra-high resolution fMRI.

Secondly, our study also afforded the unique opportunity to combine MVPA with univariate analyses to characterize the link between these lure-related novelty responses and the underlying representations of the two stimuli. Multivariate pattern analysis (MVPA) allows to determine whether fine grained patterns of distributed voxels within a region represent discriminative information (Jimura

and Poldrack, 2012; Norman et al., 2006; Sapountzis et al., 2010). MVPA analysis revealed representational stimulus information selectively in DG, but not CA2-3 or CA1. Decoding accuracies were not only significantly higher in DG compared to any other hippocampal subregion, it was also not possible to significantly decode stimulus information in regions upstream the MTL like the PrC, PhC or the ErC. These results, therefore, demonstrate that representations for similar stimuli overlap in neocortical regions but are less overlapping in the DG (McClelland et al., 1995; O'Reilly and McClelland, 1994).
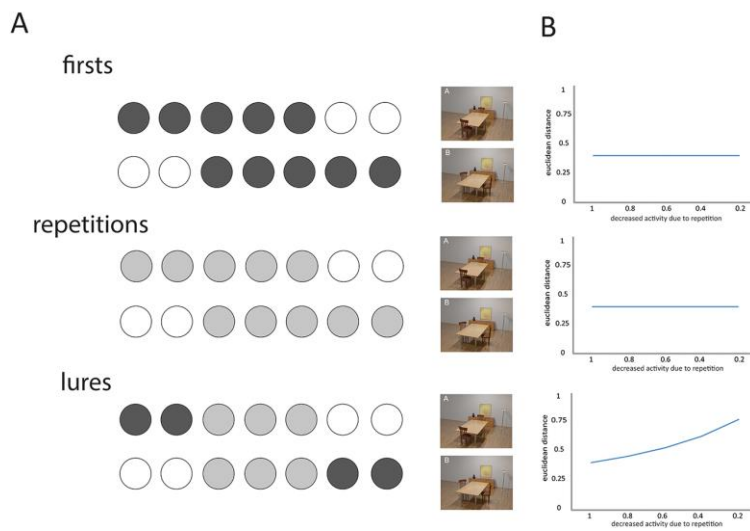

Figure 20. Simulation of degree of representational overlap of the two stimuli in DG as a function of trial type. (A) We assume that the underlying patterns of stimulus A and B are partially overlapping in DG, consistent with theoretical models (O'Reilly and McClelland, 1994; Knierim and Neunuebel, 2016). Although stimulus A activates units 1–5, stimulus B activates units 3–7. We further assume that first presentations activate these units maximally, whereas repetitions activate these units with decreased activity. For lure trials, we assume that the initially activated units (e.g., from stimulus A) are inactive by the time of the lure presentation ~3.5 s later (e.g., stimulus B). **(B)** Euclidean distance between the two patterns of activity (i.e., relating to stimulus A and B) as a function of trial type (first presentation, repetition, lure) and the amount of repetition suppression (i.e., the r parameter). See main text for details.

Of note, the accuracies of the multivariate classifier were significantly higher in DG during lure trials compared to first presentations and repetitions. In other words, when A and B were presented as lures, they could be decoded from each other, whereas this was not possible when presented as first presentations or repetitions. Our simulation (see Figure 20) provides a mechanistic account for these effects, by showing that for a region that shows repetition suppression the ability of a classifier to distinguish activity patterns is higher in lure trials (cf first, repetitions). Whilst the DG region tended to show repetition suppression (see Figure 18), this was not significant at the statistical threshold employed. However, given that our model shows that enhanced decodability is a continuous function of the degree to which the region shows repetition suppression (i.e. the r parameter in our model: Figure 6), our simulations support one potential account for why successful decoding was possible in the DG region only during lure trials.

Together with the results of the univariate analyses, our findings suggest that at least in our paradigm lure-related novelty responses do indeed reflect neural representations that are pattern separated in DG. Further, the combination of univariate results and successful multivariate decoding demonstrate that stimulus representations in the DG are both stable (i.e. across repetitions), and dynamic (i.e. show lure-related novelty responses). Whilst this result provides novel evidence about the nature of representations within the human DG, it does not necessarily arbitrate between models that include

the potential for learning within connections between the ErC and DG (e.g. Treves and Rolls 1992), in contrast to those which favour fixed random projections between these two regions (e.g. O'Reilly and McClelland 1994).

Interestingly, we did not find lure-related novelty responses or significant stimulus information at the multivariate level in the CA3 region – the main target of projections from the DG. There are several potential explanations for our findings: firstly, our results parallel previous neurophysiological evidence showing that the correlation between population activity recorded whilst the rat experienced two very similar environments was considerably lower in DG than in CA3 (Leutgeb et al., 2007) – under conditions that have parallels with our paradigm (i.e. the two environments were highly similar, akin to stimulus A and B in our experiment which differed by the location of only two objects). Interestingly, in the *Leutgeb et al.* study, this difference between DG and CA3 disappeared as the environments morphed into more dissimilar shapes – when representations in both subregions were effectively decorrelated between the two environments. Secondly, from an anatomical perspective a degree in reduction of the orthogonality of representations in CA3 (cf DG) would be expected based on the convergent nature of anatomical projections from DG to CA3 (Treves and Rolls, 1994). Thirdly, recent evidence suggests that the rodent CA3 may be functionally divided into proximal and distal regions, as a function of their proximity to the DG – with the functional (i.e. in terms of pattern separation) and anatomical (i.e. in terms of amount of recurrent excitatory connections) properties of the proximal CA3 being more akin to the DG. Given that we effectively collapsed across proximal and distal CA3 regions, one would predict based on recent evidence that representations in CA3 would be less pattern separated than DG (Lee et al., 2015).

Our findings, therefore, are highly consistent with previous studies in rodents (Lee et al., 2015; Leutgeb et al., 2007; Neunuebel and Knierim, 2014). It is important to note, however, that DG and CA3 are functionally embedded into a distributed network of brain regions that comprise other hippocampal subfields as well as extrahippocampal MTL structures. In order to understand the network level organization of pattern separation, it is necessary to simultaneously investigate activity in all of these regions and thereby to determine whether or not pattern separation is limited to DG/CA3. FMRI allows such coverage and therefore offers the potential to provide a comprehensive understanding of the network levels organization of pattern separation processes.

FMRI studies showed that patterns of activity across the hippocampus can reliably distinguish between different episodic events even if they were highly similar (Bonnici et al., 2012a; Chadwick et al., 2011). Hippocampal activity patterns of very similar scenes were also more distinct within the hippocampus compared to regions upstream the MTL (Bonnici et al., 2012b). These studies, therefore, provide evidence that the hippocampus as a whole supports pattern separation, but do not localize this computation to any subregion. Whilst a recent study presented evidence that multivariate voxel patterns of two similar environments were more distinct in DG/CA3 compared to CA1, the

interpretation of this finding is complicated because this analysis did not involve a direct comparison of the representations of the two similar environments in DG/CA3 and CA1. Instead, a "remapping" index was computed (Kyle et al., 2015) by comparing the representational similarity of each environment to itself (i.e. measure of consistency) with its average representational similarity to all other environments. Further, this study was not able to localize their effects to the DG region specifically, as in our study. One other study showed that it is possible to decode representations of similar scenes from hippocampal subfields (Bonnici et al., 2012a), accuracy of decoding was not significantly different between subfields. Compared to these previous MVPA studies at 3T, our ultra-high-resolution fMRI at 7T provided us with an opportunity to search for representations at a 6-7 fold smaller scale. A single voxel in our study would contain approximately 30 000 granule neurons while this would have been 200 000 per voxel in earlier high-resolution studies at 3T (Boldrini et al., 2013). Our methodology therefore was critical in demonstrating that representations of very similar events are indeed less overlapping in DG compared to CA1, CA2-3 and the subiculum.

To summarize, we used ultra-high resolution 7T fMRI in combination with a novel paradigm and multivariate analysis to investigate the representation of similar stimuli within human hippocampal subfields. Our MVPA results provide evidence that the representations of highly similar scenes are less overlapping in the DG compared to CA2-3 and other hippocampal subfields – as well as ErC, PhC and PrC. Further, we demonstrate a mechanistic link between the genesis of lure-related novelty signals in our paradigm and the underlying stimulus representations in DG. Taken together, our results provide strong evidence that the human DG plays a unique role in pattern separation – and suggest that stimulus representations within the DG are both stable and dynamic across time.

3.5 CONTRIBUTIONS

CHAPTER

4

FUNCTIONAL SUBREGIONS OF THE HUMAN ENTORHINAL CORTEX

4.1 INTRODUCTION

Given the anatomy and connectivity of the parahippocampal-hippocampal system as reviewed in the General Introduction, the entorhinal cortex (ErC) is a major hub within the medial temporal lobe (MTL) that mediates hippocampal-neocortical communication. However, virtually nothing is known about how hippocampal and neocortical connectivity with the ErC is organized in humans. This lack of knowledge has significantly limited the development of neurobiological theories of memory and navigation and our understanding of the clinical impact of localized ErC damage in the early stages of neurodegenerative conditions such as Alzheimer's disease.

To recapitulate, neuroanatomical evidence from studies in rodents suggests that there are two parallel input pathways that convey spatial and non-spatial input into the hippocampus via the ErC (Knierim et al., 2014). Specifically, spatial information is conveyed from the postrhinal cortex (POR, thought to be homologous to the PhC in primates and humans), which shows preferential connectivity with medial ErC (mErC). In contrast, non-spatial information is conveyed from the PrC to the lateral ErC (lErC). LErC and mErC, in turn, are differentially connected with hippocampal subfields (i.e. subiculum and CA1) along the proximo-distal (transverse) axis. Projections of the lErC preferentially target the region close to the border between CA1 and subiculum (distal CA1 and proximal subiculum), whereas the mErC preferentially projects to proximal CA1 and distal subiculum. These partially segregated pathways have been differentially associated with the processing of, and memory for, object and context information. Notably, although terminology for ErC subdivisions in the rat emphasizes the lateral to medial axis, these areas do not differ solely with respect to their position in relation to the hippocampal formation and the rhinal fissure (Witter et al., 2000b). In actuality, lErC occupies the rostrolateral portion of the ErC, whereas mErC occupies the caudomedial portion of the ErC. In primates, ventral hippocampus and the adjacent ErC are situated in a relatively more rostral position in the anterior temporal lobe. Although the position of the ErC on the cortical surface and the orientation of anatomical axes differ across species, the relative topography of ErC connectivity seems to be preserved in nonhuman primates. Anatomical studies suggest that the PrC is predominantly interconnected with the anterior third of the ErC, whereas the PhC is predominantly interconnected with approximately the posterior two-thirds (Suzuki and Amaral, 1994). In addition, PrC/PhC connectivity with ErC differs between lateral and medial domains (Suzuki and Amaral, 1994).

To summarize, findings from rodents and nonhuman primates suggest that connectivity of the human ErC might differ along the longitudinal and lateral-medial axis, but because anatomical tracing studies cannot be performed in humans, direct evidence for this idea is lacking. Recent structural and functional MRI studies have assumed a lateral-medial distinction in humans according to the rodent nomenclature of lErC and mErC. However, whether such a lateral-medial dissociation of ErC connectivity exists in humans and/or whether connectivity differs along the anterior-posterior ErC axis has not been assessed so far. Numerous studies have demonstrated that networks of brain regions

linked by direct and indirect anatomical connections exhibit temporally coherent, low-frequency fluctuations in blood-oxygen-level dependent (BOLD) functional magnetic resonance imaging (fMRI) data during both the resting and task states. Recent work has demonstrated that spatially contiguous but anatomically distinct brain regions can be reliably differentiated based on functional connectivity profiles measured with BOLD fMRI (for a review see Fox und Raichle, 2007) Using fMRI at 3 Tesla, human resting-state fMRI studies (Kahn et al., 2008; Libby et al., 2012) have reported reliable differences in connectivity between the PrC and PhC with the hippocampus. Whereas the PrC showed higher functional connectivity with the anterior hippocampus, the PhC showed stronger connectivity with the posterior hippocampus, a dissociation that was most evident for subiculum and CA1 subfields (Libby et al., 2012). Due to limitations in signal-to-noise ratio (SNR) and spatial resolution, these studies were unable to assess functional connectivity with the ErC.

Here, we used ultra-high resolution fMRI at 7T to characterize the functional organization of the human ErC. The high SNR of MRI data collected at 7T makes it feasible to acquire BOLD fMRI data at an unprecedented level of anatomical detail (Maass et al., 2014). To determine the topographic organization of ErC connectivity in humans, we analyzed data from two experiments in which fMRI data were acquired with a resolution of 0.8mm (isotropic) (Experiment 1: Maass et al., 2014; Experiment 2: Berron et al., 2016, also presented in chapter 3). Notably, this level of spatial resolution is more than 6 times higher than in previous high-resolution fMRI studies that investigated intrinsic connectivity within the MTL (Lacy and Stark, 2012; Libby et al., 2012). In two independent samples, we examined correlations of activation between individually anatomically defined PrC vs. PhC seeds and the ErC along its anterior-posterior and lateral-medial axis. In addition, we tested whether functionally distinct ErC subregions also exhibited differential connectivity with the subiculum along a transverse or longitudinal hippocampal axis. In addition, we also analyzed connectivity profiles of PrC and PhC seeds with the subiculum.

4.2 MATERIALS AND METHODS

4.2.1 PARTICIPANTS

Two independent samples of 21 and 22 young, healthy subjects underwent high resolution fMRI scanning (Exp.1: mean age 26 ± 3.6 yrs, 12 male; Exp.2: mean age 28 ± 3.9 yrs, 7 male). Participants from Experiment two overlap with the participants from the experiment presented in Chapter 3. Exclusion criteria were metallic implants (other than standard dental implants), tinnitus, known metabolic disorders or a history of neurological or psychiatric disorders. Both studies were approved by the local ethics committee of the Otto-von-Guericke University Magdeburg. All subjects gave written informed consent and consent to publish prior to participation and received monetary compensation for participation. Six subjects from Experiment 1 and six from Experiment 2 were excluded due to dropouts in the PrC and/or ErC or due to severe movement artifacts. Functional

connectivity analyses were performed on the residuals of task data after extraction of task effects ($N_{Exp.1}$ = 15, $N_{Exp.2}$ = 14).

4.2.2   TASKS

During the fMRI session of experiment 1, subjects performed an incidental visual encoding paradigm. Therefore, 120 new images (60 indoor and 60 outdoor), 60 noise images and 60 repetitions of one familiar image were presented randomly. The familiar image and the noise images were familiarized using 10 repetitions each directly before the functional MR scan. Subjects made an indoor/outdoor judgment for each image by button press (for more details, see Maass et al., 2014). For details of experiment 2 see chapter 3 (Berron et al., 2016).

4.2.3   DATA ACQUISITION AND PREPROCESSING

In both experiments the same MRI protocol was used. Please see 3.2.5 for detailed information regarding the used sequences. The fMRI session comprised 1 run (13 min) with 370 EPI volumes in Experiment 1 and 4 runs (13.5 min each) with 400 EPI volumes in Experiment 2. Total MRI duration was around 60 minutes in Experiment 1 and 100 min in Experiment 2.

FMRI data preprocessing and statistical modeling was done in SPM8 (Wellcome Trust Center for Neuroimaging, University College, London, UK). The preprocessing included slice timing correction and smoothing with a 1.5mm full-width half-maximum Gaussian kernel (FWHM < 2 × voxel size) to keep high anatomical specificity. Outliers in average intensity and/or scan-to-scan motion were identified using the *ARTRepair toolbox* for SPM (Percent threshold in global intensity: 1.3, movement threshold: 0.3mm/TR) and included as spike regressors. To remove task effects, GLMs were run (including all task conditions and movement parameters) and the residual images were saved for subsequent intrinsic functional connectivity analyses. Based on previous studies suggesting a linear superposition of task activity and spontaneous BOLD fluctuations, removing task-induced variance of event-related fMRI data should yield a remaining residual signal similar to "continuous" resting state data (Fox et al., 2006). Although quantitative differences between residuals derived from task data and continuous resting state data have been reported (Fair et al., 2007), in qualitative terms, patterns of functionally connected regions have been shown to be remarkably consistent (Fair et al., 2007; Lacy and Stark, 2012).

4.2.4   SEGMENTATION OF REGIONS OF INTEREST

In order to analyze PrC vs. PhC seed-to-voxel connectivity, we manually segmented PrC and PhC masks for each subject on the individual high resolution MPRAGE images (which had been bias-corrected and coregistered to the individual mean EPIs). Furthermore, the ErC and the subiculum were labelled on the T1-group template in order to analyze PrC vs. PhC connectivity topography within the ErC as well as PrC vs. PhC connectivity topography within the subiculum, respectively, at the group level (individual

beta-maps were registered to the template). MTL masks were traced on consecutive coronal slices bilaterally using MRIcron (Chris Rorden, Version 4, April 2011). Again, please note that the tracing of anatomical regions did not rely on the protocol that was presented in chapter 2 as it was developed later. Tracing of the ErC, PrC and PhC followed the boundaries described in chapter 3.2.6.3. We further deleted PrC mask voxels that were directly neighbored to the ErC/PrC border (leaving a gap of approx. 2 voxels ~ 1 mm) to avoid autocorrelations between PrC seed voxels and our target ErC mask. The subiculum was labeled on the T1-template (0.8mm isotropic resolution) in the hippocampal head and body (until the colliculi disappeared) according to the segmentation protocol of *Wisse et al., 2012*. Note that we did not segment the hippocampal tail as boundaries are difficult to identify. For division of the ErC and subiculum masks into anterior-posterior and lateral-medial or proximal-distal subregions, see 4.2.6.1.

Subsequently, PrC and PhC masks were coregistered and resliced to the individual mean EPI images (using FSL, epi-reg) and manually adjusted to achieve a precise overlay on the functional data. To exclude voxels susceptible to signal dropout, for each mask voxels with mean intensity (across timepoints) higher than 2 standard deviations from the mean intensity (across voxels) of the mask were removed (Libby et al., 2012). Thresholding led to the rejection of no more than 5% of voxels in any mask. Additionally, areas of PrC were occasionally subject to distortion artifacts, and these voxels were manually deleted from masks. These adjusted and thresholded masks were used as seed regions for the functional connectivity analyses. Probabilistic white matter (WM) and cerebral spinal fluid (CSF) masks were generated by automated segmentation (SPM8, New Segment routine) of the coregistered MPRAGE images and thresholded at $p_{tissue} > 0.95$.

4.2.5 *FIRST-LEVEL FUNCTIONAL CONNECTIVITY ANALYSES*

We performed seed-to-voxel correlational analyses on the native (preprocessed, unnormalized) residual fMRI data using the *conn-toolbox* (Whitfield-Gabrieli and Nieto-Castanon, 2012). First, functional connectivity patterns of PrC vs. PhC seeds with the ErC were analyzed. For each functional connectivity analysis, seed regions' average time series were generated as regressors of interest. As covariates of no interest, WM and CSF time series and realignment parameters (including spike regressors) were included to account for physiological noise and head movement, respectively. Functional data were band-pass filtered for frequencies of 0.01– 0.1 Hz. Bivariate correlations were computed, resulting in beta maps containing Fisher-transformed correlation coefficients. To perform group analyses, beta maps were registered to the group-specific T1 template (see 1.4.2 for details) and Z-standardized.

4.2.6 SECOND-LEVEL ANALYSES

4.2.6.1 Univariate

First, we calculated single-seed group connectivity maps using voxelwise one-sample t-tests to characterize the intrinsic connectivity profiles of PhC and PrC with ErC (Figure 21) and Supplementary Figure 12). Additionally, paired t-tests were performed to determine significant differences in PrC vs. PhC connectivity (Figure 22A). Resulting T-maps were masked with the ErC mask and significant clusters determined by cluster-extent based thresholding (Z > 2.3; $p_{cluster}$ < .05). In addition, we visualized the differential topographic pattern of PrC versus PhC connectivity along the x-y-z direction in three-dimensional plot of connectivity preference for each voxel (see Figure 22B). These analyses indicated relatively stronger connectivity of the PrC with the anterior-ventral-lateral ErC and stronger connectivity of the PhC with the posterior-dorsal-medial ErC.

In a next step, to directly test for significant differences between anterior/posterior and lateral/medial EC, we divided the template ErC mask into four equally-sized sections along the longitudinal and horizontal (or transverse) plane, corresponding to coronal and sagittal cuts, respectively. As mentioned previously, the planes are defined in reference to the longitudinal axis of the hippocampus (which also corresponds to the ErC long-axis). The lateral vs. medial division was performed for each coronal slice individually in order to ensure equally sized portions along the longitudinal axis. Mean parameter estimates were extracted from each of the four subsections for each subject (from the template-registered beta maps). The resulting PrC and PhC connectivity estimates were submitted to a 2 x 2 x 2 repeated-measures ANOVA with seed mask (PhC vs. PrC), longitudinal ErC section (anterior vs. posterior), and horizontal ErC section (lateral vs. medial) as factors. Furthermore, we assessed connectivity gradients across the longitudinal and horizontal axes by plotting slice-by-slice mean parameter estimates. As the number of transverse ErC slices differed along the longitudinal axis (between 5 - 11 slices), we divided each coronal ErC slice into 5 equal sections and calculated mean betas for each section. The same approach was used to test for differential connectivity of ErC subregions and PrC/PhC with the subiculum along the longitudinal or transverse axis.

4.2.6.2 Multivariate

Finally, we used a multivariate classifier (linear CSVMC) to further investigate the reliability of the topography of PrC vs. PhC preferential connectivity within the ErC. A linear support vector machine classifier (LinearCSVMC, Chang and Lin, 2009) was trained and tested on the x-y-z coordinates of all ErC voxels across all subjects using PyMVPA 2.2.0 (Hanke et al., 2009). Independent data chunks were defined according to the individual subjects of each study. Each chunk consisted of the same amount of samples (ErC voxels). For the evaluation of classification validity, a leave-one-subject-out cross-validation procedure was applied. In each of the validation steps, a linear support vector machine was trained on the data of all but one subject and tested on the remaining one. Accuracy of the validation

step was calculated as the proportion of the samples (voxels) that were classified correctly (as being preferentially connected to PrC or PhC). Overall classification accuracy was defined as the mean accuracy of all validation steps across subjects. Mean classifier accuracy was tested for significance using non-parametric permutation testing. Over 1000 iterations, samples (ErC voxels) of the training set were randomly relabeled and tested on the testing set using the same leave-one-subject-out cross-validation scheme as before, generating a non-parametric null distribution. Type I error rate was set at p < 0.001 based on this null distribution (Nichols and Holmes, 2002). Classification and permutation testing were performed separately for left and right hemisphere and separately for Experiment 1 and Experiment 2.

4.3 RESULTS

4.3.1 ENTORHINAL CONNECTIVITY TOPOGRAPHY RELATED TO PRC AND PHC SEEDS

4.3.1.1 Seed-to-voxel connectivity of PrC vs. PhC with ErC

Group-level functional connectivity profiles of each seed region for Experiment 1 and 2 are shown in Figure 21 and Supplementary Figure 12, respectively (voxelwise one-sample t-tests, Z > 2.3, $p_{cluster}$ < .05). While the PrC showed significant connectivity with bilateral ErC clusters covering approximately the anterior two-thirds of the ErC, significant functional connectivity of the PhC was found with bilateral ErC clusters comprising about the posterior two thirds of the ErC (see also peak coordinates of significant clusters in Table 7). Additionally, PrC-connectivity clusters were limited to progressively more lateral ErC regions when moving posteriorly while PhC-connectivity clusters were limited to progressively more medial ErC regions when moving anteriorly. Overlapping connectivity with both seeds was strongest in the transition zone between anterior-posterior and lateral-medial ErC (see bright regions in Figure 21 and Supplementary Figure 12).
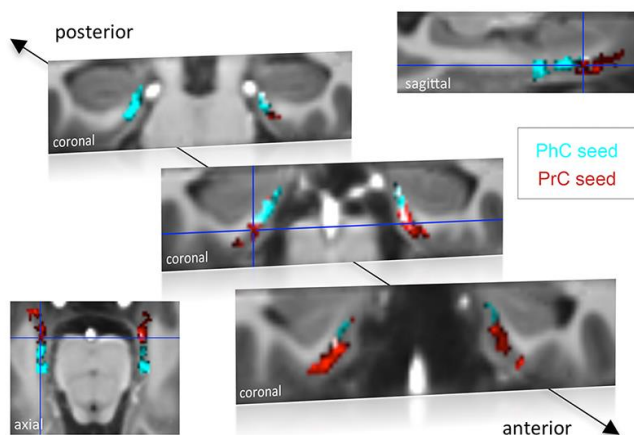
Figure 21. Functional connectivity profiles of parahippocampal cortex (PhC) and perirhinal cortex (PrC) seeds with the ErC in Experiment 1. Group results for seed-to-voxel connectivity of bilateral PrC and PhC seeds with the ErC shown for Experiment 1 (one-sample t-test; Z > 2.3, pcluster < 0.05, $N_{Exp.\ 1}$ = 15). Bright regions denote overlapping connectivity with PrC/PhC. Single-subject beta maps were normalized on the group-specific T1-template by ROI-based alignment with ANTS and masked with a manually defined ErC mask. The T1-template has the same resolution (and alignment) as the high-resolution functional EPI volumes (0.8 × 0.8 × 0.8mm). See also Supplementary Figure 12 for results of Exp. 2.

Paired t-tests revealed those ErC regions that exhibited significant stronger connectivity with PrC than PhC seeds, and vice versa (see in Table 7). While stronger functional connectivity of the PrC was found with bilateral clusters in the anterior-lateral ErC (alErC), the PhC showed relatively stronger connectivity with bilateral clusters located in the posterior-medial ErC (pmErC). Paired t-test results are illustrated for Experiment 1 in Figure 22.

Table 7. Univariate group-results for seed-to-voxel connectivity of PrC and PhC seeds with the ErC

	Cluster $P_{FWE\text{-}corr}$	Cluster $P_{FDR\text{-}corr}$	Cluster Size	Peak Z-score	Peak coordinate (Template) x	y	z	Side
Experiment 1								
PrC Seed	<0.001	<0.001	517	5.05	153	149	8	R
	<0.001	<0.001	273	4.82	108	146	12	L
PhC Seed	<0.001	<0.001	380	5.29	150	129	9	R
	<0.001	<0.001	510	5.05	106	138	12	L
PrC > PhC	0.038	0.022	42	4.31	151	150	8	R
	0.001	0.001	91	4.04	101	146	9	L
PhC > PrC	0.008	0.005	61	4.15	150	131	10	R
	0.001	0.002	87	3.53	108	136	11	L
Experiment 2								
PrC Seed	<0.001	<0.001	777	4.82	109	152	20	L
	<0.001	<0.001	849	4.73	149	145	10	R
PhC Seed	<0.001	<0.001	669	5.31	147	137	13	R
	<0.001	<0.001	637	4.91	107	139	14	L
PrC > PhC	<0.001	<0.001	167	4.70	105	153	15	L
PhC >PrC	0.022	0.024	66	4.09	153	130	9	R
	0.047	0.026	53	3.74	108	136	18	L

Entorhinal subregions showing significant functional connectivity (one-sample t-test) or differential connectivity (paired t-test) with bilateral PrC or PhC seeds (Z > 2.3, $p_{cluster}$ <.05, $N_{Exp.1}$ = 15, $N_{Exp.2}$ = 14). Single-subject beta maps were normalized on the group-specific T1-template and masked with a manually defined ErC mask. The ErC covered 26 coronal slices on the template (y = 154: most anterior slice, y=129: most posterior slice), with coronal slices being oriented orthogonal to the hippocampal long-axis. See also Figure 21 and Supplementary Figure 12.

4.3.1.2 Three-dimensional topography of entorhinal connectivity

In order to assess and visualize the 3-dimensional topography of differential ErC connectivity with PrC versus PhC seeds, we plotted the connectivity preference of each voxel along the x-y-z direction (see Figure 22B and Supplementary Figure 13). Connectivity preference was defined on the basis of the paired t-test t-maps (red: $T_{PrC\,>PhC}$ > 0; blue: $T_{PhC\,>PrC}$ > 0). These plots indicated a complex 3-dimensional topography of ErC connectivity with a gradient of PrC-to-PhC preference running from anterior-ventral-lateral to posterior-dorsal-medial ErC. In addition, we plotted functional connectivity preference of unilateral (left and right) PrC/PhC seeds with both the ipsi- and contralateral ErC to evaluate whether connectivity patterns were symmetric across hemispheres (Supplementary Figure 13 for results of dataset 1). These additional analyses confirmed the findings of bilateral connectivity

analyses with an anterior-posterior and lateral-medial gradient of ErC connectivity for contralateral PrC and PhC seeds. These findings also suggest that the dissociation of ErC connectivity cannot be simply explained by local autocorrelations of neighbored voxels.
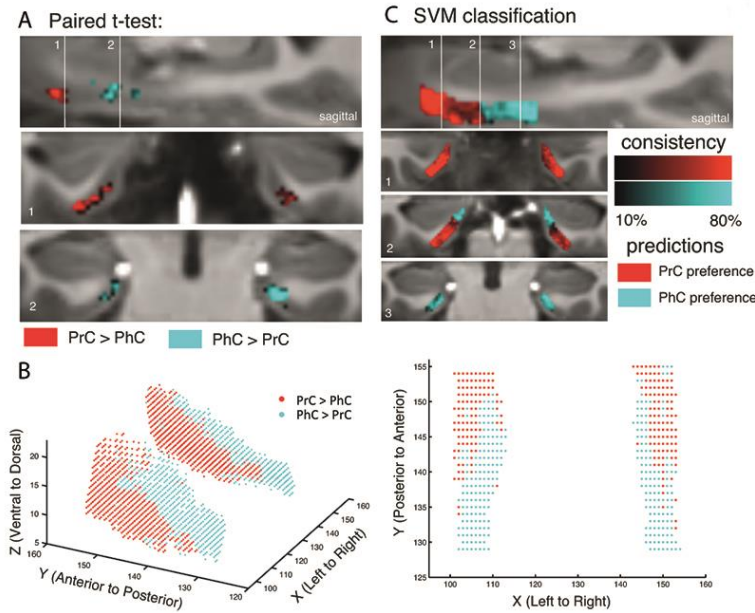

Figure 22. Differential connectivity topography of PrC vs PhC seeds with the ErC for Experiment 1. (A) To assess differential connectivity of PrC vs PhC with the ErC, voxelwise paired-sample t-tests were performed on the normalized single-subject beta maps (resulting from seed-to-voxel connectivity analyses). Significant clusters for Exp.1 are shown for two coronal sample slices (Z > 2.3. $p_{cluster}$ <0.05, $N_{Exp. 1}$ = 15) at the level of the anterior (1) and posterior (2) hippocampal head. **(B)** To visualize the 3-dimensional geometry of connectivity, the connectivity preference with PrC vs PhC of each ErC voxel was plotted along the x-, y-, and z-axis (red:$T_{PrC >PhC}$ > 0, blue:$T_{PhC >PrC}$ > 0). Axes terminology is relative to the long-axis of the hippocampus. **(C)** Classification of PrC vs PhC connectivity preference was tested across subjects based on the x-y-z coordinate of an ErC voxel. Multivariate classification (support vector machine; leave-one-subject-out cross-validation) was significant across both datasets (p < 0.001; accuracies: Exp. 1: left: 62%, right: 60%, Exp. 2: left: 67%, right: 57%), which confirms a spatial dissociation of entorhinal connectivity with PrC vs PhC. Predicted clusters are color-coded in red vs. blue, bright regions denote high consistency of the classifier (accuracy for each voxel across subjects). Results are shown for Exp. 1. See also Supplementary Figure 13 for 3D plots of Exp. 2 and for unilateral seeds of Exp 1

Our next analyses assessed the reliability of topographic differences in ErC connectivity with PhC and PrC. If the topographic organization is reliable across participants, then it should be possible to predict the connectivity preference of specific ErC voxels within any participant, simply by knowing the connectivity preferences of corresponding voxels in other participants. To test this strong prediction, we conducted a multivariate pattern classification analysis using a leave-one-subject-out cross-validation scheme. Specifically, we trained a multivariate support vector machine classifier (see 4.2.6.2) on data from all but one subject, entering only the x-, y-, and z-coordinates of each voxel and the relative preference of PrC and PhC connectivity (based on the subject's paired t-test t-maps, analogous to the definition of preference in the previous section). The classifier was then tested on the remaining subject, and the accuracy of this validation step was calculated as the proportion of ErC voxels that were classified correctly as being preferentially connected to PrC or PhC in the tested subject. The training and cross-validation steps were repeated for all combinations of participants, and a mean classification accuracy score was computed. Classification accuracy was significantly above chance across both datasets (p < 0.001). Mean classifier accuracies across all ErC voxels and subjects were around 60% (Exp. 1: left 62%, right 60%, Exp. 2: left 67%, right 57%). However, connectivity preference of voxels in the very anterior-lateral and posterior-medial ErC could be predicted with more

than 80% accuracy. These analyses confirm a spatial dissociation in connectivity between ErC subregions with regard to PrC vs. PhC seeds. Predicted clusters of preferential connectivity are color-coded in Figure 22C (bright regions denote high consistency of the classifier).

Moreover, we repeated the classification analysis on the combined data of both studies to predict alErC and pmErC functional subregions (based on preferential connectivity with PrC vs. PhC) across all participants. Anatomical landmarks for these clusters are described further below in "Landmarks for delineation of alErC and pmErC" and alErC and pmErC masks in template and MNI space are available online (http://dx.doi.org/10.7554/eLife.06426.014).

4.3.1.3 *PrC and PhC show different connectivity along the transverse and longitudinal axis of the ErC*

Anatomical studies in rodents have demonstrated a rostrolateral-caudomedial dissociation of ErC connectivity with PrC vs. PhC, and data in nonhuman primates suggest a similar gradient of differential connectivity along anterior-posterior and lateral-medial axes (Suzuki and Amaral, 1994; van Strien et al., 2009; Witter et al., 2000a). In order to directly test for significant differences of PrC vs. PhC intrinsic functional connectivity between the anterior vs. posterior and lateral vs. medial ErC, we divided the template ErC mask equally into four portions: anterior-lateral, anterior-medial, posterior-lateral and posterior-medial (see Figure 23A, right panel). Mean parameter estimates for PrC and PhC connectivity (mean betas) were extracted across all voxels in each section for each subject. Note that the lateral-medial split was performed for each coronal slice individually as the ErC is curved along the longitudinal axis and furthermore, that this separation also corresponds to a ventral-dorsal split. Repeated-measures ANOVAs with PrC and PhC connectivity estimates revealed significant two-way interactions of seed region x anterior-posterior ErC section (Exp.1: $F_{1,14}$ = 56.0, $p < 0.001$; Exp.2: $F_{1,13}$=95.9, $p < 0.001$) and seed region x lateral-medial ErC section (Exp.1: $F_{1,14}$ = 11.3, $p = 0.005$; Exp.2: $F_{1,13}$=32.8, $p < 0.001$). Follow-up paired sample t-tests confirmed significantly greater PrC than PhC connectivity with the anterior ErC (Exp.1: t_{14} = 5.3; $p < 0.001$; Exp.2: t_{13} = 4.5, $p = 0.001$) and vice versa significant higher PhC than PrC connectivity with the posterior ErC (Exp.1: t_{14} = 4.7; $p < 0.001$; Exp.2: t_{13} = 2.6; $p = 0.019$). With regard to the lateral-medial dissociation, the PrC showed significantly higher intrinsic functional connectivity than the PhC with the lateral ErC (Exp.1: t_{14} = 5.2; $p < 0.001$; Exp. 2: t_{13} = 3.8, $p = 0.002$). However, there was no significant difference in connectivity between seeds with the medial ErC (all p-values > 0.80). Although connectivity estimates did not differ in the medial ErC, the PhC showed significantly stronger connectivity with medial than lateral ErC (Exp.1: t_{14} = 4.4; $p < 0.001$; Exp.2 t_{13}= 2.6, $p = 0.021$). There were no significant three-way interactions between seed, longitudinal and sagittal ErC section (all p-values > 0.25). To characterize the topography of PrC and PhC functional connectivity with voxels along the longitudinal (anterior to posterior) and transverse (lateral to medial) axis of the ErC, we plotted mean parameter estimates for each slice (see Figure 23B). These slice-by-slice plots further confirmed a topographical organization of ErC connectivity along the longitudinal

axis with decreasing PrC connectivity and increasing PhC connectivity from anterior to posterior to ErC. Furthermore, lateral to medial connectivity plots demonstrated decreasing PrC and increasing PhC connectivity.
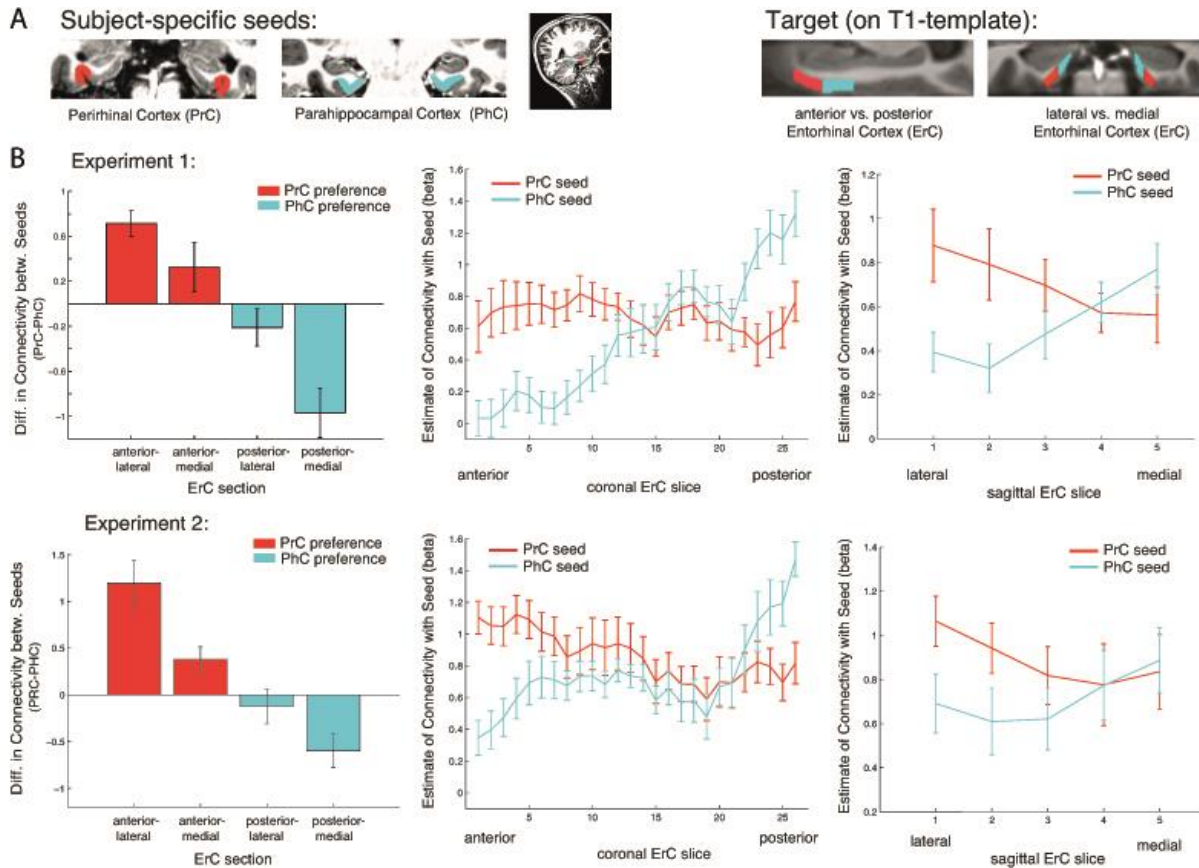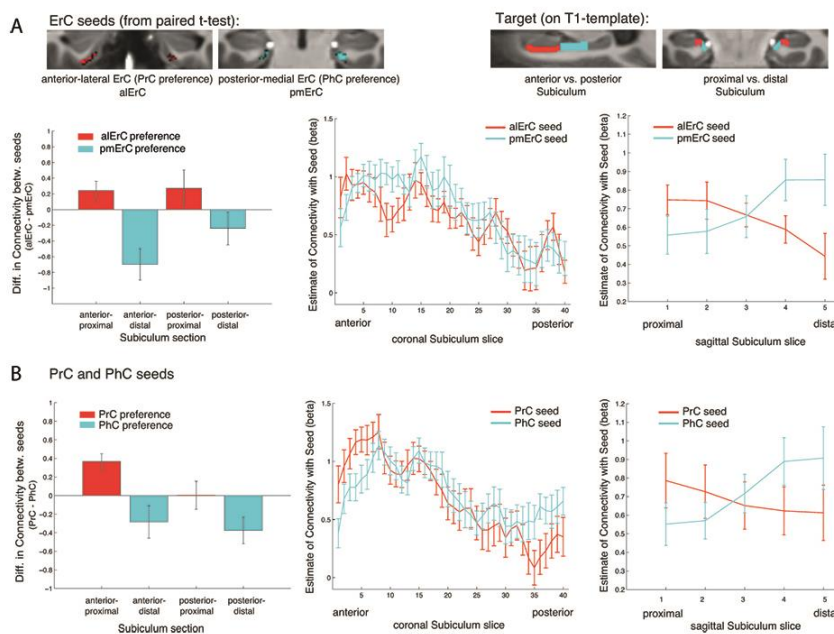

Figure 23. Anterior-posterior and lateral-medial gradients of entorhinal connectivity with PrC vs PhC seeds. (A) To test for an anterior-posterior or lateral- medial dissociation of ErC connectivity with PrC vs. PhC seeds (upper panel, left), we divided the ErC template mask into four equal portions (upper panel, right) and extracted mean parameter estimates (betas) from each subsection. **(B)** Repeated measures ANOVAs revealed significant seed (PrC vs. PhC) × anterior-posterior ErC section and seed × lateral-medial ErC section interactions ($p < 0.001$ for both datasets; $N_{Exp1} = 15$, $N_{Exp2} = 14$). Slice-by-slice plots of connectivity estimates along the longitudinal and transverse ErC axis confirmed an anterior-to-posterior and lateral-to-medial dissociation with decreasing PrC-connectivity and increasing PhC-connectivity. As the number of sagittal ErC slices differed from anterior to posterior, we divided each coronal ErC slice into 5 equal portions (with 1 being most lateral and 5 most medial ErC) and calculated mean betas for each portion.

4.3.2 SUBICULAR CONNECTIVITY PROFILES RELATED TO FUNCTIONAL ERC SUBREGIONS AND PRC/PHC

4.3.2.1 ErC subregions differentially interact with proximal and distal subiculum

Anatomical studies in rodents have demonstrated that lErC and mErC exhibit different patterns of connectivity along the proximo-distal (transverse) axis of the subiculum and CA1 (Witter et al., 2000b). Similarly, anterolateral vs. posteromedial ErC regions in nonhuman primates have been shown to exhibit differential connectivity with proximal vs. distal subiculum and CA1 (Witter and Amaral, 1991). These findings motivated us to test whether functional connectivity between our functional ErC subregions and the hippocampus is topographically organized. Within the hippocampus, we focused on the subiculum, based on previous findings demonstrating that the topographic organization of cortico-hippocampal functional connectivity is most prominent in the subiculum (Libby et al., 2012).

Consistent with our previous analyses for the ErC, we divided the subiculum into four equal portions along the longitudinal (anterior vs. posterior) and transverse (lateral ["proximal"] vs. medial ["distal"]) axis. We then extracted mean parameter estimates of functional connectivity with anterior-lateral and posterior-medial ErC for each subicular section and each subject and submitted them to a factorial ANOVA to test for connectivity differences as a function of ErC subregion (alErC vs. pmErC) and anterior vs. posterior and proximal vs. distal subiculum subregions. Similar to the division of the ErC, we performed the proximal-distal cut individually for each coronal subiculum slice. Repeated-measures ANOVAs with ErC seed connectivity estimates revealed a significant two-way interaction of seed ErC subregion x proximal vs. distal subiculum (Exp. 1: $F_{1,14}$ = 25.7, p < 0.001; Exp.2: $F_{1,13}$ = 24.3, p <0.001). However, there was no interaction between ErC seed region and longitudinal subiculum sections (p > 0.26). Follow-up t-tests confirmed that the proximal subiculum showed significantly greater connectivity with alErC than with pmErC (Exp. 1: t_{14} = 2.27; p = 0.04 ; Exp. 2: t_{13} = 2.15; p = .049) and, conversely, that distal subiculum showed significantly greater connectivity with pmErC than with alErC (Exp. 1: t_{14} = 3.06; p = 0.008 ; Exp. 2: t_{13} = 4.24, p = 0.001). Slice-by-slice plots confirmed that connectivity of the alErC decreased from proximal (lateral) to distal (medial) subiculum, whereas pmErC connectivity increased (see Figure 24 and Supplementary Figure 14 for data of Experiment 1 and 2, respectively).

Figure 24. Functional connectivity gradients in the subiculum related to ErC subregions and PrC/PhC seeds. **(A)** To test for differential connectivity of ErC functional subdivisions with the subiculum, anterior-lateral ErC (alErC) and posterior-medial ErC (pmErC) regions that exhibited preferential connectivity with PrC vs PhC, respectively (see paired t-tests in Figure 22A) were used as seed regions. The subiculum mask was equally divided into four portions along the longitudinal (anterior vs posterior) and transverse (proximal vs distal) axis and mean betas of functional connectivity with ErC seeds extracted for each subsection. Repeated-measures ANOVAs revealed a significant seed (alErC vs pmErC) × proximal-distal subiculum interaction in both datasets (p < 0.001; N_{Exp1} = 15, N_{Exp2} = 14; results shown for Exp. 1). Slice-by-slice plots of connectivity estimates demonstrated decreasing alErC-connectivity and increasing pmErC connectivity from proximal to distal subiculum but no anterior-posterior dissociation. **(B)** Similarly, connectivity for PrC vs PhC seeds with the subiculum along the longitudinal and transverse axis was evaluated. Seed (PrC vs. PhC) × proximal-distal subiculum section interactions were significant across both datasets (p < 0.01) with preferential connectivity of PrC with proximal and PhC with distal subiculum, respectively. Slice-by-slice plots of connectivity estimates along the hippocampal long axis revealed stronger PrC connectivity with the most anterior and stronger PhC connectivity with the most posterior subiculum (most anterior and most posterior 8 slices), respectively (Exp. 1). See also Supplementary Figure 14 for data of Exp. 2

4.3.2.2 Repeated-measures ANOVAs and slice-by-slice plots for PrC/PhC seeds

Previous human resting-state fMRI studies at 3 Tesla (Kahn et al., 2008; Libby et al., 2012) reported reliable differences in connectivity between the PrC and PhC with the hippocampus along the longitudinal hippocampal axis, most prominently with the subiculum (Libby et al., 2012). However, a dissociation of PrC vs. PhC connectivity along the proximo-distal axis of the subiculum, as demonstrated between PrC and POR in rodents (Agster and Burwell, 2013; Naber et al., 2001b, 1999), has not been reported so far in humans. In order to examine whether PrC vs. PhC seeds show differential intrinsic functional connectivity with the subiculum along the transverse and/or longitudinal axis, we also tested for significant interactions between PrC vs. PhC connectivity with anterior vs. posterior or proximal vs. distal subiculum. Repeated-measures ANOVAs with PrC and PhC connectivity estimates revealed a significant two-way interaction of seed region x proximal vs. distal subiculum (Exp.1: $F_{1,14}$ = 20.2, p = .001; Exp.2: $F_{1,13}$ = 14.4, p = 0.002). However, the interaction between seed and anterior vs. posterior subiculum was not significant (Exp.1: $F_{1,14}$ = 2.5, p = 0.135; Exp.2: $F_{1,13}$ = 1.4, p = 0.257). Follow-up t-tests confirmed significantly greater PrC than PhC connectivity with the proximal subiculum (Exp.1: t_{14} = 3.7; p = 0.002 ; Exp.2: t_{13} = 3.9, p = 0.002). With regard to distal subiculum there was significant higher PhC than PrC connectivity in Experiment 1 (t_{14} = 3.1, p = 0.009) and a trend towards a difference in Experiment 2 (t_{13} = 2.0; p = 0.063). Slice-by-slice plots further confirmed a dissociation of PrC/PhC connectivity along the transverse hippocampal axis with decreasing PrC connectivity and increasing PhC connectivity from proximal to distal subiculum (see Figure 24B and Supplementary Figure 14B for data of Experiment 1 and 2, respectively). Although the interaction between PrC vs. PhC seed and anterior-posterior subiculum was not significant, slice-by-slice extractions suggested that differential connectivity may be present in the most anterior and most posterior slices of subiculum. Additional analyses indeed revealed that PrC connectivity was significantly greater than PhC connectivity within the most anterior 8 slices of subiculum (Exp.1: t_{14} = 2.5; p = 0.022; Exp.2: t_{13} = 3.9, p = 0.002), while PhC connectivity was significantly higher than PrC connectivity within the most posterior 8 slices in Experiment 1 (t_{14} = 2.3; p = 0.035), but not in Experiment 2 (t_{13} < 1, p > 0.4). However, we note that we did not segment the subiculum within the hippocampal tail (where anatomical borders are difficult to delineate) and thus might underestimate any difference in the posterior subiculum.

4.3.2.3 PrC and PhC connectivity with subiculum differs from that of alErC and pmErC with subiculum

The above analyses revealed that the connectivity differences between alErC and pmErC along the transverse axis of the subiculum parallel the differences between PrC and PhC. However, only PrC and PhC seeds showed dissociable connectivity gradients along the longitudinal axis of the subiculum, whereas no such difference was seen between alErC and pmErC. This suggests that the gradients of alErC and pmErC connectivity with subiculum are not merely a reflection of their differential

connectivity with PrC and PhC. To quantify the differences between the connectivity profiles of entorhinal functional subregions and PrC/PhC along the long axis of the subiculum, we calculated differences between alErC/pmErC and PrC/PhC connectivity estimates for anterior and posterior subiculum subsections. Repeated-measures ANOVAs revealed a significant interaction between seed regions (ΔalErC/pmErC vs. ΔPrC/PhC) x longitudinal subiculum section (anterior vs. posterior) for Experiment 1 ($F_{1,14}$ = 7.3, p = 0.017) with a similar trend evident in the dataset of Experiment 2 ($F_{1,13}$ = 3.4, p = 0.087). These additional analyses show that functional connectivity profiles of PrC vs. PhC and alErC vs. pmErC with the subiculum differ along the longitudinal hippocampal axis.

4.3.3 LANDMARKS FOR DELINEATION OF ALERC AND PMERC

We used the multivariate classification approach to predict alErC and pmErC subregions across all subjects. Based on the relative connectivity preference of an ErC voxel across subjects the classifier predicts PrC or PhC connectivity preference for the left out subject. Thereby we can compute consistency maps that show the consistency of predictions for each ErC voxel across all subjects. These revealed regions of high and low consistency. Based on the predictions of the classifier we created a PrC-connectivity preference (alErC) and a PhC-connectivity preference ErC (pmErC) mask. To provide these masks in a more usable manner (not on a partial volume T1-template), we created a whole brain high-resolution T1-template based on the T1 weighted images of all participants (N = 29; voxel size: 0.6 mm^3 isotropic, AC-PC aligned). We then aligned the ErC masks on the whole-brain template (linear registration) and manually corrected outer borders, if these did not fit perfectly.

Below, we further describe the approximate boundaries of al- and pmErC subregions based on coronal slices, moving from anterior to posterior on the whole brain template. These landmarks can be used for manual delineation of ErC functional subregions. Notably, coronal slices on the whole-brain template are not orthogonally aligned to the hippocampal long-axis and have a different slice thickness compared to the partial-volume template on which results/figures are described. Furthermore, borders between alErC and pmErC differed slightly between hemispheres and thus landmarks are an intermediate approximation between sides.

At the most anterior level of the ErC (when the amygdala is visible) ErC is fully covered by alErC. Moving posteriorly, the hippocampal head (HH) starts. Around 3-4 slices (~ 2 mm) after the first appearance of the HH, pmErC appears at the very medial/dorsal tip of the ErC, touching the amygdala. The border between pmErC and alErC approximately corresponds to the uncal notch, such that pmErC covers the ambient gyrus. Moving more posteriorly the border between pmErC and alErC moves progressively down (more lateral/ventral) until alErC and pmErC are around equal size at the level of two thirds of HH. At this level the amygdala has fully disappeared. Going further posteriorly the border between pmErC and alErC moves progressively more lateral/ventral, such that pmErC also covers parts of the ventral/lateral ErC half. At the level where the uncus separates from the hippocampus (and only the
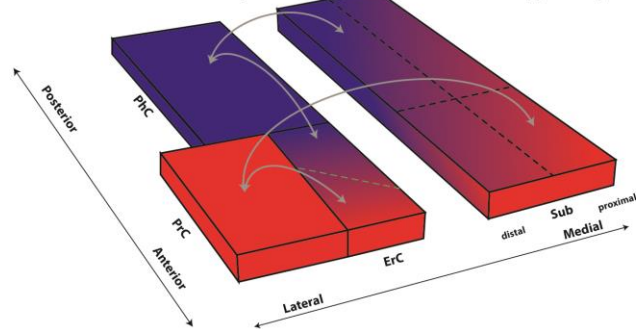
fimbria is attached to both), ErC is almost fully covered by pmErC. We delineated the ErC until the collateral sulcus (or rhinal fissure) disappeared, which was one slice (0.6mm) following the disappearance of the uncus. Approximately the 4 most posterior ErC slices (~2.4mm) were fully covered by pmErC. AlErC and pmErC masks as well as the whole brain T1-template are available online in original (resolution: $0.6mm^3$ isotropic, http://dx.doi.org/10.7554/eLife.06426.013) and MNI space (resolution: $2mm^3$ isotropic, http://dx.doi.org/10.7554/eLife.06426.014).

4.4 DISCUSSION

We report the first detailed topographic parcellation of the human ErC on the basis of its functional connectivity with neocortical and hippocampal subregions. In two independent samples, our analyses revealed that anterior-lateral and posterior-medial ErC subregions (alErC and pmErC, respectively) exhibited distinct patterns of intrinsic functional connectivity with regions in the neocortex (PrC and PhC) and hippocampal formation (subiculum). Specifically, the alErC region could be delineated on the basis of preferential connectivity with PrC, whereas the borders of pmErC were derived from connectivity with PhC. AlErC and pmErC, in turn, were found to have preferential connectivity with proximal and distal subiculum, respectively. Moreover, the pattern of subiculum connectivity with alErC and pmErC was partially distinct from its connectivity with PrC and PhC. A schematic summary of functional connectivity gradients in the subiculum related to PrC/PhC seeds and ErC subdivisions is illustrated in Figure 25. These results reveal the functional topography of the human ErC as a gateway between neocortex and hippocampus and show remarkable accordance with principles known from anatomical studies of rodents (rostrolateral vs. caudomedial; for reviews see van Strien et al. 2009 and Witter et al. 2000b) and studies of nonhuman primates (anterolateral vs. posteromedial; see e.g. Suzuki and Amaral 1994 and Witter and Amaral 1991). As we describe below, these data provide a link between basic and translational research on the human medial temporal lobes (Ranganath and Ritchey, 2012; Small et al., 2011) and results from detailed circuit level analyses of the rodent hippocampal formation (e.g. Moser and Moser, 2013). Previous fMRI studies have used functional connectivity analyses on data collected at 3T to characterize topographic patterns of connectivity between the PrC, PhC, and hippocampal subfields (Lacy and Stark, 2012; Libby et al., 2012). These studies have generally found that PrC and PhC exhibit different patterns of connectivity along the longitudinal axis of the hippocampus. Unfortunately, these studies could not address the topographic organization of connectivity within the ErC, possibly due to limitations in resolution and SNR. The present results demonstrate that the enhanced resolution and sensitivity of ultra-high field fMRI can overcome these limitations and reveal fine-grained topographical patterns in connectivity. Three-dimensional plots of entorhinal connectivity preferences revealed a gradient of decreasing PrC and increasing PhC connectivity running from anterior-lateral to posterior-medial ErC. It is notable that, by training a pattern classifier on the coordinates of ErC voxels that showed preferential connectivity with

PrC or PhC within a subset of participants, we could reliably predict these voxels in the remaining participant. This finding indicates that the topography of neocortical connectivity within the ErC is highly conserved across participants, which, in turn, could indicate fundamental functional differences between the two ErC subdivisions.
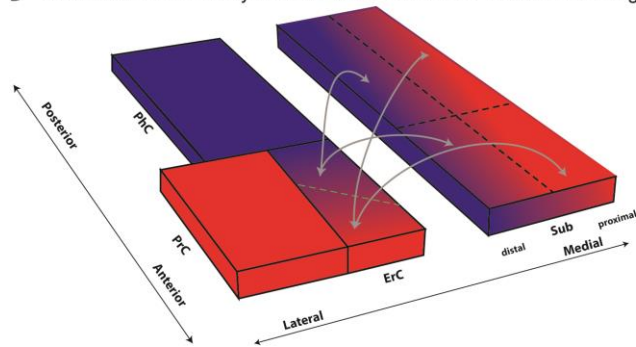

Figure 25. Schematic summary of functional connectivity gradients in the subiculum related to PrC/PhC seeds and ErC subdivisions. (A) Functional connectivity analyses revealed preferential connectivity of PrC (red) with the anterior-lateral ErC and PhC (blue) with the posterior-medial ErC. Regarding the subiculum, PrC showed strongest connectivity with most anterior and proximal parts, whereas PhC showed strongest connectivity with most posterior and distal parts of the subiculum. (B) Anterior-lateral (red) and posterior-medial (blue) ErC exhibited a similar dissociation in connectivity with the subiculum along its transverse (proximal-distal) axis but there was no trend for a dissociation of entorhinal connectivity along the longitudinal axis of the subiculum.

Two recent fMRI studies reported evidence for task-related activation differences between lateral and medial sections of the ErC in humans (Reagh and Yassa, 2014; Schultz et al., 2012) Schultz et al. reported differential activation in medial and lateral sections of the ErC during scene and face processing in a working memory task. Reagh and Yassa reported preferential activation in a medial section of ErC during mnemonic discrimination of spatial locations and preferential activation in a lateral section of ErC during mnemonic discrimination of objects. This functional dissociation was observed by splitting the ErC into equally-sized lateral and medial parts according to the rodent terminology of lErC and mErC. Notably, they also found a trend towards a dissociation between anterior and posterior ErC after a similar equal division along the longitudinal axis. Our data help to explain these findings by empirically demonstrating that alErC and pmErC exhibit differential functional connectivity with PrC and PhC. Numerous fMRI studies have shown that PhC is preferentially engaged in memory tasks that involve scenes, spatial or context information, whereas PrC is preferentially engaged in memory tasks that involve object or item information (Ranganath and Ritchey, 2012; Ritchey et al., 2015). Thus, it makes sense that ErC subregions that interact predominantly with PrC or PhC also differentially participate in item and context processing. However, our data also suggest that a simple lateral-medial distinction does not capture the functional organization of ErC. Future fMRI

studies (as well as structural MRI studies, e.g. Khan et al., 2014) could more effectively study the ErC by using the high-consistency pmErC and alErC masks derived from our data (see also "Landmarks for delineation of alErC and pmErC"), or by using functional connectivity metrics to identify subject-specific ErC subregions (see Figure 26 for a 3D rendering of alErC and pmErC masks).
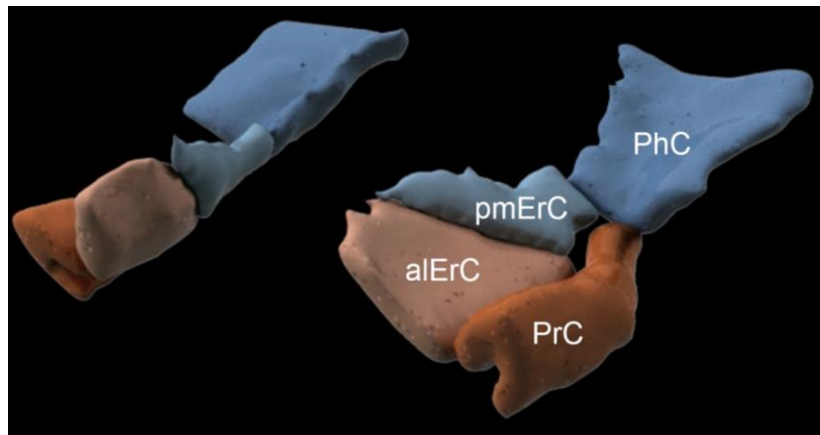

Figure 26. 3D rendering of the resulting alErC and pmErC masks based on the multivariate classification result across the whole group.

Although the ErC is a major gateway for the hippocampus, neocortical regions such as PrC and PhC also have direct reciprocal connectivity with CA1 and subiculum (Agster and Burwell, 2013; Naber et al., 2001b, 1999). Our analyses revealed that the topographic differences in subicular connectivity with PrC vs. PhC along the hippocampal transverse axis paralleled the differences of subicular connectivity with alErC vs. pmErC. Whereas alErC and PrC showed stronger connectivity with proximal subiculum, pmErC and PhC showed stronger connectivity with distal subiculum. In contrast to the transverse axis, PrC/PhC vs. alErC/pmErC connectivity profiles differed along the longitudinal hippocampal axis. For alErC and pmErC, there was no evidence or trend for an anterior-posterior dissociation, compatible with connectivity of lErC and mErC in rodents (Naber et al., 2001b, 1999; O'Reilly et al., 2013; Witter, 2006). In contrast, the most anterior subiculum showed stronger connectivity with PrC than PhC, whereas in one dataset the most posterior subiculum (in the hippocampal body) showed stronger connectivity with PhC than PrC. This finding replicated the direct anatomical connectivity profiles observed in rodents (Agster and Burwell, 2013; Naber et al., 2001b, 1999). Such an anterior-posterior dissociation of hippocampal connectivity accords with findings from human resting-state fMRI studies that investigated functional connectivity profiles of PrC and PhC (rather than ErC) with hippocampal subfields (Libby et al., 2012).

These functional connectivity data suggest that there might be two parallel cortico-hippocampal pathways in humans - one via the ErC and one that is direct. The differences in the topographic organization of ErC-subicular connectivity and PrC/PhC-subicular connectivity could have important functional implications. One implication is that the ErC is not a simple anatomical extension of the PrC and PhC. If that were the case, we would not have observed any reliable difference between neocortical-hippocampal connectivity profiles and ErC-hippocampal connectivity profiles. These results add support to the notion that the ErC is more than a mere cortico-hippocampal relay (de Curtis

and Paré, 2004; Lavenex and Amaral, 2000). One possibility is that this organization might allow a comparison between ErC-gated hippocampal memory signals with direct neocortical input (e.g. Naber et al., 1999). Furthermore, the diffuse nature of lErC/mErC projections along the anterior-posterior hippocampal axis and a structured gradient of direct PrC/POR projections that has been identified in rodents could allow for integration of information across both processing streams (Agster and Burwell, 2013; Burwell, 2000; Witter et al., 2000a).

Results from the present study may be pertinent to understanding memory impairment in clinical conditions that compromise the structural integrity of the medial temporal lobes, including neurodegenerative diseases such as Alzheimer's Disease (AD) and frontotemporal lobar degeneration (FTLD), temporal lobe epilepsy, depression, schizophrenia, developmental amnesia and ischemia. In AD, for instance, tau pathology emerges in lateral ErC regions early in the course of the disease (Braak and Braak, 1991; Braak and Del Tredici, 2004). Analyses of functional connectivity can potentially reveal how ErC degeneration in the early stages of AD could impact the functional organization of distributed cortical networks (Khan et al. 2014; also see La Joie et al. 2014) and also shed light on the transsynaptic progression of pathology in AD.

To summarize, the results of the present study have provided a detailed description of the organization of functional connectivity within the human ErC. Based on differential functional connectivity with PrC, PhC and subicular subregions, our data demonstrate that the human ErC can be reliably subdivided into anterior-lateral and posterior-medial subregions that could be critical nodes in two cortico-hippocampal processing pathways. Future studies can apply the high resolution functional connectivity analyses to differentiate the roles of alErC and pmErC in memory and alterations of ErC connectivity in AD and other neurodegenerative diseases.

4.5 CONTRIBUTIONS

This study was done in collaboration with Charan Ranganath and Laura Libby from the University of California, Davis. Anne Maass, Emrah Düzel and I designed the study. Anne Maass and I acquired, preprocessed and analyzed the data. Anne Maass performed the core functional connectivity analysis and I did the multivariate analyses. Laura Libby and Charan Ranganath were involved in the discussion and interpretation of the results. Anne Maass and I wrote the manuscript and all authors were involved in editing the manuscript.

CHAPTER

5

AGE-RELATED FUNCTIONAL CHANGES OF DOMAIN-SPECIFIC MEDIAL TEMPORAL LOBE PATHWAYS

5.1 Introduction

As already described in the earlier chapters there are domain-specific pathways in the MTL that support different types of information processing and memory (Ranganath and Ritchey, 2012; Ritchey et al., 2015). While the anterior-temporal (AT) system is more involved in item/object processing, the posterior-medial (PM) system is more involved in spatial/scene processing. The two different pathways receive information from two different visual streams, which connect regions that are involved in object and spatial vision with the PrC and PhC respectively (Kravitz et al., 2011; Mishkin et al., 1983). While the PrC is more involved in the processing of and memory for objects and content (Davachi et al., 2003; Diana et al., 2012; Ekstrom and Bookheimer, 2007; Libby et al., 2014; Litman et al., 2009; Sheldon and Levine, 2015; Staresina et al., 2013, 2011), the PhC is associated with the processing of and memory for spatial layouts, context and scenes (Diana et al., 2012; Ekstrom and Bookheimer, 2007; Epstein and Kanwisher, 1998; Libby et al., 2014; Litman et al., 2009; Schultz et al., 2012; Staresina et al., 2013, 2011). Studies in rodents suggest that the two pathways extend towards the entorhinal cortex (ErC). The lateral ErC (lErC) is more involved in object memory and processing of local landmarks and the medial ErC (mErC) is critical for spatial memory and processing of global landmarks (Knierim et al., 2014). In chapter 4 we used functional connectivity to investigate the human homologues of the lErC and mErC in rats and found strong evidence that these subdivisions correspond to the anterior-lateral (alErC) and posterior-medial (pmErC) ErC in humans, respectively. Information-based models of MTL organization assume a role for the hippocampus to integrate object and scene information which suggests involvement in object and scene processing (Diana et al., 2007; Ranganath, 2010).

Subregions in the MTL are also involved in discrimination – both in the perceptual and the memory domain. As discussed earlier, the human dentate gyrus (DG) plays an important role in pattern separation – a mechanism which is hypothesized to be critical for the discrimination of very similar memories (Leutgeb et al., 2007; Neunuebel and Knierim, 2014). Hippocampal pattern separation thereby relates to the decorrelation of similar input patterns to create distinct and independent representations that reduce the interference between these similar memories (McClelland et al., 1995; Treves and Rolls, 1992). Strong evidence for the role of the DG in human pattern separation has been shown in chapter 3 as well as other functional magnetic resonance imaging (fMRI) studies using mnemonic discrimination tasks that are likely to pose high demands on pattern separation (e.g. Bakker et al. 2008, Lacy et al. 2011). On the other hand, studies on object and scene discrimination with patients that either have impairments including the PrC or the hippocampus suggest the involvement of extrahippocampal regions. While PrC has been shown to have a special role in the discrimination of objects with high feature overlap, the hippocampus seems to be critical for scene discrimination (Barense et al., 2005; Lee et al., 2005a, 2005b). Mnemonic discrimination has been shown to decline with age (Fidalgo et al., 2016; Stark et al., 2015). Studies using mnemonic discrimination tasks could show that older adults tend to call similar items old in contrast to young individuals, whereas there is

no difference in judging repeated items as old, which is often interpreted as a deficit in pattern separation functions and a concomitant bias towards pattern completion (Stark et al., 2015; Vieweg et al., 2015; Yassa et al., 2011a). These behavioral deficits may be related to impairment of MTL subregions.

Ageing as well as neurodegenerative diseases affect the integrity of brain networks and subregions in the MTL (Jagust, 2013; Leal and Yassa, 2015; Small et al., 2011). Human functional imaging studies showed that activity in anterior PrC was associated with an impairment in object discrimination in ageing (Ryan et al., 2012). In addition, age-related degradation in perforant pathway integrity and blood-oxygen-level dependent (BOLD) hyperactivity in CA3 have been associated with impairments in mnemonic discrimination (Bakker et al., 2012; Yassa et al., 2011b). Two of the earliest cortical sites where Alzheimer's Disease related pathology can be detected even before being evident in the hippocampus are the transentorhinal region, which is part of the PrC, and the ErC (Braak and Braak, 1991). This has received support by recent neuroimaging studies demonstrating a decrease in cerebral blood volume and reduced grey matter thickness in the anterior temporal lobe including the PrC and lErC in preclinical and early Alzheimer's Disease (Khan et al., 2014; Krumm et al., 2016; Yushkevich et al., 2015b). Given that ErC, PrC and PhC are critically involved in memory for objects and scenes, the impairment in PrC-alErC and PhC-pmErC can also yield degraded inputs to the hippocampus and thus contribute to the impaired discrimination of similar lures.

To investigate age-related behavioral and functional changes related to the two memory domains we developed a novel object-scene mnemonic discrimination task, which poses high demands on pattern separation. This task was designed to allow the investigation of behavioral discrimination performance as well as the neural organization of mnemonic discrimination of objects and scenes. In addition, the paradigm provides two neural measures of functional integrity. First, we will analyze domain-specificity within both MTL pathways in order to investigate their functional architecture as well as age-related effects. Second, we will investigate the involvement of MTL pathways in mnemonic discrimination using lure-related novelty responses based on a repetition suppression approach (see Figure 4 for details). We combined this with manual segmentation of the corresponding MTL regions based on structural MR scans. In this study, we used these measures to investigate the organization and integrity of MTL pathways in a group of young as well as healthy older individuals using fMRI.

5.2 MATERIALS AND METHODS

5.2.1 PARTICIPANTS

Forty-six healthy young and 47 healthy elderly subjects participated in the experiments. Subjects were recruited in Bonn and Magdeburg. We had to exclude subjects due to extensive head motion within the scanner (> 2 mm (translation), n=3) prior to any functional analysis. Furthermore, we did not analyze data from subjects whose task performance was more than 2 standard deviations below the

group mean performance (n=3). The final sample consisted of 43 young (mean age = 24; SD = 3.5; 21 female) and 44 elderly subjects (mean age = 68.8; SD = 5.7; 21 female). Subjects were screened for known metabolic disorders and neurologic or psychiatric history and excluded from further examination in case of incidents reported during history taking. In addition, normal and corrected vision was assessed using standard procedures and printed stimulus materials comparable to the materials used during the experiments. The study was conducted and designed in accordance with the Declaration of Helsinki (Williams, 2008) and all subjects gave informed and written consent for their participation in accordance with ethic and data security guidelines of the Otto-von-Guericke University and the German Center for Neurodegenerative Diseases (DZNE). The study was approved by the local ethics committees in Magdeburg and Bonn.

5.2.2 STIMULI AND SETTING

Stimuli consisted of computer-generated (3ds Max, Autodesk Inc., San Rafael, USA) and isoluminant images. The images were comprised of every day indoor objects shown against a grey background as well as empty indoor scenes (empty rooms, see

Figure 27C). Stimuli were presented in pairs in which every stimulus either consisted of two identical (repeats) or two very similar versions (lures). As lure versions of object and scene stimuli were not equally difficult in the beginning, a total of 500 self-generated stimuli were tested in behavioral experiments on young subjects (n=20) to define the individual stimulus lure discrimination index. In the final version of the task the difficulty of all object and scene lures as well as repeats was matched with respect to the mean and variance. The fixation target was a white fixation star. Stimuli were presented on a fully MR-compatible high-resolution (1280 x 800 Px) 30'' LCD display (medres, Köln, Germany) and study participants watched them through a mirror mounted on the head coil, subtending a visual angle of about 16.8°. For experimental presentation, we used Presentation-Software (Neurobehavioral Systems, https://nbs.neuro-bs.com). Subjects' positioning in the MRI scanner, as well as sequence preparation steps, e. g. image angulation, was standardized across both sites by provided standard operating procedures and on-site training.

5.2.3 TASK AND EXPERIMENTAL DESIGN

Prior to scanning, subjects were instructed verbally and saw a standardized visual instruction with all information regarding the experiment. Subsequently, they had to learn the task within a 5-minute training session outside the scanner. In addition, a standard vision screening procedure as well as a visual discrimination test with stimuli comparable to the ones used within the experiment were conducted to rule out possible confounding effects of a deficit in visual perception. Vision was corrected using MR compatible devices if necessary. During the following fMRI session, stimuli were presented in sequences of four stimuli (see Figure 27A and B). Sequences could consist of images showing either objects or scenes. The first two stimuli of a sequence were always new images, whereas

the following two could be either an exact repetition (repeat) or a very similar version of the previous ones (lure). Stimuli were presented in an event-related design, in which each stimulus was presented for 3s and stimuli were separated by a fixation star. Inter-stimulus intervals, ranging from 0.6 to 4.2s (mean 1.63s), were jittered to optimize statistical efficiency (Dale, 1999). Intervals between sequences were longer (mean 2.43s) to stress the end of a sequence. Subjects had to respond to each stimulus with old/new judgments using their right index and middle finger. Old/new judgments were preferred over old/new/similar judgments to reduce task difficulty especially for elderly subjects. Subjects were told to press "new" for entirely new images but also for very similar versions of earlier images. "Old" responses should be given for exact repetitions. Although we consequently cannot control new responses to similar images entirely – i.e. a subject considering a similar version of an earlier stimulus as an entirely new stimulus – these were highly unlikely given the short memory delay in the task. The presentation of sequences was counterbalanced with respect to objects and scenes as well as repeats and lures. This resulted in a total of 56 sequences (where each sequence consists of 4 stimuli) across both domains with 28 first-repeat pairs and 28 first-lure pairs.
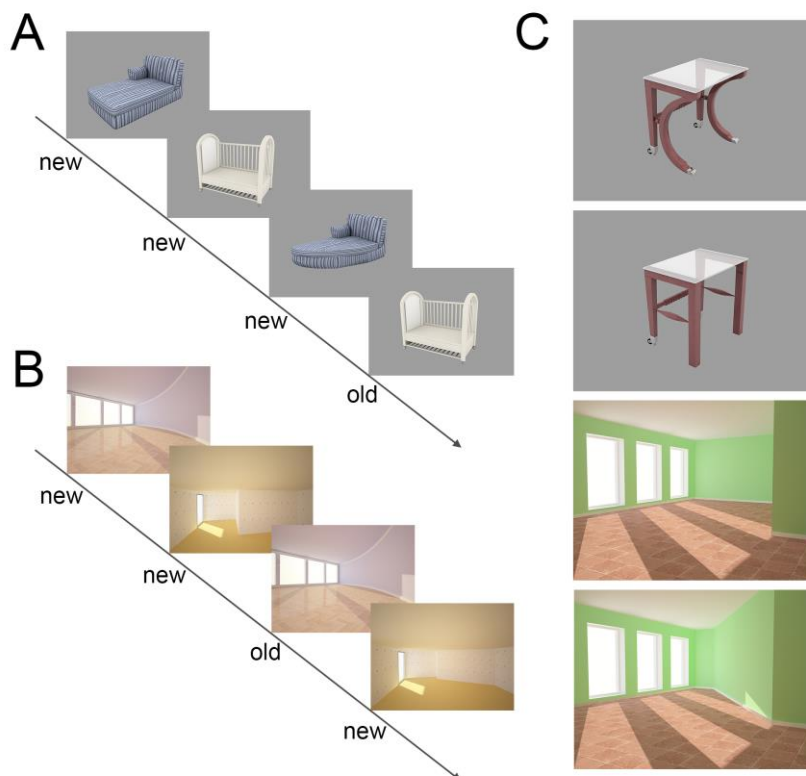

Figure 27. Task sequence and stimuli. Sequences used during the object and scene paradigm. Trials consisted of two object **(A)** or scene **(B)** stimuli that were either identically repeated (correct response: old) or presented again in a very similar but not identical version (correct response: new). Lure and repetition stimuli mostly differed in shape or geometry **(C)**.

5.2.4 BEHAVIORAL DATA ANALYSIS

Accuracy scores and reaction times were analyzed using SPSS 24 (IBM, Armonk, USA). Hit rates (repeats percent correct) and false alarm rates (lures percent incorrect) were calculated for the object and scene condition. We performed a mixed ANOVA to test for differences in task accuracy with two within-subject factors task-condition (hit rate, false alarm rate) and domain (object, scene), and the

between-subjects factor age group (young, elderly). In addition, we performed a mixed ANOVA to test for differences in reaction times for hits (correct old responses to repeats), correct rejections (correct new responses to lures) and false alarms (incorrect old responses to lures) with within-subject factors responses (hits, correct rejections and false alarms) and domain (object, scene), and between-subject factor age group (young, elderly). We did not analyze reaction times for misses (incorrect new response for repeats) as there were not enough events for a statistical test (ca. 3 events per subject).

5.2.5   IMAGING DATA ACQUISITION

The study was conducted on two different sites, each using a 3T MRI system of the same vendor (Siemens, Erlangen, Germany) and a 32-channel head coil. Site 1 (Magdeburg) used a 3T MAGNETOM Verio with software version VB19, and site 2 (Bonn) a 3T MAGNETOM Skyra with software version VD13. At both sites a group of young and a group of elderly subjects was scanned. Both sites used identical, vendor-provided sequences for the MRI acquisition. Prior to the functional MRI session, a whole-head 3D magnetization prepared rapid acquisition gradient echo (3D-MPRAGE) volume with 1mm isotropic resolution, FOV = 256 x 256mm², TR/TE/TI = 2500/4.37/1100ms, FA = 7° and BW = 140Hz/Px was acquired. Subsequently, two fMRI runs were recorded using a gradient-echo echo-planar imaging sequence (GE-EPI) with 2 x 2mm² in-plane resolution, FOV = 208 x 208mm², TR/TE = 2400/30ms, 10% slice gap, interleaved acquisition scheme, 40 slices with 3mm slice thickness (young group at site 1) and 36 slices with 3.4mm slice thickness (young group at site 2 and elderly groups at site 1 and 2).

5.2.6   FMRI DATA ANALYSES

5.2.6.1 Preprocessing and first level analysis

For preprocessing and statistical analyses, we used the Statistical Parametric Mapping software (SPM, Version 12; Wellcome Trust Centre for Neuroimaging, London, UK). First, the first functional image of the second session was realigned to the first image of the first session. Afterwards functional images were realigned to the first image of the first session following motion estimation and corrected for differences in the time of slice acquisition. The anatomical T1 image was co-registered to the mean functional image. Functional images were spatially smoothed using an isotropic Gaussian kernel of FWHM 4 x 4 x 4mm with the purpose of increasing the signal-to-noise ratio (SNR). Images were high-pass filtered (128s) to remove low-frequency signal drifts. We used a first-order autoregressive model (AR-1) for estimating temporal autocorrelations by using restricted maximum likelihood estimates of variance components. To model the functional data, delta functions defined by the onset of a stimulus on a trial-by-trial basis were convolved with a hemodynamic response function (HRF). First and second level data were analyzed using a mixed-effects general linear model (GLM) approach. All experimental conditions were entered into the GLM as separate regressors for the following conditions: first presentations, repeats, correct lures and incorrect lures separately for objects and scenes (i.e. 8

conditions total). Data from the first and second run were concatenated by adding a regressor of no interest to the GLM containing the run information. Furthermore, six motion parameters were added as regressors of no interest to minimize false positive activations due to task correlated motion (Johnstone et al., 2006). On the single subject level, contrasts were created by comparing all scene and object trials (scene firsts, repeats and lures > object firsts, repeats and lures; and vice versa). Furthermore, we built individual contrasts for all conditions to extract region specific t-values. To include all voxels in the MTL an explicit mask involving grey and white matter as well as cerebrospinal fluid (CSF) was used in SPM12.

5.2.6.2 Manual delineation of medial temporal lobe subregions

For each subject, anatomical masks for extrahippocampal MTL regions as well as for the hippocampus were manually traced on T1-weighted images. These images were coregistered to the mean EPIs beforehand. Masks were identified in bilateral MTL and traced on consecutive coronal slices. Segmentation was performed for each hemisphere separately using a freehand spline drawing tool based on MeVisLab (MeVis Medical Solutions AG, Bremen, Germany). This tool provided a user-friendly interface for spline drawing and editing, with which the outer borders of the masks were traced closely. The outer border contours were converted to NIfTI images for further processing (Kuijf, 2013; Wisse et al., 2012). All NIfTI masks were subsequently resampled to the mean functional image. Please note that the delineation of MTL subregions did not follow the segmentation protocol presented in chapter 2 as it was developed later. Segmentation of the hippocampus therefore followed the EADC-ADNI protocol (Boccardi et al., 2015). Tracing of the ErC, PrC and PhC followed the same guidelines as described in 3.2.6.3. The ErC was further subdivided in an anterior-lateral as well as a posterior-medial segment. For this purpose, MNI masks that were the result of the experiment presented in chapter 4 were transformed to the native space of each subject and manually corrected using the guidelines described in chapter 4 (see 4.3.3).

5.2.6.3 Across participant alignment (ROI-ANTs)

In order to enable precise cross-participant alignment for hippocampal and parahippocampal regions, first level contrasts were normalized to a study-specific template using region of interest-Advanced Normalization Tools (ROI-ANTS, see 1.4.2 for details) (Avants et al., 2011; Yassa and Stark, 2009). The resulting transformation matrices were then applied to each participant's contrast image as well as to the MTL masks to verify alignment precision. Finally, the aligned contrast images were submitted to second-level group analyses. During this spatial normalization procedure images were resampled to a resolution of 1 x 1 x 1mm voxel size.

5.2.6.4 Group analysis

Spatially normalized first level contrasts were subjected to a second level one sample t-test. Activations were thresholded at FDR (cluster) < 0.05 with an initial cluster defining threshold of $p < 0.001$.

5.2.6.5 ROI analysis

For region of interest analyses we calculated one sample t-tests for each condition vs. all other conditions. We then extracted mean t-values from anatomically defined masks in the MTL using REX (Region-of-Interest extraction (REX) toolbox, http://web.mit.edu/swg/software.htm) and calculated a difference score between within-subject conditions. In order to investigate domain-specificity within MTL regions we established domain-specificity contrasts by subtracting object from scene conditions (scenes - objects) which we refer to as domain-specificity score. Positive domain-specificity scores indicate higher activity for scenes whereas negative scores reflect higher activity for objects.

We also investigated lure-related novelty responses, which is the difference in activity for similar lures compared to repetitions. Therefore, we established difference scores between correct lures and repeats for objects and scenes (scene correct lures - scene repeats; object correct lures - object repeats). We used one-sample t-tests to test for domain-specificity and lure-related novelty responses in PhC, PrC, as well as pmErC, alErC and the hippocampus. Furthermore, we used multivariate ANOVAs to compare difference scores and lure related novelty responses across age groups.

5.3 Results

5.3.1 Behavioral performance across both task conditions

5.3.1.1 Accuracy

For discrimination accuracies, a mixed ANOVA with the within-subject factors domain (scene and object), measure (hit rate and false alarm rate) and the between-subjects factor age group (young and elderly) was performed. This mixed ANOVA showed no significant main or interaction effects for the domain, demonstrating that there is no difference in accuracies between the scene and object condition neither in young nor in elderly subjects. However, there was a significant interaction of measure and age group ($F_{1,85}$ = 36.9, p = 0.000) which was due to higher false alarm rates in both conditions in elderly compared to young subjects (Post-hoc t-tests: Scenes: $M_{FARyoung}$=36.7, $M_{FARelderly}$=57.9, p=0.000, Objects: $M_{FARyoung}$=37.6, $M_{FARelderly}$=54, p=0.000). Post-hoc t-tests also showed that there was no significant group difference in hit rates (Scenes: $M_{HRyoung}$=87.8, $M_{HRelderly}$=86.5, p=0.525, Objects: $M_{HRyoung}$=88.12, $M_{HRelderly}$=88.3, p=0.933). See Figure 28A.

5.3.1.1 Reaction times

We performed a mixed ANOVA with the within-subject factors domain (scene and object), condition (hit, correct rejection and false alarm) and the between-subjects factor age group (young and elderly)

to analyze reaction times. This mixed ANOVA showed no significant main or interaction effects for the domain, again indicating that there is no difference between the scene and object condition neither in young nor in elderly subjects. However, there was a significant interaction of condition and age group ($F_{1.29,168}$ = 4.4, p = 0.029 (Greenhouse-Geisser corrected)). This was due to faster reaction times associated with hits and false alarms in elderly compared to younger adults (Post-hoc t-tests: Scene hits: M_{young}=1.658, $M_{elderly}$=1.421, p=0.000, Scene false alarms: M_{young}=1.794, $M_{elderly}$=1.56, p=0.001; Object hits: M_{young}=1.649, $M_{elderly}$=1.402, p=0.000, Object false alarms: M_{young}=1.802, $M_{elderly}$=1.575, p=0.002) but no difference in reaction times associated to correct rejections (Scene correct rejections: M_{young}=1.762, $M_{elderly}$=1.645, p=0.09; Object correct rejections: M_{young}=1.726, $M_{elderly}$=1.628, p=0.137). In addition, there was a significant effect of condition indicating that response times varied across hits, correct rejections and false alarms ($F_{1.29,168}$ = 25.8, p = 0.000). See Figure 28B.
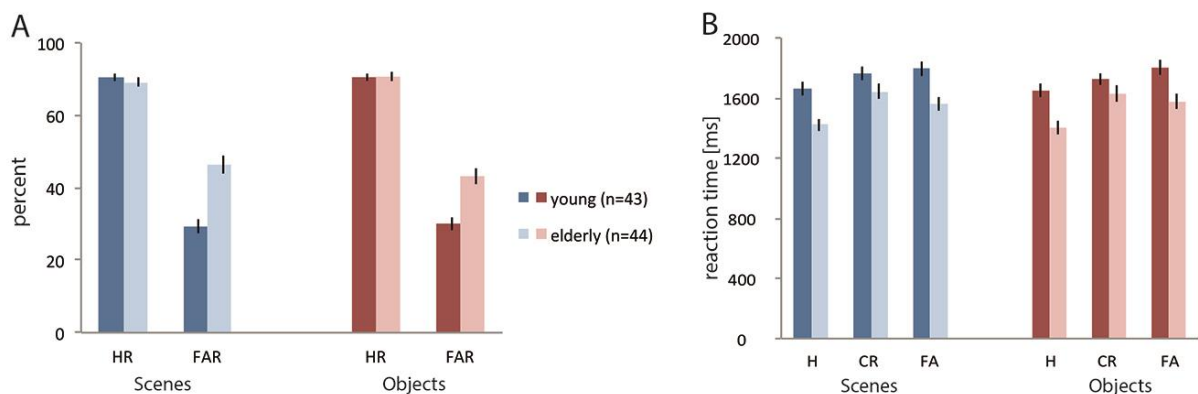

Figure 28. Hit (HR) and false alarm rates (FAR) as well as reaction times for hits (H), correct rejections (CR) and false alarms (FA) in the scene and object condition for young and elderly subjects.

5.3.2 ANTERIOR-TEMPORAL AND POSTERIOR-MEDIAL PATHWAYS ARE DIFFERENTIALLY ACTIVATED IN SCENE AND OBJECT CONDITIONS

5.3.2.1 Cortical systems are differentially involved in object and scene conditions

To investigate whether the object and scene condition indeed target different cortical systems we calculated first level contrast images comparing all object vs. scene conditions (objects > scenes) as well as the complementary contrast where we compared all scene vs. object conditions (scenes vs. objects) for young (n=43) and elderly subjects (n=44). Both task conditions targeted different functional networks (see Figure 29). While the scene condition showed higher activation in superior occipital and parietal regions, precuneus, posterior cingulum, retrosplenial cortex (RsC), PhC, cerebellum and the subiculum, the object condition showed increased activation in middle, inferior and lateral occipital cortex (LOC), fusiform gyrus (FG), amygdala (A), PrC, basal ganglia, thalamus, as well as frontal areas (see Supplementary Table 1 and 2 for coordinates in template space, and cluster statistics for young and elderly subjects respectively).
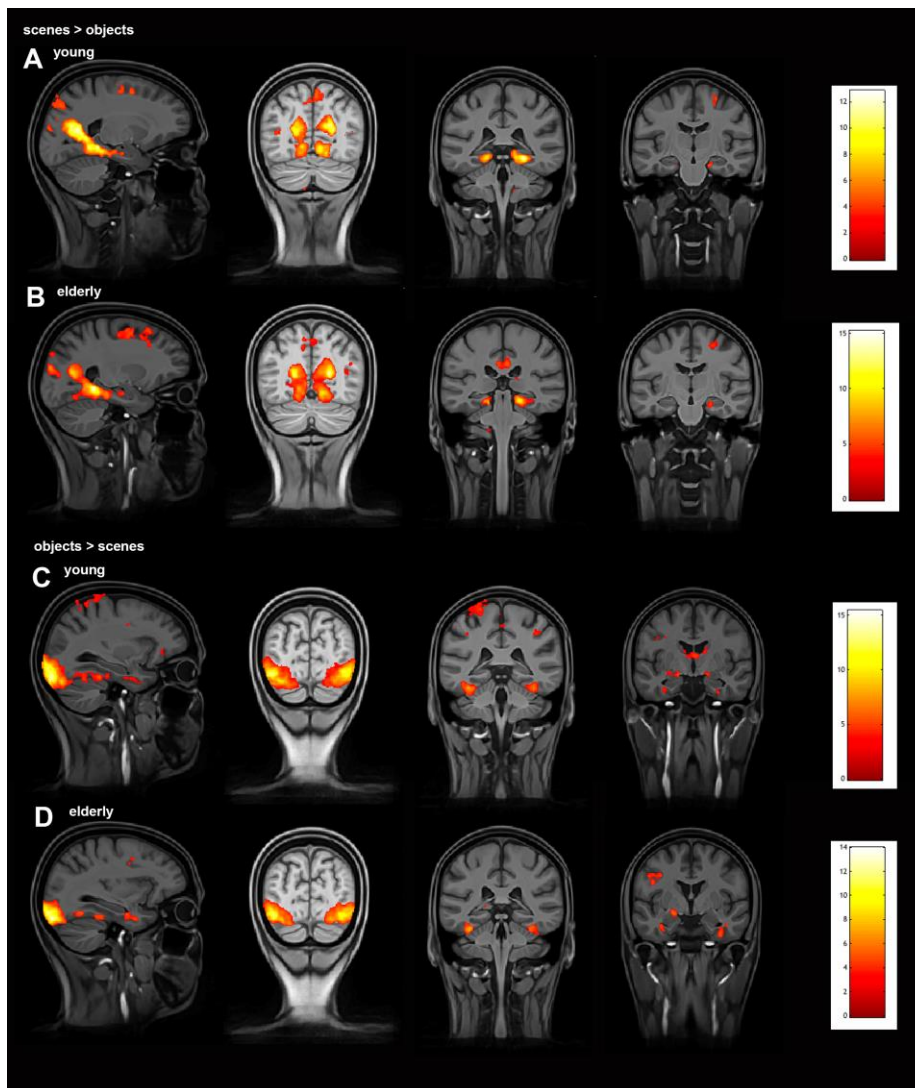
Figure 29. Whole brain posterior and anterior networks associated with scene and object conditions. Objects > scenes and scenes > objects contrasts in young (n = 43, **A** and **C**) and elderly subjects (n = 44, **B** and **D**). Results were thresholded at FDR (cluster) < 0.05 with an initial cluster-defining threshold of $p < 0.001$.

5.3.2.2 Anterior-lateral (alErC) and posterior-medial EC (pmErC) are differentially involved in object and scene conditions

To investigate the two different pathways more closely, domain-specificity in PhC and PrC, the anterior-lateral (alErC) as well as the posterior-medial portion (pmErC) of the entorhinal cortex (ErC), and the hippocampus was analyzed. To compare the results across subjects, a scene vs. object difference score was calculated by subtracting the t-values for all object conditions from all scene conditions. Consequently, a domain-specificity score higher than zero indicates preferential involvement of a specific region in the processing of scenes, while a score below zero indicates preferential involvement in object processing (see Figure 30). We tested for domain-specific involvement of regions in the MTL across all subjects, i.e. young and elderly individuals combined, using one-sample t-tests. This revealed that PhC (M_{PHC}=0.4, SEM=0.04, T=9, p=0.000) and pmErC (M_{pmErC}=0.12, SEM=0.03, T=4.1, p=0.000) had domain-specificity scores significantly higher than zero suggesting preferential scene processing, while PrC (M_{PrC}=-0.23, SEM=0.03, T=-8.9, p=0.000) showed scores significantly lower than zero suggesting preferential object processing. The hippocampus

(M_{HC}=0.03, SEM=0.02, T=1.1, p=0.295) and alErC (M_{alErC}=-0.04, SEM=0.03, T=-1.9, p=0.06), however, did not show a domain-specificity score significantly different from zero (see Figure 30A).
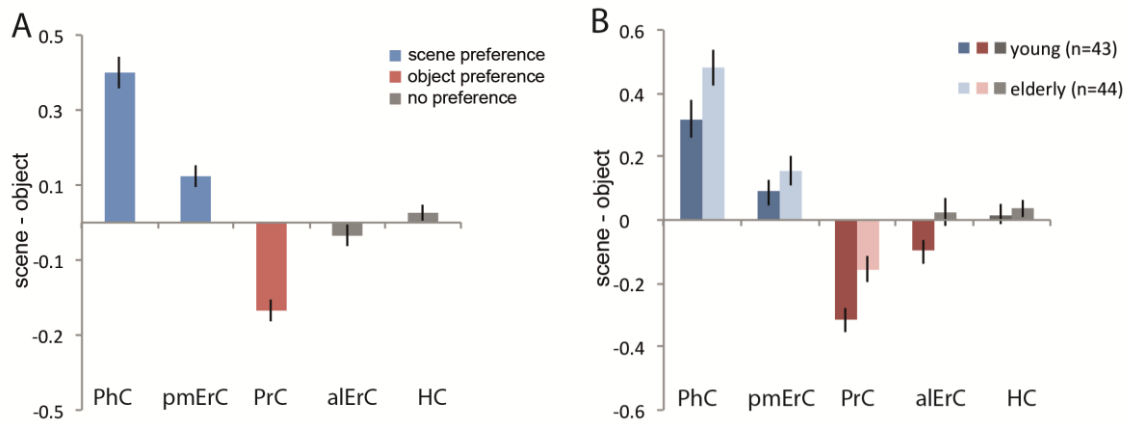

Figure 30. Domain-specificity scores showing involvement in object or scene processing (mean t-values for scene conditions minus object conditions). Positive values indicate preferential involvement in scenes (blue) whereas negative values indicate preferential involvement in objects (red). No significant differential involvement is depicted in grey. Results are shown for the whole group **(A)** as well as for young and elderly participants separately **(B)**. While young subjects show domain-specific responses in all subregions but the hippocampus, elderly subjects show domain-agnostic responses in the hippocampus and the alErC. Furthermore, domain-specificity scores in PrC were significantly reduced in elderly individuals. Error bars show the standard error of the mean (SEM). *PhC, parahippocampal gyrus; pmErC, posterior-medial entorhinal cortex; PrC, perirhinal cortex; alErC, anterior-lateral entorhinal cortex; HC, hippocampus.*

5.3.2.3 Age related changes in domain-specificity within MTL pathways

In a second step, we tested for domain-specific involvement of MTL regions separately in young and elderly subjects (see Figure 30B). For young subjects, PhC (M_{PhC}=0.32, SEM=0.06, T=4.9, p=0.000) and pmErC (M_{pmErC}=0.09, SEM=0.04, T=2.5, p=0.016) had significantly higher values than zero suggesting preferential scene processing, PrC (M_{PrC}=-0.31, SEM=0.04, T=-8.2, p=0.000) and alErC (M_{alErC}=0.10, SEM=0.03, T=-3, p=0.005) showed significantly lower values than zero suggesting preferential object processing, and the hippocampus did not show a difference from zero (M_{HC}=0.01, SEM=0.03, T=0.4, p=0.673) suggesting domain-agnostic processing. For elderly subjects, the same analysis showed that also PhC (M_{PhC}=0.48, SEM=0.06, T=8.3, p=0.000) and pmErC (M_{pmErC}=0.15, SEM=0.05, T=3.2, p=0.003) had significantly higher values than zero suggesting preferential scene processing, while PrC (M_{PrC}=-0.16, SEM=0.04, T=-4.7, p=0.000) showed significantly lower values than zero suggesting preferential object processing. However, both alErC (M_{alErC}=0.02, SEM=0.04, T=-0.03, p=0.978) and the hippocampus (M_{HC}=0.04, SEM=0.03, T=1.1, p=0.265) did not differ significantly from zero suggesting domain-agnostic processing. Finally, we performed a multivariate ANOVA with the difference scores of all regions as dependent variables (PhC, pmErC, PrC, alErC, hc) and the factor age group (young, elderly) to compare difference scores across age groups. There was a significant age effect ($F_{1,81}$ = 2.5, p = 0.036) driven by reduced domain-specificity as shown by post-hoc t-tests in PrC (M_{young}=-0.31, $M_{elderly}$=-0.16, p=0.007) and alErC (M_{young}=-0.1, $M_{elderly}$=0.02, p=0.028) in older adults, although only PrC survived Holm-Bonferroni multiple comparisons corrections. No other region showed any age

differences: PhC (M_{young}=0.32, $M_{elderly}$=0.48, p=0.059), pmErC (M_{young}=0.09, $M_{elderly}$=0.15, p=0.28), hippocampus (M_{young}=0.01, $M_{elderly}$=0.04, p=0.601).

5.3.3 *LURE-RELATED NOVELTY RESPONSES FOR OBJECT AND SCENE CONDITIONS IN MTL SUBREGIONS*

We used repetition suppression based contrasts to identify lure-related novelty responses throughout MTL subregions in all participants. Novelty responses for similar lure trials were calculated by subtracting repeat trials from correct lure trials ("lure related novelty", see Figure 31). One-sample t-tests were used to test whether those difference scores were significantly different from zero. Those revealed significant lure-related novelty responses for objects in the PrC (M_{PrC}=0.18, SEM=0.04, T=4, p=0.000), alErC (M_{alErC}=0.15, SEM=0.04, T=3.8, p=0.000), the hippocampus (M_{HC}=0.08, SEM=0.04, T=2.3, p=0.022) and PhC (M_{PhC}=-0.09, SEM=0.04, T=2.4, p=0.018), although only PrC and alErC survived Holm-Bonferroni multiple comparisons corrections. We did not find significant responses in pmErC (M_{pmErC}=0, SEM=0.05, T=0, p=0.998) (see Figure 31). For scenes, we found significant responses in the hippocampus, PrC, PhC as well as al and pmErC (M_{HC}=0.13, SEM=0.03, T=3.6, p=0.000; M_{PrC}=0.17, SEM=0.05, T=3.4, p=0.001, M_{PhC}=-0.14, SEM=0.04, T=3.6, p=0.001; M_{pmErC}=0.09, SEM=0.05, T=2, p=0.046; M_{alErC}=0.11, SEM=0.05, T=2.3, p=0.021) (see Figure 31A).

In a second step, we tested for lure-related novelty responses in the young and elderly sample separately. In the sample of young participants one sample t-tests showed that there were significant lure-related novelty responses for objects in the PrC (M_{PrC}=0.21, SEM=0.07, T=3, p=0.004) and the alErC (M_{alErC}=0.14, SEM=0.06, T=2.4, p=0.022) although only PrC survived Holm-Bonferroni multiple comparisons correction. We found no significant effects in the hippocampus, pmErC and PhC (M_{HC}=-0.08, SEM=0.05, T=1.6, p=0.12; M_{pmErC}=-0.05, SEM=0.08, T=0.7, p=0.053; M_{PhC}=-0.1, SEM=0.06, T=-1.7, p=0.099) (see Figure 5B). For scenes, we found significant effects in the hippocampus, PrC, and PhC which did not survive Holm-Bonferroni multiple comparisons corrections (M_{HC}=0.11, SEM=0.05, T=2.2, p=0.032; M_{PrC}=0.17, SEM=0.07, T=2.3, p=0.024; M_{PhC}=0.13, SEM=0.07, T=-2, p=0.05). There were no significant effects in al and pmErC (M_{alErC}=0.05, SEM=0.06, T=0.8, p=0.418; M_{pmErC}=0.04, SEM=0.06, T=0.7, p=0.475) (see Figure 31C and D).

In the sample of elderly participants one sample t-tests showed that there were significant lure-related novelty responses for objects in the PrC (M_{PrC}=0.15, SEM=0.06, T=2.6, p=0.013) and alErC (M_{alErC}=0.16, SEM=0.06, T=2.9, p=0.006). However, there were no significant effects in PhC, pmErC and the hippocampus (M_{PhC}=0.08, SEM=0.04, T=1.8, p=0.084; M_{pmErC}=-0.05, SEM=0.07, T=-0.7, p=0.498; M_{HC}=-0.08, SEM=0.05, T=1.7, p=0.098) (see Figure 31D). For scenes, there were significant responses in the hippocampus, PhC, PrC, alErC and pmErC (M_{HC}=0.14, SEM=0.05, T=2.9, p=0.006; M_{PhC}=0.14, SEM=0.04, T=3.4, p=0.002; M_{PrC}=-0.17, SEM=0.07, T=-2.4, p=0.019; M_{alErC}=0.16, SEM=0.07, T=2.5, p=0.018; M_{pmErC}=0.14, SEM=0.07, T=2, p=0.048), although only the hippocampus and PhC survived Holm-Bonferroni multiple comparisons corrections (see Figure 31C). Finally, we performed multivariate

ANOVAs to test for group differences in lure-related novelty signals. This could not reveal any age-group differences between lure-related novelty responses in objects ($F_{1,81}$ = 0.4, p = 0.816) nor scenes ($F_{1,81}$ = 0.6, p = 0.729).
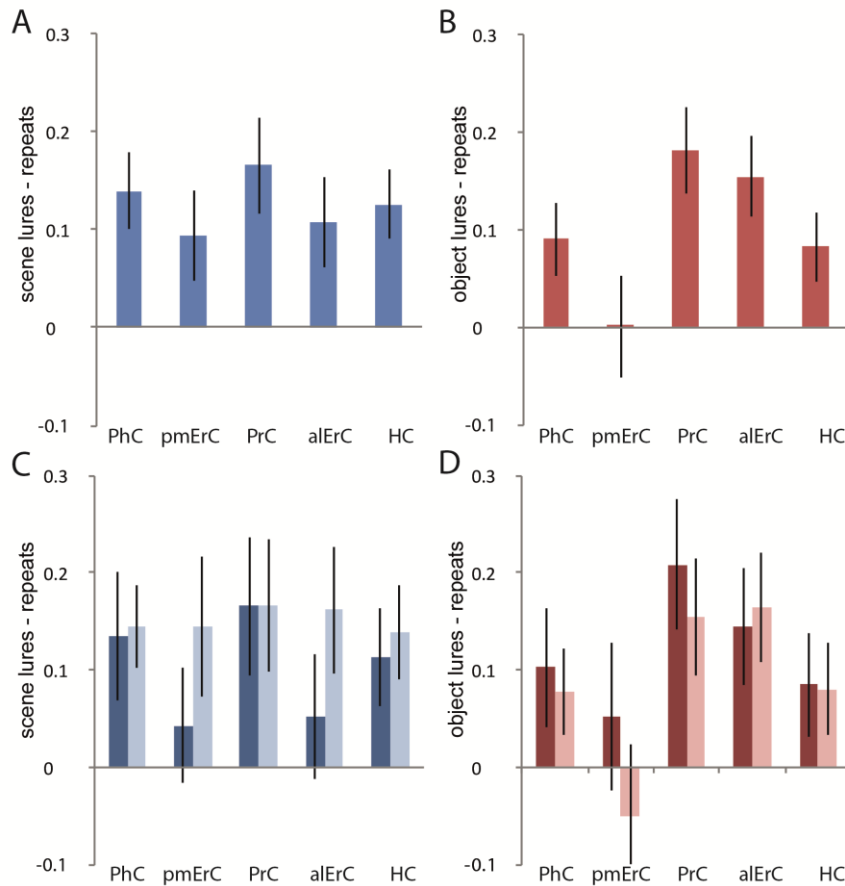

Figure 31. Activity related to correctly rejected lures > repeats for scenes (blue) and objects (red) in PhC, PrC, al- and pmErC as well as the hippocampus of the whole group (n=87) (A and B) and separately for young (n=43) and elderly participants (n=44) (C and D). Error bars show the standard error of the mean (SEM). *PhC, parahippocampal gyrus; pmErC, posterior-medial entorhinal cortex; PrC, perirhinal cortex; alErC, anterior-lateral entorhinal cortex; HC, hippocampus.*

5.4 DISCUSSION

In this study, we investigated the functional anatomy of medial temporal lobe (MTL) pathways in young and healthy older individuals using a novel domain-specific mnemonic discrimination task. Crucially, regions from different cortical systems, namely the anterior-lateral (AT) and posterior-medial (PM) system (Ranganath and Ritchey, 2012) were associated with object and scene processing, respectively. Further, we found that domain-specific MTL pathways in parahippocampal cortex (PhC) and perirhinal cortex (PrC) extend towards subregions in the entorhinal cortex (ErC). While the anterior-lateral portion was more involved in object processing and memory, the posterior-medial portion was more involved in scene processing and memory in young adults. The hippocampus, however, did neither show preference for object nor for scene processing. In addition, we investigated mnemonic discrimination across the MTL using lure-related novelty responses. While PrC and alErC were involved in object discrimination, both parts of the ErC, PhC, PrC and the hippocampus were involved in scene discrimination. Furthermore, elderly subjects showed a drop in performance for discriminating similar

lure images in both domains compared to young adults. Finally, while group comparisons did not yield any significant differences between age groups in lure-related novelty responses, elderly subjects demonstrated reduced domain-specificity scores in PrC-alErC.

Functional organization of MTL pathways

Our findings regarding the domain-specific responses in PhC and PrC fit well with earlier studies that used object and scene stimuli to investigate material-specific processing in the MTL. These studies showed that the PhC is indeed preferentially involved in scene processing whereas the PrC is more involved in object processing (Davachi et al., 2003; Ekstrom and Bookheimer, 2007; Libby et al., 2014; Schultz et al., 2012; Sheldon and Levine, 2015; Staresina et al., 2013, 2011). In our data, this was true for both groups separately and therefore extends earlier findings by showing domain-specific activity in PrC and PhC in elderly subjects, albeit being reduced in PrC.

We also assessed differential activity in entorhinal subregions. Based on the functional role of the medial (mErC) and lateral (lErC) ErC in rodents one would expect that both segments show differential involvement in the object and scene condition of our task. Whereas mErC has a higher density of head-direction and grid cells, which are modulated by spatial location and global landmarks (Hafting et al., 2005; Knierim et al., 2014; Sargolini et al., 2006), cells in lErC respond to individual objects and local landmarks (Deshmukh and Knierim, 2011; Knierim et al., 2014). However, there is also recent evidence that both segments host object representations as well as representations for spatial locations, with lErC prioritizing object over spatial information whereas mErC prioritizes spatial over object information (Keene et al., 2016). Recent human studies showed that strictly lateral and medial portions of the ErC showed differential activity in memory tasks. Reagh and colleagues showed that a strictly lateral portion was more involved in processing of object lures, whereas a strictly medial section was more involved in a task where the object location changed on the screen (Reagh and Yassa, 2014). Similarly, Schultz et al. showed differential activity in an interference working memory task where activity in a strictly lateral and medial portion was associated to the face and scene condition respectively (Schultz et al., 2012). In order to investigate domain-specificity in the ErC, we used masks that resulted from an earlier study. In that study (Chapter 4), we had used intrinsic functional connectivity to investigate the human homologues of the lateral and medial ErC in the rodent and our data suggested an anterior-lateral (alErC) and posterior-medial (pmErC) rather than a strict lateral vs. medial division (Maass et al., 2015). In our data, we found pmErC was more involved in scene processing, whereas alErC showed higher activity during object conditions. This also corroborates earlier findings from Schröder and colleagues who found very similar results associated with viewing of object and scene stimuli where they used very similar masks compared to ours (anterior-lateral vs. posterior-medial) (Schröder et al., 2015). Our results therefore show that al and pmErC are differentially involved in a domain-specific mnemonic discrimination task in young individuals. Importantly, this was not true for elderly subjects where alErC did not show domain-specific responses.

Lure-related novelty responses in the hippocampus and extrahippocampal regions

Our results also shed light on the organization of mnemonic discrimination in the MTL. Earlier studies suggest that the hippocampus, especially DG and CA3, but not other subregions in the MTL exhibit lure-related novelty responses in object mnemonic discrimination tasks that are typically viewed to be consistent with pattern separation computations (Bakker et al., 2008; Lacy et al., 2011; Reagh and Yassa, 2014). The representational-hierarchical model, however, suggests that representations across the ventral visual processing stream are organized in a hierarchical continuum of conjunctive representations, where the PrC and the hippocampus harbor more complex representations compared to regions more caudal in the ventral pathway (Kent et al 2016). Studies on object and scene discrimination suggest that while PrC plays a critical role in discriminating objects with high feature overlap, scene discrimination mostly relies on the hippocampus (Barense et al., 2005; Lee et al., 2005a, 2005b). For example, amnestic patients with hippocampal lesions that spare the PrC are specifically impaired in scene discrimination, whereas patients with more extensive damage including the PrC show additional impairments in object discrimination. This suggests that subfields of the hippocampus but also extrahippocampal regions might contain distinct representations for similar lures and therefore be involved in pattern separation computations.

In our task, it was important to rapidly encode stimuli in detail and to be able to distinguish between highly overlapping versions of objects and scenes in a later trial based on its mnemonic representation. We found that alErC and PrC showed strong lure-related novelty responses for similar objects, suggesting successful mnemonic object discrimination. This finding is in line with the representational hierarchical model by showing that extrahippocampal regions show lure-related novelty responses and that their involvement is based on their sensitivity for different stimulus material. For scenes, we found lure-related novelty responses in alErC-PrC, pmErC-PhC and the hippocampus – indicating that both pathways contributed to mnemonic discrimination of scenes. Our findings therefore suggest that although we found strong domain-specificity scores in PrC-alErC and PhC-pmErC, both pathways might be involved in mnemonic discrimination of scenes.

Although we designed our stimuli carefully in accordance to the findings from the animal literature, there is the possibility that the changes in our scene lure stimuli also engage PrC-alErC. While we only changed the shape of object features to create object lures (which was reported to engage the lErC), but did not change the color or texture, we modified the overall geometry of the rooms to create scene lures. This resulted in rather global than local feature changes in the scene images, which was reported to specifically engage the mErC but not lErC (Knierim et al., 2014). Still, there is the possibility that subjects perceive the differences between original and lure scenes as feature changes, given that our subjects are presented with images of scenes rather than being in a 3D environment. This might explain the additional engagement of PrC and alErC in addition to PhC and pmErC in mnemonic discrimination of similar scenes.

In contrast to the current findings, the results from chapter 3 as well as earlier studies reported lure-related novelty responses in the hippocampus during object as well as scene mnemonic similarity tasks (Bakker et al., 2008; Berron et al., 2016; Lacy and Stark, 2012; Reagh and Yassa, 2014; Yassa et al., 2011a). This is in contrast to the rather weak lure-related novelty responses in the hippocampus in objects in our results. However, lure-related novelty responses in earlier studies were mostly limited to DG and CA3 subregions and not evident in the remaining part of the hippocampus (e.g. Bakker et al. 2008). Given the resolution in the recent study and the resulting limitation on subfield analyses, our results should not be taken to conclude that hippocampal regions are not involved in mnemonic discrimination of objects. This has to be investigated in follow-up studies using high-resolution fMRI techniques.

Difficulties in mnemonic discrimination of objects and scenes in ageing

Our behavioral data shows that while elderly subjects do not have difficulties to identify repeated images, they have problems to identify similar lures. This has been already reported by other groups showing impairment in tasks that are meant to tax object pattern separation (Stark et al., 2013; Yassa et al., 2011a) and spatial pattern separation (Holden et al., 2012; Holden and Gilbert, 2012; Stark et al., 2010). In addition, our reaction time data suggest that elderly subjects have a bias towards "old" responses indicated by faster reaction times for false alarms and hits in contrast to correct rejections in line with the literature (Vieweg et al., 2015; Wilson et al., 2006; Yassa et al., 2011b). This is true for the object as well as the scene condition.

A recent study investigated mnemonic discrimination performance with respect to object identity and spatial object location in a group of healthy elderly subjects (Reagh et al., 2016). Although there was no evidence for a domain-specific behavioral impairment in the overall group, the authors found that subjects who performed lower in the Rey Auditory Verbal Learning Test (RAVLT) ("Impaired group") showed impairment in both the object as well as the spatial condition whereas high performers ("Unimpaired group") were only impaired in the object but not the scene condition. The authors interpret the results as an early impairment in object mnemonic discrimination. Although this would be in line with early structural and functional impairment in PrC and ErC, our analysis of accuracies and RT, however, indicate equal impairment in mnemonic discrimination of objects as well as scenes in ageing. In our study, it was not possible to subdivide subjects based on their neuropsychological test scores, since these were not available across the whole sample of aged individuals. Therefore, we cannot be certain whether there would be a difference in object and scene discrimination in impaired and unimpaired groups. However, as our data showed that lure-related novelty responses in both conditions were overlapping in the PrC and alErC, early functional impairment in PrC and alErC might result in difficulties in the discrimination of objects as well as scenes. Future studies with well-characterized clinical samples will have to further elucidate the pattern of impairment in domain-specificity and lure-related novelty responses as well as its role in memory deficits in ageing.

Functional integrity of anterior-temporal and posterior-medial pathways

To investigate age-related functional changes in both medial-temporal pathways, we compared domain-specificity scores as well as lure-related novelty signals across age groups. Lure-related novelty responses associated to objects and scenes where evident in elderly subjects and we did not find evidence for differences across age groups in any MTL subregion. However, domain-specificity scores showed that alErC was domain-agnostic in the elderly, and there was a significant reduction in domain-specificity scores in the PrC of elderly compared to young individuals. This may indicate impairment of the PrC and alErC in ageing and fits well with an earlier neuroimaging study that reported reduced activity in PrC in an object discrimination task. Here, reduced PrC activity was specifically associated to lower performance in the discrimination of objects that share high feature overlap (Ryan et al., 2012). Thus, reduced activity in our and other tasks might point towards early functional impairment of object processing pathways in ageing. In addition, postmortem data point to the lateral part of the ErC and PrC as the first cortical regions to accumulate tau tangles (NFTs) in AD (Braak and Tredici, 2012). More specifically, tau deposits in the transentorhinal region (Braak stages I/II), which is part of the PrC, are common in individuals aged 60 and above (>60%) and are considered as silent, preclinical stages of AD (Braak and Braak, 1997). In accordance with the neuropathological data, a recent study demonstrated that cognitively normal older adults that later developed AD (preclinical AD, progressors vs. non progressors) showed reduced CBV measures in the lateral entorhinal, transentorhinal and perirhinal cortex (Khan et al., 2014). Although our sample of older adults was seemingly healthy, it is thus possible that several of the older participants did already harbor tau pathology in their medial temporal lobes (Braak and Braak, 1991). Due to the lack of CSF and PET biomarkers it is impossible for us to quantify this proportion. Thus, future studies with well characterized study samples based on biomarkers have to show whether reduced domain-specificity in PrC and alErC could be an early indicator of functional impairment in MTL pathways in ageing and early AD.

Taken together, we show functional domain specificity in PrC-alErC and PhC-pmErC for objects and scenes, respectively, as well as lure-related-novelty signals associated with the discrimination of similar objects and scenes. While lure-related novelty responses in MTL subregions are maintained in old age, domain-specificity is reduced in PrC and alErC. Thus, our data suggest that ageing might affect the MTL object pathway disproportionally strongly – with a deficit in mnemonic discrimination associated with ageing in both domains. It will be important to relate the functional and behavioral underpinnings of domain-specific memory processing to preclinical AD pathology in order to understand whether pathology is associated with a domain-selective impairment.

5.5 CONTRIBUTIONS

CHAPTER

6

SUMMARY AND GENERAL DISCUSSION

6.1 SUMMARY

The findings of the current thesis add to the understanding of the structural and functional organization of memory pathways in the medial temporal lobe (MTL) throughout its subregions. In chapter 2, ultra-high-resolution structural MRI was used to provide an anatomically valid and reliable manual segmentation protocol that incorporates recent neuroanatomical findings. Critically, it provides standardized manual segmentation rules for hippocampal subfields, which are differentially involved in memory computations (e.g. dentate gyrus (DG) and CA3), as well as extrahippocampal regions including those early affected in Alzheimer's Disease (e.g. area 35 and entorhinal cortex (ErC)). In chapter 3, high-resolution functional MRI in combination with multivariate pattern analyses (MVPA) could reveal that representations of similar events are less overlapping in the DG compared to other hippocampal or extrahippocampal subregions, which is direct evidence for pattern separation in the human DG. Following an intrinsic functional connectivity approach, again leveraging the high-resolution at 7T MRI, chapter 4 revealed the first topographical organization of functional subregions in the human ErC – namely anterior-lateral (alErC) and posterior-medial ErC (pmErC) – based on their different connectivity profile with the perirhinal cortex (PrC) and parahippocampal cortex (PhC) as well as proximo-distal portions of the subiculum. Finally, chapter 5 could show that PrC, PhC but also alErC and pmErC are differentially involved in object and scene processing in a mnemonic discrimination task while the hippocampus showed domain-general involvement. Despite the domain-specificity in the processing of objects and scenes, both pathways partly overlapped in mnemonic discrimination of similar objects and scenes. In addition, healthy elderly individuals showed increased false alarm rates for similar lure stimuli as well as reduced domain-specificity in PrC-alErC, which may suggest age-related functional impairment in the object pathway.

The present results advance our knowledge of the functional and computational organization of the entorhinal-hippocampal circuitry and have implications for theories and models of memory, and mnemonic discrimination in particular. The findings are critical in informing future studies of cognitive ageing and neurodegenerative diseases. Finally, the current thesis demonstrates the potential of ultra-high-resolution MRI for fine-grained analysis of functional activity as well as structural morphometry of subregions in the human MTL.

6.2 GENERAL DISCUSSION

6.2.1 DOMAIN-SPECIFIC PATHWAYS IN THE MEDIAL TEMPORAL LOBE

The organization of the MTL in animals suggests that two parallel pathways are involved in domain-specific memory functions – namely in memory for objects or content, and scenes or locations (Knierim et al., 2014; van Strien et al., 2009). These pathways include the PrC-lErC and PhC-mErC, respectively. Functional subdivisions from the rodent and primate literature could not easily be translated to the

human ErC due to its differences in anatomy across species. Nevertheless, earlier studies in humans showed differential activity between strictly medial vs. lateral segments of the ErC in object vs. object-location memory as well as scene vs. face memory (Reagh and Yassa, 2014; Schultz et al., 2012). In the experiment presented in chapter 4, subdivisions of the human ErC were analyzed based on their connectivity with PrC and PhC homologous to the animal literature. In contrast to a strict medial-lateral split, however, the results strongly suggest an anterior-lateral and a posterior-medial split. This is further corroborated by another recent high-resolution imaging study that aimed for a parcellation of the ErC based on its connectivity with global posterior-medial and anterior-temporal cortical regions that found subregions that are remarkably similar to the findings in chapter 4 (Schröder et al., 2015, see Schultz et al., 2015 for a recent review incorporating findings from both studies). The results from both studies are very similar to the findings from anatomical studies in rodents (rostrolateral to caudomedial; see van Strien et al., 2009) and nonhuman primates (anterolateral to posteromedial, see Suzuki and Amaral, 1994 and Witter and Amaral, 1991) suggesting that they provide a link between human and animal research and that the subregions of the ErC might be similarly involved in different mnemonic functions in humans (Knierim et al., 2014). In chapter 5, it is shown that not only PrC and PhC but also alErC and pmErC are indeed differentially involved in object and scene processing using a mnemonic discrimination task. The functional architecture of the two pathways therefore shows remarkable similarities with the animal literature (Knierim et al., 2014). This highlights that memory tasks incorporating object and scene stimuli can be used to investigate domain-specific processing and networks in the human MTL.

In contrast to extrahippocampal regions, however, the hippocampus did not show differential activity associated with the processing of objects and scenes suggesting that it is domain-agnostic. This is in line with models assuming an important role of the hippocampus in binding of objects and their location (Ranganath, 2010). However, there is also growing evidence for differences within subregions of the hippocampus. An interesting theory assumes differences in the organization of representations in the anterior and posterior hippocampus where the posterior segment hosts more local and the anterior segment more global representations based on human and animal studies (Poppenk et al., 2013). Whilst there are recent findings that are in line with such a gradient (e.g. Collin et al., 2015), it remains unclear how this maps onto representations of objects and scenes. One hypothesis would be that global representations of the environment, i.e. scenes, would engage the anterior hippocampus while representations of individual objects would rather engage the posterior hippocampus. Evidence for this comes from recent work on scene processing and memory in the anterior hippocampus (Hodgetts et al., 2017; Zeidman and Maguire, 2016). In addition, findings in rodents suggest that distal and proximal portions of the subiculum, CA1 and probably CA3 are differentially involved in object and scene processing (Knierim et al., 2014; Nakamura et al., 2013; Sauvage et al., 2013). In chapter 4, we found that indeed the proximal and distal subiculum showed differential connectivity with al- and

pmErC suggesting that both portions might be differentially involved in object and scene processing. Given that spatial and non-spatial processing varies between specific subregions of the hippocampus, it is not surprising that we did not observe differences on the level of the whole hippocampus. Future studies should therefore leverage the increased resolution and SNR available with high-field MRI scanners to elucidate the local networks within the hippocampus and their involvement in domain-specific processing as these processes will be critical to understand how we integrate and remember object and spatial information in episodic memory.

6.2.2 MNEMONIC DISCRIMINATION IN THE MEDIAL TEMPORAL LOBE

Pattern separation in the human DG

Computational models of the hippocampus put high emphasis on the role of the DG in pattern separation due to its unique anatomical and physiological features (Marr, 1971; McClelland et al., 1995). The computational learning systems (CLS) model, for example, assumes that the hippocampus and especially the DG harbors distinct representations of similar events while neocortical regions are suggested to host overlapping representations (McClelland et al., 1995). The results presented in chapter 3 are in line with the predictions of the model by showing less overlapping representations of similar stimuli in DG compared to other hippocampal subregions (e.g. CA1 or CA3) or extrahippocampal structures such as ErC, PrC or PhC – which is direct evidence for pattern separation in DG. The results from chapter 5 lend further support for a role of hippocampal regions in pattern separation by showing lure-related novelty responses in the hippocampus indicating successful discrimination, specifically for scenes but not for objects. This would be in line with studies showing that the hippocampus as a whole plays a key role in spatial cognition and memory (Burgess et al., 2002; Hartley et al., 2014). However, given that earlier findings from high-resolution fMRI studies using object mnemonic discrimination tasks highlight the role of the DG and CA3, the absence of effects for objects likely result from the lack of subregional analyses (Bakker et al., 2008; Lacy et al., 2011; Reagh and Yassa, 2014). Thus, high-resolution approaches will be critical to understand the role of hippocampal subregions in domain-specific pattern separation. Taken together, this suggests that the human hippocampus hosts distinct representations for similar scenes as well as objects and therefore points to domain-general involvement of hippocampal subregions in mnemonic discrimination.

The role of extrahippocampal structures in mnemonic discrimination

Although lure-related novelty responses were limited to the DG in chapter 3, extrahippocampal regions showed significant effects in chapter 5. While PrC-alErC showed lure-related novelty signals for the discrimination of similar objects, both PhC-pmErC and PrC-alErC were involved in mnemonic discrimination of similar scenes. Further evidence for the role of the PrC in object discrimination comes from studies where patients with MTL lesions had to discriminate objects with either high or low overlap of features (Barense et al., 2005; Lee et al., 2005a). In both studies participants with damage

extending towards the PrC showed severe impairment in the high-overlap condition suggesting that the PrC is specifically involved in the discrimination of very similar objects. Although not many studies have investigated the role of the ErC in mnemonic discrimination, it is likely that it is positioned between the hippocampus and the PrC with respect to the distinctiveness of its representations. The recent study from Reagh and colleagues also yields evidence for a role of the ErC in mnemonic discrimination (Reagh and Yassa, 2014). While they found lure-related novelty responses for changes in object identity in lErC, lure-related novelty responses for changes in object locations were observed in mErC. Again, the DG/CA3 showed lure-related novelty responses for both conditions, in line with its role in more general mnemonic discrimination. This suggests region-specific involvement in mnemonic discrimination in line with the overall domain-specificity, bearing in mind though that object location discrimination is a different concept than scene discrimination. A recent study in rodents adds to this by showing that cells in the mErC can be driving pattern separation responses of cells in DG/CA3 for similar environments (Kitamura et al., 2015).

Together, these findings contradict computational models such as the CLS that assume overlapping representations in cortical regions and pattern separation limited to the DG (McClelland et al., 1995; Norman and O'Reilly, 2003). Instead, the findings presented in this thesis suggest that mnemonic discrimination may not be restricted to the hippocampus but rather extends along the two main processing pathways. The representational-hierarchical model (RHM) offers a different framework on mnemonic discrimination, which accounts for the extrahippocampal findings (Kent et al., 2016). The idea is that conjunctive representations reduce ambiguity between similar images with overlapping features. These conjunctive representations become more complex along the ventral stream from posterior to anterior regions. Thus, more complex conjunctive representations in PrC and the hippocampus help resolve feature ambiguity in lower level representations – an idea that is very similar to the reduction of interference in the pattern separation literature (e.g. Bakker et al., 2008). As the findings of this thesis as well as the literature discussed above point to an important role in mnemonic discrimination for both, hippocampal as well as extrahippocampal regions, it might be possible to integrate the CLS and the RHM to account for these recent findings. Although the RHM contrasts with the CLS in the assumption that several cortical regions and not only the DG harbor distinct representations, they both agree in a hierarchy between cortical regions and the hippocampus. The DG might represent the top of this hierarchy due to its unique physiological and anatomical properties (e.g. sparse representations). In addition, hippocampal neurogenesis results in highly plastic immature neurons in the DG which also play an important role in pattern separation (Nakashiba et al., 2012; Sahay et al., 2011). These features might enable the DG to perform a very efficient form of pattern separation and would explain why the DG is generally involved in discrimination tasks independent of the stimulus domain whenever information-rich and complex events that share significant overlap must be encoded rapidly. Taken together, this would suggest a hierarchical model of reduction of

representational overlap in a domain-specific fashion where overlap in similar spatial information is reduced via PhC-pmErC-DG and overlapping object information is decorrelated via PrC-alErC-DG.

Nevertheless, further research will have to disentangle the specific contributions of each region to object, object location and scene discrimination for a comprehensive picture of mnemonic processing across the MTL. Multivariate analyses such as machine learning classifiers or representational similarity analysis (RSA) are highly suited to investigate the domain-specific representational organization of MTL pathways in the future as they can be used to measure the degree of representational overlap in subregions along both pathways (Kriegeskorte et al., 2008). This has also been demonstrated in chapter 3 where differences in representational overlap could be demonstrated between MTL subregions. Thus, high-resolution fMRI studies at 7T in combination with multivariate analysis techniques would be highly suited to further elucidate the representational organization of MTL pathways. The findings of the current thesis lead thereby to important questions. The results of chapter 5 showed that PrC and alErC were also involved in the discrimination of similar spatial scenes. This suggests that the engagement of MTL pathways might not only depend on the stimulus domain but also on the type of changes between similar images. Consequently, studies are needed that also take different types of image manipulations into account. Also, given that there was no evidence for distinct representations in extrahippocampal regions in chapter 3, future studies aiming to investigate the representational organization of MTL pathways should rely on accurate anatomical segregation of MTL pathways (PrC-alErC, PhC-pmErC) and use stimulus material that engages both pathways separately (spatial vs. non-spatial).

Finally, the experiments presented in this thesis were focused on MTL pathways using high-resolution fMRI approaches. Most of the earlier studies on pattern separation in humans also followed high-resolution approaches at 3T and did only measure fMRI responses from MTL regions. Thus, it remains largely unclear how the MTL interacts with neocortical regions outside the MTL during mnemonic similarity tasks (Pidgeon and Morcom, 2016).

6.2.3   ROLE OF DOMAIN-SPECIFIC PATHWAYS IN AGEING AND EARLY AD

One aim of this thesis was to increase our understanding of MTL pathways which is necessary to be able to detect early changes in Alzheimer's Disease (AD) and be able to differentiate them from healthy ageing. However, it is challenging to successfully distinguish between brain ageing and neurodegeneration (see Jagust, 2013 for review). Post-mortem studies show that even cognitively normal elders presented substantial AD pathology (Bennett et al., 2006). This fits well with studies using positron emission tomography (PET) or cerebrospinal fluid (CSF) measures that show evidence of AD pathology already in cognitively normal elderly subjects (Jagust et al., 2009; Morris et al., 2011). Therefore, it is possible that a significant number of ageing studies included subjects with preclinical AD and that some of the alterations seen in ageing might be related to presymptomatic AD (Jagust,

2013). Ageing and AD especially affect regions in the MTL. While studies in ageing mostly report structural and functional impairment in the human hippocampus, AD is suggested to affect the integrity of extrahippocampal regions earlier than the hippocampus (e.g. Small et al., 2011). This is in line with neuropathological studies indicating that NFT depositions can first be detected in the transentorhinal region (Braak stage I). Subsequently NFTs spread medially towards layer II of the ErC (Braak stage II) – most likely beginning in the lateral ErC – before they progress to the hippocampus and the temporal cortex (Braak stages III and IV; Braak and Braak, 1991, 1995; Gómez-Isla et al., 1996). The findings from this thesis can be used in future studies to further our understanding of effects of ageing and early AD by providing novel subdivision criteria as well as potential functional and structural measures. Although one limitation of the segmentation protocol presented in chapter 2 is that it was developed using data from young individuals, it provides standardized rules that allow the delineation of the PrC as well as its subdivision in areas 35 and 36 – where area 35 significantly overlaps with the transentorhinal region described by Braak and Braak and others (Augustinack et al., 2013; Braak and Braak, 1991; Taylor and Probst, 2008). Consequently, it has to be validated in ageing and disease samples in future studies. The functional connectivity study presented in chapter 5 describes the functional subdivisions of the ErC into an anterior-lateral and a posterior-medial portion (Maass et al., 2015). Together this novel and more detailed parcellation of subregions in the MTL will allow a fine-grained investigation of MTL pathways.

Detection and tracking of structural changes in ageing and early AD

In early stages of AD in comparison to healthy ageing, atrophy or thinning of area 35, anterior-lateral ErC as well as hippocampal CA1 would be expected (Braak and Braak, 1991; de Flores et al., 2015a) Recent studies found indeed evidence for specific structural alterations in MTL subregions. They highlighted early atrophy in preclinical AD and amnestic MCI compared to normal controls in the PrC and mainly the lateral portion of the ErC (Miller et al., 2015; Yushkevich et al., 2015b). Olsen and colleagues divided their sample of community-dwelling older adults in a healthy and an at-risk group for dementia based on their performance in the Montreal Cognitive Assessment (MoCA) and showed that only the alErC volumes (segmentation based on the results of chapter 4) were significantly reduced in the at-risk group (Olsen et al., 2016, preprint without peer-review, https://doi.org/10.1101/080374). However, to differentiate between healthy ageing and early AD, it is important to use PET or CSF biomarkers to further characterize the study sample. Wolk and colleagues used MRI-based subregional morphometry in combination with amyloid PET to explore the sensitivity of subregional MTL volumes in the discrimination of early stages of AD (Wolk et al., 2017). While different measures of hippocampal volumes could not detect subjects before the MCI stage, the only measure that could already identify subjects that were cognitively normal but showed already signs of AD pathology was the thickness of area 35. The results nicely recapitulate Braak staging of NFTs in the MTL and therefore also highlight the potential use of the markers provided in chapter 2

and 4 for disease detection and progression. In addition, it is still unclear whether ageing independent of AD affects the hippocampus and adjacent structures disproportionately. While some studies suggest increased effects of ageing in the DG compared to other subregions (Small et al., 2011), the results are still inconclusive (de Flores et al., 2015a). Thus, detailed morphometrical studies in healthy ageing including all subregions presented in chapter 2 can help to characterize and distinguish age-related changes from those occurring in early AD.

Functional changes in ageing and early AD

It is likely that the structural changes in ageing and early stages of AD also indicate functional impairment and it might be possible to detect this using fMRI. In chapter 5 it was found that across the whole group of young and elderly subjects PhC-pmErC were more involved in scene processing while PrC-alErC were more involved in object processing. However, domain-specificity of PrC-alErC was reduced in elderly compared to young subjects. This relates to studies in aged rats that suggest functional impairment of the aged PrC. Burke and colleagues reported that during the exploration of environments including objects, aged rats showed reduced PrC Arc protein levels (Burke et al., 2012) and reduced firing rates in PrC (Burke et al., 2014), which might both explain an observed behavioral object discrimination deficit (Burke et al., 2011). Along the same lines, an fMRI study reported that the PrC of young individuals was engaged during a matching task with highly similar object pairs. Critically, elderly participants were not only performing worse but also showed reduced activity in bilateral anterior PrC (Ryan et al., 2012). Therefore, measures of functional integrity of MTL subregions as presented in chapter 5 might be sensitive for functional impairment in ageing. Given that the PrC and ErC are also very early affected by AD pathology there is the possibility that abnormalities in PrC and alErC BOLD responses might also be a sensitive early indicator of AD. Thus, it will be important in future studies to investigate functional measures of MTL integrity in combination with PET and CSF biomarkers to disentangle effects of ageing and AD.

Connectivity

In chapter 4 local connectivity networks between subregions in the MTL were analyzed and revealed on the one hand increased connectivity between alErC and PrC compared to PhC and on the other hand increased connectivity of pmErC with PhC compared to PrC. In addition, alErC and pmErC exhibited distinct patterns of preferential connectivity with proximal and distal subiculum, respectively. Effects of ageing on MTL subregions are likely to disturb local network activity and therefore impair MTL functioning (see Wilson et al., 2006). In early AD, this might predominantly affect connectivity between PrC, alErC, proximal subiculum and neocortical regions of the anterior-temporal system. Schröder and colleagues found that the alErC is preferentially connected to regions of the anterior-temporal system, which is orbitofrontal cortex, anterior temporal regions and the amygdala (Schröder et al., 2015). The pmErC showed preferential connectivity with regions in the posterior-

medial system, which is the precuneus, retrosplenial cortex (RsC) and PhC. Therefore, given the spread of AD pathology towards the posterior-medial system, later stages of AD are likely to be characterized by a profound impairment of connectivity between PhC, pmErC, distal subiculum and regions in the posterior-medial system. This has been shown by La Joie and colleagues who investigated networks that are vulnerable to AD and showed that those overlap with brain regions in the posterior medial system (Joie et al., 2014). As these regions are also part of the episodic memory network and especially involved in memory retrieval (Dickerson and Eichenbaum, 2009; Rugg and Vilberg, 2013), disconnection of the MTL and regions in the parietal cortex, the posterior cingulate and the RsC will likely have an impact on scene processing and will result in more profound impairment of episodic memory. Therefore, future studies are needed to investigate whether measures of fine-grained local and global connectivity can reveal differences between normal ageing and AD which may also further our understanding of the spread of AD related effects.

6.2.4   OUTLOOK AND FUTURE PERSPECTIVES

The current thesis highlights that high-resolution imaging techniques can successfully be used to gain understanding of the MTL memory system. However, for future studies increased development of analysis tools that are optimized for high-resolution imaging will be critical as the field moves toward increased imaging of hippocampal subfields (Berron et al., 2016; Wisse et al., 2016a), proximal and distal portions of subfields (Maass et al., 2015) and even entorhinal layers (Maass et al., 2014). Thus, it will be critical to develop tools that improve coregistration between different imaging modalities and help to account for participant induced head motion such as prospective motion correction (Stucht et al., 2015). This is particularly true for high-resolution imaging studies including patient populations (e.g. Parkinson's Disease and Alzheimer's Disease). High-resolution structural imaging in chapter 2 also revealed that spatial normalization techniques applied in chapter 3, 4 and 5 will be likely to fail in regions where there is high anatomical variability as it is the case in the PrC. Thus, group analyses in fMRI studies focused on perirhinal function should be done in native space or require very specific analysis tools (Xie et al., 2017).

Imaging techniques at high fields as used in this thesis combined with multivariate techniques make it possible to investigate the fine-grained organization of MTL pathways. Future studies could use these techniques to further understand the representational architecture of MTL regions. Therefore, domain-specificity of the stimulus material as well as the brain regions of interest have to be taken into account. The results of these future studies could yield a measure indicating functional impairment on a representational level in ageing or neurodegenerative diseases which might be independent to volumetric changes or alterations in overall activity levels.

Future high-resolution connectivity studies are needed to further understand the local connectivity patterns between the ErC and the hippocampus highlighted in chapter 4 and to shed light on intra-

hippocampal connectivity profiles. These studies in combination with well-designed cognitive paradigms drawing on spatial and non-spatial (or scene and object) processing have a high chance to elucidate whether the domain-specific pathways known in the MTL do extend towards hippocampal subfields as it is suggested in the animal literature (Knierim et al., 2014; Sauvage et al., 2013).

As recent studies have shown that MTL subregions described in chapter 2 and 4 show sensitivity for ageing as well as early disease processes, it is important to apply this morphometric approach to larger studies on ageing and neurodegenerative diseases. However, the detailed subdivision of one entire MTL takes approximately 4 hours of manual segmentation. Therefore, it will be critical to build automated segmentation algorithms that follow the rules established in chapters 2 and 4 and allow the segmentation of larger datasets (Wisse et al., 2016b; Xie et al., 2017; Yushkevich et al., 2015b). In addition to markers for early disease effects these algorithms could also be used to track the influence of disease modifying pharmacological or non-pharmacological treatment like e.g. physical exercise regimes.

A limitation of the results in chapter 5 and their interpretation is that it is unclear whether and to which extent they can be assigned to effects of early AD or ageing due to the missing pathology markers. Therefore, future studies must particularly focus on multimodal approaches where they combine task-related fMRI or carefully designed behavioral paradigms with PET/CSF measures or otherwise very well characterized study cohorts. The advent of tau PET will further enable researchers to investigate how tau deposition affects task-related BOLD signals in MTL subregions, whether performance in non-spatial- or spatial tasks correlates with tau burden and whether behavioral assessments of mnemonic discrimination can distinguish between subjects with high and low MTL tau levels.

An important issue will be to understand whether spatial or non-spatial (or object or scene) memory shows earlier decline in ageing and AD and whether such assessments will have diagnostic value. Early stages of AD (Braak stage I and II) are considered to be the clinically silent or asymptomatic period (Braak and Braak, 1995). When Tau pathology propagates to the hippocampal regions and includes the lateral temporal cortex (Braak stage II and IV), this is thought to mark the transition from the silent to the symptomatic period (Nelson et al., 2009). The assumption of Braak stage I and II being silent rests on the fact that neuropsychological tests could not detect cognitive deficits in these preclinical stages. This is likely also the reason why markers of cognitive decline are considered to change later compared to any other imaging or CSF marker during the course of AD (Jack et al., 2013). However, neuropsychological assessment batteries are designed to detect impairment in cognitive functioning in rather late disease stages and are not sensitive to subtle alterations in cognitive performance in early preclinical stages (Rentz et al., 2013). The findings in this thesis suggest that neuropsychological assessments should be focused on the cognitive functions that are subserved by brain regions that are most vulnerable to the earliest stages of AD. Given that very specific structures show NFTs, cortical thinning and abnormal BOLD activity in preclinical dementia, behavioral effects are expected to be

subtle. Most research studies that report spatial or non-spatial deficits do not compare performance in both – spatial and non-spatial or object and scene – domains. Thus, it will be important in the future to develop more tasks that compare the anterior-temporal and the posterior-medial systems using for example spatial and non-spatial tests to further investigate which memory system is impaired earlier. Results from chapter 5 as well as recent findings from other groups suggest that object-based memory tasks where the overlap of features is high could be a promising cognitive marker for early impairment, as those tasks may rely on the functional integrity of the PrC and lateral ErC. On the other hand, it is likely that the pattern of behavioral impairment will change in later stages of the disease when there is Abeta in the posterior cingulate as well as the RsC and NFTs spread outside the MTL (Buckner et al., 2005). In these stages it is likely that the posterior-medial system becomes seriously affected which is predominantly involved in spatial cognition, navigation and memory for scenes and locations (Ranganath and Ritchey, 2012). This suggests that while the object domain might be impaired very early in the disease, the spatial/scene domain might be promising to track disease progression in later stages.

REFERENCES

Agster, K.L., Burwell, R.D., 2013. Hippocampal and subicular efferents and afferents of the perirhinal, postrhinal, and entorhinal cortices of the rat. Behav. Brain Res. 254, 50–64.

Aly, M., Ranganath, C., Yonelinas, A.P., 2013. Detecting changes in scenes: the hippocampus is critical for strength-based perception. Neuron 78, 1127–37.

Amaral, D.G., Ishizuka, N., Claiborne, B., 1990. Chapter Neurons, numbers and the hippocampal network. Progress in brain research 83 1-11.

Amaral, D.G., Witter, M.P., 1989. The three-dimensional organization of the hippocampal formation: a review of anatomical data. Neuroscience 31, 571–591.

Apostolova, L.G., Zarow, C., Biado, K., Hurtz, S., Boccardi, M., Somme, J., Honarpisheh, H., Blanken, A.E., Brook, J., Tung, S., Kraft, E., Lo, D., Ng, D., Alger, J.R., Vinters, H.V., Bocchetta, M., Duvernoy, H., Jack, C.R., Frisoni, G.B., Bartzokis, G., Csernansky, J.G., de Leon, M.J., deToledo-Morrell, L., Killiany, R.J., Lehericy, S., Malykhin, N., Pantel, J., Pruessner, J.C., Soininen, H., Watson, C., 2015. Relationship between hippocampal atrophy and neuropathology markers: A 7T MRI validation study of the EADC-ADNI Harmonized Hippocampal Segmentation Protocol. Alzheimers Dement. 11, 139–150.

Augustinack, J.C., Huber, K.E., Stevens, A.A., Roy, M., Frosch, M.P., Kouwe, A.J., Wald, L.L., Leemput, K., C, M., Ann, Fischl, B., 2013. Predicting the location of human perirhinal cortex, Brodmann's area 35, from MRI. NeuroImage 64, 32–42.

Avants, B.B., Tustison, N.J., Song, G., Cook, P.A., Klein, A., Gee, J.C., 2011. A reproducible evaluation of ANTs similarity metric performance in brain image registration. NeuroImage 54, 2033–44.

Avants, B.B., Yushkevich, P., Pluta, J., Minkoff, D., Korczykowski, M., Detre, J., Gee, J.C., 2010. The optimal template effect in hippocampus studies of diseased populations. NeuroImage 49, 2457–66.

Azab, M., Stark, S.M., Stark, C., 2014. Contributions of human hippocampal subfields to spatial and temporal pattern separation. Hippocampus 24, 293–302.

Bakker, A., Albert, M.S., Krauss, G., Speck, C.L., Gallagher, M., 2015. Response of the medial temporal lobe network in amnestic mild cognitive impairment to therapeutic intervention assessed by fMRI and memory task performance. Neuroimage Clin 7, 688–698.

Bakker, A., Kirwan, C., Miller, M., Stark, C.E., 2008. Pattern separation in the human hippocampal CA3 and dentate gyrus. Science 319, 1640–2.

Bakker, A., Krauss, G.L., Albert, M.S., Speck, C.L., Jones, L.R., Stark, C.E., Yassa, M.A., Bassett, S.S., Shelton, A.L., Gallagher, M., 2012. Reduction of Hippocampal Hyperactivity Improves Cognition in Amnestic Mild Cognitive Impairment. Neuron 74, 467–474.

Barense, M.D., Bussey, T.J., Lee, A.C., Rogers, T.T., Davies, R.R., Saksida, L.M., Murray, E.A., Graham, K.S., 2005. Functional specialization in the human medial temporal lobe. J. Neurosci. 25, 10239–10246.

Bennett, D., Schneider, J., Arvanitakis, Z., Kelly, J., Aggarwal, N., Shah, R., Wilson, R., 2006. Neuropathology of older persons without cognitive impairment from two community-based studies. Neurology 66, 1837–44.

Bernasconi, N., Bernasconi, A., Caramanos, Z., Antel, S.B., Andermann, F., Arnold, D.L., 2003. Mesial temporal damage in temporal lobe epilepsy: a volumetric MRI study of the hippocampus, amygdala and parahippocampal region. Brain. 126, 462–9.

Berron, D., Schütze, H., Maass, A., Arturo, C.-B., Kuijf, H.J., Kumaran, D., Düzel, E., 2016. Strong Evidence for Pattern Separation in Human Dentate Gyrus. J. Neurosci. 36, 7569–7579.

Boccardi, M., Bocchetta, M., Morency, F.C., Collins, L.D., Nishikawa, M., Ganzola, R., Grothe, M.J., Wolf, D., Redolfi, A., Pievani, M., Antelmi, L., Fellgiebel, A., Matsuda, H., Teipel, S., Duchesne, S., Jack, C.R., Frisoni, G.B., 2015. Training labels for hippocampal segmentation based on the EADC-ADNI harmonized hippocampal protocol. Alzheimers Dement.

Boldrini, M., Santiago, A.N., Hen, R., Dwork, A.J., Rosoklija, G.B., Tamir, H., Arango, V., Mann, J.J., 2013. Hippocampal Granule Neuron Number and Dentate Gyrus Volume in Antidepressant-Treated and Untreated Major Depression. Neuropsychopharmacology.

Bonnici, H.M., Chadwick, M.J., Kumaran, D., Hassabis, D., Weiskopf, N., Maguire, E.A., 2012a. Multi-voxel pattern analysis in human hippocampal subfields. Front. Hum. Neurosci. 6, 290.

Bonnici, H.M., Kumaran, D., Chadwick, M.J., Weiskopf, N., Hassabis, D., Maguire, E.A., 2012b. Decoding representations of scenes in the medial temporal lobes. Hippocampus 22, 1143–1153.

Boutet, C., Chupin, M., Lehéricy, S., Marrakchi-Kacem, L., Epelbaum, S., Poupon, C., Wiggins, C.J., Vignaud, A., Hasboun, D., Defontaines, B., Hanon, O., Dubois, B., Sarazin, M., Hertz-Pannier, L., Colliot, O., 2014. Detection of volume loss in hippocampal layers in Alzheimer's disease using 7 T MRI: a feasibility study. NeuroImage Clin. 5, 341–8.

Braak, H., Alafuzoff, I., Arzberger, T., Kretzschmar, H., Tredici, K., 2006. Staging of Alzheimer disease-associated neurofibrillary pathology using paraffin sections and immunocytochemistry. Acta Neuropathol 112, 389–404.

Braak, H., Braak, E., 1997. Frequency of stages of Alzheimer-related lesions in different age categories. Neurobiol. Aging 18, 351–7.

Braak, H., Braak, E., 1991. Neuropathological stageing of Alzheimer-related changes. Acta Neuropathol. (Berl.) 82, 239–59.

Braak, H., Del Tredici, K., 2004. Alzheimer's disease: intraneuronal alterations precede insoluble amyloid-beta formation. Neurobiol. Aging 25, 713-718-746.

Braak, H., Tredici, K., 2012. Alzheimer's disease: Pathogenesis and prevention. Alzheimers Dement.

Braak, H., Tredici, K., 2011. The pathological process underlying Alzheimer's disease in individuals under thirty. Acta Neuropathol. (Berl.) 121, 171–81.

Bronen, R.A., Cheung, G., 1991. Relationship of hippocampus and amygdala to coronal MRI landmarks. Magn. Reson. Imaging 9, 449–457.

Buckner, R.L., Snyder, A.Z., Shannon, B.J., Gina, L., Sachs, R., Fotenos, A.F., Sheline, Y.I., Klunk, W.E., Mathis, C.A., Morris, J.C., Mintun, M.A., 2005. Molecular, structural, and functional characterization of Alzheimer's disease: evidence for a relationship between default activity, amyloid, and memory. J. Neurosci. 25, 7709–17.

Burgess, N., Maguire, E.A., O'Keefe, J., 2002. The Human Hippocampus and Spatial and Episodic Memory. Neuron 35, 625–641.

Burke, S., Hartzell, A., Lister, J., Hoang, L., Barnes, C.A., 2012. Layer V perirhinal cortical ensemble activity during object exploration: a comparison between young and aged rats. Hippocampus 22, 2080–2093.

Burke, S.N., Maurer, A.P., Nematollahi, S., Uprety, A., Wallace, J.L., Barnes, C.A., 2014. Advanced age dissociates dual functions of the perirhinal cortex. J. Neurosci. 34, 467–480.

Burke, S.N., Wallace, J.L., Hartzell, A.L., Nematollahi, S., Plange, K., Barnes, C.A., 2011. Age-associated deficits in pattern separation functions of the perirhinal cortex: a cross-species consensus. Behav Neurosci 125, 836–47.

Burwell, R., 2000. The parahippocampal region: corticocortical connectivity. Ann. N. Y. Acad. Sci. 911, 25–42.

Burwell, R.D., Amaral, D.G., 1998a. Cortical afferents of the perirhinal, postrhinal, and entorhinal cortices of the rat. J. Comp. Neurol. 398, 179–205.

Burwell, R.D., Amaral, D.G., 1998b. Perirhinal and postrhinal cortices of the rat: interconnectivity and connections with the entorhinal cortex. J. Comp. Neurol. 391, 293–321.

Carr, V.A., Rissman, J., Wagner, A.D., 2010. Imaging the Human Medial Temporal Lobe with High-Resolution fMRI. Neuron 65, 298–308.

Chadwick, M.J., Hassabis, D., Maguire, E.A., 2011. Decoding overlapping memories in the medial temporal lobes using high-resolution fMRI. Learn. Mem. 18, 742–746.

Chang, C.-C., Lin, C.-J., 2011. LIBSVM: A library for support vector machines. Trans. Intell. Syst. Technol. 2, 27:1–27:27.

Colgin, L., Moser, E.I., Moser, M.-B., 2008. Understanding memory through hippocampal remapping. Trends Neurosci 31, 469–77.

Coutanche, M.N., 2013. Distinguishing multi-voxel patterns and mean activation: Why, how, and what does it tell us? Cogn. Affect. Behav. Neurosci. 13, 667–73.

Dale, A., 1999. Optimal experimental design for event-related fMRI. Hum. Brain Mapp. 8, 109–14.

Das, S.R., Pluta, J.B., Mancuso, L., Kliot, D., Yushkevich, P.A., Wolk, D.A., 2015. Anterior and posterior MTL networks in aging and MCI. Neurobiol. Aging 36, 141–50.

Daugherty, A.M., Bender, A.R., Raz, N., Ofen, N., 2015. Age Differences in Hippocampal Subfield Volumes from Childhood to Late Adulthood. Hippocampus.

Davachi, L., Mitchell, J.P., Wagner, A.D., 2003. Multiple routes to memory: Distinct medial temporal lobe processes build item and source memories. Proc. Natl. Acad. Sci. U. S. A. 100, 2157–2162.

Davis, T., Poldrack, R.A., 2013. Measuring neural representations with fMRI: practices and pitfalls. Ann. N. Y. Acad. Sci. 1296, 108–134.

de Curtis, M., Paré, D., 2004. The rhinal cortices: a wall of inhibition between the neocortex and the hippocampus. Prog. Neurobiol. 74, 101–110.

de Flores, R., Joie, L.R., Chételat, G., 2015a. Structural imaging of hippocampal subfields in healthy aging and Alzheimer's disease. Neuroscience.

de Flores, R., Joie, R., Landeau, B., Perrotin, A., Mézenge, F., de Sayette, V., Eustache, F., Desgranges, B., Chételat, G., 2015b. Effects of age and Alzheimer's disease on hippocampal subfields: comparison between manual and FreeSurfer volumetry. 36, 463–74.

Deshmukh, S.S., Knierim, J.J., 2011. Representation of Non-Spatial and Spatial Information in the Lateral Entorhinal Cortex. Front. Behav. Neurosci. 5.

Diamantaki, M., Frey, M., Berens, P., Patricia, P.-F., Burgalossi, A., 2016. Sparse activity of identified dentate granule cells during spatial exploration. eLife 5.

Diana, R.A., Yonelinas, A.P., Ranganath, C., 2012. Adaptation to cognitive context and item information in the medial temporal lobes. Neuropsychologia 50, 3062–9.

Diana, R.A., Yonelinas, A.P., Ranganath, C., 2007. Imaging recollection and familiarity in the medial temporal lobe: a three-component model. Trends Cogn Sci 11, 379386.

Dice, L.R., 1945. Measures of the Amount of Ecologic Association Between Species. Ecology 26, 297–302.

Dickerson, B., Salat, D., Greve, D., Chua, E., E, R.-G., Rentz, D., Bertram, L., Mullin, K., Tanzi, R., Blacker, D., Albert, Sperling, R., 2005. Increased hippocampal activation in mild cognitive impairment compared to normal aging and AD. Neurology 65, 404–411.

Dickerson, B.C., Eichenbaum, H., 2009. The Episodic Memory System: Neurocircuitry and Disorders. Neuropsychopharmacology 35, 86–104.

Dickerson, B.C., Feczko, E., Augustinack, J.C., Pacheco, J., Morris, J.C., Fischl, B., Buckner, R.L., 2009. Differential effects of aging and Alzheimer's disease on medial temporal lobe cortical thickness and surface area. Neurobiol. Aging 30, 432–440.

Dickerson, B.C., Salat, D.H., Bates, J.F., Atiya, M., Killiany, R.J., Greve, D.N., Dale, A.M., Stern, C.E., Blacker, D., Albert, M.S., Sperling, R.A., 2004. Medial temporal lobe function and structure in mild cognitive impairment. 56, 27–35.

Dickerson, B.C., Sperling, R.A., 2008. Functional abnormalities of the medial temporal lobe memory system in mild cognitive impairment and Alzheimer's disease: insights from functional MRI studies. Neuropsychologia 46, 1624–35.

Didic, M., Barbeau, E.J., Felician, O., Tramoni, E., Guedj, E., Poncet, M., Ceccaldi, M., 2011. Which memory system is impaired first in Alzheimer's disease? J Alzheimers Dis 27, 11–22. doi:10.3233/jad-2011-110557

Ding, S., Van Hoesen, G.W., 2015. Organization and detailed parcellation of human hippocampal head and body regions based on a combined analysis of Cyto- and chemoarchitecture. J Comp Neurol 523, 2233–2253.

Ding, S.-L., 2013. Comparative anatomy of the prosubiculum, subiculum, presubiculum, postsubiculum, and parasubiculum in human, monkey, and rodent. J. Comp. Neurol. 521, 4145–4162.

Ding, S.-L., Royall, J.J., Sunkin, S.M., Ng, L., Facer, B.A.C., Lesnar, P., Guillozet-Bongaarts, A., McMurray, B., Szafer, A., Dolbeare, T.A., Stevens, A., Tirrell, L., Benner, T., Caldejon, S., Dalley, R.A., Dee, N., Lau, C., Nyhus, J., Reding, M., Riley, Z.L., Sandman, D., Shen, E., van der Kouwe, A., Varjabedian, A., Write, M., Zollei, L., Dang, C., Knowles, J.A., Koch, C., Phillips, J.W., Sestan, N., Wohnoutka, P., Zielke, H.R., Hohmann, J.G., Jones, A.R., Bernard, A., Hawrylycz, M.J., Hof, P.R., Fischl, B., Lein, E.S., 2016. Comprehensive cellular-resolution atlas of the adult human brain. J. Comp. Neurol. 524, 3127–3481.

Ding, S.-L., Van Hoesen, G.W., 2010. Borders, extent, and topography of human perirhinal cortex as revealed using multiple modern neuroanatomical and pathological markers. Hum. Brain Mapp. 31, 1359–1379.

Ding, S.-L., Van Hoesen, G.W., Cassell, M.D., Poremba, A., 2009. Parcellation of human temporal polar cortex: A combined analysis of multiple cytoarchitectonic, chemoarchitectonic, and pathological markers. J. Comp. Neurol. 514, 595–623.

Du, A.-T., Schuff, N., Kramer, J.H., Rosen, H.J., Maria, G.-T., Rankin, K., Miller, B.L., Weiner, M.W., 2007. Different regional patterns of cortical thinning in Alzheimer's disease and frontotemporal dementia 130, 1159–1166.

Duncan, K., Tompary, A., Davachi, L., 2014. Associative Encoding and Retrieval Are Predicted by Functional Connectivity in Distinct Hippocampal Area CA1 Pathways. J. Neurosci. 34, 11188–98.

Duvernoy, H.M., Cattin, F., Risold, P.-Y., Vannson, J.L., Gaudron, M., 2013. The human hippocampus: functional anatomy, vascularization, and serial sections with MRI. Springer.

Eichenbaum, H., Sauvage, M., Fortin, N., Komorowski, R., Lipton, P., 2012. Towards a functional organization of episodic memory in the medial temporal lobe. Neurosci. Biobehav. Rev. 36, 1597–608.

Eichenbaum, H., Yonelinas, A.P., Ranganath, C., 2007. The Medial Temporal Lobe and Recognition Memory 30, 123–152.

Ekstrom, A.D., Bazih, A.J., Suthana, N.A., Al-Hakim, R., Ogura, K., Zeineh, M.M., Burggren, A.C., Bookheimer, S.Y., 2009. Advances in high-resolution imaging and computational unfolding of the human hippocampus. NeuroImage 47, 42–49.

Ekstrom, A.D., Bookheimer, S.Y., 2007. Spatial and temporal episodic memory retrieval recruit dissociable functional networks in the human brain. Learn. Mem. 14, 645–54.

Ekstrom, A.D., Kahana, M.J., Caplan, J.B., Fields, T.A., Isham, E.A., Newman, E.L., Fried, I., 2003. Cellular networks underlying human spatial navigation. Nature 425, 184–188.

Epstein, R., Kanwisher, N., 1998. A cortical representation of the local visual environment. Nature 392, 598–601.

Epstein, R.A., 2008. Parahippocampal and retrosplenial contributions to human spatial navigation. Trends Cogn. Sci. 12, 388–396.

Fair, D.A., Schlaggar, B.L., Cohen B.A., A.L., Miezin, F.M., Dosenbach, N.U.F., Wenger, K.K., Fox, M.D., Snyder, A.Z., Raichle, M.E., Petersen, S.E., 2007. A method for using blocked and event related fMRI data to study "resting state" functional connectivity. NeuroImage 35, 396–405.

Feczko, E., Augustinack, J.C., Fischl, B., Dickerson, B.C., 2009. An MRI-based method for measuring volume, thickness and surface area of entorhinal, perirhinal, and posterior parahippocampal cortex. Neurobiol. Aging 30, 420–431.

Fidalgo, C.O., Changoor, A.T., Elizabeth, P.-G., Lee, A.C., Barense, M.D., 2016. Early cognitive decline in older adults better predicts object than scene recognition performance. Hippocampus 26, 1579–1592.

Fjell, A.M., Walhovd, K.B., 2010. Structural brain changes in aging: courses, causes and cognitive consequences. Rev. Neurosci. 21, 187–221.

Fox, M.D., Raichle, M.E., 2007. Spontaneous fluctuations in brain activity observed with functional magnetic resonance imaging. Nat. Rev. Neurosci. 8, 700–711.

Fox, M.D., Snyder, A.Z., Zacks, J.M., Raichle, M.E., 2006. Coherent spontaneous activity accounts for trial-to-trial variability in human evoked brain responses. Nat. Neurosci. 9, 23–25.

Fraser, M.A., Shaw, M.E., Cherbuin, N., 2015. A systematic review and meta-analysis of longitudinal hippocampal atrophy in healthy human ageing. NeuroImage.

Frisoni, G.B., Jack, C.R., Bocchetta, M., Bauer, C., Frederiksen, K.S., Liu, Y., Preboske, G., Swihart, T., Blair, M., Cavedo, E., Grothe, M.J., Lanfredi, M., Martinez, O., Nishikawa, M., Portegies, M., Stoub, T., Ward, C., Apostolova, L.G., Ganzola, R., Wolf, D., Barkhof, F., Bartzokis, G., DeCarli, C., Csernansky, J.G., Detoledo-Morrell, L., Geerlings, M.I., Kaye, J., Killiany, R.J., Lehericy, S., Matsuda, H., O'Brien, J., Silbert, L.C., Scheltens, P., Soininen, H., Teipel, S., Waldemar, G., Fellgiebel, A., Barnes, J., Firbank, M., Gerritsen, L., Henneman, W., Malykhin, N. V., Pruessner, J.C., Wang, L., Watson, C., Wolf, H., Deleon, M., Pantel, J., Ferrari, C., Bosco, P., Pasqualetti, P., Duchesne, S., Duvernoy, H.M., Boccardi, M., Albert, M.S., Bennet, D., Camicioli, R., Collins, D.L., Dubois, B., Hampel, H., Denheijer, T., Hock, C., Jagust, W., Launer, L., Maller, J.J., Mueller, S., Sachdev, P., Simmons, A., Thompson, P.M., Visser, P.J., Wahlund, L.O., Weiner, M.W., Winblad, B., 2015. The EADC-ADNI harmonized protocol for manual hippocampal segmentation on magnetic resonance: Evidence of validity. Alzheimers Dement. 11, 111–125.

Furtak, S.C., Wei, S.-M.M., Agster, K.L., Burwell, R.D., 2007. Functional neuroanatomy of the parahippocampal region in the rat: the perirhinal and postrhinal cortices. Hippocampus 17, 709–22.

Garrido, L., Maryam, V.-P., Nakayama, K., Wilmer, J., 2013. The consequences of subtracting the mean pattern in fMRI multivariate correlation analyses. Front. Neurosci. 7.

Gorbach, T., Pudas, S., Lundquist, A., Orädd, G., Josefsson, M., Salami, A., de Luna, X., Nyberg, L., 2016. Longitudinal association between hippocampus atrophy and episodic-memory decline. Neurobiol. Aging.

Goubran, M., Rudko, D.A., Santyr, B., Gati, J., Szekeres, T., Peters, T.M., Khan, A.R., 2014. In vivo normative atlas of the hippocampal subfields using multi-echo susceptibility imaging at 7 Tesla 35, 3588–3601.

Grady, C., 2012. The cognitive neuroscience of ageing. Nat. Rev. Neurosci.

Grady, C., Craik, F., 2000. Changes in memory processing with age. Curr. Opin. Neurobiol. 10, 224–31.

Greve, D.N., Fischl, B., 2009. Accurate and robust brain image alignment using boundary-based registration. NeuroImage 48, 63–72.

Grill-Spector, K., Henson, R., Martin, A., 2006. Repetition and the brain: neural models of stimulus-specific effects. Trends Cogn. Sci. 10, 14–23.

Hafting, T., Fyhn, M., Molden, S., Moser, M.-B.B., Moser, E.I., 2005. Microstructure of a spatial map in the entorhinal cortex. Nature 436, 801–6.

Hanke, M., Halchenko, Y.O., Sederberg, P.B., Hanson, S.J., Haxby, J.V., Pollmann, S., 2009. PyMVPA: A python toolbox for multivariate pattern analysis of fMRI data. Neuroinformatics 7, 37–53.

Hartley, T., Lever, C., Burgess, N., O'Keefe, J., 2014. Space in the brain: how the hippocampal formation supports spatial cognition. Philos. Trans. R. Soc. B Biol. Sci. 369.

Haynes, J.-D., 2015. A Primer on Pattern-Based Approaches to fMRI: Principles, Pitfalls, and Perspectives. Neuron 87, 257–270.

Haynes, J.-D., Rees, G., 2006. Decoding mental states from brain activity in humans. Nat. Rev. Neurosci. 7, 523–534.

Hedden, T., Gabrieli, J.D., 2004. Insights into the ageing mind: a view from cognitive neuroscience. Nat. Rev. Neurosci. 5, 87–96.

Hedden, T., Schultz, A.P., Rieckmann, A., Mormino, E.C., Johnson, K.A., Sperling, R.A., Buckner, R.L., 2016. Multiple Brain Markers are Linked to Age-Related Variation in Cognition. Cereb. Cortex 26, 1388–1400.

Hodgetts, C.J., Voets, N.L., Thomas, A.G., Clare, S., Lawrence, A.D., Graham, K.S., 2017. Ultra-high-field fMRI reveals a role for the subiculum in scene perceptual discrimination. J. Neurosci. 3225–16.

Holden, H.M., Gilbert, P.E., 2012. Less efficient pattern separation may contribute to age-related spatial memory deficits. Front. Aging Neurosci 4.

Holden, H.M., Hoebel, C., Loftis, K., Gilbert, P.E., 2012. Spatial pattern separation in cognitively normal young and older adults. Hippocampus 22, 1826–1832.

Hölscher, C., Rolls, E.T., 2002. Perirhinal cortex neuronal activity is actively related to working memory in the macaque. Neural Plast. 9, 41–51.

Huang, Y., Coupland, N.J., Lebel, R.M., Carter, R., Seres, P., Wilman, A.H., Malykhin, N. V., 2013. Structural Changes in Hippocampal Subfields in Major Depressive Disorder: A High-Field Magnetic Resonance Imaging Study. Biol. Psychiatry 74, 62–68.

Huijbers, W., Mormino, E.C., Schultz, A.P., Wigman, S., Ward, A.M., Larvie, M., Amariglio, R.E., Marshall, G.A., Rentz, D.M., Johnson, K.A., Sperling, R.A., 2015. Amyloid-β deposition in mild cognitive impairment is associated with increased hippocampal activity, atrophy and clinical progression. Brain 138, 1023–1035.

Hyman, B.T., Phelps, C.H., Beach, T.G., Bigio, E.H., Cairns, N.J., Carrillo, M.C., Dickson, D.W., Duyckaerts, C., Frosch, M.P., Masliah, E., Mirra, S.S., Nelson, P.T., Schneider, J.A., Thal, D., Thies, B., Trojanowski, J.Q., Vinters, H.V., Montine, T.J., 2012. National Institute on Aging–Alzheimer's Association guidelines for the neuropathologic assessment of Alzheimer's disease. Alzheimers Dement. 8, 1–13.

Iglesias, J.E., Augustinack, J.C., Nguyen, K., Player, C.M., Player, A., Wright, M., Roy, N., Frosch, M.P., McKee, A.C., Wald, L.L., Fischl, B., Van Leemput, K., 2015. A computational atlas of the hippocampal formation using ex vivo, ultra-high resolution MRI: Application to adaptive segmentation of in vivo MRI. NeuroImage 115, 117–137.

Insausti, R., Amaral, D.G., 2012. Hippocampal Formation. in The Human Nervous System. Elsevier Inc., pp 896-942.

Insausti, R., Juottonen, K., Soininen, H., Insausti, A.M., Partanen, K., Vainio, P., Laakso, M.P., Pitkänen, A., 1998. MR volumetric analysis of the human entorhinal, perirhinal, and temporopolar cortices. Am. J. Neuroradiol. 19, 659–71.

Ishizuka, N., Weber, J., Amaral, D.G., 1990. Organization of intrahippocampal projections originating from CA3 pyramidal cells in the rat. J. Comp. Neurol. 295, 580–623.

Jack, C., Petersen, R., Xu, Y., PC, O., Smith, G., 1999. Prediction of AD with MRI-based hippocampal volume in mild cognitive impairment. Neurology.

Jack, C.R., Holtzman, D.M., 2013. Biomarker modeling of Alzheimer's disease. Neuron 80, 1347–58.

Jack, C.R., Knopman, D.S., Jagust, W.J., Petersen, R.C., Weiner, M.W., Aisen, P.S., Shaw, L.M., Vemuri, P., Wiste, H.J., Weigand, S.D., 2013. Tracking pathophysiological processes in Alzheimer's disease: an updated hypothetical model of dynamic biomarkers. Lancet Neurol. 12, 207–216.

Jagust, W., 2013. Vulnerable Neural Systems and the Borderland of Brain Aging and Neurodegeneration. Neuron 77, 219–234.

Jagust, W., Landau, Shaw, L., Trojanowski, J., 2009. Relationships between biomarkers in aging and dementia. Neurology.

Jimura, K., Poldrack, R.A., 2012. Analyses of regional-average activation and multivoxel pattern information tell complementary stories. Neuropsychologia 50, 544–552.

Johnstone, T., Walsh, K.S., Greischar, L.L., Alexander, A.L., Fox, A.S., Davidson, R.J., Oakes, T.R., 2006. Motion correction and the use of motion covariates in multiple-subject fMRI analysis. Hum. Brain Mapp.

Joie, R., Landeau, B., Perrotin, A., Bejanin, A., Egret, S., Pélerin, A., Mézenge, F., Belliard, S., de Sayette, V., Eustache, F., Desgranges, B., Chételat, G., 2014. Intrinsic Connectivity Identifies the Hippocampus as a Main Crossroad between Alzheimer's and Semantic Dementia-Targeted Networks. Neuron 81, 1417–1428.

Joie, R., Perrotin, A., de Sayette, V., Egret, S., Doeuvre, L., Belliard, S., Eustache, F., Desgranges, B., Chételat, G., 2013. Hippocampal subfield volumetry in mild cognitive impairment, Alzheimer's disease and semantic dementia. 3, 155–62.

Jung, M.W., McNaughton, B.L., 1993. Spatial selectivity of unit activity in the hippocampal granular layer. Hippocampus 3, 165–182.

Kahn, I., R, A.-H., Jessica, Vincent, J.L., Snyder, A.Z., Buckner, R.L., 2008. Distinct Cortical Anatomy Linked to Subregions of the Medial Temporal Lobe Revealed by Intrinsic Functional Connectivity. J. Neurophysiol. 100, 129–139.

Kajiwara, R., Wouterlood, F.G., Sah, A., Boekel, A.J., Baks-te Bulte, L.T.G., Witter, M.P., 2008. Convergence of entorhinal and CA3 inputs onto pyramidal neurons and interneurons in hippocampal area CA1—An anatomical study in the rat. Hippocampus 18, 266–280.

Kalus, P., Slotboom, J., Gallinat, J., Mahlberg, R., Katja, C.-L., Wiest, R., Nyffeler, T., Buri, C., Federspiel, A., Kunz, D., 2006. Examining the gateway to the limbic system with diffusion tensor imaging: the perforant pathway in dementia. NeuroImage 30, 713–720.

Keene, C.S., Bladon, J., Sam, M., Liu, C.D., Joseph, O., Eichenbaum, H., 2016. Complementary Functional Organization of Neuronal Activity Patterns in the Perirhinal, Lateral Entorhinal, and Medial Entorhinal Cortices. J Neurosci 36, 3660–3675.

Kent, M, H.-E., Saksida, L.M., Bussey, T.J., 2016. The representational–hierarchical view of pattern separation: Not just hippocampus, not just space, not just memory? Neurobiol Learn Mem 129, 99–106.

Kerchner, G., Hess, C., KE, H.-R., Xu, D., Rabinovici, G., Kelley, D., Vigneron, D., Nelson, S., Miller, B., 2010. Hippocampal CA1 apical neuropil atrophy in mild Alzheimer disease visualized with 7-T MRI. Neurology 75, 1381–1387.

Kerchner, G.A., Deutsch, G.K., Zeineh, M.M., Dougherty, R.F., Saranathan, M., Rutt, B.K., 2012. Hippocampal CA1 apical neuropil atrophy and memory performance in Alzheimer's disease. NeuroImage 63, 194–202.

Kerr, K.M., Agster, K.L., Furtak, S.C., Burwell, R.D., 2007. Functional neuroanatomy of the parahippocampal region: The lateral and medial entorhinal areas. Hippocampus 17, 697–708.

Kesner, R.P., Rolls, E.T., 2015. A computational theory of hippocampal function, and tests of the theory: new developments. Neurosci. Biobehav. Rev. 48, 92–147.

Khan, U.A., Liu, L., Provenzano, F.A., Berman, D.E., aci, C.P., Sloan, R., Mayeux, R., Duff, K.E., Small, S.A., 2014. Molecular drivers and cortical spread of lateral entorhinal cortex dysfunction in preclinical Alzheimer's disease. Nat Neurosci 17, 304–311.

Kirwan, C., Stark, C., 2007. Overcoming interference: An fMRI investigation of pattern separation in the medial temporal lobe. Learn. Mem. 14, 625–633.

Kitamura, T., Sun, C., Martin, J., Kitch, L.J., Schnitzer, M.J., Tonegawa, S., 2015. Entorhinal Cortical Ocean Cells Encode Specific Contexts and Drive Context-Specific Fear Memory. Neuron 87, 1317–1331.

Kivisaari, S.L., Probst, A., Taylor, K.I., 2013. The Perirhinal, Entorhinal, and Parahippocampal Cortices and Hippocampus: An Overview of Functional Anatomy and Protocol for Their Segmentation in MR Images, in: fMRI. Springer Berlin Heidelberg, Berlin, Heidelberg, pp. 239–267.

Knierim, J.J., Neunuebel, J.P., 2016. Tracking the flow of hippocampal computation: Pattern separation, pattern completion, and attractor dynamics. Neurobiol. Learn. Mem. 129, 38–49.

Knierim, J.J., Neunuebel, J.P., Deshmukh, S.S., 2014. Functional correlates of the lateral and medial entorhinal cortex: objects, path integration and local–global reference frames. Philos Trans R Soc Lond B Biol Sci 369, 20130369.

Kravitz, D.J., Saleem, K.S., Baker, C.I., Mishkin, M., 2011. A new neural framework for visuospatial processing. Nat. Rev. Neurosci. 12, 217–30.

Krekelberg, B., Boynton, G.M., van Wezel, R.J., 2006. Adaptation: from single cells to BOLD signals. Trends Neurosci. 29, 250256.

Kriegeskorte, N., Mur, M., Bandettini, P.A., 2008. Representational similarity analysis - connecting the branches of systems neuroscience. Front. Syst. Neurosci. 2, 4.

Krumm, S., Kivisaari, S.L., Probst, A., Monsch, A.U., Reinhardt, J., Ulmer, S., Stippich, C., Kressig, R.W., Taylor, K.I., 2016. Cortical thinning of parahippocampal subregions in very early Alzheimer's disease. Neurobiol. Aging 38, 188–196.

Kuijf, H.J., 2013. Image Processing Techniques for Quantification and Assessment of Brain MRI. Utrecht University.

Kumaran, D., Maguire, E.A., 2009. Novelty signals: a window into hippocampal information processing. Trends Cogn. Sci. 13, 47–54.

Kyle, C.T., Stokes, J.D., Lieberman, J.S., Hassan, A.S., Ekstrom, A.D., 2015. Successful retrieval of competing spatial environments in humans involves hippocampal pattern separation mechanisms. Elife 4.

La Joie, R., Fouquet, M., Mézenge, F., Landeau, B., Villain, N., Mevel, K., Pélerin, A., Eustache, F., Desgranges, B., Chételat, G., 2010. Differential effect of age on hippocampal subfields assessed using a new high-resolution 3T MR sequence. NeuroImage 53, 506–514.

Lacy, J.W., Stark, C., 2012. Intrinsic functional connectivity of the human medial temporal lobe suggests a distinction between adjacent MTL cortices and hippocampus. Hippocampus 22, 2290–2302.

Lacy, J.W., Yassa, M.A., Stark, S.M., Muftuler, T.L., Stark, C., 2011. Distinct pattern separation related transfer functions in human CA3/dentate and CA1 revealed using high-resolution fMRI and variable mnemonic similarity. Learn. Mem. 18, 15–18.

Lavenex, P., Amaral, D., 2000. Hippocampal-neocortical interaction: a hierarchy of associativity. Hippocampus 10, 420–30.

Leal, S.L., Landau, S.M., Bell, R.K., Jagust, W.J., 2017. Hippocampal activation is associated with longitudinal amyloid accumulation and cognitive decline. eLife 6, e22978.

Leal, S.L., Yassa, M.A., 2015. Neurocognitive Aging and the Hippocampus across Species. Trends Neurosci. 38, 800–812.

Lee, A.C., Buckley, M.J., Pegman, S.J., Spiers, H., Scahill, V.L., Gaffan, D., Bussey, T.J., Davies, R., Kapur, N., Hodges, J.R., Graham, K.S., 2005a. Specialization in the medial temporal lobe for processing of objects and scenes. Hippocampus 15, 782–97.

Lee, A.C., Bussey, T.J., Murray, E.A., Saksida, L.M., Epstein, R.A., Kapur, N., Hodges, J.R., Graham, K.S., 2005b. Perceptual deficits in amnesia: challenging the medial temporal lobe "mnemonic" view. Neuropsychologia 43, 1–11.

Lee, H., Wang, C., Deshmukh, S.S., Knierim, J.J., 2015. Neural Population Evidence of Functional Heterogeneity along the CA3 Transverse Axis: Pattern Completion versus Pattern Separation. Neuron 87, 1093–1105.

Lee, J.K., Ekstrom, A.D., Ghetti, S., 2014. Volume of hippocampal subfields and episodic memory in childhood and adolescence. NeuroImage 94, 162–171.

Leutgeb, J.K., Leutgeb, S., Moser, M.-B., Moser, E.I., 2007. Pattern Separation in the Dentate Gyrus and CA3 of the Hippocampus. Science 315, 961–966.

Li, X.-G., Somogyi, P., Ylinen, A., Buzsáki, G., 1994. The hippocampal CA3 network: An in vivo intracellular labeling study. J. Comp. Neurol. 339, 181–208.

Libby, L.A., Ekstrom, A.D., Ragland, D.J., Ranganath, C., 2012. Differential Connectivity of Perirhinal and Parahippocampal Cortices within Human Hippocampal Subregions Revealed by High-Resolution Functional Imaging. J. Neurosci. 32, 6550–6560.

Libby, L.A., Hannula, D.E., Ranganath, C., 2014. Medial Temporal Lobe Coding of Item and Spatial Information during Relational Binding in Working Memory. J. Neurosci. 34, 14233–14242. doi:10.1523/JNEUROSCI.0655-14.2014

Lim, C., Mufson, E.J., Kordower, J.H., Blume, H.W., Madsen, J.R., Saper, C.B., 1997. Connections of the hippocampal formation in humans: II. The endfolial fiber pathway. J. Comp. Neurol. 385.

Litman, L., Awipi, T., Davachi, L., 2009. Category-specificity in the human medial temporal lobe cortex. Hippocampus 19, 308–19.

Liu, K.Y., Gould, R.L., Coulson, M.C., Ward, E.V., Howard, R.J., 2016. Tests of pattern separation and pattern completion in humans—A systematic review. Hippocampus 26, 705–717.

Liu, L., Drouet, V., Wu, J.W., Witter, M.P., Small, S.A., Clelland, C., Duff, K., 2012. Trans-synaptic spread of tau pathology in vivo. Plos ONE 7, e31302.

Maass, A., Berron, D., Libby, L.A., Ranganath, C., Düzel, E., 2015. Functional subregions of the human entorhinal cortex. eLife 4, 1–20.

Maass, A., Schütze, H., Speck, O., Yonelinas, A.P., Tempelmann, C., Heinze, H.-J., Berron, D., Cardenas-Blanco, A., Brodersen, K.H., Enno Stephan, K., Düzel, E., 2014. Laminar activity in the hippocampus and entorhinal cortex related to novelty and episodic encoding. Nat. Commun. 5, 5547.

Maguire, E.A., Hassabis, D., 2011. Role of the hippocampus in imagination and future thinking. Proc. Natl. Acad. Sci. U. S. A. 108, E39–E39.

Mai, J.K., Majtanik, M., Paxinos, G., 2015. Atlas of the human brain. Elsevier, Oxford.

Malykhin, N. V., Lebel, R.M., Coupland, N.J., Wilman, A.H., Carter, R., 2010. In vivo quantification of hippocampal subfields using 4.7 T fast spin echo imaging. NeuroImage 49, 1224–1230. d

Marr, D., 1971. Simple memory: a theory for archicortex. Philos. Trans. R. Soc. Lond. B. Biol. Sci. 262, 23–81.

Maruszak, A., Thuret, S., 2014. Why looking at the whole hippocampus is not enough—a critical role for anteroposterior axis, subfield and activation analyses to enhance predictive value of hippocampal changes for Alzheimer's disease diagnosis. Front. Cell. Neurosci. 8.

McClelland, J.L., McNaughton, B.L., O'Reilly, R.C., 1995. Why there are complementary learning systems in the hippocampus and neocortex: insights from the successes and failures of connectionist models of learning and memory. Psychol. Rev. 102, 419–457.

McHugh, T.J., Jones, M.W., Quinn, J.J., Balthasar, N., Coppari, R., Elmquist, J.K., Lowell, B.B., Fanselow, M.S., Wilson, M.A., Tonegawa, S., 2007. Dentate gyrus NMDA receptors mediate rapid pattern separation in the hippocampal network. Science 317, 94–99.

McNaughton, B.L., Morris, R.G.M., 1987. Hippocampal synaptic enhancement and information storage within a distributed memory system. Trends Neurosci. 10, 408–415.

Miller, E., Desimone, R., 1994. Parallel neuronal mechanisms for short-term memory. Science 263, 520–2.

Miller, M.I., Ratnanather, T.J., Tward, D.J., Brown, T., Lee, D.S., Ketcha, M., Mori, K., Wang, M.-C., Mori, S., Albert, M.S., Younes, L., Team, B., 2015. Network Neurodegeneration in Alzheimer's Disease via MRI Based Shape Diffeomorphometry and High-Field Atlasing. Front. Bioeng. Biotechnol. 3, 54.

Mishkin, M., Ungerleider, L.G., Macko, K.A., 1983. Object vision and spatial vision: two cortical pathways. Trends Neurosci. 6, 414–417.

Morris, J., Roe, C., Xiong, C., Fagan, A., 2010. APOE predicts amyloid-beta but not tau Alzheimer pathology in cognitively normal aging. Ann. Neurol.

Morris, M., Maeda, S., Vossel, K., Mucke, L., 2011. The many faces of tau. Neuron.

Moser, E.I., Moser, M.-B., 2013. Grid Cells and Neural Coding in High-End Cortices. Neuron 80, 765–774.

Mueller, S.G., Stables, L., Du, A.T., Schuff, N., Truran, D., Cashdollar, N., Weiner, M.W., 2007. Measurement of hippocampal subfields and age-related changes with high resolution MRI at 4T. Neurobiol. Aging 28, 719–726.

Mueller, S.G., Weiner, M.W., 2009. Selective effect of age, Apo e4, and Alzheimer's disease on hippocampal subfields. Hippocampus 19, 558–64.

Mumford, J.A., Turner, B.O., Ashby, G.F., Poldrack, R.A., 2012. Deconvolving BOLD activation in event-related designs for multivoxel pattern classification analyses. NeuroImage 59.

Mur, M., Bandettini, P.A., Kriegeskorte, N., 2009. Revealing representational content with pattern-information fMRI—an introductory guide. Soc. Cogn. Affect. Neurosci. 4, 101–109.

Naber, P.A., Lopes da Silva, F.H., Witter, M.P., 2001a. Reciprocal connections between the entorhinal cortex and hippocampal fields CA1 and the subiculum are in register with the projections from CA1 to the subiculum. Hippocampus 11, 99–104.

Naber, P.A., Witter, M.P., Lopes da Silva, F.H., 2001b. Evidence for a direct projection from the postrhinal cortex to the subiculum in the rat. Hippocampus 11, 105–117.

Naber, P.A., Witter, M.P., Lopez da Silva, F.H., 1999. Perirhinal cortex input to the hippocampus in the rat: evidence for parallel pathways, both direct and indirect. A combined physiological and anatomical study. Eur. J. Neurosci. 11, 4119–4133.

Nakamura, N.H., Flasbeck, V., Maingret, N., Kitsukawa, T., Sauvage, M.M., 2013. Proximodistal Segregation of Nonspatial Information in CA3: Preferential Recruitment of a Proximal CA3-Distal CA1 Network in Nonspatial Recognition Memory. J. Neurosci. 33, 11506–11514.

Nakashiba, T., Cushman, J.D., Pelkey, K.A., Renaudineau, S., Buhl, D.L., McHugh, T.J., Barrera, V.R., Chittajallu, R., Iwamoto, K.S., McBain, C.J., Fanselow, M.S., Tonegawa, S., 2012. Young Dentate Granule Cells Mediate Pattern Separation, whereas Old Granule Cells Facilitate Pattern Completion. Cell 149, 188–201.

Nelson, P.T., Braak, H., Markesbery, W.R., 2009. Neuropathology and Cognitive Impairment in Alzheimer Disease: A Complex but Coherent Relationship 68, 1.

Neunuebel, J.P., Knierim, J.J., 2014. CA3 Retrieves Coherent Representations from Degraded Input: Direct Evidence for CA3 Pattern Completion and Dentate Gyrus Pattern Separation. Neuron 81, 416–427. d

Neunuebel, J.P., Yoganarasimha, D., Rao, G., Knierim, J.J., 2013. Conflicts between Local and Global Spatial Frameworks Dissociate Neural Representations of the Lateral and Medial Entorhinal Cortex. J Neurosci 33, 9246–9258.

Nichols, T.E., Holmes, A.P., 2002. Nonparametric permutation tests for functional neuroimaging: A primer with examples. Hum. Brain Mapp. 15, 1–25. doi:10.1002/hbm.1058

Norman, K.A., O'Reilly, R.C., 2003. Modeling hippocampal and neocortical contributions to recognition memory: a complementary-learning-systems approach. Psychol. Rev. 110, 611–646.

Norman, K.A., Polyn, S.M., Detre, G.J., Haxby, J.V., 2006. Beyond mind-reading: multi-voxel pattern analysis of fMRI data. Trends Cogn. Sci. 10, 424430.

O'Brien, J., KM, O., PS, L., AN, D., Blacker, D., Dickerson, B., Sperling, R., 2010. Longitudinal fMRI in elderly reveals loss of hippocampal activation with clinical decline. Neurology 74, 1969–1976.

Ogawa, S., Lee, T., Kay, A., Tank, D., 1990. Brain magnetic resonance imaging with contrast dependent on blood oxygenation. Proc. Natl. Acad. Sci. U. S. A. 87, 9868–9872.

Oh, H., Madison, C., Haight, T.J., Markley, C., Jagust, W.J., 2012. Effects of age and -amyloid on cognitive changes in normal elderly people. Neurobiol. Aging 33, 2746–2755.

O'Keefe, J., 1976. Place units in the hippocampus of the freely moving rat. Exp Neurol 51, 78–109. doi:10.1016/0014-4886(76)90055-8

O'Keefe, J., Dostrovsky, J., 1971. The hippocampus as a spatial map. Preliminary evidence from unit activity in the freely-moving rat. Brain Res 34, 171–5.

Olsen, R.K., Palombo, D.J., Rabin, J.S., Levine, B., Ryan, J.D., Rosenbaum, R.S., 2013. Volumetric analysis of medial temporal lobe subregions in developmental amnesia using high-resolution magnetic resonance imaging. Hippocampus 23, 855–860.

Op de Beeck, H.P., 2010. Against hyperacuity in brain reading: Spatial smoothing does not hurt multivariate fMRI analyses? NeuroImage 49, 1943–1948.

O'Reilly, K.C., Gulden Dahl, A., Ulsaker Kruge, I., Witter, M.P., 2013. Subicular-parahippocampal projections revisited: development of a complex topography in the rat. J. Comp. Neurol. 521, 4284–4299.

O'Reilly, R.C., McClelland, J.L., 1994. Hippocampal conjunctive encoding, storage, and recall: avoiding a trade-off. Hippocampus 4, 661–682.

O'Shea, A., Cohen, R.A., Porges, E.C., Nissim, N.R., Woods, A.J., 2016. Cognitive Aging and the Hippocampus in Older Adults. Front. Aging Neurosci 8.

Palombo, D.J., Amaral, R.S.C., Olsen, R.K., Muller, D.J., Todd, R.M., Anderson, A.K., Levine, B., 2013. KIBRA Polymorphism Is Associated with Individual Differences in Hippocampal Subregions: Evidence from Anatomical Segmentation using High-Resolution MRI. J. Neurosci. 33, 13088–13093.

Parekh, M.B., Rutt, B.K., Purcell, R., Chen, Y., Zeineh, M.M., 2015. Ultra-high resolution in-vivo 7.0T structural imaging of the human hippocampus reveals the endfolial pathway. NeuroImage 112, 1–6.

Pereira, J.B., Cinta, V.-P., Ros, E., Palacios, E., Falcón, C., Bargalló, N., David, B.-F., Wahlund, L., Westman, E., Junque, C., 2014. Regional vulnerability of hippocampal subfields to aging measured by structural and diffusion MRI. Hippocampus 24, 403–414.

Pidgeon, L.M., Morcom, A.M., 2016. Cortical pattern separation and item-specific memory encoding. Neuropsychologia 85, 256–271.

Pohmann, R., Speck, O., Scheffler, K., 2016. Signal-to-noise ratio and MR tissue parameters in human brain imaging at 3, 7, and 9.4 tesla using current receive coil arrays. Magn. Reson. Med. 75, 801–809.

Poppenk, J.L., Evensmoen, H.R., Moscovitch, M., Nadel, L., 2013. Long-axis specialization of the human hippocampus. Trends Cogn. Sci. 17, 230–40.

Prasad, K.M.R., Patel, A.R., Muddasani, S., Sweeney, J., Keshavan, M.S., 2004. The Entorhinal Cortex in First-Episode Psychotic Disorders: A Structural Magnetic Resonance Imaging Study. Am. J. Psychiatry 161, 1612–1619.

Preston, A.R., Bornstein, A.M., Hutchinson, J.B., Gaare, M.E., Glover, G.H., Wagner, A.D., 2010. High-resolution fMRI of Content-sensitive Subsequent Memory Responses in Human Medial Temporal Lobe. J. Cogn. Neurosci. 22, 156–173.

Pruessner, J.C., Köhler, S., Crane, J., Pruessner, M., Lord, C., Byrne, A., Kabani, N., Collins, D.L., Evans, A.C., 2002. Volumetry of temporopolar, perirhinal, entorhinal and parahippocampal cortex from high-resolution MR images: considering the variability of the collateral sulcus. Cereb. Cortex 12, 1342–1353.

Ranganath, C., 2010. Binding Items and Contexts The Cognitive Neuroscience of Episodic Memory. Curr. Dir. Psychol. Sci. 19, 131–137.

Ranganath, C., Ritchey, M., 2012. Two cortical systems for memory-guided behaviour. Nat. Rev. Neurosci. 13, 713–26.

Raz, N., Lindenberger, U., Rodrigue, K.M., Kennedy, K.M., Head, D., Williamson, A., Dahle, C., Gerstorf, D., Acker, J.D., 2005. Regional Brain Changes in Aging Healthy Adults: General Trends, Individual Differences and Modifiers. Cereb. Cortex 15, 1676–1689.

Raz, N., Rodrigue, K.M., 2006. Differential aging of the brain: Patterns, cognitive correlates and modifiers. Neurosci. Biobehav. Rev. 30, 730–748.

Reagh, Z.M., Ho, H.D., Leal, S.L., Noche, J.A., Chun, A., Murray, E.A., Yassa, M.A., 2016. Greater loss of object than spatial mnemonic discrimination in aged adults. Hippocampus.

Reagh, Z.M., Yassa, M.A., 2014. Object and spatial mnemonic interference differentially engage lateral and medial entorhinal cortex in humans. Proc. Natl. Acad. Sci. U. S. A. 111, E4264–E4273.

Rentz, D.M., Rodriguez, M.A., Amariglio, R., Stern, Y., Sperling, R., Ferris, S., 2013. Promising developments in neuropsychological approaches for the detection of preclinical Alzheimer's disease: a selective review. Alzheimers Res. Ther. 5, 58.

Ritchey, M., Libby, L.A., Ranganath, C., 2015. Cortico-hippocampal systems involved in memory and cognition: the PMAT framework. Prog. Brain Res. 219, 45–64.

Rolls, E.T., Treves, A., 1994. Neural networks in the brain involved in memory and recall. Prog. Brain Res. 102, 335–341.

Rugg, M.D., Vilberg, K.L., 2013. Brain networks underlying episodic memory retrieval. Curr. Opin. Neurobiol. 23, 255–260.

Rusinek, H., Endo, Y., Santi, D.S., Frid, D., Tsui, -H W, Segal, S., Convit, A., de Leon, M., 2004. Atrophy rate in medial temporal lobe during progression of Alzheimer disease 63, 2354–2359.

Ryan, L., Cardoza, J.A., Barense, Kawa, K.H., J, W.-F., Arnold, W.T., Alexander, G.E., 2012. Age-related impairment in a complex object discrimination task that engages perirhinal cortex. Hippocampus 22, 1978–1989.

Sahay, A., Hen, R., 2007. Adult hippocampal neurogenesis in depression. Nat. Neurosci. 10, 1110–1115.

Sahay, A., Wilson, D.A., Hen, R., 2011. Pattern Separation: A Common Function for New Neurons in Hippocampus and Olfactory Bulb. Neuron 70, 582–588.

Salat, D.H., Buckner, R.L., Snyder, A.Z., Greve, D.N., Desikan, R., Busa, E., Morris, J.C., Dale, A.M., Fischl, B., 2004. Thinning of the Cerebral Cortex in Aging. Cereb. Cortex 14.

Sapountzis, P., Schluppeck, D., Bowtell, R., Peirce, J.W., 2010. A comparison of fMRI adaptation and multivariate pattern classification analysis in visual cortex. NeuroImage 49, 1632–40.

Sargolini, F., Fyhn, M., Hafting, T., L, M., Bruce, Witter, M.P., Moser, M.-B.B., Moser, E.I., 2006. Conjunctive representation of position, direction, and velocity in entorhinal cortex. Science 312, 758–62.

Sauvage, M., Nakamura, N., Beer, Z., 2013. Mapping memory function in the medial temporal lobe with the immediate-early gene Arc. Behav. Brain Res.

Schacter, D.L., Addis, D., Hassabis, D., Martin, V.C., Spreng, N.R., Szpunar, K.K., 2012. The Future of Memory: Remembering, Imagining, and the Brain. Neuron 76, 677–694.

Schröder, T., Haak, K.V., Jimenez, N.I., Beckmann, C.F., Doeller, C.F., 2015. Functional topography of the human entorhinal cortex. eLife 4.

Schultz, H., Sommer, T., Peters, J., 2015. The Role of the Human Entorhinal Cortex in a Representational Account of Memory. Front. Hum. Neurosci. 9.

Schultz, H., Sommer, T., Peters, J., 2012. Direct Evidence for Domain-Sensitive Functional Subregions in Human Entorhinal Cortex. J. Neurosci. 32, 4716–4723.

Sheldon, S., Levine, B., 2015. The medial temporal lobes distinguish between within-item and item-context relations during autobiographical memory retrieval. Hippocampus.

Shing, Y.L., Rodrigue, K.M., Kennedy, K.M., Fandakova, Y., Bodammer, N.C., Werkle-Bergner, M., Lindenberger, U., Raz, N., 2011. Hippocampal subfield volumes: age, vascular risk, and correlation with associative memory. Front. Aging Neurosci. 3, 2.

Shrout, P., Fleiss, J., 1979. Intraclass correlations: uses in assessing rater reliability. 86, 420–8.

Simić, G., Kostović, I., Winblad, B., Bogdanović, N., Simic, G., 1997. Volume and number of neurons of the human hippocampal formation in normal aging and Alzheimer's disease. J. Comp. Neurol. 379, 482–94.

Small, S.A., Chawla, M.K., Buonocore, M., Rapp, P.R., Barnes, C.A., 2004. Imaging correlates of brain function in monkeys and rats isolates a hippocampal subregion differentially vulnerable to aging. Proc. Natl. Acad. Sci. U. S. A. 101, 7181–7186.

Small, S.A., Schobel, S.A., Buxton, R.B., Witter, M.P., Barnes, C.A., 2011. A pathophysiological framework of hippocampal dysfunction in ageing and disease. Nat. Rev. Neurosci. 12, 585–601.

Small, S.A., Tsai, W., Robert, D., Mayeux, R., Stern, Y., 2002. Imaging hippocampal function across the human life span: Is memory decline normal or not? Ann. Neurol. 51, 290–295.

Smith, T., Adams, M., Gallagher, M., 2000. Circuit-specific alterations in hippocampal synaptophysin immunoreactivity predict spatial learning impairment in aged rats. J. Neurosci.

Squire, L.R., Stark, C., Clark, R.E., 2004. THE MEDIAL TEMPORAL LOBE* 27, 279–306.

Staresina, B.P., Cooper, E., Henson, R.N., 2013. Reversible Information Flow across the Medial Temporal Lobe: The Hippocampus Links Cortical Modules during Memory Retrieval. J. Neurosci. 33, 14184–14192.

Staresina, B.P., Duncan, K.D., Davachi, L., 2011. Perirhinal and Parahippocampal Cortices Differentially Contribute to Later Recollection of Object- and Scene-Related Event Details. J. Neurosci. 31, 8739–8747.

Stark, S.M., Stevenson, R., Wu, C., Rutledge, S., Stark, C.E., 2015. Stability of age-related deficits in the mnemonic similarity task across task variations. Behav. Neurosci. 129, 257–68.

Stark, S.M., Yassa, M.A., Lacy, J.W., Stark, C., 2013. A task to assess behavioral pattern separation (BPS) in humans: Data from healthy aging and mild cognitive impairment 51.

Stark, S.M., Yassa, M.A., Stark, C.E., 2010. Individual differences in spatial pattern separation performance associated with healthy aging in humans. Learn. Mem. 17, 284–8.

Steward, O., Scoville, S.A., 1976. Cells of origin of entorhinal cortical afferents to the hippocampus and fascia dentata of the rat. J. Comp. Neurol. 169, 347–370.

Stoub, T., Bulgakova, M., Leurgans, S., Bennett, D., 2005. MRI predictors of risk of incident Alzheimer disease A longitudinal study. Neurology.

Stucht, D., Danishad, A.K., Schulze, P., Godenschweger, F., Zaitsev, M., Speck, O., 2015. Highest Resolution In Vivo Human Brain MRI Using Prospective Motion Correction. Plos ONE 10, e0133921.

Suthana, N.A., Donix, M., Wozny, D.R., Bazih, A.J., Jones, M., Heidemann, R.M., Trampel, R., Ekstrom, A.D., Scharf, M., Knowlton, B.J., Turner, R., Bookheimer, S.Y., 2015. High-resolution 7T fMRI of Human Hippocampal Subfields during Associative Learning. J. Cogn. Neurosci. 27, 1194–1206.

Suzuki, W.A., Amaral, D.G., 1994. Perirhinal and parahippocampal cortices of the macaque monkey: cortical afferents. J. Comp. Neurol. 350, 497–533.

Swanson, L.W., Cowan, W.M., 1977. An autoradiographic study of the organization of the efferet connections of the hippocampal formation in the rat. J. Comp. Neurol. 172, 49–84.

Swanson, L.W., Köhler, C., 1986. Anatomical evidence for direct projections from the entorhinal area to the entire cortical mantle in the rat. J. Neurosci. 6, 3010–3023.

Tamamaki, N., Nojyo, Y., 1995. Preservation of topography in the connections between the subiculum, field CA1, and the entorhinal cortex in rats. J. Comp. Neurol. 353, 379–390.

Taylor, K.I., Probst, A., 2008. Anatomic localization of the transentorhinal region of the perirhinal cortex. Neurobiol. Aging 29, 1591–1596.

Theysohn, J.M., Kraff, O., Maderwald, S., Schlamann, M., de Greiff, A., Forsting, M., Ladd, S., Ladd, M., Gizewski, E., 2009. The human hippocampus at 7 T–in vivo MRI. Hippocampus 19, 1–7.

Theysohn, N., Qin, S., Maderwald, S., Poser, B.A., Theysohn, J.M., Ladd, M.E., Norris, D.G., Gizewski, E.R., Fernandez, G., Tendolkar, I., 2013. Memory Related Hippocampal Activity Can Be Measured Robustly Using fMRI at 7 Tesla. J. Neuroimaging 23, 445–451.

Thomas, B.P., Welch, B.E., Niederhauser, B.D., Whetsell, W.O., Anderson, A.W., Gore, J.C., Avison, M.J., Creasy, J.L., 2008. High-resolution 7T MRI of the human hippocampus in vivo. J. Magn. Reson. Imaging 28, 1266–1272.

Travis, S.G., Huang, Y., Fujiwara, E., Radomski, A., Olsen, F., Carter, R., Seres, P., Malykhin, N. V., 2014. High field structural MRI reveals specific episodic memory correlates in the subfields of the hippocampus. Neuropsychologia 53, 233–245.

Treves, A., Rolls, E.T., 1994. Computational analysis of the role of the hippocampus in memory. Hippocampus 4, 374–391.

Treves, A., Rolls, E.T., 1992. Computational constraints suggest the need for two distinct input systems to the hippocampal CA3 network. Hippocampus 2, 189–199.

Triantafyllou, C., Hoge, R.D., Krueger, G., Wiggins, C.J., Potthast, A., Wiggins, G.C., Wald, L.L., 2005. Comparison of physiological noise at 1.5 T, 3 T and 7 T and optimization of fMRI acquisition parameters. NeuroImage 26, 243–250.

van Strien, N., Cappaert, N., Witter, M., 2009. The anatomy of memory: an interactive overview of the parahippocampal–hippocampal network. Nat. Rev. Neurosci. 10, 272–282.

van Veluw, S.J., Wisse, L.E.M., Kuijf, H.J., Spliet, W.G.M., Hendrikse, J., Luijten, P.R., Geerlings, M.I., Biessels, G.J., 2013. Hippocampal T2 hyperintensities on 7Tesla MRI. NeuroImage Clin. 3, 196–201.

Vieweg, P., Stangl, M., Howard, L.R., Wolbers, T., 2015. Changes in pattern completion – A key mechanism to explain age-related recognition memory deficits? Cortex.

Walther, A., Nili, H., Ejaz, N., Alink, A., Kriegeskorte, N., Diedrichsen, J., 2015. Reliability of dissimilarity measures for multi-voxel pattern analysis. NeuroImage.

Wang, Z., Neylan, T.C., Mueller, S.G., Lenoci, M., Truran, D., Marmar, C.R., Weiner, M.W., Schuff, N., 2010. Magnetic Resonance Imaging of Hippocampal Subfields in Posttraumatic Stress Disorder. Arch. Gen. Psychiatry 67, 296.

West, M., 1993. Regionally specific loss of neurons in the aging human hippocampus. 14, 287–93.

Whitfield-Gabrieli, S., Nieto-Castanon, A., 2012. Conn: a functional connectivity toolbox for correlated and anticorrelated brain networks. Brain Connect. 2, 125–141.

Williams, J.R., 2008. The Declaration of Helsinki and public health. Bull World Health Organ 86, 650–2.

Wilson, I.A., Gallagher, M., Eichenbaum, H., Tanila, H., 2006. Neurocognitive aging: prior memories hinder new hippocampal encoding. Trends Neurosci. 29, 662–670.

Winterburn, J.L., Pruessner, J.C., Chavez, S., Schira, M.M., Lobaugh, N.J., Voineskos, A.N., Chakravarty, M.M., 2013. A novel in vivo atlas of human hippocampal subfields using high-resolution 3 T magnetic resonance imaging. NeuroImage 74, 254–65.

Wisse, L.E.M., Daugherty, A.M., Olsen, R.K., Berron, D., Carr, V.A., Stark, C.E.L., Amaral, R.S.C., Amunts, K., Augustinack, J.C., Bender, A.R., Bernstein, J.D., Boccardi, M., Bocchetta, M., Burggren, A.C., Chakravarty, M.M., Chupin, M., Ekstrom, A.D., de Flores, R., Insausti, R., Kanel, P., Kedo, O., Kennedy, K.M., Kerchner, G.A., LaRocque, K.F., Liu, X., Maass, A., Malykhin, N. V., Mueller, S.G., Ofen, N., Palombo, D.J., Parekh, M.B., Pluta, J.B., Pruessner, J.C., Raz, N., Rodrigue, K.M., Schoemaker, D., Shafer, A.T., Steve, T.A., Suthana, N.A., Wang, L., Winterburn, J.L., Yassa, M.A., Yushkevich, P.A., la Joie, R., 2016a. A harmonized segmentation protocol for hippocampal and parahippocampal subregions: Why do we need one and what are the key goals? Hippocampus 27, 3–11.

Wisse, L.E.M., Gerritsen, L., Zwanenburg, J.J.M., Kuijf, H.J., Luijten, P.R., Biessels, G.J., Geerlings, M.I., 2012. Subfields of the hippocampal formation at 7 T MRI: in vivo volumetric assessment. NeuroImage 61, 1043–9.

Wisse, L.E.M., Kuijf, H.J., Honingh, A.M., Wang, H., Pluta, J.B., Das, S.R., Wolk, D.A., Zwanenburg, J.J.M., Yushkevich, P.A., Geerlings, M.I., 2016b. Automated Hippocampal Subfield Segmentation at 7T MRI. Am. J. Neuroradiol. 37, 1050–1057. doi:10.3174/ajnr.A4659

Wisse, L.E.M., Kuijf, H.J., Honingh, A.M., Wang, H., Pluta, J.B., Das, S.R., Wolk, D.A., Zwanenburg, J.J.M., Yushkevich, P.A., Geerlings, M.I., 2016c. Automated Hippocampal Subfield Segmentation at 7T MRI. 37, 1050–7.

Witter, M.P., 2007. Intrinsic and extrinsic wiring of CA3: Indications for connectional heterogeneity. Learn. Mem. 14, 705–713.

Witter, M.P., 2006. Connections of the subiculum of the rat: Topography in relation to columnar and laminar organization. Behav. Brain Res., The Mammalian Subiculum: Contrasting and complementary in vivo and in vitro approaches to subicular function 174, 251–264.

Witter, M.P., Amaral, D.G., 1991. Entorhinal cortex of the monkey: V. Projections to the dentate gyrus, hippocampus, and subicular complex. J. Comp. Neurol. 307, 437–459.

Witter, M.P., Naber, P.A., van Haeften, T., Machielsen, W.C.M., Rombouts, S.A.R.B., Barkhof, F., Scheltens, P., Lopes da Silva, F.H., 2000a. Cortico-hippocampal communication by way of parallel parahippocampal-subicular pathways. Hippocampus 10, 398–410.

Witter, M.P., Wouterlood, F., Naber, P., Haeften, V.T., 2000b. Anatomical organization of the parahippocampal-hippocampal network. Ann. N. Y. Acad. Sci. 911, 1–24.

Wolbers, T., Büchel, C., 2005. Dissociable retrosplenial and hippocampal contributions to successful formation of survey representations. 25, 3333–40.

Wolk, D.A., Das, S.R., Mueller, S.G., Weiner, M.W., Yushkevich, P.A., 2017. Medial temporal lobe subregional morphometry using high resolution MRI in Alzheimer's disease. Neurobiol. Aging 49, 204–213.

Xie, L., Pluta, J.B., Das, S.R., Wisse, L.E.M., Wang, H., Mancuso, L., Kliot, D., Avants, B.B., Ding, S.-L., Manjón, J. V., Wolk, D.A., Yushkevich, P.A., 2017. Multi-template analysis of human perirhinal cortex in brain MRI: Explicitly accounting for anatomical variability. NeuroImage 144, 183–202.

Xie, L., Wisse, L.E., Das, S.R., Wang, H., Wolk, D.A., Manjón, J.V., Yushkevich, P.A., 2016. Accounting for the Confound of Meninges in Segmenting Entorhinal and Perirhinal Cortices in T1-Weighted MRI. doi:10.1007/978-3-319-46723-8_65

Yassa, M.A., Lacy, J.W., Stark, S.M., Albert, M.S., Gallagher, M., Stark, C., 2011a. Pattern separation deficits associated with increased hippocampal CA3 and dentate gyrus activity in nondemented older adults. Hippocampus 21, 968–979. doi:10.1002/hipo.20808

Yassa, M.A., Mattfeld, A.T., Stark, S.M., Stark, C.E., 2011b. Age-related memory deficits linked to circuit-specific disruptions in the hippocampus. Proc. Natl. Acad. Sci. U. S. A. 108, 8873–8878. doi:10.1073/pnas.1101567108

Yassa, M.A., Muftuler, T.L., Stark, C.E., 2010a. Ultrahigh-resolution microstructural diffusion tensor imaging reveals perforant path degradation in aged humans in vivo. Proc. Natl. Acad. Sci. U. S. A. 107, 12687–12691.

Yassa, M.A., Stark, C., 2011. Pattern separation in the hippocampus. Trends Neurosci. 34.

Yassa, M.A., Stark, C., 2009. A quantitative evaluation of cross-participant registration techniques for MRI studies of the medial temporal lobe. NeuroImage 44, 319–327.

Yassa, M.A., Stark, S.M., Bakker, A., Albert, M.S., Gallagher, M., Stark, C., 2010b. High-resolution structural and functional MRI of hippocampal CA3 and dentate gyrus in patients with amnestic Mild Cognitive Impairment. NeuroImage 51, 1242–1252.

Yushkevich, P.A., Amaral, R.S.C., Augustinack, J.C., Bender, A.R., Bernstein, J.D., Boccardi, M., Bocchetta, M., Burggren, A.C., Carr, V. a., Chakravarty, M.M., Chételat, G., Daugherty, A.M., Davachi, L., Ding, S.-L., Ekstrom, A.D., Geerlings, M.I., Hassan, A.S., Huang, Y., Eugenio Iglesias, J., La Joie, R., Kerchner, G. a., LaRocque, K.F., Libby, L.A., Malykhin, N. V., Mueller, S.G., Olsen, R.K., Palombo, D.J., Parekh, M.B., Pluta, J.B., Preston, A.R., Pruessner, J.C., Ranganath, C., Raz, N., Schlichting, M.L., Schoemaker, D., Singh, S., Stark, C.E.L., Suthana, N.A., Tompary, A., Turowski, M.M., Van Leemput, K., Wagner, A.D., Wang, L., Winterburn, J.L., Wisse, L.E.M., Yassa, M.A., Zeineh, M.M., Hippocampal Subfields Group (HSG), 2015a. Quantitative comparison of 21 protocols for labeling hippocampal subfields and parahippocampal subregions in in vivo MRI: Towards a harmonized segmentation protocol. NeuroImage 111, 526–541.

Yushkevich, P.A., Piven, J., Hazlett, H.C., Smith, R.G., Ho, S., Gee, J.C., Gerig, G., 2006. User-guided 3D active contour segmentation of anatomical structures: Significantly improved efficiency and reliability. NeuroImage 31, 1116–1128.

Yushkevich, P.A., Pluta, J.B., Wang, H., Xie, L., Ding, S.-L., Gertje, E.C., Mancuso, L., Kliot, D., Das, S.R., Wolk, D.A., 2015b. Automated volumetry and regional thickness analysis of hippocampal subfields and medial temporal cortical structures in mild cognitive impairment. Hum. Brain Mapp. 36, 258–287. doi:10.1002/hbm.22627

Yushkevich, P.A., Wang, H., Pluta, J.B., Das, S.R., Craige, C., Avants, B.B., Weiner, M.W., Mueller, S.G., 2010. Nearly automatic segmentation of hippocampal subfields in in vivo focal T2-weighted MRI. NeuroImage 53, 1208–1224.

Zaitsev, M., Hennig, J., Speck, O., 2004. Point spread function mapping with parallel imaging techniques and high acceleration factors: fast, robust, and flexible method for echo-planar imaging distortion correction. Magn Reson Med 52, 1156–66.

Zeidman, P., Maguire, E.A., 2016. Anterior hippocampus: the anatomy of perception, imagination and episodic memory. Nat Rev Neurosci 17, 173–182.

Zeineh, M.M., Engel, S.A., Thompson, P.M., Bookheimer, S.Y., 2001. Unfolding the human hippocampus with high resolution structural and functional MRI 265, 111–120.

LIST OF FIGURES

LIST OF TABLES

LIST OF ABBREVIATIONS

A	*Amygdala*	LOC	*Lateral Occipital Cortex*
Abeta	*Amyloid-beta*	M	*Mammillary Bodies*
ACC	*Anterior Cingulate Cortex*	mErC	*Medial Entorhinal Cortex*
AD	*Alzheimer's Disease*	MFG	*Middle Frontal Gyrus*
AG	*Ambient Gyrus*	mL	*Milliliter*
alErC	*Anterior-lateral Entorhinal Cortex*	mm	*Millimeter*
Alv	*Alveus*	MoCA	*Montreal Cognitive Assessment*
ANOVA	*Analysis of Variance*	MOG	*Middle Occipital Gyrus*
ANTs	*Advanced Normalization Tools*	MPRAGE	*Magnetization-Prepared Rapid Gradient-Echo*
ASHS	*Automated Segmentation of Hippocampal Subfields*	MR	*Magnetic Resonance*
AT	*Anterior-Temporal*	MRI	*Magnetic Resonance Imaging*
BOLD	*Blood-Oxygen-Level Dependent*	MST	*Mnemonic Similarity Task*
CA	*Cornu Ammonis*	MTG	*Middle Temporal Gyrus*
CaS	*Calcarine Sulcus*	MTL	*Medial Temporal Lobe*
CBV	*Cerebral Blood Volume*	MVPA	*Multi Voxel Pattern Analysis*
CLS	*Complementary Learning Systems Model*	NFT	*Neurofibrillary Tangles*
Col	*Colliculi*	NIfTI	*Neuroimaging Informatics Technology Initiative*
CS	*Collateral Sulcus*	OFC	*Orbitofrontal Cortex*
CSa	*Anterior Collateral Sulcus*	OTS	*Occipito-temporal Sulcus*
CSF	*Cerebrospinal Fluid*	PET	*Positron Emission Tomography*
CSp	*Posterior Collateral Sulcus*	PhC	*Parahippocampal Cortex*
DG	*Dentate Gyrus*	PhG	*Parahippocampal Gyrus*
DSI	*Dice Similarity Index*	PhligS	*Parahippocampal Ligual Gyrus*
EPI	*Echo-Planar Imaging*	PM	*Posterior-Medial*
ErC	*Entorhinal Cortex*	pmErC	*Posterior-medial Entorhinal Cortex*
FAR	*False Alarm Rate*	POR	*Postrhinal Cortex*
FDR	*False Discovery Rate*	PrC	*Perirhinal Cortex*
FG	*Fusiform Gyrus*	RAVLT	*Raven Auditory Verbal Learning Test*
FIM	*Fimbria*	RHM	*Representational Hierarchical Model*
fMRI	*Functional Magnetic Resonance Imaging*	ROI	*Region of Interest*
FSL	*FMRIB Software Library*	RSA	*Representational Similarity Analysis*
GLM	*General Linear Model*	RsC	*Retrosplenial Cortex*
HB	*Hippocampal Body*	SaS	*Semiannular Sulcus*
HC	*Hippocampus*	SEM	*Standard Error of the Mean*
HH	*Hippocampal Head*	SFG	*Superior Frontal Gyrus*
HR	*Hit Rate*	SNR	*Signal-to-Noise*
HRF	*Hemodynamic Response Function*	SOG	*Superior Occipital Gyrus*
HT	*Hippocampal Tail*	SPM	*Statistical Parametric Mapping*
ICC	*Intraclass Correlation Coefficient*	SRLM	*Stratum Radiatum Lacunosum Moleculare*
IFG	*Inferior Frontal Gyrus*	Sub	*Subiculum*
IOG	*Inferior Occipital Gyrus*	T	*Tesla*
IPL	*Inferior Parietal Lobule*	TE	*Echo Time*
ISI	*Inter Stimulus Interval*	TR	*Repetition Time*
ITG	*Inferior Temporal Gyrus*	TSE	*Turbo Spin Echo*
lErC	*Lateral Entorhinal Cortex*	vmPFC	*Ventromedial Prefrontal Cortex*
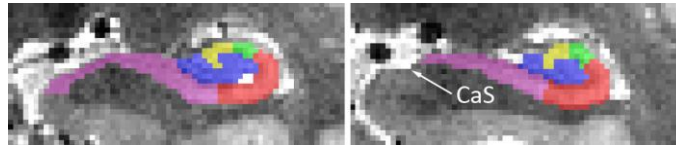
Supplementary Figure 1. Chapter 2 - Calcarine sulcus (CaS) appears and its banks are spared from segmentation.
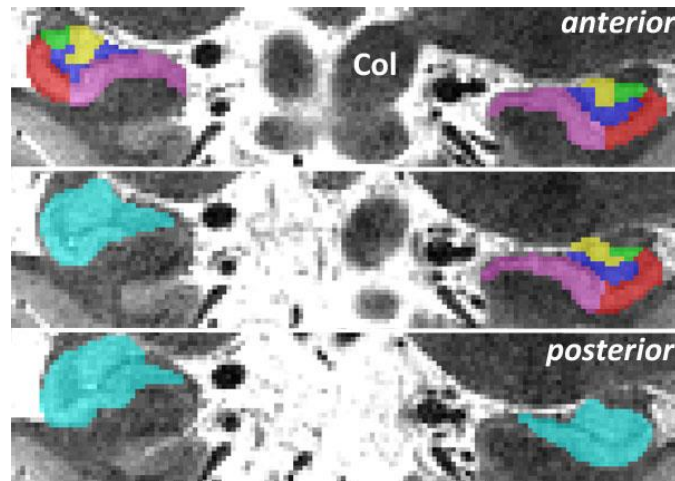
Supplementary Figure 2. Chapter 2 - Transition from hippocampal body (top) to hippocampal tail (bottom) dependent on the presence of the inferior und superior colliculi (Col) for each hemisphere separately. Hippocampal subfields are only segmented in the body, and not in the tail.
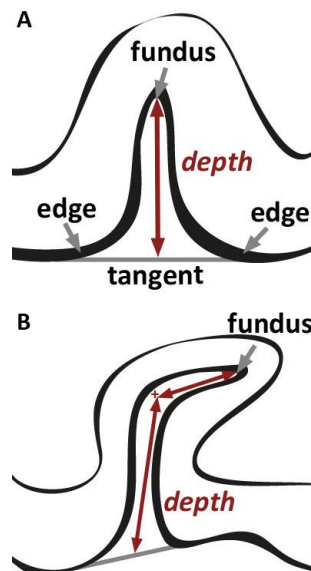
Supplementary Figure 3. Chapter 2 - Sulcus depth measurement. The edges adjacent to the sulcus are connected via a tangent line (grey line). (A) The depth of a straight sulcus is measured from the middle of the tangent to the fundus of the sulcus (red arrow). (B) If the sulcus bends, the depth is measured along the middle of the sulcus in separate legs, the lengths of which are summed up (red arrows connected via +).
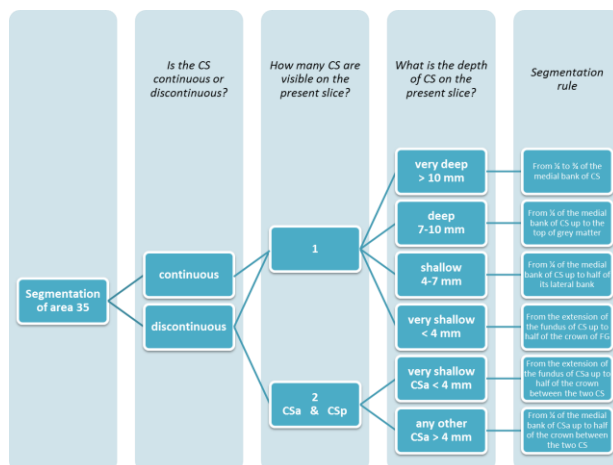
Supplementary Figure 4. Chapter 2 - Decision tree for segmentation of area 35. Applies to every coronal slice.
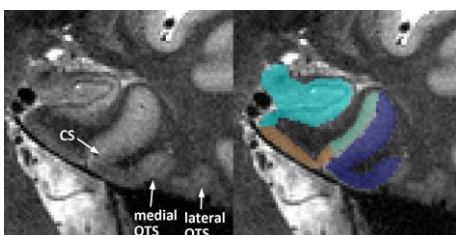
Supplementary Figure 5. Chapter 2 - double OTS. This is an example of the variability of OTS. In case of two OTS or a bifurcated OTS, the more medial OTS is chosen as the lateral border of area 36.

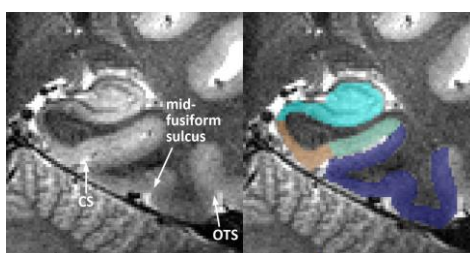**Supplementary Figure 6. Chapter 2 - Mid-fusiform sulcus.** This sulcus lies between the collateral sulcus (CS) and the occipitotemporal sulcus (OTS). It can be identified as it is considerably shallower than OTS, and it usually appears only in very posterior slices; mostly it even appears after perirhinal cortex segmentation has stopped.
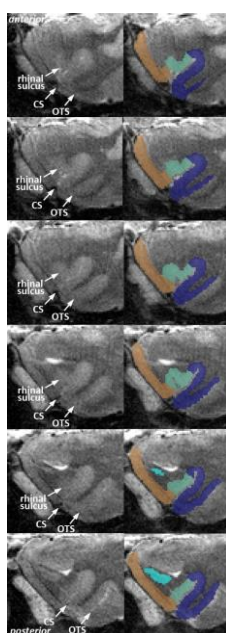
Supplementary Figure 7. Chapter 2 - Rhinal sulcus. It lies medial to the collateral sulcus (CS) and is more shallow; it often 'moves' up the CS. Usually, it is visible in very anterior slices, mostly even before segmentation starts. If the rhinal sulcus is separate from CS within the segmentation range the rules change (see main text), but this occurs only in very rare cases.
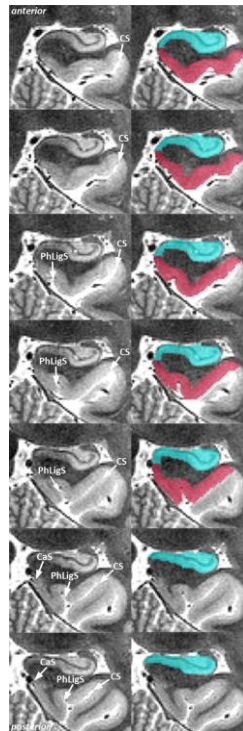
Supplementary Figure 8. Chapter 2 - Parahippocampal-ligual sulcus (PhligS) and calcarine sulcus (CaS). The PhligS often 'moves' laterally up along the collateral sulcus (CS). CaS is always medial to PhligS.
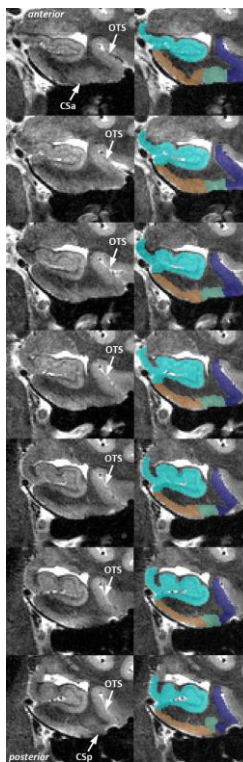
Supplementary Figure 9. Chapter 2 - Gap between anterior and posterior collateral sulcus (CS). When neither CSa nor CSp are visible in the coronal slice, the boundaries between entorhinal cortex, area 35 and 36 should be extrapolated from the next slices were the collateral sulci can be identified.

Post segmentation checklist

For all structures:

- cysts, CSF, wide sulci, blood vessels, fimbria, alveus and meninges are excluded from segmentation

Hippocampus:

- SRLM is equally divided between structures
- all borders are applied orthogonally to the structure
- HH → until uncal apex
  (1) Sub and ErC are connected when the uncal sulcus can be followed from surface to its fundus
  (2) DG replaces the SRLM as the most lateral point for CA1/Sub border when DG appears
  (3) CA1 replaces Sub superiorly 2 slices (2.2 mm) posterior to where DG appears
  (4) last 4 HH slices (4.4 mm) include CA2/CA3 segmentation
    - borders extrapolated from slice where the uncus is separate from the hippocampus
    - CA1/Sub border at ¼ medial to lateral DG
- HB → when uncus has disappeared
  (1) CA1/Sub border at ½ medial to lateral DG
  (2) CaS is excluded from segmentation
  (3) subfield segmentation stops when colliculi of the particular hemisphere disappear entirely

Extrahippocampal regions:

- ErC/area 35/area 36 start 4 slices (4.4 mm) anterior to HH
- ErC superiorly ends at SaS (possibly extrapolated from posterior slices)
- Sulcus depths: see decision tree in Supplementary Figure 4
- ErC stops 2 slices (2.2 mm) posterior to HH (uncal apex)
- Area 35/36 stop 4 slices (4.4. mm) posterior to HH (uncal apex)
- Transitions:
  (1) last slice of ErC
  (2) on CSa slice for type II when CSa only changes to CSp only
  (3) when OTS jumps
- PhC begins 5 slices (5.5 mm) posterior to HH directly after the end of area 35/area 36
-
- PhC stops when CaS appears

Supplementary Figure 10. Chapter 2 - Post segmentation checklist.
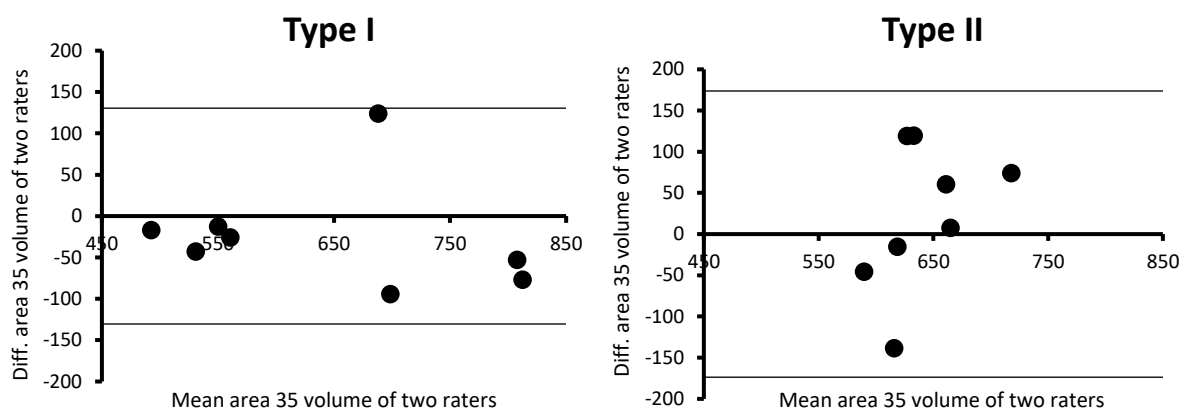
Supplementary Figure 11. Chapter 2 - Bland Altman plots of area 35 volume for type I and type II sulcal patterns. The lines indicate the limits of agreement (0 ± 1.96 SD).
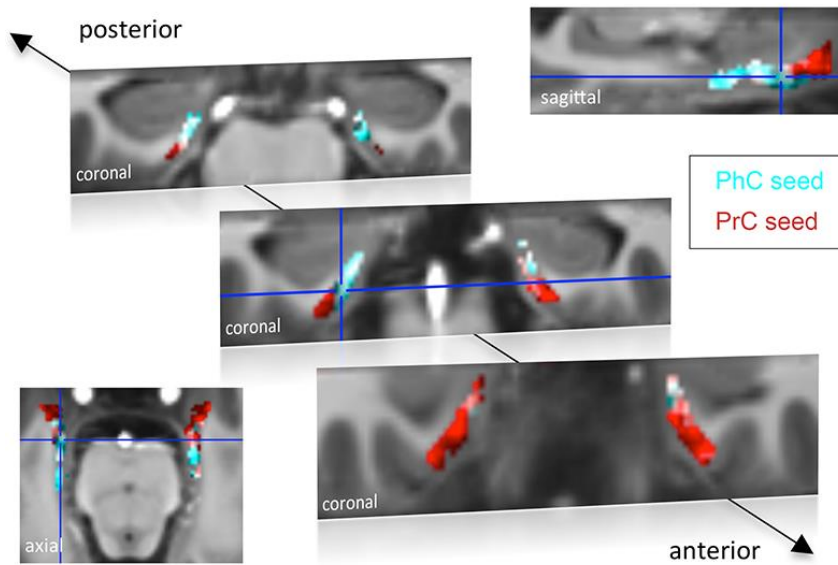
Supplementary Figure 12. Chapter 4 –Functional connectivity profiles of PhC/PrC seeds with the ErC for dataset 2. Group results for seed-to-voxel connectivity of bilateral PrC and PhC seeds with the ErC shown for dataset 2 (one-sample t-test; Z > 2.3, $p_{cluster}$ < 0.05, N = 15). Bright regions denote overlapping connectivity with PrC/PhC. Single-subject beta maps were normalized on the group-specific T1-template by ROI-based alignment with ANTS and masked with a manually defined ErC mask. The T1-template has the same resolution as the high-resolution functional EPI volumes (0.8 mm x 0.8 mm x 0.8 mm). ROI: region of interest. This figure is taken from Maass et al., 2015.
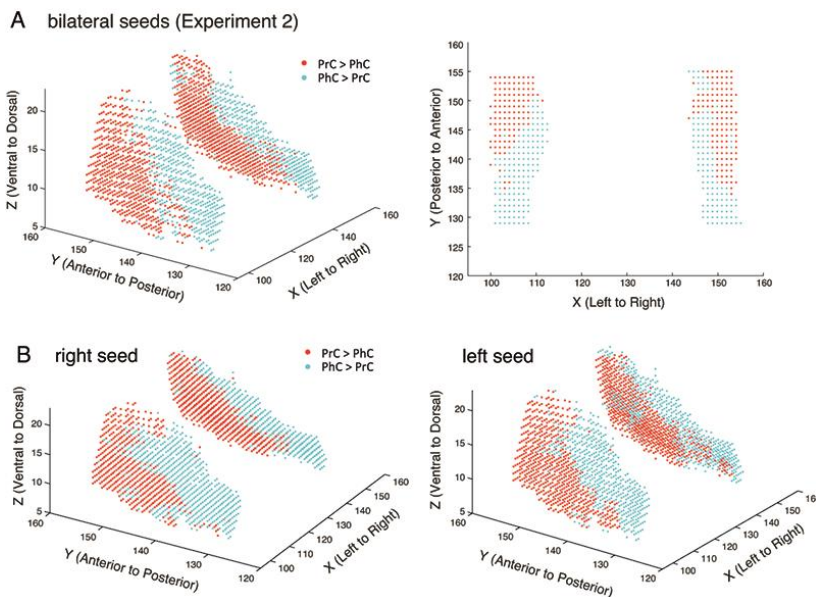
Supplementary Figure 13: Chapter 4 - Differential connectivity topography of bilateral (A) and unilateral (B) PrC vs. PhC seeds with the ErC for dataset 2 (A) and dataset 1 (B). (A) To visualize the 3-dimensional geometry of connectivity, the connectivity preference with PrC vs. PhC of each ErC voxel was plotted along the x-, y-, and z-axis (red: $T_{PRC > PHC}$ > 0, blue: $T_{PHC > PRC}$ > 0). These plots indicated a complex 3-dimensional topography of ErC connectivity with a gradient of PrC-to-PhC preference running from anterior-ventral-lateral to posterior-dorsal-medial ErC also for dataset 2. (B) In addition, the functional connectivity preference of unilateral (left and right) PrC/PhC seeds with both the ipsi- and contralateral ErC was plotted to evaluate whether connectivity patterns were symmetric across hemispheres. This figure is taken from Maass et al., 2015.
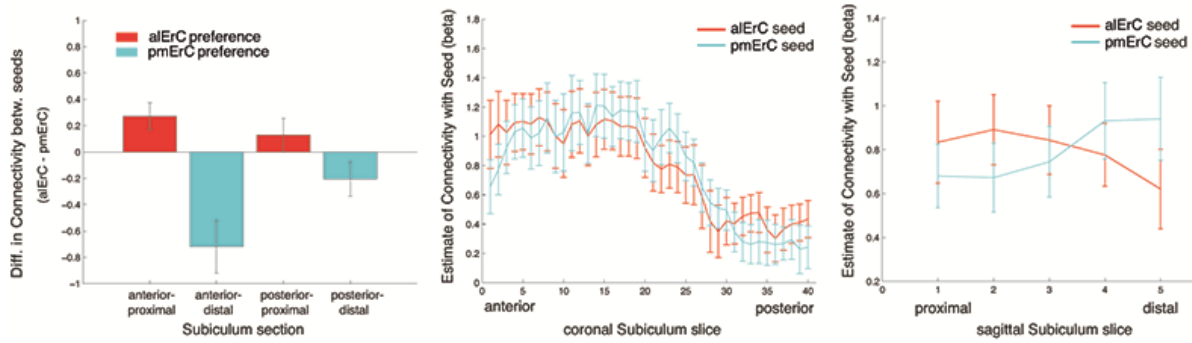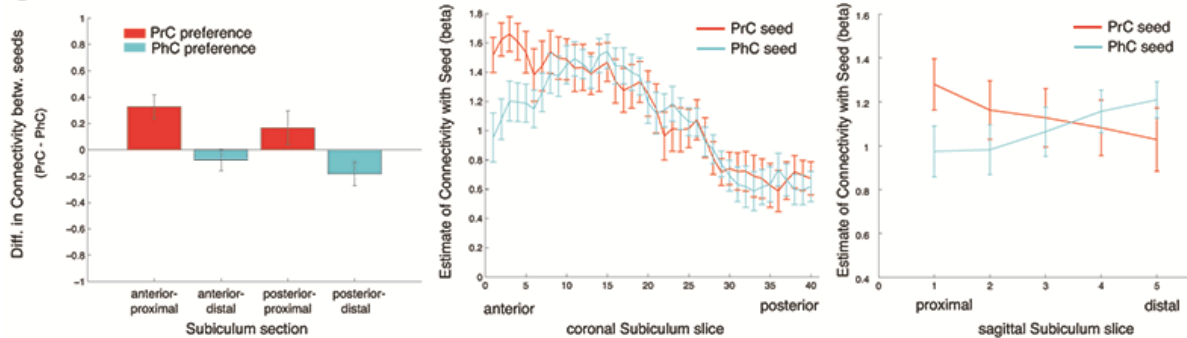
Supplementary Figure 14: Chapter 4 - Functional connectivity gradients in the subiculum related to ErC subregions (A) and PrC/PhC seeds (B) for dataset 2. (A) To test for differential connectivity of ErC functional subdivisions with the subiculum, anterior-lateral ErC (alErC) and posterior-medial ErC (pmErC) regions that exhibited preferential connectivity with PrC vs. PhC, respectively (see paired t-tests in Figure 22A) were used as seed regions. The subiculum mask was equally divided into four portions along the longitudinal (anterior vs. posterior) and transverse (proximal vs. distal) axis and mean betas of functional connectivity with ErC seeds were extracted for each subsection. Repeated-measures ANOVAs revealed a significant seed (alErC vs. pmErC) x proximal-distal subiculum interaction in both datasets ($p < 0.001$; $N_1 = 15$, $N_2 = 14$; results shown for dataset 2). Slice-by-slice plots of connectivity estimates demonstrated decreasing alErC-connectivity and increasing pmErC connectivity from proximal to distal subiculum but no anterior-posterior dissociation. (B) Similarly, connectivity for PrC vs. PhC seeds with the subiculum along the longitudinal and transverse axis was evaluated. Seed (PrC vs. PhC) x proximal-distal subiculum section interactions were significant across both datasets ($p < 0.01$) with preferential connectivity of PrC with proximal and PhC with distal subiculum, respectively. Slice-by-slice plots of connectivity estimates along the hippocampal long axis revealed stronger PrC than PhC connectivity with the most anterior subiculum (= 8 slices) in dataset 2. This figure is taken from Maass et al., 2015.

Supplementary Table 1. Group activation for young individuals

Contrast	Cluster size	Cluster p$_{FDR}$	Cluster p$_{unc}$	Peak T	Peak location	Template x, y, z	hemisphere
Young: Scenes vs. objects							
	66266	0.000	0.000	12.79	PhC	-17 -38 -11.7	L
				12.79	PCC	14 -53 5.3	R
				12.58	PhC	22 -33 -14.7	R
	5989	0.000	0.000	9.97	SOG	34 -78 7.3	R
				8.02	Precuneus	37 -81 15.3	R
				5.35	MTG	40 -68 9.3	R
	2471	0.000	0.000	6.25	SOG	-37 -83 9.3	L
				5.34	SOG	-30 -88 15.3	L
				4.59	SOG	-36 -83 17.3	L
	558	0.000	0.000	4.86	SFG	19 3 47.3	R
				4.62	SFG	26 -1 48.3	R
				4.60	MFG	21 -10 46.3	R
Young: Objects vs. scenes							
	30506	0.000	0.000	15.35	MOG	45 -64 -20.7	R
				14.52	IOG	33 -79 -22.7	R
				13.55	Cuneus	18 -95 -16.7	R
	36099	0.000	0.000	14.76	IOG	-42 -75 -22.7	L
				14.59	IOG	-30 -83 -25.7	L
				14.02	Lingual Gyrus	-22 -88 -23.7	L
	7347	0.000	0.000	6.19	MFG	-3 41 26.3	L
				5.70	ACC	9 28 31.3	R
				5.40		12 27 56.3	R
	1836	0.000	0.000	5.92	Caudate	14 11 10.3	R
				5.35		3 -5 10.3	R
				4.74	Thalamus	-5 -7 9.3	L
	548	0.001	0.000	5.87	IFG	25 22 -3.7	R
				4.97	IFG	32 25 5.3	R
				3.68	Insula	32 21 12.3	R
	469	0.001	0.000	5.82	MFG	57 19 26.3	R
				4.87	IFG	60 10 22.3	R
	703	0.000	0.000	5.51	Amygdala	-17 -3 -9.7	L
				3.98	Amygdala	-25 -3 -8.7	L
	2273	0.000	0.000	5.45	IFG	44 22 3.3	R
				5.01	IFG	51 19 11.3	R
				4.71	IFG	42 26 -3.7	R
	413	0.003	0.000	5.43	Thalamus	-10 -31 0.3	L
				4.84		-18 -26 -3.7	L
	5669	0.000	0.000	5.34	IPL	-41 -44 37.3	L
				5.25		-23 -34 59.3	L
				5.21		-22 -52 59.3	L
	699	0.000	0.000	5.23		-36 35 -0.7	L
				4.85	IFG	-40 27 -0.7	L
				3.44	MFG	-26 34 0.3	L
	276	0.017	0.001	5.06	PrC	28 1 -25.7	R
	208	0.047	0.004	5.02	ITG	-39 -12 -23.7	L
				3.89	ITG	-36 -3 -24.7	L
	1602	0.000	0.000	5.01	MFG	48 30 26.3	R
				4.52	MFG	48 39 29.3	R
				4.46	MFG	40 49 18.3	R
	1550	0.000	0.000	4.99	IFG	-47 27 18.3	L
				4.77	MFG	-50 30 25.3	L
				4.26	IFG	-44 19 13.3	L
	516	0.001	0.000	4.96	IFG	-9 7 60.3	L
				4.67		-15 0 66.3	L
				4.03		-9 7 69.3	L
	417	0.003	0.000	4.89	PrC	-25 2 -28.7	L
				4.69	PrC	-27 12 -29.7	L
				4.09	PrC	-32 -4 -24.7	L
	233	0.033	0.003	4.85	Amygdala	20 -8 -9.7	R
	1143	0.000	0.000	4.81	SPL	22 -49 60.3	R
				4.75	SPL	39 -47 46.3	R
				4.40	SPL	29 -49 56.3	R
	402	0.003	0.000	4.72	Precentral Gyrus	-34 0 30.3	L
				3.82	IFG	-41 2 25.3	L
	280	0.017	0.001	4.66	Postcentral Gyrus	38 -35 34.3	R
				3.49	Postcentral Gyrus	30 -41 37.3	R
	300	0.013	0.001	4.39	MFG	-4 -31 54.3	L
				4.37	Paracentral Lobule	-0 -32 41.3	L
				3.56	MFG	-3 -25 47.3	L
	218	0.041	0.003	3.99	SPL	24 -62 53.3	L
				3.85	SPL	35 -60 45.3	L

PhC, parahippocampal cortex, SOG, superior occipital gyrus; MTG, middle temporal gyrus; SFG, superior frontal gyrus; MOG, middle occipital gyrus; IOG, inferior occipital gyrus; ACC, anterior cingulate cortex; IFG, inferior frontal gyrus; IPL, inferior parietal lobule; PrC, perirhinal cortex; ITG, inferior temporal gyrus, SPL, Superior Parietal Lobule

Supplementary Table 2. Group activation for elderly individuals

Contrast	Cluster size	Cluster p$_{FDR}$	Cluster p$_{unc}$	Peak T	Peak location	Template x, y, z	hemisphere
Elderly: Scenes vs. objects							
	99911	0.000	0.000	15.13	SOG	18 -60 4.3	R
				14.95	PhC	24 -39 -11.7	R
				13.46	Cerebellum	-20 -39 -15.7	L
	1170	0.000	0.000	10.00	Cerebellum	-10 -35 -49.7	L
	801	0.000	0.000	6.54	Cerebellum	10 -33 -48.7	L
	1274	0.000	0.000	5.74	SFG	25 0 50.3	R
				4.62	SFG	23 -11 45.3	R
				3.75	SFG	20 -18 42.3	R
	1199	0.000	0.000	5.50	Cingulate Gyrus	4 -28 23.3	R
				5.33	Cingulate Gyrus	-5 -26 22.3	L
				4.50	Cingulate Gyrus	-6 -36 19.3	L
	1117	0.000	0.000	5.32	MFG	28 20 48.3	R
				4.72	MFG	27 29 43.3	R
				4.66	SFG	23 13 43.3	R
	270	0.026	0.002	5.00	PhC/ErC/Sub	20 -12 -19.7	R
	356	0.008	0.001	4.87	Cerebellum	-31 -49 -56.7	L
				3.56	Cerebellum	-33 -57 -55.7	L
Elderly: Objects vs. scenes							
	25925	7	0.000	13.89	MOG	-28 -90 -17.7	L
				13.85	IOG	-30 -82 -26.7	L
				13.70	IOG	-37 -78 -23.7	L
	24941	0.000	0.000	13.78	MOG	34 -84 -18.7	R
				13.32	MOG	26 -80 -18.7	R
				11.73	MOG	27 -90 -11.7	R
	594	0.000	0.000	6.30	PrC	-28 5 -26.7	L
				4.89	PrC	-32 -3 -22.7	L
				3.91	STG	-26 14 -27.7	L
	1106	0.000	0.000	5.71	Amygdala	-18 -2 -8.7	L
				5.33	Putamen	-17 11 5.3	L
				4.98	Putamen	-23 7 -1.7	L
	407	0.003	0.000	5.48	Posterior hc	-27 -28 -8.7	L
	1338	0.000	0.000	5.35	IFG	-50 6 29.3	L
				4.83	IFG	-40 4 32.3	L
				4.73	IFG	-33 0 32.3	L
	627	0.000	0.000	5.29	MFG	-42 24 27.3	l
				4.48	IFG	-50 34 24.3	L
				4.36	MFG	-51 25 30.3	l
	443	0.002	0.000	4.89	Caudate Head	12 12 8.3	l
				4.26	Caudate Body	17 8 14.3	R
				4.22	Caudate Body	10 3 12.3	R
	516	0.001	0.000	4.72	PrC	28 5 -29.7	R
				4.23	PrC	38 -1 -21.7	R

PhC, parahippocampal cortex, SOG, superior occipital gyrus; MTG, middle temporal gyrus; SFG, superior frontal gyrus; MOG, middle occipital gyrus; IOG, inferior occipital gyrus; ACC, anterior cingulate cortex; IFG, inferior frontal gyrus; IPL, inferior parietal lobule; PrC, perirhinal cortex; ITG, inferior temporal gyrus; ErC, entorhinal cortex; Sub, subiculum; STG, superior temporal gyrus; HC, hippocampus.

CURRICULUM VITAE

date of birth	15/03/1986	
place of birth	Riedlingen, Germany	
nationality	German	

education	04/2012-	**Otto-von-Guericke-University Magdeburg, Germany**
		Institute of Cognitive Neurology and Dementia Research (IKND) and German Center
		for Neurodegenerative Diseases Magdeburg (DZNE)
		PhD student
		Supervisor: Prof. Dr. Emrah Düzel
	2010	**Massachusetts Institute of Technology, Boston, MA (USA)**
		Department of Brain and Cognitive Sciences
		3 month research stay, PI: John Gabrieli
	10/2006	**University of Bremen**
	-12/2011	*Diploma in Psychology*
		Majors: Neuropsychology and Clinical Psychology
		Minor: Clinical Neurology, Work and Organizational Psychology

grants and	2012-2015	*Excellence doctoral scholarship*
scholarships		German National Academic Foundation
	2009-2012	*Excellence student scholarship*
		German National Academic Foundation
	2010	*Short term grant*
		Felgenhauer Foundation of the German Neurological Society (DGN)

publications

Berron, D.*, Vieweg, P.*, Hochkeppler, A., Pluta, J.B., Ding, S.-L., Maass, A., Luther, A., Xie, L., Das, S.R., Wolk, D.A., Wolbers, T., Yushkevich, P.A., Düzel, E., Wisse, L.E.M., 2017. A protocol for manual segmentation of medial temporal lobe subregions in 7Tesla MRI. **NeuroImage: Clinical** 15, 466–482. *Denotes equal first and senior author contributions.

Berron, D., Schütze, H., Maass, A., Cardenas-Blanco, A., Kuijf, H., Kumaran, D., Düzel, E., 2016. Strong Evidence for Pattern Separation in Human Dentate Gyrus. *The Journal of Neuroscience* 36, 7569–7579.

Loh, E., Kurth-Nelson, Z., **Berron, D**., Dayan, P., Duzel, E., Dolan, R., Guitart-Masip, M., 2016. Parsing the Role of the Hippocampus in Approach–Avoidance Conflict. *Cerebral Cortex*.

Moon, H., Becke, A., **Berron, D**., Becker, B., Sah, N., Benoni, G., Janke, E., Lubejko, S., Greig, N., Mattison, J., Duzel, E., van Praag, H., 2016. Running-Induced Systemic Cathepsin B Secretion Is Associated with Memory Function. *Cell Metabolism*.

Loh, E., Kumaran, D., Koster, R., **Berron, D**., Dolan, R., Duzel, E., 2016. Context-specific activation of hippocampus and SN/VTA by reward is related to enhanced long-term memory for embedded objects. *Neurobiology of Learning and Memory* 134, 65–77.

Wisse, L.E.M., Daugherty, A.M., Olsen, R.K., **Berron, D**., Carr, V.A., et al. for the Hippocampal Subfields Group. 2016. A harmonized segmentation protocol for hippocampal and parahippocampal subregions: Why do we need one and what are the key goals? *Hippocampus*.

Berron, D., Frühholz, S., Herrmann, M., 2015. Neural Control of Enhanced Filtering Demands in a Combined Flanker and Garner Conflict Task. *Plos One* 10, e0120582.

Maass, A.*, **Berron, D.***, Libby, L., Ranganath, C.*, Düzel, E.*, 2015. Functional subregions of the human entorhinal cortex. *eLife* 4. *Denotes equal first and senior author contributions.

Maass, A., Schütze, H., Speck, O., Yonelinas, A., Tempelmann, C., Heinze, H.-J., **Berron, D**., Cardenas-Blanco, A., Brodersen, K., Stephan, K., Düzel, E., 2014. Laminar activity in the hippocampus and entorhinal cortex related to novelty and episodic encoding. *Nature communications* 5, 5547.

XII

DECLARATION OF ORIGINALITY/EIGENSTÄNDIGKEITSERKLÄRUNG

I herewith declare that this thesis entitled *Functional Architecture of Medial Temporal Lobe Pathways and Mnemonic Discrimination in Young and Elderly Adults* is the result of my own independent work/investigation, except where otherwise stated. Other sources are acknowledged by explicit references. Additionally, this work has not been submitted in substance for any other degree or award at this or any other university or place of learning, nor is being submitted concurrently in candidature for any degree or other award.

Hiermit erkläre ich, dass ich die von mir eingereichte Dissertation zum Thema *Functional Architecture of Medial Temporal Lobe Pathways and Mnemonic Discrimination in Young and Elderly Adults* selbständig verfasst, nicht bereits als Dissertation verwendet habe und die benutzten Hilfsmittel und Quellen vollständig angegeben wurden. Weiterhin erkläre ich, dass ich weder diese noch eine andere Arbeit zur Erlangung des akademischen Grades doctor rerum naturalium (Dr. rer. nat.) an anderen Einrichtungen eingereicht habe.

Magdeburg, 21.02.2017

David Berron